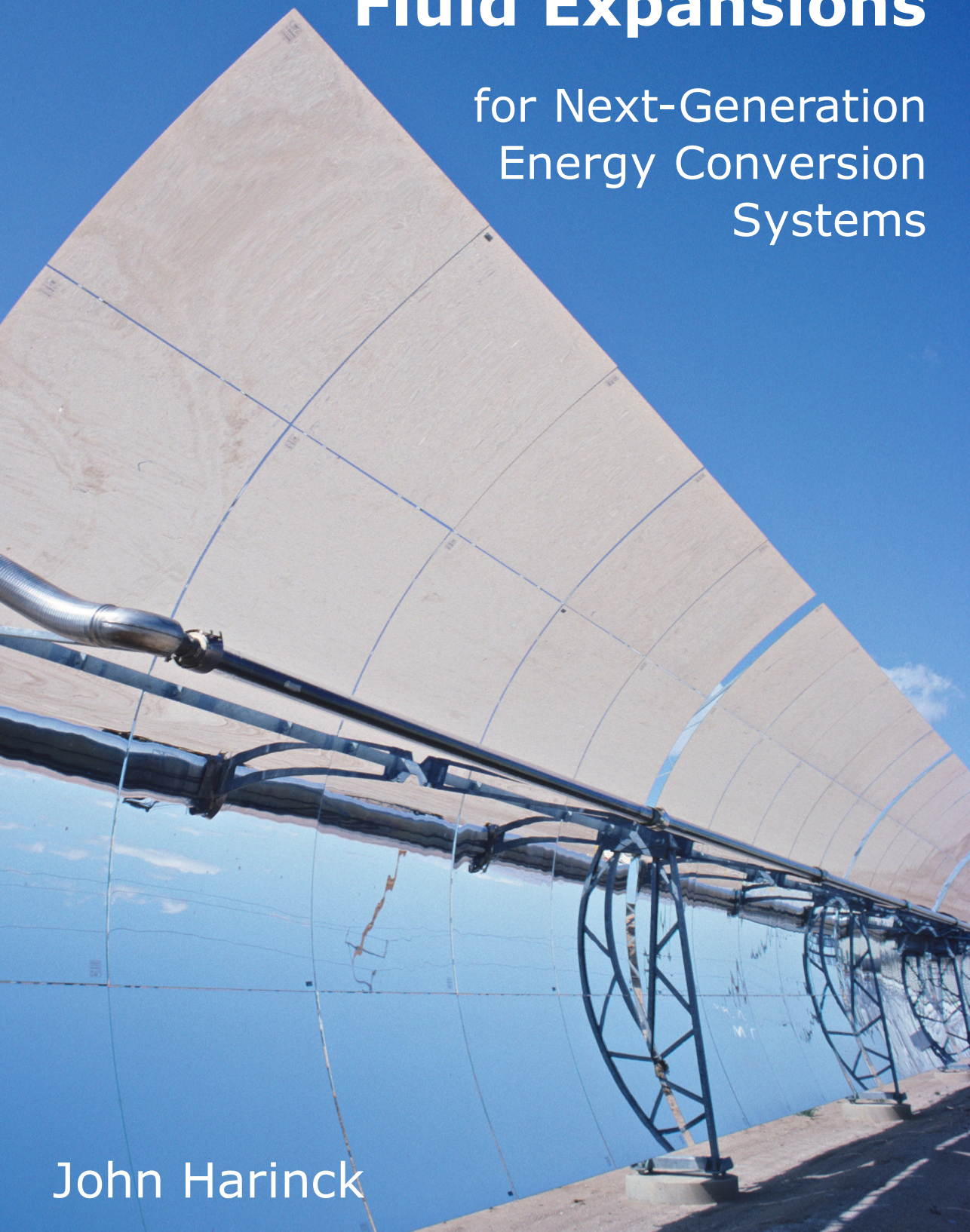# Super- and Transcritical Fluid Expansions

for Next-Generation Energy Conversion Systems

John Harinck

SUPER- AND TRANSCRITICAL FLUID EXPANSIONS FOR NEXT-GENERATION ENERGY CONVERSION SYSTEMS

Proefschrift

ter verkrijging van de graad van doctor
aan de Technische Universiteit Delft,
op gezag van de Rector Magnificus prof. ir. K. C. A. M. Luyben,
voorzitter van het College voor Promoties
in het openbaar te verdedigen op dinsdag 12 januari 2010 om 15.00 uur.

door

John HARINCK

werktuigkundig ingenieur
geboren te Breda, Nederland

Dit proefschrift is goedgekeurd door de promotor:

Prof. dr. G.J. Witkamp

en de copromotor:

Dr. P. Colonna

Samenstelling promotiecommissie:

Rector Magnificus	voorzitter
Prof. dr. G. J. Witkamp	Technische Universiteit Delft, promotor
Dr. P. Colonna	Technische Universiteit Delft, copromotor
Prof. ir. J. P. van Buijtenen	Technische Universiteit Delft
Prof. dr. ir. B. Koren	Universiteit Leiden
Dr. S. Rebay	Università degli Studi di Brescia, Italië
Prof. dr. J. Larjola	Lappeenranta University of Technology, Finland
Prof. dr. P. Cinnella	Arts et Métiers ParisTech, Frankrijk
Prof. dr. F. Scarano	Technische Universiteit Delft, reservelid

---

[1] Author e-mail address: j.harinck@tudelft.nl

Summary

The thermodynamic power cycles of the next generation offer great potential as the conceptual basis of sustainable energy converters. Examples are the supercritical and superheated Organic Rankine cycle, the transcritical condensation cycle, the supercritical Brayton cycle, the Organic Stirling cycle and the transcritical vapor compression cycle. They can be considered the next generation of well-known thermodynamic cycles, because they work with different working fluids and operate at different thermodynamic conditions, namely, close to or above the critical point of the working fluid or, at slightly lower pressures, in the dense-gas region. These characteristics offer various advantages, such as expansion across a limited number of turbine stages, reduced compression work and a better match between the heating trajectory of the working fluid and the cooling trajectory of the heat source in the heat exchanger. By taking advantage of the anomalous thermodynamic behavior of the working fluid at these conditions, it would be possible to attain higher conversion efficiency, lower cost and greater compactness of the system. In addition, more environmentally friendly working fluids could be used. This new generation of energy conversion systems would be a very attractive option for the utilization of sustainable energy sources.

The anomalous phenomena in flows involving supercritical and transcritical states are not well understood. The aim of the work documented in this thesis is to gain a better understanding of the fluid dynamics of expansions of super- and close-to-critical dense-gas fluids, which are of primary importance in the development of the next generation of thermodynamic energy conversion systems. The work documented in this thesis therefore contributes to allowing the potential efficiency gains offered by employing super- and transcritical thermodynamic cycles to be exploited in the energy systems of the future. To this purpose, this thesis presents theoretical and numerical research conducted into various aspects of the fluid dynamics of supercritical, transcritical, and dense-gas expansions. It addresses research questions of how the different thermodynamic behavior of supercritical and dense gases and different working fluid characteristics change the fluid dynamic behavior upon expansion.

Part I: Fundamental Aspects

The first part is focussed on the theoretical and fundamental physics of supercritical and dense-gas flows of fluids and its dependence on fluid characteristics.

Chapter 2 presents an investigation about the effect of the complexity of a fluid molecule on the fluid dynamic quantities sound speed, velocity and Mach number in isentropic expansions.

Ideal gas and dense gas expansions are analyzed, using the polytropic ideal gas and Van der Waals thermodynamic models to compute the properties of the fluid. In these equations, the number of active degrees of freedom of the molecule is made explicit and it is taken as a measure of molecular complexity. The obtained results are subsequently verified using highly accurate multiparameter equations of state. For isentropic expansions, the Mach number does not depend on the molecular weight of the fluid, but only on its molecular complexity and pressure ratio. Remarkably enough, the Mach number can either increase or decrease with molecular complexity, depending on the considered pressure ratio. The exit speed of sound and flow velocity, however, are dependent on both molecular complexity and weight, as well as on the inlet total temperature.

The exit flow velocity is found to be a monotonically increasing function of molecular complexity for all expansion ratios, whereas the speed of sound monotonically increases with molecular complexity only at high pressure ratios. The speed of sound is not monotone for pressure ratios around 3, which leads to the Mach number being nonmonotone at pressure ratios around 10. It should be noted that the sound speed and flow velocity depend much more strongly on molecular weight than on molecular complexity, which in realistic expansions often obscures the influence of the latter. Quantitative differences are observed between ideal and dense-gas expansions, which are dependent on the reduced inlet conditions.

The chapter concludes with the numerical simulation of two-dimensional expansions in a turbine nozzle, to document the occurrence of real-gas effects and their dependence on molecular complexity in realistic applications.

Chapter 3 presents a quantitative comparison of the effect of using thermodynamic models of various degree of complexity if applied to fluid dynamic simulations of dense-gas and transcritical (turbo)expanders, which are affected by strong real-gas effects. The 2D flow field of a standard transonic turbine stator is simulated using the state-of-the-art inviscid ZFLOW Computational Fluid Dynamics (CFD) solver coupled with a fluid property library containing the thermodynamic models. The considered thermodynamic models are, in order of increasing complexity, the polytropic ideal gas (PIG) law, the Peng-Robinson-Stryjek-Vera

(PRSV) cubic equation of state and highly accurate multiparameter equations of state (MPEoS), which are adopted as benchmark reference. The fluids are steam, toluene and R245fa. The two processes under scrutiny are a moderately nonideal subcritical expansion and a highly nonideal supercritical expansion characterized by the same pressure ratio.

Using the PIG model for moderately nonideal subcritical expansions leads to large deviations with magnitudes of at least $18 - 25\%$ in density, sound speed, velocity and total pressure loss and at least $4 - 10\%$ in Mach number, pressure, temperature and mass flow rate. The PIG model applied to highly nonideal supercritical expansions leads to a doubling of the deviations' magnitudes. The advantage of the PIG model is that its computational cost is roughly one eleventh (or one third if saturation-checks in the MPEoS are omitted) of the cost of the MPEoS. For the subcritical expansion, adopting the physically more correct cubic PRSV model leads to comparatively smaller deviations, namely $< 2\%$ (toluene and R245fa) and $< 4\%$ (steam) in all flow parameters, except for the total pressure loss error, which is comparable to that of the PIG model.

The PRSV model is reasonably accurate even for the highly nonideal supercritical expansion, for which the errors are at most 4%. The computational cost of the PRSV model is roughly nine times higher than the cost of the PIG model (or twice as high if saturation-checks in the PRSV are omitted).

Contrary to low complexity fluids like water, for complex fluids like toluene and R245fa the deviations in density, speed of sound and velocity ensuing from the use of the PIG model vary strongly along the isentropic expansions. This invalidates the approach commonly used in practice of correcting the PIG model with a properly chosen constant compressibility factor.

Part II: Applications
The second part presents two studies of the aforementioned flows in existing applications of thermodynamic energy conversion cycles. It also documents preliminary results of the simulation of supersonic free-jets and the development of an optimization system that can greatly aid the design of unconventional real-gas fluid dynamic designs.

Chapter 4 presents an investigation of real-gas effects occurring in stator nozzles of subcritical and supercritical Organic Rankine Cycles (ORCs). Two-dimensional Euler simulations of an existing axial ORC stator nozzle were carried out using a CFD code, which is linked to an accurate thermodynamic model for the working fluid (siloxane MDM). The results show that, in order to obtain efficient super- and transcritical expansions in supercritical ORCs, the pressure ratio needs

to be significantly reduced if the same stator nozzle is to be used or, reversely, a nozzle geometry with a much higher exit-to-throat area ratio is required. Furthermore, super- and transcritical expansions are characterized by a low sound speed and velocity and a very high density and mass flow rate as compared to subcritical expansions.

Chapter 5 is focussed on the comparison of various flow solver submodels for the case of the simulated flow field of an existing radial ORC stator nozzle with very high expansion ratio. In addition to real-gas effects, the flow fields of such ORCs are characterized by a distinct shock wave structure. The models under investigation included the real-gas flow solvers FLUENT, FINFLO and ZFLOW, two turbulence models and two accurate thermodynamic models of the working fluid toluene. The results showed that the commercial flow solver FLUENT is by far the most dissipative flow solver, resulting in large differences in all flow quantities and appreciably lower predictions of the isentropic nozzle efficiency. If the combination of the $k - \omega$ turbulence model and FINFLO solver is adopted, a shock-induced separation bubble appears in the calculated results, which affects in particular the variation of flow velocity and angle along the stator outlet. The accurate thermodynamic models by Lemmon-Span and Goodwin lead to small differences in the flow field, especially if compared to the large deviations that would be present if the flow were simulated based on the ideal gas law. However, the older thermodynamic model by Goodwin, which is assumed to be less accurate, does differ significantly from the accurate Lemmon-Span thermodynamic model in its prediction of the specific enthalpy difference, which leads to a considerably different value for the specific work and stator isentropic efficiency. The above differences point to a need for experimental validation of flow solvers in real-gas conditions, if CFD tools are to be applied for performance improvements of high expansion-ratio turbines operating (partly) in the dense-gas regime.

Chapter 6 treats the validation of the inviscid ZFLOW code for the underexpanded free-jet fluid dynamic case. The flow solver is well able to represent supersonic free-jets, except for the parts that are dominated by viscous effects. This work serves as the first step towards the simulation and validation of ZFLOW for highly underexpanded free jets generated by the expansion of supercritical fluids for the purpose of particle production processes.

Chapter 7 documents preliminary results of a global optimization system for unconventional real-gas fluid dynamic designs that has been developed. The system comprises a Genetic Algorithm, an Artificial Neural Network (ANN) and the ZFLOW flow solver. Considerable acceleration of the global optimization strategy, which typically requires a very high number of fluid dynamic evaluations,

was achieved by means of an optimal use of the ANN. Preliminary results have been obtained by applying it to the optimization of a nozzle expanding a Bethe-Zel'dovich-Thompson (BZT) fluid.

Samenvatting

De volgende generatie thermodynamische cycli biedt veel potentie als de conceptuele basis voor duurzame energieomzetters. Voorbeelden zijn de superkritische en oververhitte Organische Rankine cyclus, de transkritische condensatie cyclus, de superkritische Brayton cyclus, de Organische Stirling cyclus en de transkritische dampcompressie cyclus. Zij kunnen worden beschouwd als de volgende generatie van de welbekende thermodynamische cycli, omdat ze met andere werkmedia en onder andere thermodynamische condities werken, namelijk, dicht bij of boven het kritische punt van het werkmedium, of, bij iets lagere drukken, in het dichte-gas gebied. Deze kenmerken bieden verschillende voordelen, zoals expansie in een beperkt aantal turbinetrappen, lagere compressiearbeid en een betere overeenstemming van de opwarmingscurve van het werkmedium met de afkoelingscurve van de warmtebron in de warmtewisselaar. Door het aparte thermodynamische gedrag van werkmedia bij deze condities uit te buiten, zou het mogelijk zijn hogere omzettingsrendementen en lagere kosten te behalen en compactere systemen te realiseren. Bovendien zouden milieuvriendelijkere werkmedia kunnen worden gebruikt. Deze nieuwe generatie energieconversiesystemen zou een aantrekkelijke optie zijn voor het benutten van duurzame energiebronnen.

De ongewone fenomenen in stromingen die plaatsvinden rond superkritische en transkritische thermodynamische staten zijn niet goed begrepen. Het doel van het werk dat is gedocumenteerd in deze dissertatie is het verkrijgen van een beter begrip van de stromingsleer van expansies van super- en dichtbij-kritische dichtegas fluïda. Deze stromingen zijn van groot belang in de ontwikkeling van de volgende generatie van thermodynamische energieconversiesystemen. Het hierin gedocumenteerde werk draagt bij aan het benutten van de potentiële rendementsverbeteringen die toekomstige super- en transkritische thermodynamische cycli bieden. Deze dissertatie beschrijft daartoe theoretisch en numeriek onderzoek dat is uitgevoerd naar verscheidene aspecten van de stromingsleer van superkritische, transkritische en dichtegas-expansies. Het werk beantwoordt onderzoeksvragen met betrekking tot hoe het afwijkende thermodynamisch gedrag bij deze condities en de eigenschappen van werkmedia het stromingsgedrag van ex-

pansies veranderen.

Part I: Fundamentele Aspecten

Het eerste deel is gericht op de theoretische en fundamentele fysica van superkritische en dichte-gas stromingen en hun afhankelijkheid van de eigenschappen van het werkmedium.

Hoofdstuk 2 presenteert een onderzoek naar het effect van de complexiteit van een fluïdum molecuul op het stromingsgrootheden geluidssnelheid, stromingssnelheid en Mach getal in isentrope expansies.

Ideale-gas en dichte-gas expansies worden geanaliseerd, waarbij de eigenschappen van de werkmedia worden berekend met de polytropische ideale-gas en Van der Waals thermodynamische modellen. In deze toestandsvergelijkingen wordt het aantal actieve graden van vrijheid van het molecuul expliciet uitgedrukt en dit wordt gebruikt als maat voor de moleculaire complexiteit. De verkregen waarden worden vervolgens geverifieerd met uiterst nauwkeurige multiparameter toestandsvergelijkingen. Voor isentrope expansies blijkt het Mach getal niet afhankelijk te zijn van het moleculaire gewicht van het medium, maar enkel van de moleculaire complexiteit en drukverhouding. Verassend genoeg blijkt het Mach getal zowel te kunnen toenemen als afnemen als functie van de moleculaire complexiteit, afhankelijk van de beschouwde drukverhouding. De geluidssnelheid en stromingssnelheid, daarentegen, zijn afhankelijk van zowel de complexiteit als het gewicht van een molecuul, alsmede van de totale stagnatie temperatuur van de expansie.

De stromingssnelheid blijkt een monotoon toenemende functie te zijn van de moleculaire complexiteit voor alle drukverhoudingen, terwijl de geluidssnelheid alleen monotoon toeneemt met moleculaire complexiteit bij hoge drukverhoudingen. Het gedrag van de geluidssnelheid is niet monotoon voor drukverhoudingen rond 3, hetgeen leidt tot een niet-monotoon gedrag van het Mach getal rond drukverhoudingen rond 10. Er moet worden opgemerkt dat de geluidssnelheid en stromingssnelheid veel sterker afhangen van het moleculaire gewicht dan van de moleculaire complexiteit, hetgeen in realistische expansies vaak de invloed van de laatstgenoemde verbergt. Kwantitatieve verschillen zijn zichtbaar in de vergelijking tussen ideale en dichte-gas expansies en deze zijn afhankelijk van de gereduceerde stagnatiecondities.

Het hoofdstuk sluit af met de numerieke simulatie van tweedimensionale expansies in een turbinestraalbuis, teneinde de aanwezigheid van reële gas-effecten en hun afhankelijkheid van moleculaire complexiteit in realistische toepassen te documenteren.

Hoofdstuk 3 beschrijft een kwantitatieve vergelijking van de invloed van het gebruik van thermodynamische modellen van verschillende complexiteit indien toegepast op stromingssimulaties van dichte-gas en transkritische (turbo)expansie-machines, waarin sterke reële gas-effecten voorkomen. Het tweedimensionale stromingsveld van een standaard transone turbinestator wordt gesimuleerd gebruikmakende van de meest moderne invisceuze numerieke stromingssolver die is gekoppeld aan een bibliotheek van thermodynamische modellen. Deze laatste zijn, in volgorde van toenemende complexiteit, de polytropische ideale gaswet (PIG), de Peng-Robinson-Stryjek-Vera (PRSV) kubische toestandsvergelijking en uiterst nauw-keurige multiparameter toestandsvergelijkingen (MPEoS), waarbij de laatste worden gebruikt als referentiepunt. De werkmedia zijn stoom, tolueen en R245fa. De twee onderzochte processen bestaan uit een gematigd niet-ideale subkritische expansie en een zeer niet-ideale superkritische expansie gekarakteriseerd door dezelfde drukverhouding.

Het gebruik van het PIG model leidt in het geval van gematigd niet-ideale subkritische expansies tot grote afwijkingen van ten minste $18 - 25\%$ in dichtheid, geluidssnelheid, stromingsnelheid en totale drukverlies en ten minste $4 - 10\%$ in Mach getal, druk, temperatuur en massastroom. In het geval van zeer niet-ideale superkritische expansies leidt het PIG model tot een afwijking die dubbel zo hoog is. Het PIG model heeft als voordeel dat de berekeningskosten slechts een elfde (of een derde indien verzadigingschecks in de MPEoSs achterwege worden gelaten) bedragen van de kosten van het MPEoS model. In het geval van de subkritische expansie leidt het gebruik van het fysisch meer correcte kubische PRSV model tot relatief kleinere afwijkingen, namelijk $< 2\%$ (tolueen en R245fa) en $< 4\%$ (stoom) in alle stromingsgrootheden, behalve het totale drukverlies, die vergelijkbaar is met de waarde verkregen op basis van het PIG model.

Het PRSV model is redelijk nauwkeurig zelfs voor de zeer niet-ideale superkritische expansie, in welk geval de afwijkingen ten hoogste 4% bedragen. De berekeningskosten bij gebruik van dit model zijn grofweg negen maal hoger in vergelijking met het PIG model (of tweemaal zo hoog indien verzadigingschecks in het PRSV model achterwege worden gelaten.

In tegenstelling tot werkmedia die een bestaan uit relatief simpele moleculen, variëren de afwijkingen in dichtheid, geluidssnelheid en stromingsnelheid ten gevolge van het gebruik van het PIG model voor werkmedia bestaande uit een complex molecuul sterk langs de isentrope expansie. Dit bevestigt de correctheid van de vaak in de praktijk gebruikte benaderingsmethode, waarin het PIG model wordt gecorrigeerd door een correct gekozen constante waarde voor de compressibiliteitsfactor.

Part II: Toepassingen

Het tweede deel toont twee studies van de eerdergenoemde stromingen in bestaande toepassingen van thermodynamische energieconversiesystemen. Het beschrijft ook voorlopige resultaten van de simulatie van supersone vrije-jet expansies en de ontwikkeling van een optimalisatiesysteem dat aanzienlijk kan bijdragen aan het ontwerp van geometrieën en processen waarin onconventionele reële gasstromen een rol spelen.

Hoofdstuk 4 toont een studie naar reële gas-effecten aanwezig in de stator straalbuizen van subkritische en superkritische Organische Rankine Cycli (ORCs). Twee-dimensionale Euler simulaties van een bestaande axiale ORC stator straalbuis zijn uitgevoerd met behulp van een CFD code die is gekoppeld aan nauwkeurige thermodynamische modellen voor het werkmedium (siloxaan MDM). De resultaten tonen aan dat, ten einde efficiënte super- en transkritische expansies in superkritische ORCs te verkrijgen, de drukverhouding significant lager dient te zijn bij gelijkblijvende stator straalbuis-geometrie. Andersom is bij gelijkblijvende drukverhouding een straalbuis met een veel hogere uitlaat-keel verhouding nodig. Verder worden super- en transkritische expansies gekarakteriseerd door een lage geluids- en expansiesnelheid en een hoge dichtheid en massastroom in vergelijking met subkritische expansies.

Hoofdstuk 5 beschrijft de vergelijking van verscheidene codes en submodellen voor de numerieke simulatie van stromingen toegepast op de simulatie van de stroming van een bestaande radiale ORC stator straalbuis die een zeer hoge drukverhouding heeft. Naast reële gaseffecten worden de stromingsvelden van dit type ORC gekenmerkt door een duidelijke schokgolf-structuur. De beschouwde codes en modellen omvatten de reële gas-stromingssolvers FLUENT, FINFLO en ZFLOW, twee turbulentiemodellen en twee nauwkeurige thermodynamische modellen voor het werkmedium tolueen. De resultaten laten zien dat van de beschouwde commerciële stromingssolvers FLUENT veruit de meest dissipatieve stromingssolver is, hetgeen resulteert in grote verschillen in alle stromingsgrootheden en aanzienlijk lagere voorspellingen voor het isentrope rendement van de stator straalbuis. De combinatie van het $k - \omega$ turbulentiemodel en de FINFLO stromingssolver resulteert in lokale loslating van de stroming waar de schokgolf reflecteert van de statorwand. Deze loslating beïnvloedt met name de variatie in de stromingssnelheid en -hoek beschouwd langs de stator uitlaat. De nauwkeurige thermodynamische modellen ontwikkeld door Lemmon-Span en Goodwin leiden tot relatief kleine verschillen in het stromingsveld, zeker vergeleken met de grote afwijkingen die aanwezig zouden zijn indien de stroming zou zijn gesimuleerd op basis van de ide-

ale gaswet. Echter, het oudere Goodwin model, waarvan wordt aangenomen dat het minder nauwkeurig is, verschilt wel significant van het nauwkeurige Lemmon-Span thermodynamische model voor wat betreft de voorspelling van het specifieke enthalpieverschil, hetgeen leidt tot een aanzienlijk afwijkende waarde voor de specifieke arbeid van de turbine en isentropisch rendement van de stator. Deze verschillen duiden op de noodzaak tot experimentele validatie van stromings-solvers onder reële gas-condities, indien deze als ontwerpmiddel worden gebruikt om prestatieverbeteringen te verwezenlijken in turbines die (deels) opereren in het dichte-gas gebied onder hoge drukverhoudingen.

Hoofdstuk 6 behandelt de validatie van de invisceuze zFLOW code voor on-dergeëxpandeerde vrije-jet expansiestromingen. Deze stromingssolver blijkt goed in staat te zijn de stroming van de supersone vrije jet te beschrijven, behalve de delen die worden gedomineerd door visceuze effecten. Dit werk kan wor-den beschouwd als de eerste stap in de richting van de simulatie en validatie van zFLOW voor sterk ondergeëxpandeerde vrije-jets die worden gegenereerd door de expansie van superkritische fluïda in deeltjesproductieprocessen.

Hoofdstuk 7 documenteert de eerste voorlopige resultaten van een globaal optimalisatiesysteem voor onconventionele reële gasstromingsontwerpen dat is ontwikkeld. Het systeem bestaat uit een Genetisch Algoritme, een Artificieel Neuraal Netwerk (ANN) en de zFLOW flow solver. Aanzienlijke acceleratie van de globale optimalisatiestrategy, waarvoor in het algemeen een zeer groot aantal stromingssimulaties is benodigd, is bereikt door middel van een optimaal gebruik van de ANN. Voorlopige resultaten tonen de optimalisatie van het ontwerp van een straalbuis die een Bethe-Zel'dovich-Thompson (BZT) fluïdum expandeert.

Table of Contents

1

Introduction

The strong economic growth that many developed countries have experienced during the last two centuries was made possible by the discovery and large-scale utilization of fossil energy sources such as coal, oil and natural gas. At present day, the onset of the depletion of easily accessible fossil energy reserves combined with the exponentially growing world primary energy consumption resulting from rapid population growth and industrialization in developing countries has lead to fossil-based energy becoming a scarce commodity, as indicated by its upward price trend and the increasingly prominent role it plays in geopolitics [1]. Moreover, during recent decades, the harmful influence of large-scale fossil fuel utilization for the quality of the environment, and the global climate in particular, have become alarmingly apparent [2]. It is clear that the current situation cannot be sustained indefinitely and a transition to sustainable sources of energy should start now, in order not to further compromise the living conditions and ability of future generations to meet their needs. The next generation of energy conversion systems must therefore be sustainable.

1.1   Next-Generation Energy Conversion Systems

The thermodynamic cycles of the next generation offer great potential as the conceptual basis of sustainable energy converters. These cycles involve processes that take place entirely above the critical pressure and temperature of the fluid, which is referred to as *supercritical*, or processes in which either the pressure or the temperature crosses its critical point value, which are called *transcritical*. Examples are the supercritical and superheated organic Rankine cycle [3, 4, 5, 6], the transcritical condensation cycle [7, 8, 9], the supercritical Brayton cycle [10, 11, 12], the Organic Stirling cycle [13, 14] and the transcritical vapor compression cycle [15, 16, 17]. They can be considered the next generation of well-known thermodynamic cycles, because they work with different working fluids and operate at different thermodynamic conditions, namely, close to or above the critical point of the working fluid or, at slightly lower pressures, in the dense-gas region.

As will be explained in the following, these characteristics offer various advantages, such as expansion across a limited number of turbine stages, reduced compression work and a better match between the heating trajectory of the working fluid and the cooling trajectory of the heat source in the heat exchanger. Furthermore, these cycles could potentially allow for the exploitation of nonclassical gasdynamic phenomena and enhanced heat transfer close to the critical point of the working fluid, which is, however, outside the scope of this work [18, 19, 20]. By taking advantage of the anomalous thermodynamic behavior of the working

fluid at these conditions, it would be possible to attain higher conversion efficiency, lower cost and greater compactness of the system. In addition, more environmentally friendly working fluids could be used. This new generation of energy conversion systems would be a very attractive option for the utilization of sustainable energy sources, because of the following main advantages:

1. Their capability of using external heat sources, allowing for the conversion into electricity of renewable energy sources such as solar radiation, geothermal reservoirs and biomass;

2. Their capability of utilizing small amounts of low-grade energy that would otherwise be wasted and dissipated to the environment, such as geothermal heat and low to medium-temperature waste heat from industrial processes and large-scale electricity production;

3. They will have low to negligible operational costs and competitive investment costs even for small-scale applications.

One of the challenges to be tackled in order to realize renewable energy systems based on transcritical and supercritical thermodynamic cycles is the optimal fluid dynamic design of fluid machinery operating at these peculiar thermodynamic conditions, since the anomalous behavior of expanding flows at these conditions is not well understood. The work documented in this thesis aims to provide more knowledge and insight into the physics of expanding flows in the dense gas regime, and to bring forward tools and methodologies which enable the fluid dynamic design of industrial processes operating at these conditions. The following presents a short overview of next-generation energy converters, followed by a more detailed explanation about supercritical and dense-gas flows and details on the motivation of this work.

1.1.1 Supercritical Organic Rankine Cycle Turbogenerator

The Rankine power cycle, which is the basic thermodynamic cycle in all conventional steam power plants, offers great potential to utilize external sustainable energy sources such as solar, geothermal, biomass and waste heat for conversion into electricity. To efficiently apply it for the utilization of low-to-medium temperature waste heat (starting from approximately 90°C) and in the small to medium power range (from few kW_e up to few MW_e) typical for economic utilization of biomass, solar or geothermal energy, the working fluid needs to be an organic substance, e.g., a straight chain or aromatic hydrocarbon, fluorohydrocarbon, perfluorocarbon or a siloxane [3, 4, 21, 22]. The heat of vaporization of organic fluids

is much lower than that of water, so that a better match between the heating tra-
jectory of the working fluid and the cooling trajectory of the heat source can be
obtained, thus increasing the conversion efficiency [23, 6]. The expansion process
of the organic fluid entails a small specific enthalpy drop, which allows for the
adoption of a cost-effective turbine with one or two stages, without running into
the problem of high rotational speed and associated penalties on efficiency [4].
By selecting a suitable organic fluid, the power output or cycle efficiency can be
optimized for a given heat source temperature and heat input. The process flow
diagram of the so-called Organic Rankine Cycle (ORC) is shown in Figure 1.1
and the thermodynamic cycle is shown in the temperature-entropy diagram in
Fig. 1.2(a).
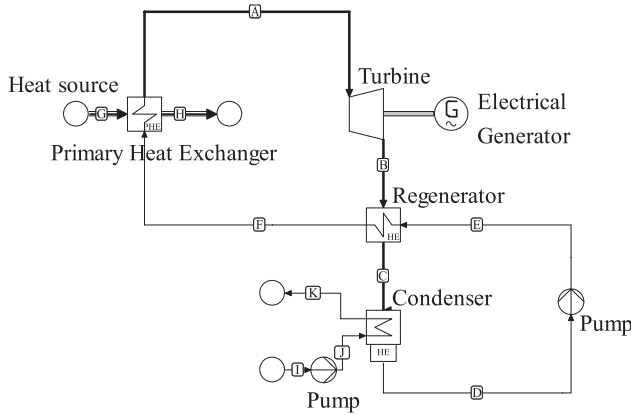
Figure 1.1: *Process flow diagram of an Organic Rankine Cycle.*

The ORC operates partially in the thermodynamic dense-gas region at condi-
tions close to the critical point of the organic working fluid, as can be observed
by looking at the temperature-entropy diagram in Fig. 1.2(a). So far, all ORC
power plants have been designed to operate at subcritical maximum cycle pres-
sures. However, by designing ORCs to operate at supercritical pressures, a pinch
point is absent and the match between the working fluid heating trajectory and
the cooling trajectory of the sensible heat source could be improved even fur-
ther. Moving towards the critical pressure, the average temperature of heat ad-
dition would also increase. This would considerably increase the conversion ef-
ficiency and power output for a given available (waste) heat source, as shown in
Refs. [5, 6] and in Fig. 1.2 for an existing ORC design. Super- and ultracriti-
cal technology is already the state-of-the-art for large-scale Rankine steam power

plants and has allowed modern steam power plants to approach efficiencies of 50 percent [24, 25, 26].
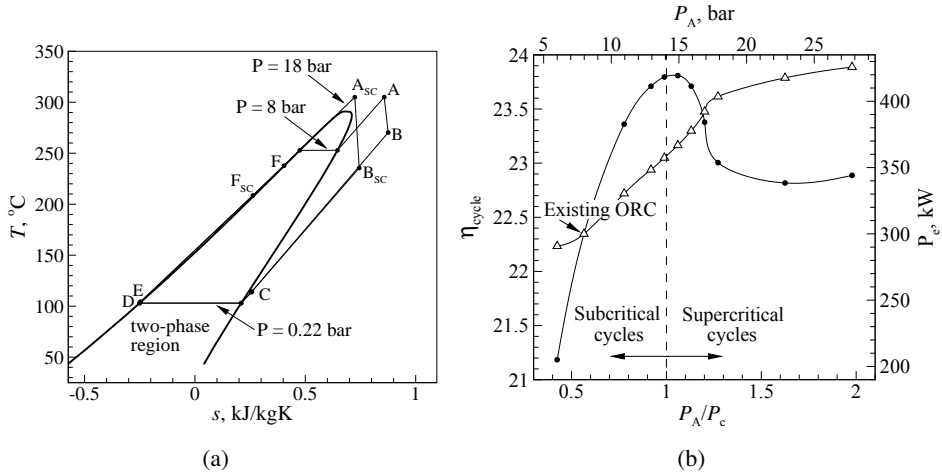
Figure 1.2: *a) Existing superheated and envisioned supercritical (SC) ORC in the temperature-entropy diagram of siloxane MDM. b) Cycle efficiency (•) and electric power output (△) as function of design turbine inlet pressure for the existing ORC. All other design parameters, except the maximum cycle pressure and power output, of which the latter is an outcome of the simulation, are kept fixed and their values are listed in Table 4.1 of Chapter 4 [27].*

Current applications of ORC turbogenerators are the electricity generation from low-grade geothermal heat reservoirs, from biomass, and the heat recovery from turbogas or reciprocating engines and industrial waste heat. Their market is growing at a rapid pace, with already hundreds of units and more than 1000 MW$_e$ installed. The use in the near future of ORC power systems coupled with solar concentrators [28, 29, 30], high-temperature fuel cells [31, 32] and for domestic cogeneration [33] is also very attractive, since they allow for small-size plants and have low investment costs. In particular solar collectors of the parabolic trough type work efficiently at medium temperatures, i.e., between 300°C and 400°C. Hence, the first plant of this type that was constructed again after a twenty years absence is a 1 MW$_e$ solar plant based on ORC technology [34]. It is also worth noting that extensive studies and experimentation on the use of ORC turbogenerators for space applications were performed in the recent past [35, 5, 36, 37].

1.1.2   Transcritical Condensation Cycle Power System

Related to the supercritical ORC, condensation and partial-condensation cycles with carbon dioxide as working fluid that operate at small-scale partially in the supercritical region (see Fig. 1.3) have been proposed, analyzed (see, e.g., Refs. [7, 8, 9]) and tested. Proposed applications range from waste heat recovery of automotive engines to concentrated solar power [38, 39, 40, 41]. These compact units offer potential for small-scale solar energy utilization, by co-generating electricity and heat for residential use.

(a)   (b)
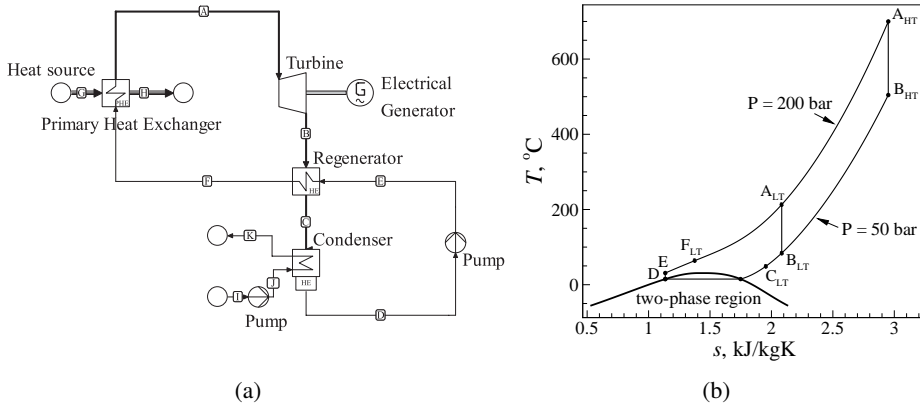
Figure 1.3: *a) Process flow diagram of a transcritical condensation cycle. b) A high-temperature (HT) and low-temperature (LT) transcritical condensation cycle with carbon dioxide as working fluid in the temperature-entropy diagram, assuming isentropic compression and expansion [7, 8, 9].*

1.1.3   Supercritical Brayton Cycle Gas Turbine

The supercritical closed Brayton cycle (gas turbine) is promising both for power and for heat pump applications [10, 11]. A conventional open Brayton cycle operates with air at pressures far from the critical point and the work required for compression is typically half of the expansion work. A supercritical closed Brayton cycle gas turbine is proposed for stationary power applications, mainly for nuclear and medium-to-large solar power conversion. In this case, carbon dioxide or helium are the working fluids. The compression process in the supercritical Brayton cycle takes place close to the working fluid's critical point (see Fig. 1.4(a)), where, due to the compressibility of the fluid, the specific volume of the fluid is

three to four times smaller as it is in the ideal gas region [10, 11, 12]. This reduces the required compression work considerably and thus increases the thermal efficiency of the cycle, which, in case of supercritical CO_2, can surpass 50 percent at a turbine inlet temperature of 550°C. The cycle is simple, very compact and costs may be reduced by as much as 20 percent if compared to a conventional Rankine steam cycle [42].
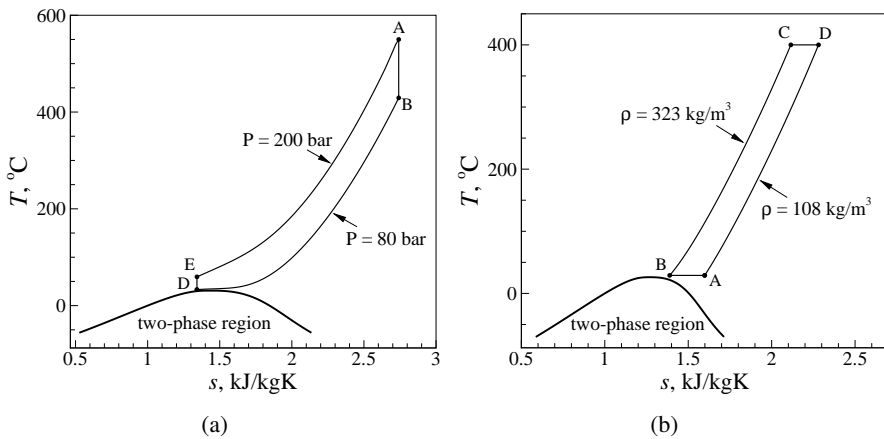
Figure 1.4: *Simplified cycles in the temperature-entropy diagram: a) the supercritical carbon dioxide Brayton power cycle, assuming isentropic compression and expansion [43]; b) the Organic Stirling cycle with refrigerant HFC-23 as working fluid, assuming isothermal compression and expansion [13].*

The supercritical CO_2 Brayton cycle has received increasing worldwide attention as power cycle for solar thermal power utilization and small and medium-size nuclear reactors for electricity generation, local heating for cities and islands or for maritime propulsion systems [44, 43, 45, 46, 47]. These systems are currently under development at Sandia National Laboratories in the US [48, 49, 50, 51].

1.1.4 Organic Stirling Cycle Engine and Heat Pump

Similarly, it has been shown that the Stirling power cycle with compression taking place in the vicinity of the critical point would have considerably diminished compression work as compared to an ideal-gas Stirling cycle [13]. To properly exploit this effect for the various technical applications that have different minimum cycle temperatures, the practical option would be to employ organic substances as

working fluids, since organic fluids allow for selection from a wide range of critical temperatures. An example of an Organic Stirling cycle using the refrigerant HFC-23 as working fluid is shown in Fig. 1.4(b).

Conversely, a reversed Stirling heat pump cycle (Philips machine) with expansion close to the critical point would allow for efficiencies similar to those of vapor-compression refrigeration cycles, but using working fluids that have zero ozone depletion and global warming potential [14].

1.1.5 Transcritical Vapor Compression Cycle System

HCFC refrigerants such as R-134a that are used in vapor-compression heat pump and refrigeration cycles will be progressively phased out, because of their still high ozone depletion potential. Alternatives such as HFC R-410A unfortunately have a very high global warming potential.

Transcritical cycles with carbon dioxide as working fluid (R-744), in which heat rejection takes place at supercritical pressure, are currently subject of research and development [15, 16, 17]. Carbon dioxide has zero ozone depletion potential and negligible global warming potential. Being a viable and more environmentally friendly alternative, transcritical carbon dioxide refrigeration cycles are promising alternatives that could replace the HCFC and HFC-based refrigeration cycles in the future [52]. They have similar efficiencies, require higher operating pressures, but have moderate pressure ratios and smaller volumes, thus enabling compact refrigeration systems that are suitable for water heating and indoor climate cooling and heating, e.g. as air conditioning system in automobiles. Moreover, by substituting the throttling valve with a turboexpander, which would need to operate across the critical point region and into the two-phase region (see Fig. 1.5(b)), the cycle coefficient of performance can be increased by, on average, 30 percent [53, 54].

1.2 Supercritical and Dense Gas Flows

An important characteristic of next-generation thermodynamic energy converters with respect to conventional ones is the fact that the expansion or compression process, as well as the heat transfer processes, take place comparatively close to or above the critical point of the working fluid.

For fluids at low pressures and high temperatures, the polytropic (constant isobaric and isochoric specific heat) ideal gas law can be used to provide the required thermodynamic property data with good accuracy as long as no phase
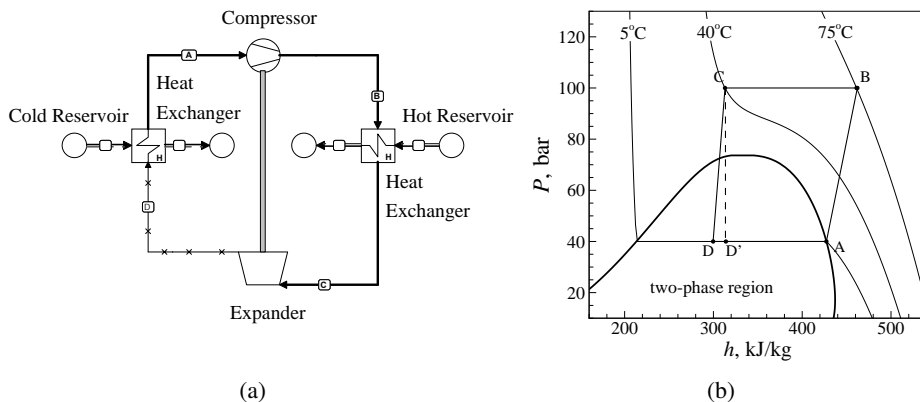
Figure 1.5: *Transcritical carbon dioxide refrigeration cycle: a) Process flow diagram of the cycle with turboexpander; b) Simplified cycle in the pressure-enthalpy diagram, assuming isentropic compression and isentropic expansion (C-D) in a turboexpander, which increases the coefficient of performance in comparison with the conventional isenthalpic throttling (C-D') across a restriction or valve.*

change occurs. However, for thermodynamic states close to or above the critical point of the working fluid, i.e., pressure and temperature within approximately $0.9 < P/P_c < 1.2$ and $0.8 < T/T_c < 1.3$, or $P > P_c$ and $T > T_c$, respectively, molecular interactions start to become significant and the ideal gas equation of state is no longer appropriate. Fluids at these thermodynamic states simultaneously have characteristics that are typical of liquids and others typical of gases. In this thermodynamic region, called the dense-gas region, the actual thermodynamic behavior of gases can deviate significantly from that predicted by the polytropic ideal gas law.

Firstly, the volumetric $P-v-T$-behavior of dense gases is different from their behavior in the ideal-gas region. The deviation in volumetric properties is shown in the temperature-entropy of toluene in Fig. 1.6(a) and in the pressure-specific volume diagram of water in Fig. 1.6(b). Secondly, the caloric behavior of dense gases is also different from their behavior in the ideal-gas region. Consequently, the variation of properties along the same process isentrope is much larger at conditions close to and above the critical point in the dense-gas region than at low pressures. This is indicated by the difference in isentropic behavior in the ideal gas and dense gas regions, as depicted in the reduced pressure-specific-volume diagram of an arbitrary fluid in Fig. 1.7.

(a)

(b)
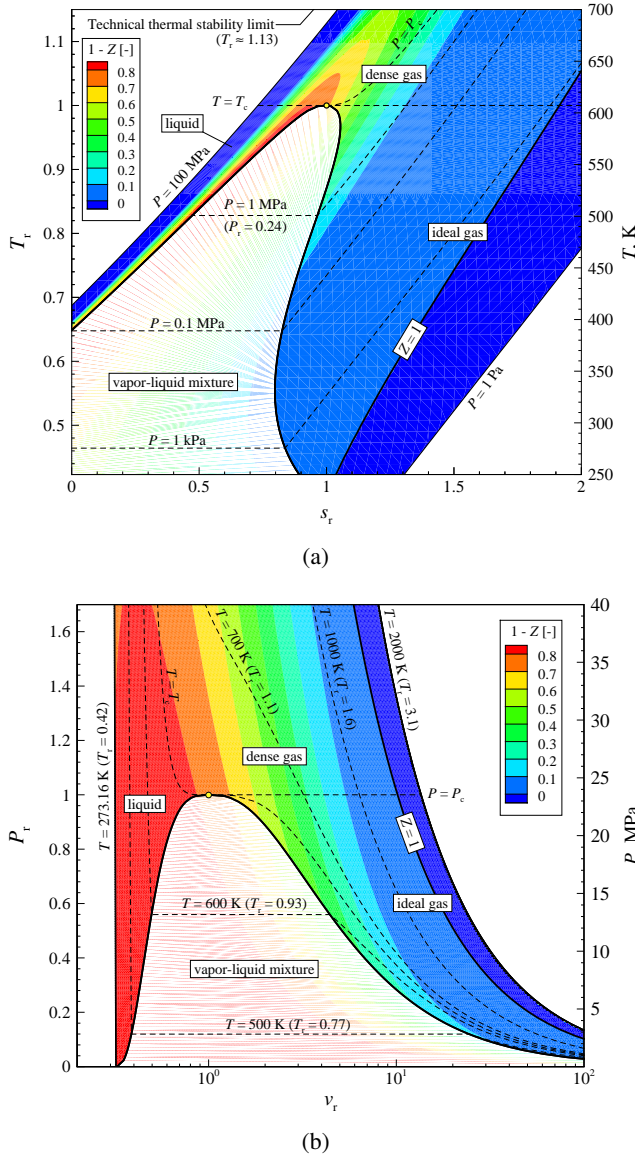
Figure 1.6: *Deviation of volumetric properties from the ideal gas law, i.e., the compressibility factor, in (a) the reduced temperature-entropy diagram of toluene [55] and (b) the reduced pressure-specific volume diagram of water [56]. The deviation is given by $1 - Z = 1 - (Pv)/(RT)$, where v denotes the specific volume and $R = \mathcal{R}/M$ is the specific gas constant with $\mathcal{R} = 8.314$ J/(mol-K) being the universal gas constant and M the molecular weight of the fluid. Both figures are taken from Ref. [57].*
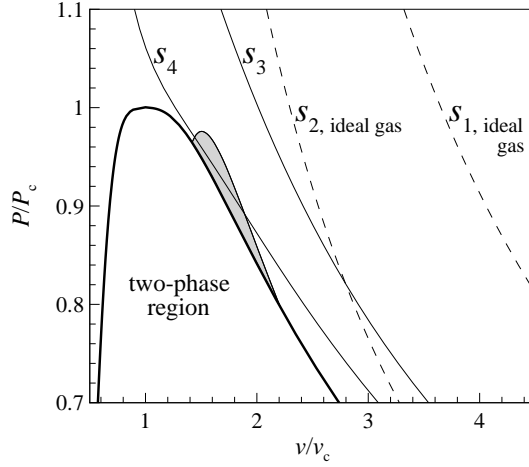
Figure 1.7: *Qualitative differences in the entropy in the reduced pressure-specific-volume diagram of D_6. In the dilute-gas region, isentropic behavior is correctly given by the polytropic ideal-gas law model ($S_{1,\text{ideal gas}}$). In the dense-gas region, the polytropic ideal gas law model ($S_{2,\text{ideal gas}}$) is different from actual fluid isentropic behavior (S_3). Isentrope S_4 exhibits a region of concavity, allowing for nonclassical gasdynamic phenomena. The shaded area represents the region of concavity of this BZT fluid, where the fundamental derivative of gasdynamics is less than zero [58].*

These thermodynamic deviations in turn lead to deviations in fluid dynamics quantities, which are known as real- or dense-gas effects. For fluids composed of simple molecules, dense-gas effects are limited to quantitative deviations with respect to ideal-gas fluid dynamic behavior [59]. For high molecular complexity fluids, also qualitative differences in fluid dynamic behavior can be observed in a limited thermodynamic region close to saturation [60, 61, 62]. Most notable is the increase in the speed of sound upon isentropic expansion, possibly leading to a local decrease in the Mach number (see, e.g., Refs. [62, 63, 64, 65, 66, 67] and Chapters 2, 3 and 4 of this thesis) which instead increases monotonically for an isentropic ideal-gas expansion. So-called Bethe-Zel'dovich-Thompson (BZT) fluids (see Refs. [18, 68, 69]) have even more complex molecules, enabling them to exhibit a (smaller) finite thermodynamic region (see Fig. 1.7) where nonclassical gasdynamic phenomena including rarefaction shock waves may possibly occur, although no experimental evidence of these "exotic" wave fields is available, yet [70, 71, 72].

1.3   Motivation and Scope

The anomalous phenomena in flows involving supercritical and transcritical states are not well understood. Some have been theoretically predicted but not verified, others have been observed but not understood. Firstly, because the fluid dynamic and heat transfer behavior at these conditions is highly unconventional and often counterintuitive. Secondly, hypotheses must be validated with experiments that are difficult to set up and run due to the necessary operating conditions, which, depending on the fluid, include high pressure and high temperature [73, 72]. The scarcity of experimental evidence and lack of knowledge about the fluid dynamics and heat transfer properties of supercritical and transcritical flows means it is very difficult or impossible to accurately design the aforementioned next-generation energy converters and their components. It is therefore important to gain a better understanding of super- and transcritical flows in order to be able to take advantage of the potential efficiency gains that next-generation energy converters can offer.

The recent development of state-of-the-art fluid dynamic algorithms, specific and highly accurate thermodynamic models and sufficient computing power has only recently made it possible to use computer models to simulate these complex flows [74, 75, 76, 77, 78, 79, 80, 81, 82, 83]. Due to the lack of data for comparison, validating these algorithms and models is problematic. However, given the complexity of the phenomena, such simulations, and their analyses, are indispensable tools for developing predictive theories.

The aim of the work documented in this thesis is to shed light on the fluid dynamics of expansions of super- and close-to-critical dense-gas fluids. To this purpose, this thesis addresses research questions of how the different thermodynamic behavior of supercritical and dense gases and different fluid characteristics (in particular the fluid molecular complexity) of, e.g., organic working fluids, change the fluid dynamic behavior upon expansion. As part of this, the capabilities and limitations of the available thermodynamic models are determined in case of their application to the fluid dynamic simulations of such flows. Furthermore, implications are pointed out for practical applications such as the performance and design of next-generation energy converters. The influence of super- and transcritical transport properties on, e.g., heat transfer at conditions close to and above the critical point, is beyond the scope of this thesis. Their influence on viscous flows involving boundary layers is only briefly discussed. Nonetheless, the theory and methods described in this work can be used to study the heat transfer characteristics of super- and transcritical flows.

1.4 Thesis Outline

This thesis is divided into two parts. The first part focusses on the theoretical and fundamental physics of supercritical and dense-gas flows of fluids and its dependence on fluid characteristics. The second part deals with two studies of applications of the aforementioned flows. The chapters are formed by four articles that have been published in scientific journals in the field of energy technology, with two chapters that document preliminary results of additional work.

1.4.1 Part I: Fundamental Aspects

Chapter 2 presents an investigation of the effect of the complexity of a fluid molecule on the fluid dynamic quantities sound speed, velocity and Mach number in isentropic expansions. Ideal gas and dense gas expansions are analyzed, using the polytropic ideal gas and van der Waals thermodynamic models to compute the properties of the fluid. In these equations, the number of active degrees of freedom of the molecule is made explicit and it is taken as a measure of molecular complexity. Theoretical results are subsequently verified using highly accurate multiparameter equations of state. The chapter concludes with the numerical simulation of two-dimensional expansions in a turbine nozzle, to document the occurrence of dense-gas effects and their dependence on molecular complexity in realistic applications.

Chapter 3 presents a comparison of the effect of using thermodynamic models of various degree of complexity if applied to flow field simulations of dense-gas and transcritical expansions. The considered thermodynamic models are, in order of increasing complexity, the polytropic ideal gas (PIG) law, the Peng-Robinson-Stryjek-Vera (PRSV) cubic equation of state and highly accurate multiparameter equations of state (MPEoS), which are adopted as benchmark reference. The fluids are steam, toluene and R245fa. The two processes under scrutiny are a moderately nonideal subcritical expansion and a highly nonideal transcritical expansion characterized by the same pressure ratio.

1.4.2 Part II: Applications

Chapter 4 investigates dense-gas effects occurring in subcritical and supercritical ORC nozzles. Two-dimensional Euler simulations of an existing axial ORC stator nozzle are carried out using a CFD code that is linked to an accurate thermodynamic model for the organic working fluid (siloxane MDM). The cases an-

alyzed include the expansions starting from actual subcritical conditions, i.e., the design-point and part-load operation, and three expansions starting from super-critical conditions. The implications of supercritical operating conditions on the nozzle geometry are demonstrated, in particular the different exit-to-throat area ratio that is required to maintain efficient expansion. Other peculiar characteristics of supercritical expansions such as low sound speed and velocity, high density and mass flow rate, are also discussed.

Chapter 5   focusses on radial turbines operating at high expansion ratios, which are commonly used in small-scale turbogenerators of next-generation energy converters such as ORCs. A numerical study is presented of the flow field through the stator of an existing radial ORC turbine operating with toluene at a very high expansion ratio. The analysis takes into consideration the influence on the simulated flow field of i) the thermodynamic model of the working fluid, ii) the turbulence model, and iii) the numerical solver. The influence of super- and transcritical transport properties on boundary layers is briefly discussed.

Chapter 6   introduces the flow structure of supersonic free-jets, followed by the validation of the inviscid CFD zFLOW code for the supersonic free-jet fluid dynamic case. This work serves as the first step towards the simulation and validation of zFLOW for highly underexpanded free jets generated by the expansion of supercritical fluids for the purpose of particle production processes.

Chapter 7   documents the development and application of the optimization system for unconventional dense-gas fluid dynamic designs such as BZT nozzles, ORC stator nozzles and turbomachinery components of next-generation energy converters in general. The expansion and compression processes of these cycles involve unconventional fluid dynamics due to dense-gas effects and possibly nonclassical gasdynamic phenomena in case of BZT fluids. This demands for unconventional nozzle shapes, the optimal design of which greatly benefits from automated optimization systems based on advanced algorithms, such as the one developed and documented in this chapter.

Nomenclature

h	=	specific enthalpy
P	=	pressure
v	=	specific volume

M	=	molecular weight
R	=	specific gas constant
$\mathcal{R}$	=	universal gas constant
s	=	specific entropy
T	=	temperature
Z	=	compressibility factor

Greek symbols

η	=	efficiency

Subscripts

A	=	turbine inlet
B	=	turbine outlet
c	=	critical point
cycle	=	cycle
D	=	condenser outlet
e	=	electric
G	=	flue gas inlet
I	=	cooling water inlet
ideal gas	=	ideal gas
K	=	cooling water outlet
LT	=	low temperature
HT	=	high temperature
r	=	reduced quantity
SC	=	supercritical

Acronyms

BZT	=	Bethe-Zel'dovich-Thompson
CFC	=	chlorofluorocarbon
CFD	=	Computational Fluid Dynamics
HCFC	=	hydrochlorofluorocarbon
HFC	=	hydrofluorocarbon
MPEoS	=	multiparameter equation of state
ORC	=	Organic Rankine Cycle
PIG	=	polytropic ideal gas law

PRSV   =   Peng-Robinson-Stryjek-Vera cubic equation of state

References

[1] International Energy Agency. *World Energy Outlook 2009*. 2009.

[2] Intergovernmental Panel on Climate Change. *The Fourth Assessment Report on Climate Change 2007*. WMO and United Nations Environment Programme, 2007.

[3] H.M. Curran. Use of Organic Working Fluids in Rankine Engines. *Journal of Energy*, 5(4):218–223, 1981.

[4] G. Angelino, M. Gaia, and E. Macchi. A review of Italian activity in the field of organic Rankine cycles. In *VDI Berichte - Proceedings of the International VDI Seminar*, volume 539, pages 465–482, Düsseldorf, 10–12 September 1984. VDI Verlag.

[5] J. E. Boretz. Supercritical organic Rankine engines (SCORE). In *21$^{\text{st}}$ Intersociety Energy Conversion Engineering Conference (IECEC)*, volume 3, pages 2050–2054, Washington, DC, August 1986. ACS.

[6] Schuster A. Karellas, S. Supercritical fluid parameters in organic rankine cycle applications. *International Journal of Thermodynamics*, 11(3):101–108, 2008.

[7] G. Angelino. Carbon Dioxide Condensation Cycles for Power Production. *Journal of Engineering for Power*, pages 287–295, July 1968.

[8] G. Angelino. Real gas effects in carbon dioxide cycles. *ASME Journal of Engineering for Power*, 10(13):272, 1969.

[9] E. Cayer, N. Galanis, M. Desilets, H. Nesreddine, and P. Roy. Analysis of a carbon dioxide transcritical power cycle using a low temperature source. *Applied Energy*, 86(7-8):1055–1063, 2009.

[10] G. Angelino and C. Invernizzi. Real gas Brayton cycles for organic working fluids. *Proceedings of the Institution of Mechanical Engineers, Part A: Journal of Power and Energy*, 215(1):27–38, 2001.

[11] G. Angelino and C. Invernizzi. Prospects for real gas reversed Brayton cycles heat pumps. *Int. J. Refrig.*, 18:272, 1995.

[12] Yasuyoshi Kato, Takeshi Nitawaki, and Yasushi Muto. Medium temperature carbon dioxide gas turbine reactor. *Nucl. Eng. Des.*, 230(1-3):195–207, 2004.

[13] G. Angelino and C. Invernizzi. Real Gas Effects in Stirling Engines. In *35th Intersociety Energy Conversion Engineering (IECEC), LasVegas,NV*, pages 69–75, Reston, VA, July 2000. AIAA, AIAA.

[14] G. Angelino and C. Invernizzi. Potential performance of real gas Stirling cycles heat pumps. *Int. J. Refrig.*, 19(6):390, 1996.

[15] G. Angelino and C. Invernizzi. Supercritical heat pump cycles. *Int. J. Refrig.*, 17(8):543–554, 1994.

[16] G. Lorentzen. The use of natural refrigerants: a complete solution to the CFC/HCFC predicament. *International Journal of Refrigeration*, 18(3):190–7, 1995.

[17] M.-H. Kim, J. Pettersen, and C.W. Bullard. Fundamental process and system design issues in CO_2 vapor compression systems. *Progress in Energy and Combustion Science*, 30:119–174, 2004.

[18] H. A. Bethe. The theory of shock waves for an arbitrary equation of state. Technical paper 545, Office Sci. Res. & Dev., 1942.

[19] P.A. Thompson. A fundamental derivative in gasdynamics. *Phys. Fluids*, 14(9):1843–1849, 1971.

[20] B. P. Brown and B. M. Argrow. Application of Bethe-Zel'dovich-Thompson fluids in organic Rankine cycle engines. *J. Propul. Power*, 16(6):1118–1123, November-December 2000.

[21] P. Colonna. *Fluidi di Lavoro Multi Componenti Per Cicli Termodinamici di Potenza (Multicomponent Working Fluids for Power Cycles)*. PhD thesis, Politecnico di Milano, October 1996.

[22] G. Angelino and P. Colonna. Multicomponent working fluids for Organic Rankine Cycles (ORCs). *Energy*, 23(6):449–463, 1998.

[23] J. Larjola. Electricity from industrial waste heat using high-speed organic Rankine cycle (ORC). *Int. J. Prod. Econ.*, 41(1-3):227–235, October 1995.

[24] R. Swanekamp. Return of the supercritical boiler. *Power*, 146(4):32–33, 37–40, 2002.

[25] P.E. Chew. Pf-fired supercritical power plant. *Proceedings of the Institution of Mechanical Engineers, Part A: Journal of Power and Energy*, 217(1):35–43, 2003.

[26] G. Tsiklauri, R. Talbert, B. Schmitt, G. Filippov, R. Bogoyavlensky, and E. Grishanin. Supercritical steam cycles for nuclear power plant. *Nuclear Engineering Design*, 235(15):1651–1664, 2005.

[27] P. Colonna, J. Harinck, S. Rebay, and A. Guardone. Real-gas effects in organic Rankine cycle turbine nozzles. *J. Propul. Power*, 24(2):282–294, March–April 2008.

[28] V. Hassani and H. W. Price. Modular trough power plants. In *Solar Forum 2001: Solar Energy: The Power to Choose*, pages 1–7, Washington, DC, April 21–25 2001. ASME.

[29] H. Yamaguchi, X. R. Zhang, K. Fujima, M. Enomoto, and N. Sawada. Solar energy powered Rankine cycle using supercritical CO_2. *Appl. Therm. Eng.*, 26(17-18):2345–2354, 2006.

[30] X. R. Zhang, H. Yamaguchi, D. Uneno, K. Fujima, M. Enomoto, and N. Sawada. Analysis of a novel solar energy-powered Rankine cycle for combined power and heat generation using supercritical carbon dioxide. *Renew. Energ.*, 31(12):1839–1854, 2006.

[31] G. Angelino and P. Colonna. Organic Rankine cycles for energy recovery from molten carbonate fuel cells. In 35th *Intersociety Energy Conversion Engineering Conference (IECEC)*, number 2000-3052, pages 1–11. AIAA, July 2000.

[32] G. Angelino and P. Colonna. Air cooled siloxane bottoming cycle for molten carbonate fuel cells. In *Fuel Cell Seminar*, pages 667–670, October 2000.

[33] M. Brentegani. A μ-ORC system for domestic cogeneration. M.Sc. Thesis ET-2389, Politecnico di Milano - Delft University of Technology, July 2009.

[34] S. Canada, G. Cohen, R. Cable, D. Brosseau, and H. Price. Parabolic Trough Organic Rankine Cycle Solar Power Plant. National Renewable Energy Laboratory, US, Technical Report NREL/ CP-550-37077, 2005.

[35] D. W. Chaudoir, R. E. Niggeman, and T. J. Bland. A solar dynamic ORC power system for space station application. In 20th *Intersociety Energy Conversion Engineering Conference (IECEC)*, number 859085, pages 1.58–1.65. SAE, August 1985.

[36] R. L. Cole, J. C. Demirgian, and J. W. Allen. Predicting toluene degradation in organic Rankine cycle engines. In *22nd Intersociety Energy Conversion Engineering Conference (IECEC)*, volume 3, pages 1402–1407, New York, NY, August 1987. AIAA.

[37] G. Angelino and C. Invernizzi. Cyclic methylsiloxanes as working fluids for space power cycles. *J. Sol. Energ. - Trans. ASME*, 115(3):130–137, 1993.

[38] Y Chen, P. Lundqvist, and P. Platell. Theoretical research of carbon dioxide power cycle application in automobile industry to reduce vehicle's fuel consumption. *Appl Therm Eng*, 25(14-15):2041–2053, 2005.

[39] D. Uneno K. Fujima M. Enomoto X.R. Zhang, H. Yamaguchi and N. Sawada. Analysis of a novel solar energy-powered rankine cycle for combined power and heat generation using supercritical carbon dioxide. *Renewable Energy*, 31(12):1839–1854, 2006.

[40] Y. Chen, P. Lundqvist, A. Johansson, and P. Platell. A comparative study of the carbon dioxide transcritical power cycle compared with an organic Rankine cycle with R123 as working fluid in waste heat recovery. *Appl. Therm. Eng.*, 26(17-18):2142–2147, 2006.

[41] K. Fujima M. Enomoto H. Yamaguchi, X.R. Zhang and N. Sawada. Solar energy powered rankine cycle using supercritical CO2. *Applied Thermal Engineering*, 26:2345–2354, 2006.

[42] V. Dostal. *A Supercritical Carbon Dioxide Cycle for Next Generation NuclearReactors*. PhD thesis, Massachusetts Institute of Technology, 2004.

[43] Y. Wang, G Guenette, P. Hejzlar, and M. Driscoll. Compressor design for the supercritical CO_2 Brayton cycle. In *2nd International Energy Conversion Engineering Conference*, pages 1–13, Providence, Rhode Island, 16 - 19 August 2004 2004. AIAA.

[44] V. Dostal. *A Supercritical Carbon Dioxide Cycle for Next Generation Nuclear Reactors*. PhD thesis, Massachusetts Institute of Technology, 2004.

[45] V. Dostal, M. Driscoll, P. Hejzlar, and Y. Wang. Supercritical CO_2 cycle for fast gas-cooled reactors. In *Proceedings of ASME Turbo Expo 2004*, Vienna, 17 June, 2004 2004. ASME.

[46] P. Hejzlar, V. Dostal, and M. J. Driscoll. A supercritical CO_2 cycle - a promising power conversion system for generation IV reactors. In *2006 International Congress on Advances in Nuclear Power Plants (ICAPP '06)*, Reno, Nevada, June 4-8, 2006 2006.

[47] Y. Kato, T. Ishizuka, Y. Muto, M. Mito, and K. Tozawa. Supercritical CO_2 gas turbine fast reactors. In *2007 International Congress on Advances in Nuclear Power Plants (ICAPP '07)*, Nice, France, May 13-18, 2007 2007.

[48] S.A. Wright and R.J. Lipinski. Operational curves for HTGR's coupled to closed brayton cycle power conversion systems. In *2008 International Congress on Advances in Nuclear Power Plants (ICAPP '06)*, Reno, NV, USA, June 4-8 2006.

[49] S.A. Wright, R. Fuller, P.S. Pickard, and M.E. Vernon. Initial status and test results from a supercritical CO_2 Brayton cycle test loop. In *2008 International Congress on Advances in Nuclear Power Plants (ICAPP '08)*, Anaheim, California, June 8-12, 2008 2008.

[50] S.A. Wright, P.S. Pickard, M.E. Vernon, and R.F. Radel. Description and test results from a supercritical CO_2 brayton cycle development program. In *7th International Energy Conversion Engineering Conference*, page 4607. American Institute of Aeronautics and Astronautics, 2009.

[51] S.A. Wright, P.S. Pickard, R. Fuller, R.F. Radel, and M.E. Vernon. Supercritical CO_2 brayton cycle power generation development program and initial test results. In *ASME Power 2009*, page 4607, Albuquerque, New Mexico, USA, July 21-23 2009.

[52] G. Lorentzen and J. Pettersen. A new, efficient and environmentally benign system for car air conditioning. *International Journal of Refrigeration*, 16(1):4–12, 1993.

[53] D.M. Robinson and E.A. Groll. Efficiencies of transcritical CO_2 cycles with and without an expansion turbine. *International Journal of Refrigeration*, 21(7):577–89, 1998.

[54] J.L. Yang, Y.T. Ma, M.X. Li, and H.Q. Guan. Exergy analysis of transcritical carbon dioxide refrigeration cycle with an expander. *Energy*, 30:1162–1175, 2005.

[55] E.W. Lemmon and R. Span. Short fundamental equations of state for 20 industrial fluids. *J. Chem. Eng. Data*, 51(3):785–850, 2006.

[56] W. Wagner and A. Pruss. The IAPWS Formulation 1995 for the Thermodynamic Properties of Ordinary Water Substance for General and Scientific Use. *J. Phys. Chem. Ref. Data*, 31(2):387–535, 2002.

[57] W.C. Reynolds and P. Colonna. *THERMODYNAMICS - Fundamentals and Engineering Applications*. To be published by Cambridge University Press, 2011.

[58] P. Colonna, A. Guardone, and N. R. Nannan. Siloxanes: a new class of candidate Bethe-Zel'dovich-Thompson fluids. *Phys. Fluids*, 19:086102–1–12, 2007.

[59] W. Bober and W. L. Chow. Nonideal Isentropic Gas Flow Through Converging-Diverging Nozzles. *J. Fluids Eng.*, 112:455–460, 1990.

[60] M. S. Cramer. On the Mach number variation in steady flows of dense hydrocarbons. *J. Fluids Eng.*, 113, 1991.

[61] M. S. Cramer and L. M. Best. Steady, isentropic flows of dense gases. *Phys. Fluids A*, 3(1):219–226, 1991.

[62] M.S. Cramer and N.R. Fry. Nozzle flows of dense gases. *Phys. Fluids A*, 5(5):1246–1259, 1993.

[63] G.H. Schnerr and P. Leidner. Diabatic Supersonic Flows of Dense Gases. *Physics of Fluids A*, 3(10):2445–2458, 1991.

[64] A. Kluwick. Internal flows of dense gases. *Acta Mechanica*, 169:123–143, 2004.

[65] P. Colonna and A. Guardone. Molecular interpretation of nonclassical gas dynamics of dense vapors under the van der Waals model. *Phys. Fluids*, 18:056101–1–14, 2006.

[66] P. Colonna, J. Harinck, S. Rebay, and A. Guardone. Real-gas effects in organic rankine cycle turbine nozzles. *AIAA Journal of Propulsion and Power*, 24(2):282–294, 2008.

[67] J. Harinck, A. Guardone, and P. Colonna. The influence of molecular complexity on expanding flows of ideal and dense gases. *Phys. Fluids*, 21(8), 2009.

[68] Ya. B. Zel'dovich. On the possibility of rarefaction shock waves. *Zh. Eksp. Teor. Fiz.*, 4:363–364, 1946.

[69] P. A. Thompson and K. C. Lambrakis. Negative shock waves. *J. Fluid Mech.*, 60:187–208, 1973.

[70] P. A. Thompson. *Compressible Fluid Dynamics*. McGraw-Hill, 1988.

[71] R. Menikoff and B. J. Plohr. The Riemann problem for fluid flow of real material. *Rev. Mod. Phys.*, 61(1):75–130, 1989.

[72] Colonna, Guardone, Nannan, and Zamfirescu. Design of the dense gas flexible asymetric shock tube. *Journal of Fluids Engineering*, 130(3):6, 2008.

[73] S. H. Fergason, A. Guardone, and B. M. Argrow. Construction and validation of a dense gas shock tube. *J. Thermophys. Heat Tr.*, 17(3):326–333, 2003.

[74] C. Cravero and A Satta. A CFD model for real gas flows. In *Proceedings of ASME Turbo Expo*, number 2000-GT-518, pages 1–10, New York, NY, May 2000. ASME.

[75] P. Colonna, S. Rebay, and P. Silva. Computer simulations of dense gas flows using complex equations of state for pure fluids and mixtures and state-of-the-art numerical schemes. Scientific report, Università di Brescia, Via Branze, 38, 25123 Brescia, Italy, March 2002.

[76] J. Hoffren, T. Talonpoika, J. Larjola, and T. Siikonen. Numerical simulation of real-gas flow in a supersonic turbine nozzle ring. *J. Eng. Gas Turb. Power*, 124(2):395–403, April 2002.

[77] P. Boncinelli, F. Rubechini, A. Arnone, M. Cecconi, and C. Cortese. Real gas effects in turbomachinery flows - A Computational Fluid Dynamics model for fast computations. *J. Turbomach.*, 126:268–276, April 2004.

[78] P. Cinnella and P. Congedo. A numerical solver for dense gas flows. In *34th AIAA Fluid Dynamics Conference and Exhibit*, number AIAA 2004-2137, pages 1–12. AIAA, June-July 2004.

[79] P. Colonna and S. Rebay. Numerical simulation of dense gas flows on unstructured grids with an implicit high resolution upwind Euler solver. *Int. J. Num. Meth. Fluids*, 46:735–765, 2004.

[80] M. Cirri, P. Adami, and F. Martelli. Development of a CFD Real Gas Flow Solver for Hybrid Grid. *Int. J. Numer. Methods Fluids*, 47(8-9):931–938, March 2005.

[81] T. Turunen-Saaresti, J. Tang, and J Larjola. A practical real gas model in CFD. In P. Wesseling, E. Onate, and J. Périau, editors, *European Conference on Computational Fluid Dynamics (ECCOMAS CFD 2006)*, Egmond aan Zee, The Netherlands, September 2006.

[82] P. Cinnella and P.M. Congedo. Inviscid and viscous aerodynamics of dense gases. *Journal of Fluid Mechanics*, 580:179–217, 2007.

[83] S. Rebay, P. Colonna, D. Pasquale, and A. Ghidoni. Simulation of the turbulent dense gas flow through the nozzle of an organic Rankine cycle turbine. In F. Heitmeir, F. Martelli, and M. Manna, editors, *Proceedings of the 8th European Turbomachinery Conference*, pages 1137–1148, March 2009.

Part I

Fundamental Aspects

The first part of this thesis presents the contribution to the theoretical and fundamental understanding of the physics of supercritical and dense-gas flows of fluids and its dependence on fluid characteristics.

Chapter 2 investigates the effect of the fluid molecular characteristics, in particular the complexity of the fluid molecule, on the fluid dynamic quantities sound speed, velocity and Mach number in isentropic expansions. Ideal gas and dense gas expansions are analyzed, using the polytropic ideal gas and Van der Waals thermodynamic models to compute the properties of the fluid. In these equations, the number of active degrees of freedom of the molecule is made explicit and it is used as a measure of molecular complexity.

Chapter 3 compares the effect of using thermodynamic models of various degree of complexity if applied to flow field simulations of dense-gas and transcritical expansions. The considered thermodynamic models are, in order of increasing complexity, the polytropic ideal gas law, the Peng-Robinson-Stryjek-Vera equation of state, which represents the class of cubic equations of state and, thirdly, highly accurate multiparameter equations of state, which are adopted as benchmark reference. The two processes under scrutiny are a moderately nonideal subcritical expansion and a highly nonideal transcritical expansion characterized by the same pressure ratio. The thermodynamic models are compared in terms of the deviation of distributed and integral flow quantities compared to accurate values and their computational cost. Results are compared for fluids of various molecular complexities so as to include in the analysis the dependence of thermodynamic model validity on fluid molecular complexity.

2

The Influence of Molecular Complexity on Expanding Flows of Ideal and Dense Gases

Abstract *This chapter presents an investigation about the effect of the complexity of a fluid molecule on the fluid dynamic quantities sound speed, velocity and Mach number in isentropic expansions. Ideal gas and dense gas expansions are analyzed, using the polytropic ideal gas and Van der Waals thermodynamic models to compute the properties of the fluid. In these equations, the number of active degrees of freedom of the molecule is made explicit and it is taken as a measure of molecular complexity. The obtained results are subsequently verified using highly accurate multiparameter equations of state. For isentropic expansions, the Mach number does not depend on the molecular weight of the fluid, but only on its molecular complexity and pressure ratio. Remarkably enough, the Mach number can either increase or decrease with molecular complexity, depending on the considered pressure ratio. The exit speed of sound and flow velocity, however, are dependent on both molecular complexity and weight, as well as on the inlet total temperature. The exit flow velocity is found to be a monotonically increasing function of molecular complexity for all expansion ratios, whereas the speed of sound monotonically increases with molecular complexity only at high pressure ratios. The speed of sound is not monotone for pressure ratios around 3, which leads to the Mach number being nonmonotone at pressure ratios around 10. It should be noted that the sound speed and flow velocity depend much more strongly on molecular weight than on molecular complexity, which in realistic expansions often obscures the influence of the latter. Quantitative differences are observed between ideal and dense-gas expansions, which are dependent on the reduced inlet conditions. The present study concludes with the numerical simulation of two-dimensional expansions in a turbine nozzle, to document the occurrence of real-gas effects and their dependence on molecular complexity in realistic applications.*

2.1 Introduction

Gas expansions are common processes in numerous industrial applications. Examples can be found in the power, oil and gas, chemical, process and refrigeration industries. Fluids are expanded in order to generate mechanical power (e.g., in turbines, rockets, mixers, wind tunnels for aerodynamic testing, and for material removal, etc). Fluid expansions are also used in order to reduce the pressure and/or temperature (e.g., for refrigeration purposes or to separate heavier fluid fractions from lighter ones by condensation). In general terms, the process conditions, namely, the initial thermodynamic state and expansion ratio, together with the fluid characteristics determine the dynamics of an expansion.
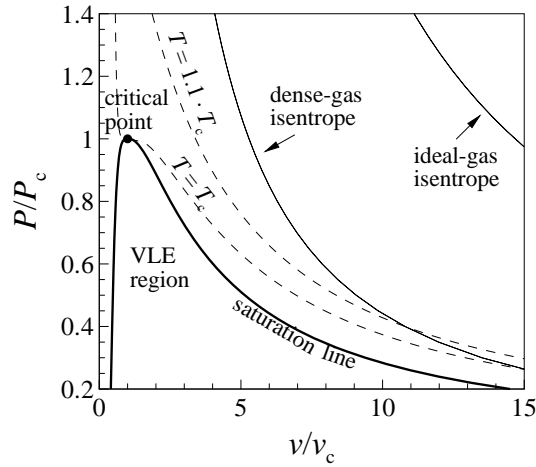
Figure 2.1: *The reduced pressure-specific-volume v/v_c-P/P_c diagram, with v_c and P_c the critical specific volume and pressure, respectively, of water based on the Wagner-Pruß thermodynamic model [7], showing an isentrope in the ideal-gas region and one in the dense-gas region. The vapor-liquid equilibrium (VLE) region is bounded by the liquid-vapor saturation curve. The critical isotherm $T = T_c$ and the isotherm $T = 1.1 \cdot T_c$ are also indicated.*

The choice of the working fluid is driven by different requirements arising from the specific application. A great variety of substances, with different thermophysical properties, are used in industry, ranging from the simple monatomic fluids to the heavy fluids formed by complex molecules. An example is the Rankine power cycle, in which, for large-scale applications, the common working medium is steam, but for small-scale and low-temperature applications, organic fluids such as hydrocarbons, perfluorocarbons or siloxanes are more suitable [1, 2, 3]. Gases made of heavy molecules can be used in supersonic wind tunnels instead of air to achieve higher Reynolds numbers which can be varied almost independently from the Mach number [4, 5, 6]. Complex fluids with low boiling point are used also as working fluids in refrigeration and air conditioning equipment, and in heat pumps. For certain energy applications, even mixtures of fluids could be used to further tailor the fluid thermophysical properties to the application– see, e.g., Ref. [3].

The process conditions can vary from expansions entirely embedded in the ideal-gas thermodynamic region, i.e., the region where volumetric properties can be calculated from the ideal gas equation of state $Pv = RT$, where P denotes pressure, v specific volume, R the specific gas constant and T temperature, to those

occurring close to the liquid-vapor saturation line and to the critical point, namely within the so-called dense-gas thermodynamic region. The latter is for example the case for supercritical CO_2 nozzle flows, which are increasingly adopted in the pharmaceutical industry for the nucleation of chemicals [8, 9]. Exemplary ideal- and dense-gas expansion processes are represented by the isentropes depicted in the reduced pressure-specific-volume diagram of an arbitrary fluid in Fig. 2.1. In the dense-gas region, the actual thermodynamic behavior of gases can deviate significantly from that predicted by the ideal polytropic (constant isobaric and isochoric specific heat) gas law. These deviations in turn lead to deviations in fluid dynamics quantities, which are known as real-gas effects. Hence, more complex thermodynamic models must be used to complement the fluid dynamic analysis of a dense-gas process [10, 11, 12, 13].

Recent gas dynamic studies have focussed on the influence of fluid molecular characteristics on the real-gas behavior of a fluid flow. Investigations in Ref. [14] concluded, based on a sensitivity analysis using various fluids, that real-gas behavior is strongly influenced by the dimensionless isochoric specific heat and by the acentric factor, which are both qualitative measures of molecular complexity. Here molecular complexity indicates the effect of both molecular configuration and molecular interactions. In Ref. [15], the authors derived, by means of a physically based equation of state (EoSs), the relation between the molecular complexity—defined as the capacity of the fluid molecules to store energy into the internal vibrational modes—and the variation of the sound speed along isentropes, whose value influences real-gas behavior.

The aim of this work is to relate the fluid dynamic quantities sound speed, velocity and Mach number along isentropic expansions to the fluid molecular characteristics and to the molecular complexity in particular. The influence of molecular complexity is analyzed for fluids being expanded in the ideal-gas thermodynamic region and in the (mildly nonideal) dense-gas region. The study starts with a nonstandard interpretation of well-known results of the polytropic ideal-gas law. The discussion then moves to the physically-based but still relatively simple Van der Waals EoS, which allows for a treatment based on physical grounds. These results are then verified using highly accurate empirical EoSs. The study concludes with the numerical simulation of two-dimensional expansions in a turbine nozzle, to document the occurrence of real-gas effects and their dependence on molecular complexity in realistic applications.

This study is structured as follows. Section 2.2 introduces the fundamental derivative of gasdynamics and shows how it relates to molecular complexity quantified by the number of active degrees of freedom of a fluid molecule. In Sec-

tion 2.3, the effect of molecular complexity on the Mach number, flow velocity and sound speed is analyzed for isentropic expansions in the ideal-gas and dense-gas thermodynamic region. In Section 2.4 the influence of molecular complexity on expansions is furthermore exemplified by presenting the fluid dynamic simulations of expansions of three fluids of practical interest, namely, steam, carbon dioxide and propane, which are conveniently different in molecular complexity and weight. Concluding remarks complete this work.

2.2   Molecular Complexity and the Fundamental Derivative of Gasdynamics

In 1971 Thompson [16], following the work of Bethe [17], formally introduced the so-called fundamental derivative of gasdynamics Γ,

$$\Gamma \equiv 1 - \frac{v}{c}\left(\frac{\partial c}{\partial v}\right)_s, \tag{2.1}$$

where v is the specific volume, c is the sound speed and s is the specific entropy. The value of Γ can be used to classify gasdynamic behavior. For an ideal polytropic gas, Γ is constant and reduces to $\Gamma = (\gamma + 1)/2$, where γ denotes the (constant) ratio of the isobaric to the isochoric specific heat. Therefore, the speed of sound derivative with respect to the volume in isentropic expansions reads $(\partial c/\partial v)_s = (c/v)(1 - \gamma)/2 < 0$ and $\Gamma > 1$, since $\gamma > 1$ for thermodynamic stability.

Modern thermodynamic models indicate that the minimum value of Γ in the single-phase vapor region for a given fluid decreases as the molecular complexity of the fluid increases [14]. The above can be appreciated already in the case of an ideal polytropic gas, for which molecular complexity can be conveniently defined as the number N of active degrees of freedom of the molecule [15]. In the temperature range of interest here, these are the translational, rotational and vibrational degrees of freedom. Both the translational and the rotational modes are assumed to be fully excited, whereas the activation of the vibrational ones occurs only at temperatures higher than the vibrational temperature associated with each mode, hence, $N = N(T)$. According to the energy equipartition principle (see, e.g., Ref. [18]), at a given temperature, each fully active degree of freedom contributes $R/2$, where R is the specific gas constant, to the overall value of the ideal-gas isochoric specific heat, C_v^0, so that

$$C_v^0(T) = \frac{\bar{R}}{2} \frac{N(T)}{M} \tag{2.2}$$

where $\bar{R}$ is the universal gas constant equal to $\bar{R} = 8.314$ J/(mol K) and M is the molecular weight. In this work, the number of active degrees of freedom of a fluid is evaluated at its critical temperature, denoted by T_c, i.e., $N = 2MC_v^0(T_c)/\bar{R}$. Therefore, $\gamma = 1 + 2/N$ and the (complete) polytropic ideal gas model reads

$$\text{PIG:} \qquad P(T, v) = \frac{1}{M}\frac{\bar{R}T}{v}, \qquad e(T) = \frac{N}{M}\frac{\bar{R}T}{2} + e_0 \qquad (2.3)$$

where e is the specific internal energy per unit mass and the subscript 0 denotes its value at an arbitrary reference state. The fundamental derivative for an ideal polytropic gas is then

$$\text{PIG:} \qquad \Gamma \equiv 1 + \frac{1}{N},$$

and its value, which is constant for a given fluid, decreases with increasing molecular complexity.

In the dense gas region Γ is no longer a constant and its value depends on the thermodynamic state as well as on the fluid properties. For example, in the polytropic Van der Waals model,

$$\text{PVdW:} \qquad P(T, v) = \frac{1}{M}\frac{\bar{R}T}{v-b} - \frac{a}{v^2}, \qquad e(T, v) = \frac{N}{M}\frac{\bar{R}T}{2} - \frac{a}{v} + e_0, \qquad (2.4)$$

the effects of long- and short-range intermolecular forces are included via the two fluid-dependent parameters $a = 3P_c v_c^2$ and $b = v_c/3$, respectively, where the subscript c indicates critical point quantities [19]. Note that the Van der Waals model can be written in a so-called reduced form,

$$\text{PVdW:} \qquad \widetilde{P}(\widetilde{T}, \widetilde{v}) = \frac{8\widetilde{T}}{3\widetilde{v} - 1} - \frac{3}{\widetilde{v}^2}, \qquad \widetilde{e}(\widetilde{T}, \widetilde{v}) = \frac{4}{3}N\widetilde{T} - \frac{3}{\widetilde{v}} + \widetilde{e}_0, \qquad (2.5)$$

where $\widetilde{P} = P/P_c$, $\widetilde{T} = T/T_c$, $\widetilde{v} = v/v_c$ and $\widetilde{e} = e/(P_c v_c)$ in which the parameters M, a and b are no longer present and the only substance-specific quantity is the molecular complexity N. Therefore, the fundamental derivative of a polytropic Van der Waals gas is a decreasing function of the molecular complexity N and its value depends also on the reduced thermodynamic state, e.g., $(\widetilde{T}, \widetilde{v})$, as follows [15]:

$$\text{PVdW:} \qquad \Gamma(\widetilde{T}, \widetilde{v}) = \frac{\left(1 + \frac{1}{N}\right)\left(1 + \frac{2}{N}\right)\frac{3\widetilde{T}\widetilde{v}}{(3\widetilde{v}-1)^3} - \frac{1}{\widetilde{v}^3}}{\left(1 + \frac{2}{N}\right)\frac{\widetilde{T}}{(3\widetilde{v}-1)^2} - \frac{2}{3}\frac{1}{\widetilde{v}^3}}. \qquad (2.6)$$

More complex models, such as the multiparameter EoSs (MPEoSs) include a large number of fluid-dependent parameters, which in turn influence the evaluation of the fundamental derivative Γ.
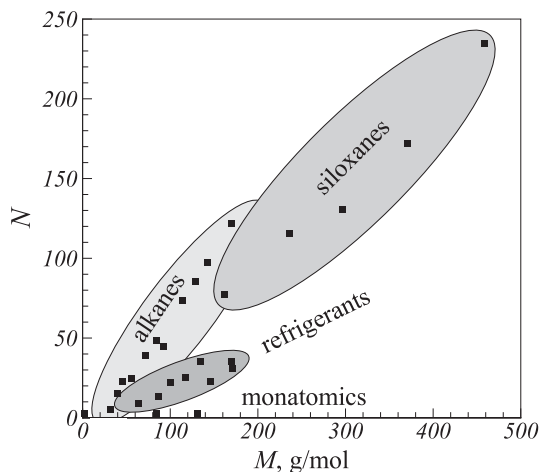
Figure 2.2: *Molecular complexity (in terms of the number of active degrees of freedom) versus molecular weight for selected fluids listed in Table 2.2.*

Multiparameter equations of state can be classified as technical or reference equations of state [20, 21]. Both reference and technical equations of state are able to describe all the best experimental thermodynamic property data available for a certain fluid within their experimental uncertainty. Reference equations of state have been developed only for few substances, simple gases and water, for which a large number of accurately evaluated experimental data of all kind of thermodynamic properties are available (hundreds or thousands of data whose high accuracy has been determined). Their development requires therefore a large amount of work, because also the functional form of the equation, specialized to the fluid, is optimized. Technical equations of state fulfill to a lower set of requirements and are therefore less accurate, but they are able to satisfy the demand of modern technical applications. Their functional form is simpler and it is not fluid-specific, but rather applies to a class of substances. Still the relatively large number of parameters allow for the correct fitting of a wide variety of experimental points (liquid and vapor pressure-volume-temperature points, saturation pressure and density, enthalpies of vaporization, speed of sound, etc.). The main limitation of MPEoSs is that their development requires the availability of a set of carefully evaluated experimental data of many different thermodynamic properties. For this reason, the number of fluids for which reference or technical equations of state is available is still quite limited (6 reference and 30 technical equations of state). Another draw-

back of MPEoSs is that their empirical nature prevents from assigning a physical significance to parameters, as opposed, for instance, to the Van der Waals family of cubic equations of state.

An example is the Wagner-Pruß MPEoS for water, for which the uncertainty in the vapor phase is less than 0.1% and 0.2% for all volumetric and caloric properties, respectively [7]. By comparison, the MPEoSs for carbon monoxide, toluene and R245fa are technical and their accuracy is between 0.2-1% for volumetric properties and 2% for caloric properties [22]. In this work, the MPEoSs implemented in the REFPROP code by NIST have been used [23].

It is worthwhile pointing out that, if evaluated from a highly accurate thermodynamic model such as a MPEoS, the fundamental derivative of gasdynamics Γ is a more general parameter than the number of active degrees of freedom N, if used as a measure of molecular complexity. Indeed, Γ quantifies the thermodynamic effect of all possible mechanism for storing energy, thereby implicitly also taking into account the contribution from intermolecular attractive and repulsive forces to the isochoric heat capacity, such as the aforementioned Coulomb, dipole-dipole, three and many body potentials. In this respect, the following classification was proposed in Ref. [15]. Fluids with $\Gamma > 1$ everywhere ($(\partial c/\partial v)_s < 0$) in the vapor thermodynamic region are classified as Low Molecular Complexity (LMC) fluids [16, 15]. For LMC fluids, which are made of simple molecules, real-gas effects are limited to quantitative deviations with respect to ideal-gas fluid dynamic behavior [24], an exception being the temperature increase due to the Joule-Thompson isenthalpic expansion above a fluid's inversion temperature. Similarly, fluids with $0 < \Gamma < 1$ in a finite thermodynamic region are termed High Molecular Complexity (HMC) fluids since $(\partial c/\partial v)_s > 0$. For HMC fluids also qualitative differences in fluid dynamic behavior can be observed in the dense gas region, close to saturation [25, 26, 27]. Most notable is the increase in the speed of sound upon isentropic expansion, possibly leading to a local decrease in the Mach number [27, 28, 29, 11], which instead increases monotonically for an isentropic ideal-gas expansion. Ref. [25] reports examples of expansions of a group of alkanes in the dense-gas region. Finally, so-called Bethe-Zel'dovich-Thompson [17, 30, 31] (BZT) fluids exhibit a (smaller) finite thermodynamic region where $\Gamma < 0$ [32]. BZT fluids are made of complex molecules such as perfluorocarbon PP10 ($C_{13}F_{22}$) or siloxane D_6 ($[Si-O-(CH_3)_2]_6$), nonclassical gasdynamic phenomena including rarefaction shock waves [33] may possibly occur, although no experimental evidence of these "exotic" wave fields is available yet [34].

In Ref. [14], the dependence of Γ on selected fluid parameters including the

acentric factor, the critical compressibility and the assumption of polytropicity has been assessed using several simple thermodynamic models. It was concluded that, within the same fluid family or class, the minimum value of Γ depends on the ratio of the isochoric heat capacity to the gas constant R. In the nomenclature used here, this translates into the fact that the molecular complexity of a fluid family depends only on the active degrees of freedom N. In Ref. [31], the observation that, for a given reduced thermodynamic state, Γ decreases with increasing N (cf. Eq. (2.6)) is demonstrated to hold also for a general EoS. In the following, N is the only parameter used to indicate molecular complexity.

For a given fluid family or class, molecular weight and molecular complexity are related, because their molecular structure does not vary. Within a single fluid family, an increase in the number of active degrees of freedom is proportional to an increase in molecular weight, at least for the heavier fluids belonging to the family. The value of the complexity-to-weight ratio N/M depends on the molecular structure of the fluid family, i.e., on the weight and configuration of the individual atoms in the molecule, and is therefore different for each class of fluids, as shown for a selection of fluids in Fig. 2.2. The figure sets into evidence that molecules of high-molecular-weight fluids often also have a high number of degrees of freedom (high molecular complexity). Note that this is true to some extent also for fluids belonging to different families. The correlation of molecular complexity and weight makes it difficult to attribute fluid dynamic properties to these properties separately, and hence these terms are often used interchangeably in literature, even though this practice is questionable if different fluid families are considered [25, 28]. In Section 2.3 the separate influence of the values of N and M on isentropic expansions is investigated.

2.3 Influence of Molecular Complexity and Weight on Isentropic Expansions

In this section, the influence of molecular complexity and weight on the speed of sound c, the flow velocity u and the Mach number $\text{Ma} = u/c$ along isentropic expansions is investigated. The flow is assumed to undergo a steady isentropic expansion from an infinitely large reservoir, where the fluid is at rest and at so-called reservoir or total conditions, into an ambient where the pressure is uniform. For the expansion to be isentropic, the hypothesis is that shock waves are absent and the effects of viscosity and thermal conductivity can be neglected, which is often the case at high Reynolds number, if no separation occurs. Isentropic conditions are therefore often assumed during the preliminary design of any expander and

also in the following. Finally, the flow is assumed to be quasi-onedimensional, allowing for a scalar velocity u to represent the average axial velocity.

First, the procedure to compute c, u and Ma is presented for a general EoS and it is then specialized to the case of ideal polytropic gases in section 2.3.1 and of dense gases in section 2.3.2. The properties of dense gases are modelled using both the Van der Waals and very accurate multi-parameter EoSs.

Given an arbitrary pressure-explicit equation of state $P = P(T, v)$, the sound speed c is given by

$$c^2 \equiv \left(\frac{\partial P}{\partial \rho}\right)_s = -v^2 \left[\left(\frac{\partial P}{\partial v}\right)_T - \frac{T}{C_v}\left(\frac{\partial P}{\partial T}\right)_v^2\right], \tag{2.7}$$

where the density $\rho = 1/v$. The isochoric specific heat capacity is computed as the sum of an ideal-gas contribution $C_v^0 = C_v^0(T)$ and a real-gas residual that is only dependent on the pressure EoS, i.e., [35]

$$C_v(T, v) = C_v^0(T) + T \int_\infty^v \left(\frac{\partial^2 P}{\partial T^2}\right)_v dv. \tag{2.8}$$

Note that even if C_v^0 is independent from T under the polytropic assumption, the real gas C_v is not constant and depends on both the temperature and the specific volume.

The fluid velocity can be computed from the energy conservation for an isentropic transformation, which implies that the total or stagnation enthalpy h^t is constant. Therefore, if h_1^t is the total enthalpy at the inlet of the one-dimensional channel, the so-called inlet or reservoir total enthalpy, then, from the definition of h^t, $h^t = h + u^2/2$, with $h = e + Pv$ the specific enthalpy, one immediately obtains $u^2 = 2(h_1^t - h)$. In particular, if one considers an isentropic expansion to an outlet pressure P_2, with the outlet state being denoted by subscript 2, then the flow velocity at the end of the expansion reads

$$u_2^2 = 2(h_1^t - h_2), \tag{2.9}$$

where the exit enthalpy h_2 is computed as $h_2 = h(s_1, P_2)$, since $s = s_1 = $ constant under the isentropic assumption. The exit or outlet speed of sound and Mach number are computed as function of s_1 and P_2 as well. In Sections 2.3.1 and 2.3.2 results for ideal and dense-gas flows are given.

2.3.1 Polytropic Ideal-Gas

In case of expansions occurring in the dilute-gas thermodynamic region, the polytropic ideal gas (PIG) law defined in Eq. (3.1) can be used to quantify the influ-
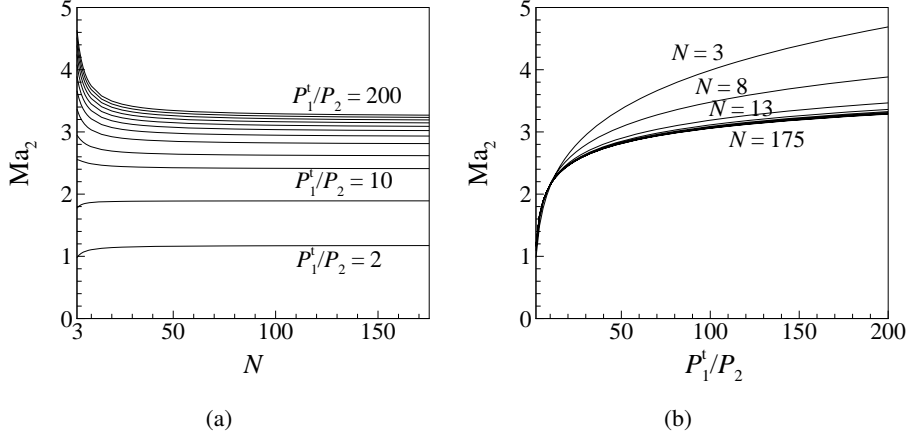
Figure 2.3: *Influence of (a) molecular complexity and (b) pressure ratio on the exit Mach number Ma$_2$ for fluids expanded in the ideal gas region, as given by Eq. (2.10).*
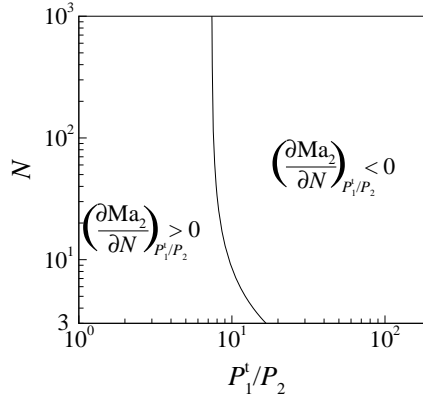
Figure 2.4: *Locus of exit Mach number maxima at fixed pressure ratios.*

ence of the molecular complexity and weight on the flow field. By substituting $\gamma = 1 + 2/N$ and $R = \bar{R}/M$ into the well-known relations for Ma, c and u for steady isentropic flows of polytropic ideal gases, see, e.g., Ref. [32], the dependence of the flow quantities on the molecular complexity N and weight M can be derived immediately. For the Mach number Ma one has

$$\text{Ma}_{2,\text{PIG}}^2 = N \left[\left(\frac{P_1^{\text{t}}}{P_2} \right)^{\frac{2}{N+2}} - 1 \right], \tag{2.10}$$

an expression that places into evidence the dependence of the exit Mach number on molecular complexity and shows as a rather unpredictable results that Ma_2 does not depend directly on the molecular weight of the fluid. It is remarkable that such a well-known relation, commonly written using γ, has still some information to unveil if the simple substitution $\gamma = 1 + 2/N$ is made.

The exit Mach number depends of course also on the pressure or expansion ratio P_1^{t}/P_2, where P_1^{t} is the inlet total pressure. Figs. 2.3(a) and 2.3(b) report the exit Mach number for different values of molecular complexity and expansion ratio. The dependence on P_1^{t}/P_2 is relevant for all considered pressure ratios; as well known, the larger the expansion ratio, the higher the exit Mach number. The effect of molecular complexity is large from $N = 3$ up to $N \approx 30$. Remarkably enough, the Mach number can either increase or decrease with molecular complexity, depending on the considered pressure ratio. This is evident in Fig. 2.3(a), where the $P_1^{\text{t}}/P_2 \approx 10$ curve separates the two trends. More precisely, for low pressure ratios, the Mach number is a monotonically increasing function of N. For higher pressure ratios, the Mach number first sharply increases to a maximum between approximately $0 < N < 5$ and then decreases for fluids of increasing molecular complexity. The occurrence of a maximum is the result of the counteracting influences of N in Eq. (2.10). Above the minimum number of degrees of freedom of a molecule, i.e., $N = 3$ corresponding to a monatomic gas, the Mach number is a decreasing function of N at these high pressure ratios. The locus of the Mach number extrema is given in Fig. 2.4. Fig. 2.4 can be used to determine the effect of a change in the fluid properties (N) or pressure ratio on the exit Mach number. For example, if the operating conditions are in the upper right portion of the diagram, then $(\partial \text{Ma}_2/\partial N)_{P_1^{\text{t}}/P_2} < 0$ and employing a more complex fluid would lead to a decrease in the exit Mach number, and vice versa for the left part.

Considering now the sound speed, from Eq. (2.7), the ideal polytropic gas sound speed reduces to

$$c_{2,\text{PIG}}^2 = \gamma R T_2 = \left(1 + \frac{2}{N} \right) \frac{\bar{R} T_1^{\text{t}}}{M} \left(\frac{P_1^{\text{t}}}{P_2} \right)^{-\frac{2}{N+2}} \tag{2.11}$$

(a) Dimensionless sound speed

(b) Dimensionless velocity
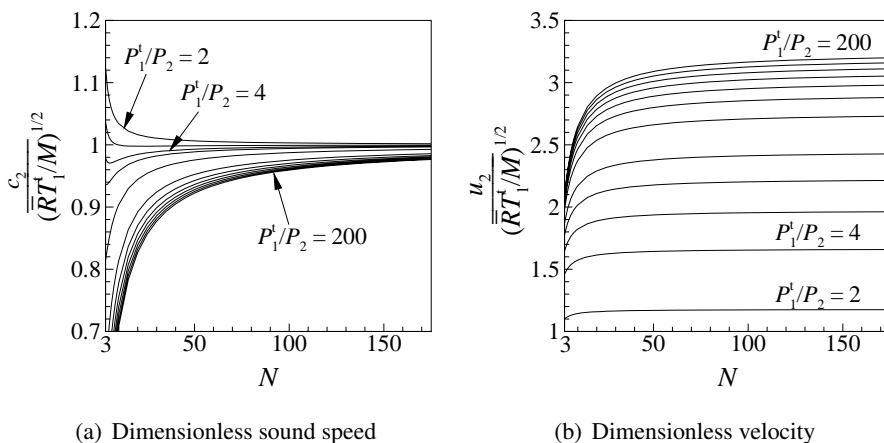
Figure 2.5: *Dimensionless outlet sound speed and velocity for fluids with different molecular complexity expanded in the ideal-gas region at various expansion ratios. The reference velocity used in the adimensionalisation is $\sqrt{\bar{R}T_1^t/M}$ to remove the dependence on both the reservoir state and the molecular weight.*

(a) Sound speed
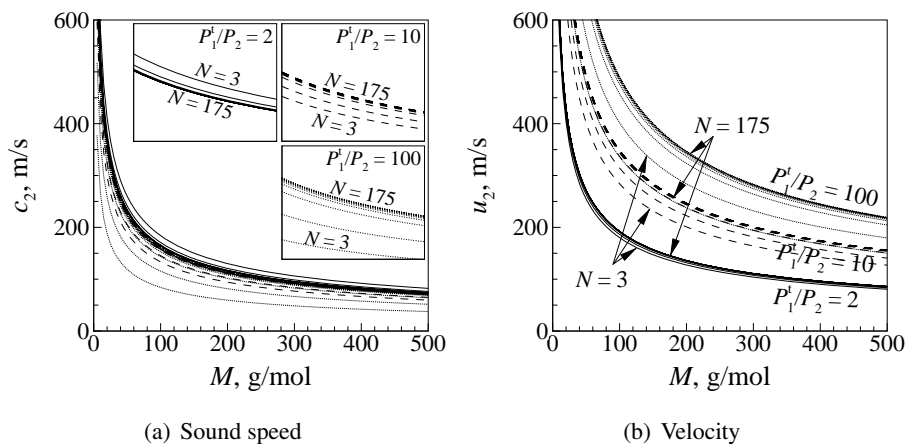
(b) Velocity

Figure 2.6: *Outlet sound speed and flow velocity as functions of molecular weight for fluids of various molecular complexity and for three different expansion ratios. The total temperature at the inlet of the one-dimensional channel is 322.5 K.*

where T_1^t is the total (stagnation) temperature at inlet. In the above expression, the term $(1 + 2/N)\bar{R}$ is the molar specific heat at constant pressure which decreases with increasing molecular complexity. The term $1/M$ decreases with the molecular weight. Increasing the inlet total temperature T_1^t results in an increase of the exit speed of sound. Finally, the term $(P_1^t/P_2)^{\frac{-2}{N+2}} = T_2/T_1^t$ is a positive increasing function of N, since $P_1^t/P_2 > 1$. This contribution is due to the temperature ratio resulting from a given expansion ratio, which is higher for complex fluids, i.e., the outlet temperature is closer to the inlet value, a result that is confirmed also by more complex thermodynamic models.

The flow velocity (2.9) reads instead

$$u_{2,\text{PIG}}^2 = 2(h_1^t - h_2) = (N + 2)\frac{\bar{R}T_1^t}{M}\left[1 - \left(\frac{P_1^t}{P_2}\right)^{-\frac{2}{N+2}}\right] \tag{2.12}$$

where the PIG relations $h - h_{\text{ref}} = C_P^0(T - T_{\text{ref}})$, with $h_{\text{ref}} = 0$ J/kg at $T_{\text{ref}} = 0$ K have been applied. Therefore, two contributions from molecular complexity can be singled out. The first term, $N + 2$, is in fact $2C_P^0\bar{R}/M$, and it is linear with N. The term $(1 - P_1^t/P_2)^{-\frac{2}{N+2}}$ is the relative temperature difference between the total inlet temperature and the outlet temperature, which is a mildly decreasing function of N.

Relations (2.11) and (2.12) show that the exit speed of sound and flow velocity are dependent on both molecular complexity N and weight M, as well as on the inlet total temperature T_1^t. To remove the dependence on M and T_1^t, the exit speed of sound and flow velocity are made dimensionless by $\sqrt{(\bar{R}T_1^t/M)}$ and plotted in Fig. 2.3 for different expansion ratios and for fluids with different molecular complexity. The dimensionless exit flow velocity is found to be a monotonically increasing function of N regardless of the expansion ratio, whereas the speed of sound increases monotonically with N for P_1^t/P_2 larger than about 3. The non-monotone behavior of the speed of sound explains the similar trend of the Mach number shown in Fig. 2.3(a).

The influence of the molecular weight M can be appreciated from Fig. 2.6, where the dimensional sound speed and velocity at the outlet are plotted for $T_1^t = 322.5$ K and for different values of N and M. Three different pressure ratios are considered. Due to the presence of the term $1/M$ in expressions (2.11) and (2.12), both c_2 and u_2 are monotonic decreasing functions of M. Note again the reversed behavior with respect to N of the sound speed for pressure ratios larger than about 3. For the physically relevant interval of $3 < N < 200$—which for the selected fluids corresponds to approximately $0 < M < 500$ g/mol, see Fig. 2.2 and

Table 2.2—the sound speed depends much more strongly on molecular weight than on molecular complexity, as shown in Fig. 2.6(a).

2.3.2 Dense-Gas Region

To analyze the effect of the molecular complexity in the dense-gas thermodynamic region, where the the polytropic ideal gas assumption is no longer valid, two types of thermodynamic models are employed here, the polytropic Van der Waals [19] (PVdW) EoS model (2.4) and a multiparameter equations of state (MPEoSs).

The sound speed relation at the outlet for a polytropic Van der Waals fluid is obtained by substituting the model definition (2.4) into relation (2.7) which gives

$$c_{2,\text{PVdW}}^2 = \frac{\bar{R}T_{\text{c}}}{M}\left[\left(1+\frac{2}{N}\right)\widetilde{T}_1^{\text{t}}\left(\frac{3\widetilde{v}_1^{\text{t}}-1}{3\widetilde{v}_2-1}\right)^{\frac{2}{N}}\left(\frac{3\widetilde{v}_2}{3\widetilde{v}_2-1}\right)^2-\frac{6}{\widetilde{v}_2}\right] \qquad (2.13)$$

where in the second expression, the isentropic assumption, $s(T_1^{\text{t}}, v_1^{\text{t}}) = s(T_2, v_2)$, with

$$s(T,v) = s_0 + \frac{N}{M}\frac{\bar{R}}{2}\ln\frac{T}{T_0} + \frac{\bar{R}}{M}\ln\frac{v-b}{v_0-b}$$

here s_0, T_0 and v_0 are evaluated at a suitably defined reference state, has been used to compute the outlet temperature in terms of the stagnation inlet temperature and specific volume. In the last expression of (2.13), the temperature and the specific volume are made dimensionless (reduced) with their corresponding critical point values. The total specific volume at inlet v_1^{t} is computed using the Van der Waals pressure EoS, namely, by solving for v_1^{t} the equation $P(T_1^{\text{t}}, v_1^{\text{t}}) - P_1^{\text{t}} = 0$. The outlet specific volume v_2 is instead computed using the isentropic assumption $s(P_1^{\text{t}}, v_1^{\text{t}}) = s(P_2, v_2)$, where

$$s(P,v) = s_0 + \frac{N}{2}\frac{\bar{R}}{M}\ln\left[\frac{M\left(P+\dfrac{a}{v^2}\right)(v-b)^{1+\frac{2}{N}}}{\bar{R}T_0(v_0-b)^{\frac{2}{N}}}\right].$$

Similarly, the exit velocity is computed from (2.9) and (2.4) as

$$\begin{aligned}
u_{2,\text{PVdW}}^2 &= 2[h_1^{\text{t}}-h_2]\\
&= \frac{\bar{R}T_{\text{c}}}{M}\left[\widetilde{T}_1^{\text{t}}\left(\frac{N}{2}\left(1-\left(\frac{3\widetilde{v}_1^{\text{t}}-1}{3\widetilde{v}_2-1}\right)^{\frac{2}{N}}\right)\right.\right.\\
&\quad\left.\left.+\frac{3\widetilde{v}_1^{\text{t}}}{3\widetilde{v}_1^{\text{t}}-1}\left(\frac{3\widetilde{v}_1^{\text{t}}-1}{3\widetilde{v}_2-1}\right)^{\frac{2}{N}}\frac{3\widetilde{v}_2}{3\widetilde{v}_2-1}\right)-6\frac{\widetilde{v}_1^{\text{t}}-\widetilde{v}_2}{\widetilde{v}_1^{\text{t}}\widetilde{v}_2}\right]
\end{aligned} \qquad (2.14)$$
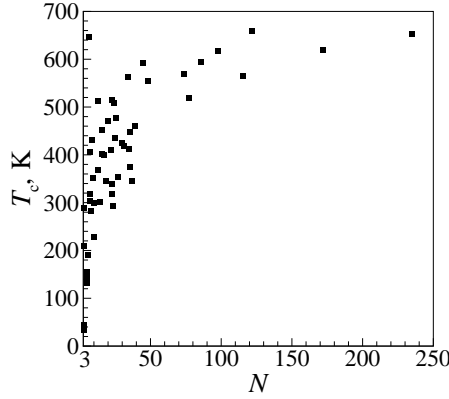
Figure 2.7: *Critical temperature versus the number of active degrees of freedom for selected fluids listed in Table 2.2.*

where the expression of the enthalpy for a polytropic Van der Waals fluid,

$$h(T,v) = RT\left[\frac{N}{2} + \frac{v}{v-b}\right] - 2\frac{a}{v} + e_0,$$

has been used to compute the difference between the inlet total and the outlet enthalpy.

In a given reduced state, the exit sound speed c_2 (2.13) and flow velocity u_2 (2.14) depend on the molecular complexity N, on the molecular weight M as well as on the critical temperature of the fluid T_c. The dependence on M is the same as in the ideal gas case and both the speed of sound and the flow velocity decrease with M. Instead, c_2 and u_2 increase with T_c, which is higher for complex molecules. Fig. 2.7 reports the critical temperature of the fluids listed in Table 2.2 as a function of molecular complexity. From relations (2.13) and (2.14), the exit Mach number is found to be independent of either the molecular weight M or the critical temperature T_c, as in the ideal gas case.

In the following, to eliminate the dependence on M and T_c, the speed of sound and the flow velocity are made dimensionless by means of the reference velocity $\sqrt{\bar{R}T_c/M}$. However, differently from the ideal-gas case, the behavior of the dimensionless flow variables in dense-gas expansions is dependent on the reduced inlet conditions, cf. Eqs. (2.13) and (2.14). Therefore, it is not possible to repeat the extended analysis performed for the ideal gas case, see Figs. 2.4-2.6, also for the dense-gas case. Here, only three different reduced inlet conditions are considered to evaluate the influence of the molecular complexity N on the exit Mach

(a) Mach number (b) Dimensionless sound speed (c) Dimensionless velocity
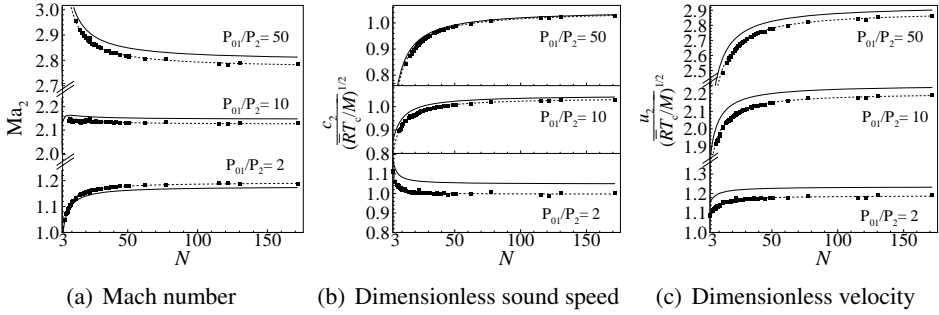
Figure 2.8: *Fluid dynamic quantities at outlet for fluids of increasing complexity listed in Table 2.2 at pressure ratios $P_1^t/P_2 = 2$, 10 and 50. Inlet conditions are given in Table 3.2, for an inlet compressibility factor $Z_1 = 0.9$. Results are given for the PIG model (———), PVdW model (− − −) and the MPEoSs of various fluids (■). Results of the MPEoS models for which condensation occurs, have been omitted.*

number, the speed of sound and the velocity.

Table 2.1: *Inlet conditions for the three dense-gas expansions in terms of reduced values.*

Reduced total inlet pressure	P_1^t/P_c	0.4	0.7	1
Reduced total inlet temperature	T_1^t/T_c	1.1	1.1	1.1
Compressibility factor at the inlet	Z_1	0.9	0.8	0.7

The inlet conditions of the three expansion processes are given in reduced terms in Table 3.2. In this table, the compressibility factor $Z \equiv Pv/(RT)$ quantifies the degree of thermodynamic nonideality, i.e., the deviation of volumetric properties from ideal gas behavior, for which $Z \equiv 1$. These processes represent dense-gas expansions starting from state point of increasing non-ideality, as put into evidence by their respective inlet compressibility factors of $Z_1 = 0.9, 0.8$ and 0.7.

(a) Mach number   (b) Dimensionless sound speed   (c) Dimensionless velocity
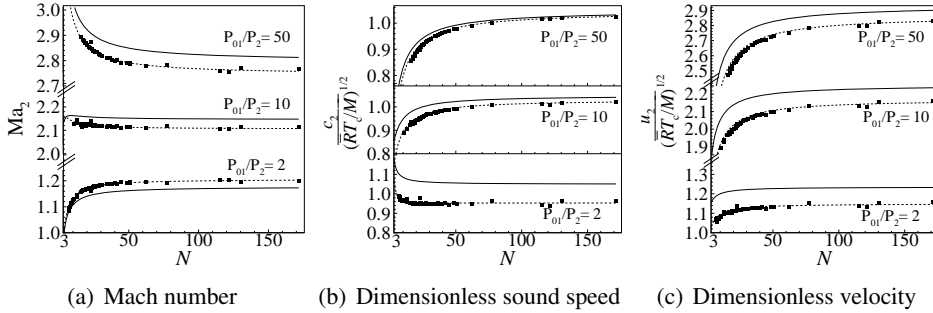
Figure 2.9: *Fluid dynamic quantities at outlet for fluids of increasing complexity listed in Table 2.2 at pressure ratios $P_1^t/P_2 = 2$, 10 and 50. Inlet conditions are given in Table 3.2, for an inlet compressibility factor $Z_1 = 0.8$. Results are given for the PIG model (———), PVdW model (− − −) and the MPEoSs of various fluids (■). Results of the MPEoS models for which condensation occurs, have been omitted.*

(a) Mach number   (b) Dimensionless sound speed   (c) Dimensionless velocity
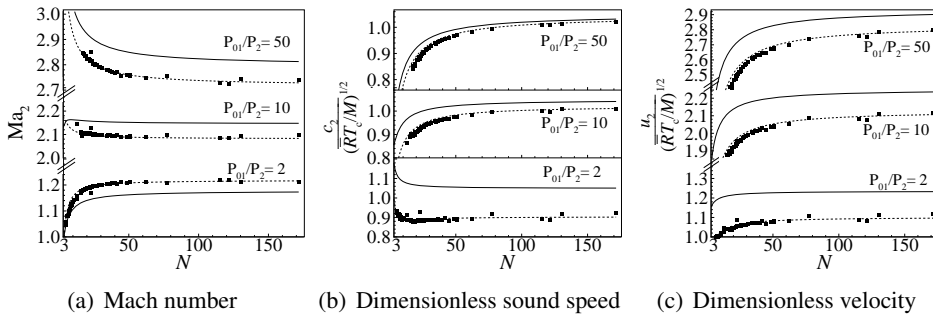
Figure 2.10: *Fluid dynamic quantities at outlet for fluids of increasing complexity listed in Table 2.2 at pressure ratios $P_1^t/P_2 = 2$, 10 and 50. Inlet conditions are given in Table 3.2, for an inlet compressibility factor $Z_1 = 0.7$. Results are given for the PIG model (———), PVdW model (− − −) and the MPEoSs of various fluids (■). Results of the MPEoS models for which condensation occurs, have been omitted.*

Table 2.2: *Fluids used in the dense gas study (Figs. 2.8-2.10). The number of active degrees of freedom of these fluids is plotted against the molecular weight in Fig. 2.2 and their critical temperature versus their number of active degrees of freedom in Fig. 2.7. Information about the source of experimental data and accuracy of the MPEoS can be found in Ref. [23].*

Name	Chemical formula	M, g/mol	N, -	P_c, bar	T_c, °C
Hydrogen	H_2	2.02	3.00	13.0	-240
Parahydrogen	$p\text{-}H_2$	2.02	3.00	12.9	-240
Helium	He	4.00	3.00	2.27	-268
Deuterium	D	4.03	3.35	16.7	-235
Methane	CH_4	16.04	6.04	46.0	-82.6
Ammonia	NH_3	17.03	7.33	113	132
Water	H_2O	18.02	6.87	221	374
Heavy water	D_2O	20.03	7.52	217	371
Neon	Ne	20.18	3.00	26.8	-229
Carbon monoxide	CO	28.01	5.00	34.9	-140
Nitrogen	N_2	28.01	5.00	34.0	-147
Ethylene	C_2H_4	28.05	7.95	50.4	9.2
Ethane	C_2H_6	30.07	10.8	48.7	32.2
Oxygen	O_2	32.00	5.00	50.4	-119
Methanol	CH_3OH	32.04	12.6	82.2	240
Fluoromethane	CH_3F	34.03	7.27	59.0	44.1
Hydrogen sulfide	H_2S	34.08	6.45	90.0	100

Table 2.2: *Fluids and properties used in the analysis (continued).*

Name	Chemical formula	M, g/mol	N, -	P_c, bar	T_c, °C
Fluorine	F_2	38.00	5.03	51.7	-129
Argon	Ar	39.95	3.00	48.6	-122
Propyne	C_3H_4	40.06	15.5	56.3	129
Propylene	C_3H_6	42.08	16.0	45.6	91.1
Cyclopropane	C_3H_6	42.08	16.4	55.8	125
Carbon dioxide	CO_2	44.01	7.00	73.8	31.0
Nitrous oxide	N_2O	44.01	7.40	72.5	36.4
Propane	C_3H_8	44.10	19.1	42.5	96.7
Dimethylether	C_2H_6O	46.07	17.2	53.4	127
Ethanol	CH_3CH_2OH	46.07	22.6	61.5	241
Difluoromethane	CH_2F_2	52.02	9.36	57.8	78.1
Butene	C_4H_8	56.11	24.9	40.1	146
Cis-Butene	c-C_4H_8	56.11	24.6	42.3	163
Isobutene	i-C_4H_8	56.11	25.6	40.1	145
Trans-butene	t-C_4H_8	56.11	25.6	40.3	155
Acetone	CH_3COCH_3	58.08	24.3	47.0	235
n-Butane	C_4H_{10}	58.12	29.5	38.0	152
Isobutane	i-C_4H_{10}	58.12	28.4	36.3	135
Carbon oxide sulfide	COS	60.08	8.84	63.7	106
Sulfur dioxide	SO_2	64.06	8.70	78.8	157

Table 2.2: *Fluids and properties used in the analysis (continued).*

Name	Chemical formula	M, g/mol	N, -	P_c, bar	T_c, °C
R152a	CHF_2CH_3	66.05	17.5	45.2	113
Trifluoromethane	CHF_3	70.01	10.3	48.3	26.1
Nitrogen trifluoride	NF_3	71.02	9.21	44.6	-39.2
Isopentane	$i\text{-}C_5H_{12}$	72.15	39.3	33.8	187
Neopentane	$neo\text{-}C_5H_{12}$	72.15	38.1	32.0	161
Pentane	C_5H_{12}	72.15	39.8	33.7	197
Benzene	C_6H_6	78.11	34.2	48.9	289
Krypton	Kr	83.80	3.00	55.3	-63.7
R143a	CF_3CH_3	84.04	18.7	37.6	72.7
Cyclohexane	C_6H_{12}	84.16	48.4	40.8	280
Hexane	C_6H_{14}	86.18	50.9	30.3	235
Isohexane	$i\text{-}C_6H_{14}$	86.18	50.7	30.4	225
R22	$CHClF_2$	86.47	13.2	49.9	96.1
R14	CF_4	88.01	10.3	37.5	-45.6
Toluene	C_7H_8	92.14	44.8	41.3	319
Heptane	C_7H_{16}	100.2	62.2	27.4	267
R142b	$C_2H_3ClF_2$	100.5	22.3	40.6	137
R134a	CH_2FCF_3	102.0	21.6	40.6	101
R21	$CHCl_2F$	102.9	15.8	51.8	178
R13	$CClF_3$	104.5	14.1	38.8	28.9

Continued on next page...

Table 2.2: *Fluids and properties used in the analysis (continued).*

Name	Chemical formula	M, g/mol	N, -	P_c, bar	T_c, °C
Octane	C_8H_{18}	114.2	73.8	25.0	296
R141b	$C_2H_3Cl_2F$	116.9	25.4	42.1	204
R125	$HF_2C\text{-}CF_3$	120.0	22.5	36.2	66.0
R12	CCl_2F_2	120.9	17.7	41.4	112
Nonane	C_9H_{20}	128.3	85.6	22.8	321
Xenon	Xe	131.3	3.00	58.4	16.6
R245ca	$CHF_2CF_2CH_2F$	134.0	35.4	39.3	174
R245fa	$CF_3CH_2CHF_2$	134.0	32.9	36.5	154
R124	$CHClFCF_3$	136.5	26.1	36.2	122
R11	CCl_3F	137.4	20.2	44.1	198
R116	CF_3CF_3	138.0	23.3	30.5	19.9
Decane	$C_{10}H_{22}$	142.3	97.5	21.0	345
Sulfur hexafluoride	SF_6	146.1	22.5	37.5	45.6
R236ea	$CF_3CHFCHF_2$	152.0	35.1	35.0	139
R236fa	$CF_3CH_2CF_3$	152.0	34.0	32.0	125
R123	$CHCl_2CF_3$	152.9	28.6	36.6	184
R115	$CClF_2CF_3$	154.5	27.1	31.3	80.0
MM	$C_8H_{18}OSi_2$	162.4	77.4	19.4	246
R227ea	CF_3CHFCF_3	170.0	35.4	29.3	102
Dodecane	$C_{12}H_{26}$	170.3	122	18.2	385

Continued on next page...

Table 2.2: *Fluids and properties used in the analysis (continued).*

Name	Chemical formula	M, g/mol	N, -	P_c, bar	T_c, °C
R114	$CClF_2CClF_2$	170.9	31.2	32.6	146
R113	CCl_2FCClF_2	187.4	34.0	33.9	214
R218	$CF_3CF_2CF_3$	188.0	36.8	26.4	71.9
RC318	C_4F_8	200.0	41.9	27.8	115
MDM	$C_8H_{24}O_2Si_3$	236.5	115	14.2	291
D4	$C_8H_{24}O_4Si_4$	296.6	130	13.3	313
D5	$C_{10}H_{30}O_5Si_5$	370.8	172	11.6	346
MD4M	$C_8H_{24}O_2Si_3$	459.0	235	8.77	380

Results for the three initial conditions in Table 3.2 are shown in Figs. 2.8-2.10, where three different expansion ratios are also considered in order to investigate the dependence on this parameter. Polytropic Van der Waals results are plotted together with ideal-gas results and with those obtained using highly accurate multiparameter EoSs of the 75 fluids listed in Table 2.2.

The qualitative behavior of dense-gas expansions is similar to the one observed in ideal-gas expansions, possibly because the chosen inlet conditions, which are representative for industrial applications, are not far from the ideal-gas region [36]. This includes the change in monotonicity in the speed of sound at a given expansion ratio that results in the nonmonotone behavior of the Mach number with respect to molecular complexity. For dense gases, this behavior depends on the reduced thermodynamic state, as well as on the molecular complexity and expansion ratio as discussed in the ideal gas case. Quantitative differences between the polytropic ideal and the polytropic Van der Waals models are limited to about 25% for the speed of sound and the flow velocity, and to 5% for the Mach number and are most relevant for the lowest pressure ratio, for which the outlet state is closest to the initial, non-ideal, one. The difference in sound speed reduces at higher pressure ratios since these expansions have outlet states which are located well into the ideal gas region ($Z_2 = 1$). The PIG model does not account for intermolecular forces and hence overpredicts both sound speed and velocity [15]. Sound speed and velocity are overpredicted to a different extent, so that as a net result the Mach number, defined as $Ma_2 = u_2/c_2$, is underpredicted by the PIG model. In dense-gas expansions, the contribution of the repulsive molecular forces in the dense-gas region leads to a lower sound speed, as shown in Ref. [15], and, due to a lower specific enthalpy difference, to a lower flow velocity than what would be expected assuming an ideal gas. It is remarkable that the prediction from the very accurate MPEoS is indistinguishable from the Van der Waals model, within 1% in the worst cases. As anticipated, the MPEoSs implicitly takes into account additional parameters which allows for the molecular complexity of the fluid to include others characteristics such as, for example, Coulomb, dipole-dipole, three and many body potentials. It is therefore confirmed here that the most relevant parameter which determines the dense gas behavior of a given fluid is its molecular complexity defined simply in terms of active degrees of freedom N, as observed also in Ref. [14], using very simple models. Moreover, the fact that the Van der Waals and the MPEoS results are almost coincident if expressed in reduced variables points to the fact that the law of corresponding states can be used to compute dense-gas expansions accurately, at least in the mildly nonideal conditions considered here.

Table 2.3: *Parameters characterizing the expansion processes of steam, carbon dioxide and propane. The expansions correspond to the moderate ($Z_1 = 0.8$) dense-gas expansion defined in Section 2.3.2, as specified in reduced conditions in Table 3.2.*

		Steam	Carbon dioxide	Propane
Chemical formula		H_2O	CO_2	C_3H_8
Molecular weight	M, g/mol	18.02	44.01	44.1
Fundamental derivative of gasdynamics	Γ_{min}^V, -	1.162	1.257	0.864
Nr. of active degrees of freedom	N, -	6.9	7.0	19.1
Critical pressure	P_c, bar	220.6	73.8	42.5
Critical temperature	T_c, °C	374	32	96.7
MPEoS		Ref. [7]	Ref. [38]	Ref. [39]
Total inlet pressure	P_1^t, bar	154.4	51.6	29.76
Total inlet temperature	T_1^t, °C	438.7	61.4	133.7
Compressibility factor at inlet	Z_1, -	0.81	0.8	0.8
Static outlet pressure	P_2, bar	79.7	26.6	15.4
Compressibility factor at outlet	Z_2, -	0.82	0.82	0.87

To conclude, it should be noted that only post-expansion fluid dynamic quantities are considered here. The qualitative trends in the sound speed, velocity and Mach number along the expansion is possibly very different for complex fluids compared to that of simple molecules, as discussed in Section 2.4.

2.4 2D Flow Simulations of Expanding Flows

The flow through the stator of an exemplary turbine cascade has been simulated as an application of the findings of Section 2.3.2. The cascade is formed by two VKI LS-89 turbine blades, which is a standard high pressure turbine nozzle guide vane [37]. It should be noted that in reality the fluid dynamic design of the stator would lead to a different blade profile, depending on the fluid and operating conditions. Three industrial working fluids for power and refrigeration cycles are considered, namely, steam, carbon dioxide and propane. Example of applications are power plants (steam), particle separation processes (CO_2) and refrigeration (propane).

Steam, carbon dioxide and propane belong to different so-called fluid families
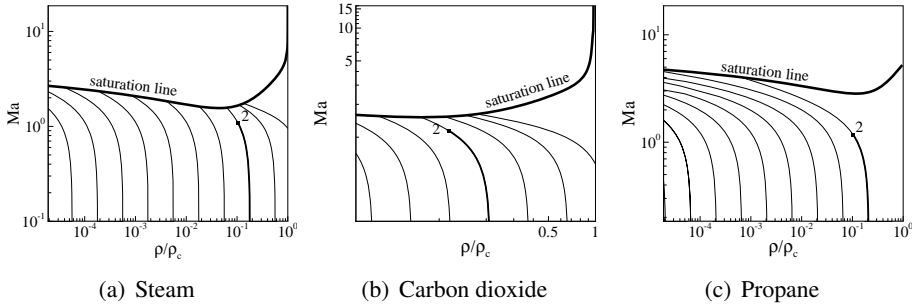
Figure 2.11: *Variation of Mach number with density along expansion isentropes starting from the inlet total pressure $P_1^t/P_c = 0.7$, which is equal to the inlet state of the expansion with $Z_1 = 0.8$ given in Table 3.2. Thick lines indicate saturation curves; thin ones isentropes. Initial or total conditions are at* Ma = 0.

because they have different molecular structures and are made of different atomic species. These fluids are chosen here because they are conveniently different in molecular complexity and weight. Their molecular weight and complexity, in terms of both the number of active molecular degrees of freedom, N, and the minimum value of the fundamental derivative along the saturation line, Γ_{min}^V, are given in Table 2.3. As it is evident from the table, steam and carbon dioxide have very similar molecular complexities, but due to their different molecular structures and atoms, they have very different molecular weights. Similarly, carbon dioxide and propane have nearly the same molecular weight but propane is much more complex. The inlet conditions for the simulated dense-gas expansions are taken from the moderate ($Z_1 = 0.8$) dense-gas expansion defined in Section 2.3.2 and are specified in Table 3.2 in terms of reduced variables. In this case a pressure ratio of $P_1^t/P_2 = 1.94$ is used. The dimensional process conditions are also listed in Table 2.3. The compressibility factor indicates that, even though the expansions occur in the dense gas region, they occur quite close to the region of gas ideality.

For each fluid, a Mach-density plot is given in Fig. 2.11, which shows a monotonous increase of the Mach number with decreasing density. Only HMC fluids may possibly feature a nonmonotonous Mach number variation with density in a limited thermodynamic region [25, 26]. This is not the case for the thermodynamic conditions considered here.

The ZFLOW code [40] is used to simulate the inviscid two-dimensional flow field generated by the expansion of the three fluids through the passage formed by two blades. To take into account thermodynamic nonideality and molecular
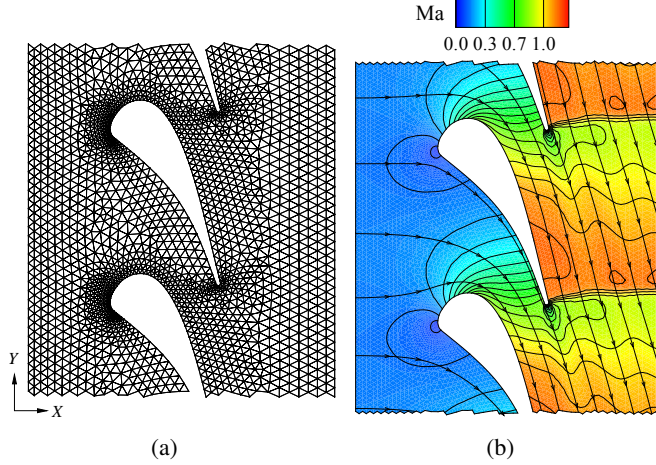
Figure 2.12: *(a) Coarse grid (1302 nodes) of the VKI LS-89 blade. X denotes the axial coordinate of the nozzle and Y the nozzle ring circumferential coordinate. Periodicity allowed the computations to be performed using only the top half of the grid depicted here. (b) Mach number flow field for steam and the expansion conditions given in Table 2.3.*

influences additional to the number of active molecular degrees of freedom, the MPEoSs of water [7], carbon dioxide [38] and propane [39] of the respective fluids are used to evaluate the thermodynamic properties. All flow solutions have converged up to at least a reduction of five orders of magnitude, with respect to the first iteration, measured in the L^2-norm of the conserved variables. To ensure a small discretization error, a grid convergence study has been performed by computing the solution on three grids with decreasing element size [11]. The coarse grid is shown in Fig. 2.12, together with the Mach number field and streamlines obtained on the finer grid for steam. The finest grid used in the computation is made of 4153 nodes and 6939 triangles.

The blade surface distributions of relevant flow quantities obtained from the simulation on the fine grid are depicted in Fig. 2.13 and 2.14. Surface distributions are plotted as a function of the reduced coordinate X/C_{ax}, where X is the axial coordinate and C_{ax} is the axial blade chord.

The distribution of the fundamental derivative of gasdynamics in Fig. 2.13(a) indicates that, for the chosen expansion conditions, steam and carbon dioxide both exhibit LMC behavior ($\Gamma > 1$), whereas propane behaves as a HMC fluid ($\Gamma < 1$).

Fig. 2.13(b) shows that the sound speed in steam is almost twice as high as that of carbon dioxide and propane, as they have a higher molecular weight. The

(a) Fundamental derivative of gasdynamics

(b) Sound speed

(c) Dimensionless sound speed

(d) $J = 1 - \Gamma \rho / c - 1/\mathrm{Ma}^2$

(e) Mach number

(f) Pressure coefficient

(g) Velocity

(h) Dimensionless velocity
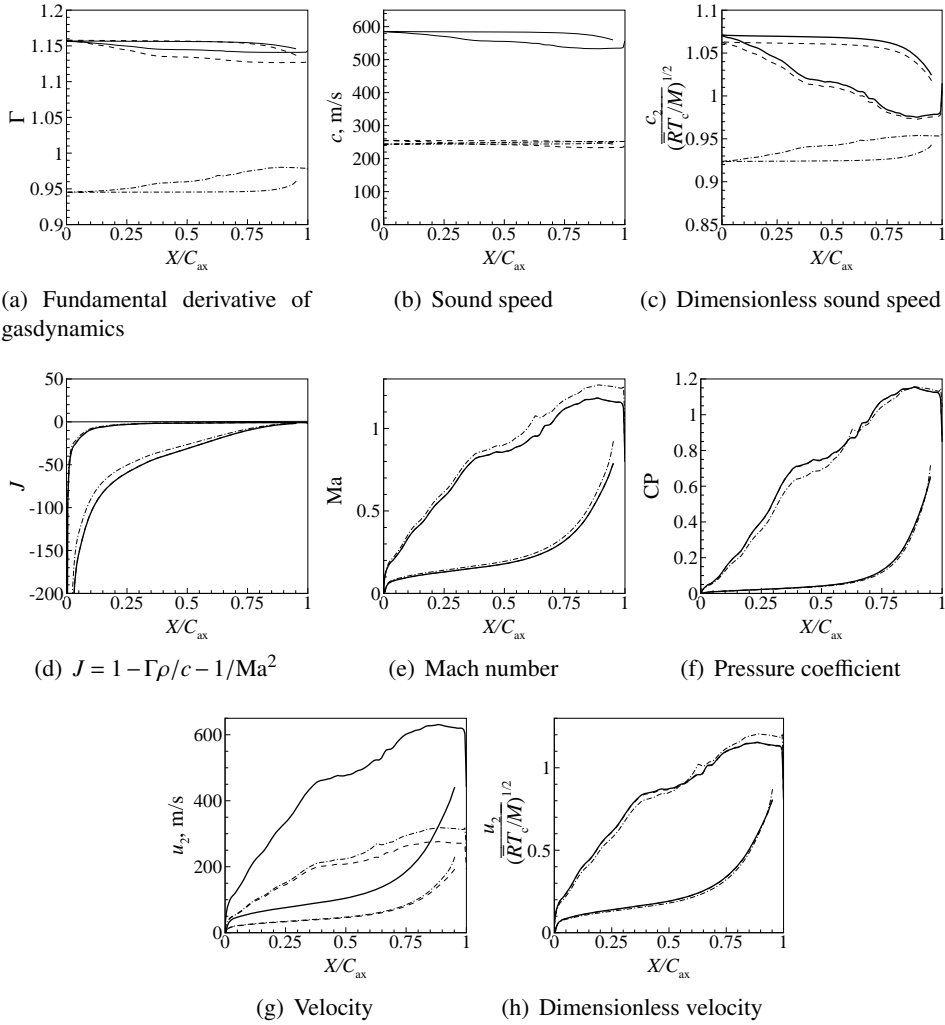
Figure 2.13: *Blade surface distributions of fluid dynamic quantities for steam (———), carbon dioxide (− − −) and propane (− · − · −).*

dimensional sound speed is strongly influenced by molecular weight. More importantly, the small difference between the sound speeds in carbon dioxide and propane, which have almost the same molecular weight, is the result of the weak influence of molecular complexity on the speed of sound, as explained in Section 2.3. By nondimensionalizing the sound speed with the reference velocity $\sqrt{\bar{R}T_c/M}$, which is different for each of the three fluids, the strong contribution of the molecular weight is eliminated. The HMC behavior of propane is clearly visible in Fig. 2.13(c), which shows that the speed of sound increases along the expansion. The quantitative differences in Fig. 2.13(c) are solely due to the weak influence of molecular complexity, as was observed in Fig. 2.9(b).

The variation of the Mach number with density is quantified by the variable $J = 1 - \Gamma\rho/c - 1/\text{Ma}^2$, see, e.g., Ref. [26]. The Mach number decreases with decreasing density (i.e., for an expansion) only if $J > 0$. For $J < 0$, the Mach number increases with decreasing density, which is the case for the three expanded fluids and for the considered conditions, as shown in Fig. 2.13(d).

The Mach number distribution itself, plotted in Fig. 2.13(e), is identical for steam and carbon dioxide which have molecules of similar complexity, and is not influenced by their different molecular weights and critical temperatures, as expected based on the observations made in Section 2.3. For the same pressure ratio, the more complex fluid propane achieves significantly higher Mach numbers.

The pressure coefficient along the blade, which is defined as $\text{CP} = (P_1^t - P)/(P_1^t - P_2)$ and exhibits no relevant differences for the three fluids, is reported in Fig. 2.13(f). Note that the pressure ratio is the same for the three fluids and hence only minor differences in the pressure coefficient along the blade can be expected.

Similarly to the speed of sound, the flow velocity, depicted in Fig. 2.13(g), is strongly influenced by molecular weight. The expansion of steam leads to velocities more than a factor of two higher than those obtained for the much heavier carbon dioxide and propane. However, the difference between these two fluids having nearly the same molecular weight, is also appreciable. Since the dimensionless velocity in the flows of carbon dioxide and propane are almost coincident, see Fig. 2.13(h), the differences in the dimensional velocity is a result of the different molecular complexity, which has a weak effect at this pressure ratio, see Section 2.3. The differences in the dimensionless velocities at the outflow are coherent with the results shown in Fig. 2.9(c), in which the velocity only slightly varies for $P_1^t/P_2 = 2$, even for low values of N.

Fig. 2.14(a) reports the compressibility factor Z along the blade. As expected, Z is always close to one for all fluids and hence the considered expansions are only mildly non-ideal. The fluids are expanded from the same inlet state in reduced

terms, and hence, following the principle of corresponding states, their compressibility factors are very similar. The small deviation is due to the fact that the principle of corresponding states cannot take into account influences other than the critical pressure and temperature on the volumetric behavior. As is evident from Fig. 2.14(a), the expansion of the more complex fluid propane ends closer to its ideal-gas region than those of steam and carbon dioxide. This becomes clear when considering the temperature.

(a) Compressibility factor   (b) Density   (c) Temperature
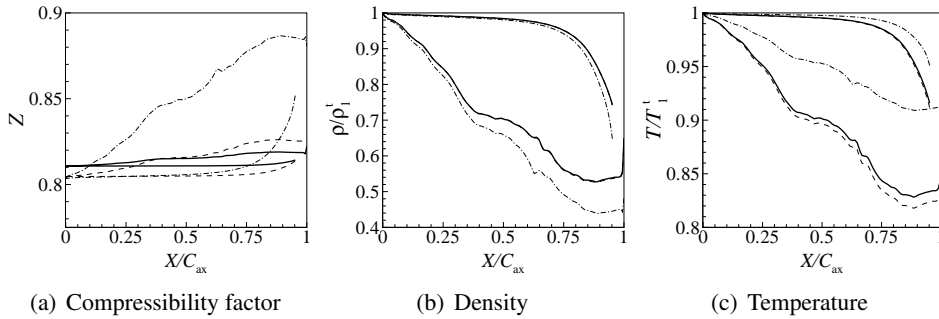
Figure 2.14: *Blade surface distributions of thermodynamic quantities for steam (———), carbon dioxide ($- - -$) and propane ($- \cdot - \cdot -$).*

The absolute value of the density is very different for the three fluids, because it is determined by the critical density ρ_c. However, the qualitative behavior of the density, shown in Fig. 2.14(b) in terms of the density reduced with respect to the inlet value, is near identical for the similarly complex fluids steam and carbon dioxide. The more complex propane has a different distribution, because for the same pressure ratio, the expansion of a more complex fluid leads to lower reduced densities. Finally, the qualitative behavior of the temperature, given in Fig. 2.14(c) in terms of the temperature reduced by the inlet value, is also similar for steam and carbon dioxide. As discussed in Section 2.3.1, for complex fluids, the outlet temperature is closer to the inlet value. Conversely, LMC fluids such as steam and carbon dioxide exhibit a fairly large reduced temperature drop. The expansion of the more complex propane leads to only half of this reduced temperature drop.

2.5   Conclusions

An investigation was presented on the effect of the complexity of a fluid molecule on the fluid dynamic quantities sound speed, velocity and Mach number in ideal

and mildly nonideal isentropic expansions. The influence of molecular complexity on expanding flows was investigated for ideal-gas and dense-gas expansions, respectively. The analysis was carried out using the number of active degrees of freedom as a measure of molecular complexity, in combination with the polytropic ideal gas and Van der Waals gas model. These results were then verified using highly accurate multiparameter equations of state.

For isentropic expansions, the Mach number does not depend on the molecular weight of the fluid, but only on molecular complexity and pressure ratio. Remarkably enough, the Mach number can either increase or decrease with molecular complexity, depending on the considered pressure ratio. More precisely, for low pressure ratios, the Mach number is a monotonically increasing function of molecular complexity. For higher pressure ratios, the Mach number first sharply increases to a maximum (at molecular complexities approximately corresponding to monatomic fluids) and then decreases for fluids of increasing molecular complexity. The exit speed of sound and flow velocity, however, are dependent on both molecular complexity and weight, as well as on the inlet total temperature. The exit flow velocity was found to be a monotonically increasing function of molecular complexity regardless of the expansion ratio, whereas the speed of sound increases monotonically with molecular complexity for high pressure ratios. Nonmonotone behavior of the speed of sound exists for pressure ratios around 3, which leads to similarly nonmonotone behavior of the Mach number at pressure ratios around 10. It is important to note, however, that sound speed and flow velocity depend much more strongly on molecular weight than on molecular complexity, which, in realistic expansions, often obscures the influence of the latter. The results confirm that the most relevant parameter which determines the dense gas behavior of a given fluid is its molecular complexity defined simply in terms of the number of active degrees of freedom.

Differently from the ideal gas case, in dense-gas expansions the behavior of the dimensionless flow variables sound speed and flow velocity is dependent on the reduced inlet conditions. The deviation from gas ideality affects the change in monotonicity in the exit speed of sound and exit Mach number at a given expansion ratio. For the dense-gas expansions considered here, the quantitative deviations from the ideal gas case include a lower sound speed and, due to a lower specific enthalpy difference, a lower flow velocity.

The distinction made here between the influence of molecular complexity and weight helps to explain the difficulties in determining the correct similitude criteria in high-Reynolds number transonic wind tunnels employing heavy gases as the working fluid [4, 5, 6]. Thanks to its relatively high molecular weight, which

is roughly six times that of air, sulfur hexafluoride is used in existing wind tunnels to increase the flow Reynolds number. However, due to the different molecular complexity ($N \simeq 5$ for air and $N \simeq 20$ for SF$_6$ at ambient temperature), the Mach number of the flow leaving the nozzle and entering the test chamber is different for the two fluids. In Ref. [6], a correction is proposed in which the similitude parameter is obtained using a value of γ that is computed from the inlet value of Γ, namely, the fluid molecular complexity.

The outcome of this investigation is also applicable in the design of turbines for ORC turbogenerators. These power plants are suitable for the conversion of an external heat source into electricity in the low-power range (few kW up to few MW), by virtue of an organic working fluid, whose molecule is both complex and heavy. The results of this study show that the low rotational speed typical of ORC turbines is made possible by the high molecular weight of the organic working fluid, not by its complexity. For instance, assume that a cycle analysis yields two suitable organic working fluids that have similar molecular complexity but different molecular weights. The Mach number per turbine stage is limited, to avoid the occurrence of supersonic flow and associated shock losses in the rotor. The findings of this study show that the heavier organic substance leads to lower nozzle expansion velocities, thus allowing for lower rotational speeds of the turbine. This, together with a higher volumetric flow rate, explains why heavy organic fluids are favorable for obtaining high turbine efficiencies.

Nomenclature

a	=	attractive intermolecular force parameter
A	=	number of atoms in a molecule
b	=	covolume excluded by a mole of particles
c	=	speed of sound
C	=	specific heat capacity
CP	=	pressure coefficient
e	=	internal energy
h	=	specific enthalpy
M	=	molecular weight
Ma	=	Mach number
N	=	number of degrees of freedom of a fluid molecule
P	=	pressure
R	=	specific gas constant
$\bar{R}$	=	universal gas constant

s	=	entropy
T	=	temperature
u	=	flow velocity
v	=	specific volume
X	=	nozzle axial coordinate
Y	=	nozzle ring circumferential coordinate
Z	=	compressibility factor

Greek symbols

Γ	=	fundamental derivative of gasdynamics
γ	=	ratio of specific heat capacities
ρ	=	density

Subscripts

0	=	total (or stagnation) conditions
1	=	inlet
2	=	outlet
c	=	critical point
min	=	minimum
P	=	at constant pressure (isobaric), pressure
ref	=	reference
v	=	at constant volume

Superscripts

0	=	ideal-gas contribution
V	=	saturated vapor

Acronyms

BZT	=	Bethe-Zel'dovich-Thompson
HMC	=	high molecular complexity
LMC	=	low molecular complexity
MPEoS	=	multiparameter equation of state
ORC	=	Organic Rankine Cycle
PIG	=	polytropic ideal gas law

PVdW   =   polytropic Van der Waals model

References

[1] G. Angelino, M. Gaia, and E. Macchi. A review of Italian activity in the field of organic Rankine cycles. In *VDI Berichte - Proceedings of the International VDI Seminar*, volume 539, pages 465–482, Düsseldorf, 10–12 September 1984. VDI Verlag.

[2] J. Larjola. Electricity from industrial waste heat using high-speed organic Rankine cycle (ORC). *Int. J. Prod. Econ.*, 41(1-3):227–235, October 1995.

[3] G. Angelino and P. Colonna. Multicomponent working fluids for Organic Rankine Cycles (ORCs). *Energy*, 23(6):449–463, 1998.

[4] J. J. Korte. Inviscid Design of Hypersonic Wind Tunnel Nozzles for Real Gas. In E. Camhi, editor, *38th Aerospace Sciences Meeting and Exhibit, Reno, NV*, pages 1–8, Reston, VA, Jan. 10-13 2000. AIAA, AIAA.

[5] W. K. Anderson. Numerical Study of the Aerodynamic Effects of Using Sulfur Hexafluoride as a Test Gas in Wind Tunnels. Technical Paper 3086, NASA, NASA Langley Research Center, Hampton, VA, May 1991.

[6] J. B. Anders, W. K. Anderson, and A. V. Murthy. Transonic Similarity Theory Applied to a Supercritical Airfoil in Heavy Gases. *J. Aircr.*, 36(6):957–964, November-December 1999.

[7] W. Wagner and A. Pruss. The IAPWS Formulation 1995 for the Thermodynamic Properties of Ordinary Water Substance for General and Scientific Use. *J. Phys. Chem. Ref. Data*, 31(2):387–535, 2002.

[8] J.W. Tom and P.G. Debenedetti. Particle formation with supercritical fluids – a review. *Journal of Aerosol Science*, 22(5):555–584, 1991.

[9] M. Türk. Influence of thermodynamic behaviour and solute properties on homogeneous nucleation in supercritical solutions. *Journal of Supercritical Fluids*, 18:169–184, 2000.

[10] J. Hoffren, T. Talonpoika, J. Larjola, and T. Siikonen. Numerical simulation of real-gas flow in a supersonic turbine nozzle ring. *J. Eng. Gas Turb. Power*, 124(2):395–403, April 2002.

[11] P. Colonna, J. Harinck, S. Rebay, and A. Guardone. Real-gas effects in organic rankine cycle turbine nozzles. *AIAA Journal of Propulsion and Power*, 24(2):282–294, 2008.

[12] J. Harinck, P. Colonna, A. Guardone, and S. Rebay. Influence of thermodynamic models in 2D flow simulations of turboexpanders. *J. Turbomach.*, 132(1), 011001, 2010.

[13] J. Harinck, T. Turunen-Saaresti, P. Colonna, and J. van Buijtenen. Computational study of a high-expansion ratio radial ORC turbine stator. *J. Eng. Gas Turb. Power*, 2009. Accepted for Publication.

[14] A. Guardone and B. M. Argrow. Nonclassical gasdynamic region of selected fluorocarbons. *Phys. Fluids*, 17(116101):17, 2005.

[15] P. Colonna and A. Guardone. Molecular interpretation of nonclassical gasdynamics of dense vapors under the van der waals model. *Phys. Fluids*, 18(5):056101–1–14, 2006.

[16] P.A. Thompson. A fundamental derivative in gasdynamics. *Phys. Fluids*, 14(9):1843–1849, 1971.

[17] H. A. Bethe. The theory of shock waves for an arbitrary equation of state. Technical paper 545, Office Sci. Res. & Dev., 1942.

[18] H. B. Callen. *Thermodynamics and an introduction to thermostatistics*. Wiley, 2nd edition, 1985.

[19] J.D. van der Waals. *On the continuity of the gas and liquid state*. PhD thesis, University of Leiden, 1873.

[20] R. Span. *Multiparameter Equations of State - An Accurate Source of Thermodynamic Property Data*. Springer-Verlag, Berlin, 2000.

[21] R. Span, W. Wagner, E. W. Lemmon, and R. T. Jacbosen. Multiparameter equations of state - recent trends and future challenges. *Fluid Phase Equilib.*, 183–184:1–20, 2001.

[22] E.W. Lemmon and R. Span. Short fundamental equations of state for 20 industrial fluids. *J. Chem. Eng. Data*, 51(3):785–850, 2006.

[23] E. W. Lemmon, M. O. McLinden, and M. L. Huber. REFPROP - REFerence fluid PROPerties. software, ©NIST 2002.

[24] W. Bober and W. L. Chow. Nonideal Isentropic Gas Flow Through Converging-Diverging Nozzles. *J. Fluids Eng.*, 112:455–460, 1990.

[25] M. S. Cramer. On the Mach number variation in steady flows of dense hydrocarbons. *J. Fluids Eng.*, 113, 1991.

[26] M. S. Cramer and L. M. Best. Steady, isentropic flows of dense gases. *Phys. Fluids A*, 3(1):219–226, 1991.

[27] M.S. Cramer and N.R. Fry. Nozzle flows of dense gases. *Phys. Fluids A*, 5(5):1246–1259, 1993.

[28] G.H. Schnerr and P. Leidner. Diabatic Supersonic Flows of Dense Gases. *Physics of Fluids A*, 3(10):2445–2458, 1991.

[29] A. Kluwick. Internal flows of dense gases. *Acta Mechanica*, 169:123–143, 2004.

[30] Ya. B. Zel'dovich. On the possibility of rarefaction shock waves. *Zh. Eksp. Teor. Fiz.*, 4:363–364, 1946.

[31] P. A. Thompson and K. C. Lambrakis. Negative shock waves. *J. Fluid Mech.*, 60:187–208, 1973.

[32] P. A. Thompson. *Compressible Fluid Dynamics*. McGraw-Hill, 1988.

[33] R. Menikoff and B. J. Plohr. The Riemann problem for fluid flow of real material. *Rev. Mod. Phys.*, 61(1):75–130, 1989.

[34] Colonna, Guardone, Nannan, and Zamfirescu. Design of the dense gas flexible asymetric shock tube. *Journal of Fluids Engineering*, 130(3):6, 2008.

[35] J.M. Smith, H.C. Van Ness, and M.M. Abbott. *Introduction to Chemical Engineering Thermodynamics*. McGraw-Hill International Edition, Singapore, 2001.

[36] H.P. Bloch and C. Soares. *Turboexpanders and Process Applications*. Gulf Professional Publishing, 2001.

[37] T. Arts, M. Lambert de Rouvroit, and A. W. Rutherford. Aero-thermal investigation of a highly loaded transonic linear turbine guide vane cascade. Technical Note 174, Von Karman Institute for Fluid Dynamics, September 1990.

[38] R. Span and W. Wagner. A new equation of state for carbon dioxide covering the fluid region from the triple-point temperatureto 1100 K at pressures up to 800 MPa. *J. Phys. Chem. Ref. Data*, 25(6):1509–1596, 1996.

[39] R. Span and W. Wagner. Equations of state for technical applications. II. Results for nonpolar fluids. *Int. J. Thermophys.*, 24(1):41–109, January 2003.

[40] P. Colonna and S. Rebay. Numerical simulation of dense gas flows on unstructured grids with an implicit high resolution upwind Euler solver. *Int. J. Num. Meth. Fluids*, 46:735–765, 2004.

3

The Influence of Thermodynamic Models in 2D Flow Simulations of Turboexpanders

Abstract   *This chapter presents a quantitative comparison of the effect of using thermodynamic models of various degree of complexity if applied to fluid dynamic simulations of turboexpanders operated at conditions affected by strong real-gas effects. The 2D flow field of a standard transonic turbine stator is simulated using the state-of-the-art inviscid* ZFLOW *CFD solver coupled with a fluid property library containing the thermodynamic models. The considered thermodynamic models are, in order of increasing complexity, the polytropic ideal gas (PIG) law, the Peng-Robinson-Stryjek-Vera (PRSV) cubic equation of state and highly accurate multiparameter equations of state (MPEoS), which are adopted as benchmark reference. The fluids are steam, toluene and R245fa. The two processes under scrutiny are a moderately nonideal subcritical expansion and a highly nonideal supercritical expansion characterized by the same pressure ratio. Using the PIG model for moderately nonideal subcritical expansions leads to large deviations with magnitudes of at least 18 − 25% in density, sound speed, velocity and total pressure loss and at least 4 − 10% in Mach number, pressure, temperature and mass flow rate. The PIG model applied to highly nonideal supercritical expansions leads to a doubling of the deviations' magnitudes. The advantage of the PIG model is that its computational cost is roughly one eleventh (or one third if saturation-checks in the MPEoS are omitted) of the cost of the MPEoS. For the subcritical expansion, adopting the physically more correct cubic PRSV model leads to comparatively smaller deviations, namely < 2% (toluene and R245fa) and < 4% (steam) in all flow parameters, except for the total pressure loss error, which is comparable to that of the PIG model. The PRSV model is reasonably accurate even for the highly nonideal supercritical expansion, for which the errors are at most 4%. The computational cost of the PRSV model is roughly nine times higher than the cost of the PIG model (or twice as high if saturation-checks in the PRSV are omitted). Contrary to low complexity fluids like water, for complex fluids like toluene and R245fa the deviations in density, speed of sound and velocity ensuing from the use of the PIG model vary strongly along the isentropic expansions. This invalidates the approach commonly used in practice of correcting the PIG model with a properly chosen constant compressibility factor.*

3.1   Introduction

Turboexpanders are widely used in industry to expand high pressure gas producing useful mechanical work. They can be found in the power, oil and gas, process and refrigeration industries. Examples of power applications are Organic Rankine Cycle (ORC) turbogenerators [1, 2, 3, 4] which are rapidly spreading as energy

converters for biomass fuels and low-grade heat (from geothermal or industrial waste heat sources). ORCs feature the same working principle as conventional steam power plants, except for the working fluid, which is formed by organic molecules. The choice of the fluid allows for the optimal design of the cycle and turbine, depending on the temperature of the heat source and the design power output [2]. In the low power range, steam turbines cannot attain the same level of efficiency of ORC turbines with the same level of technology.

In the oil and gas industry, high-pressure turboexpanders are used in cryogenic natural gas processing to condense and remove heavy hydrocarbons from natural gas streams. Given a certain pressure reduction, an almost isentropic expansion in a turboexpander allows for a lower temperature of the expanded gases than an isenthalpic expansion by means of a throttling valve (in which the refrigerating effect is caused by the Joule-Thompson effect). In addition, a turboexpander recovers some of the energy released during expansion and converts it into power that is often used for recompression of the methane. Turboexpanders are typically used in large-capacity liquefaction plants with high feed gas pressures, where efficiency, compact plant layout, varying feed products and a large amount of ethane recovery are desired [5].

Often the design and performance assessment of (turbo)expanders is based on computational fluid dynamics (CFD) simulations employing the ideal gas law to describe the fluid's thermodynamic properties. This choice is based on the assumption that the deviation of the real thermodynamic behavior from ideal gas behavior is small, which should result in equally small deviations in the predicted flow field and calculated performance parameters. (Turbo)expanders in the aforementioned applications are, however, often operated at reduced pressures and temperatures (made dimensionless with the critical values of the fluid) close to and above unity [5]. They therefore operate, at least partly, in the dense-gas thermodynamic region where the ideal gas law is a poor approximation of the true thermodynamic behavior. Using the ideal gas assumption can in this case lead to inaccurate predictions of the flow structure and performance parameters of the (turbo)expander.

In the case of ORCs for example, accurate thermodynamic models are required for both a correct cycle analysis and turboexpander design. This is exemplified by a study of a recently developed ORC turbogenerator with toluene as working fluid [6, 7], whose cycle and turbine were designed using the most accurate thermodynamic model for the working fluid available at that time [8]. The prototype, however, showed a considerable deviation from the calculated power output in design conditions. After analysis [9] using a more recent and accu-

rate thermodynamic model of toluene [10], it became apparent that this was attributable to the inaccuracy of the original thermodynamic model, which, for the considered expansion, overpredicts the specific enthalpy and underpredicts the density both by as much as 6%. This deviation has in turn a significant effect on the fluid dynamic design of the turbine.

The motivation for this study is the current potential for improvement of dense-gas (turbo)expander performance through fluid-dynamic design that properly takes into account the nonideal thermodynamic behavior of the fluid. This requires a better understanding of how the fluid dynamics deviates from ideal-gas fluid dynamic behavior and of the capabilities and limitations of the available thermodynamic models if applied to fluid dynamic simulations. This study addresses this issue by studying the influence of real-gas thermodynamic models on the flow field and performance parameters.

Previous studies reported in literature have addressed real-gas effects in transonic and supersonic flows in the classical gasdynamic region. These studies focus on one-dimensional steady flows in simple geometries, such as, for example, the one-dimensional converging-diverging nozzle [11], which allows for the use of analytical solutions. Others also studied two-dimensional flows of simple geometries, e.g., using linearized theory [12] or finite volume numerical schemes for simple nozzle flows [13] and around simple airfoil geometries in cryogenic wind tunnels [14, 15].

Practical simulations of real-gas flow through more complex two- and three dimensional geometries have been conducted in the field of turbomachinery. Here, the need for simulating fluid dynamic processes in the dense gas region has lead to the interfacing of existing finite-volume CFD solvers with more accurate thermodynamic property data. Four different approaches can be distinguished; the direct analytical calculation from the equation of state for both primitive quantities and derivatives [16, 17, 18], the analytical calculation for primitive quantities and numerical differencing for derivatives [19], the interpolation of thermodynamic property data (look-up) tables [20, 6, 21] and the use of relatively simple polynomial functions that are fitted to these tables prior to the simulation [22, 23]. The analytical calculation from the equation of state allows for the highest accuracy, however, the evaluation of derivatives and properties that are represented by the independent variables in the EoS can be computationally costly, in particular when they are evaluated iteratively from complex EoSs. The two latter approximate methods, on the other hand, are simpler to implement and allow for property evaluation at limited extra cost with respect to the ideal gas model case. Their disadvantage is their inherently lower accuracy due to the introduction of fitting

or interpolation errors (see Refs. [20, 21] for more details).

Numerous EoSs exist which account for nonideal gas behavior with various degrees of accuracy. They range from cubic EoSs such as the Van der Waals model [24], applied to fluid dynamic simulations of nozzles in Ref. [13, 25] and Redlich-Kwong/Peng-Robinson-type EoSs [26, 27] used for nozzle [11, 28] and turbomachinery simulations [19], to state-of-the-art multiparameter EoSs (MPEoSs) [29, 30]. The functional form of a MPEoS is often specific for a single fluid or type of fluid and often highly complex (e.g., the MPEoS for water contains 51 terms [31]). This allows for accurate predictions of thermodynamic properties (in most cases within experimental data uncertainty) over the entire thermodynamic region and for some MPEoSs even close to the critical point. The validation of flow solvers linked to accurate thermodynamic models for simulations in the non-ideal gas region is unfortunately hindered by a lack of experimental fluid dynamic data in this region.

In the aforementioned real-gas studies, relatively simple EoSs or gas tables were adopted to model fluid properties and their results were not compared to highly accurate predictions of fluid properties, since the latter have only recently become available for the fluids under scrutiny [29]. A study of the influence of thermodynamic models employed on the flow field and performance parameters as detailed in this chapter calls for the use of MPEoSs as a reference, because of their highly accurate predictions and validity. In Ref. [32] it is shown that, from a computational point of view, evaluating the fluid properties including analytical derivatives is more convenient than the use of numerical differencing formulas. The inclusion of highly accurate thermodynamic fluid models such as MPEoSs into CFD codes was made possible only lately [16] and consequently the thorough analysis that these simulation tools allow is a recent achievement.

As an exemplary case of a dense-gas turboexpander, this study considers the flow field generated by the expansion through a standard two-dimensional axial turbine stator blade profile designed for the transonic flow regime. Expansions in the dense-gas region are simulated for subcritical and supercritical inflow conditions, representing cases of moderate to high thermodynamic nonideality. The influence of the thermodynamic model and the molecular complexity of the fluid is analyzed based on blade surface distributions and integral performance parameters. The conclusions that are drawn can be used as guidance in the preliminary design phase of dense-gas expanders.

The fluids chosen for the comparison vary in molecular complexity and weight. They are steam, toluene and refrigerant R245fa (HFC245fa), all expanded from the same reduced pressure and temperature. These fluids are currently used in

power applications. In particular, both toluene and R245fa are used in ORCs. They are taken as examples of fluids of high molecular complexity.

The influence of real-gas thermodynamic models is studied by comparing thermodynamic models that differ in complexity and accuracy. In other words, they vary in their ability to take into account nonideal thermodynamic behavior. Three thermodynamic models are selected which represent the three most widely used types of thermodynamic models. The thermodynamic models employed are the polytropic (i.e., with constant isochoric specific heat) ideal gas law (PIG), the Peng-Robinson (Stryjek-Vera modified) cubic equation of state (PRSV) [26, 27], and state-of-the-art reference multiparameter EoSs (MPEoSs) [29, 30].

The effect of the different fluid models on the fluid dynamics and performance parameters is evaluated by comparing distributions of the Mach number, pressure coefficient, flow velocity, temperature, density along the blade, outlet flow angles, mass flows and shock losses.

In the following section, the novel Euler solver and the three thermodynamic models are briefly described. Section 3.2.3 presents the validation of the numerical scheme and demonstrates that grid convergence is obtained for the grid used in the comparison as well as that the solver and the method for evaluating the thermodynamic properties are validated for the transonic fluid dynamic problem under consideration. Section 3.3 proceeds with the study of the effect of the thermodynamic models on the fluid dynamic behavior, starting from subcritical inflow conditions, to more nonideal supercritical inflow conditions, followed by the conclusions.

3.2   The Euler Solver and the Thermodynamic Models

3.2.1   The Euler Solver

Numerical solutions of the two-dimensional inviscid Navier-Stokes (Euler) equations are computed with the ZFLOW program, [16, 33, 34, 35] linked to a fluid property library containing several thermodynamic models and a large set of fluid data [36]. The main features characterizing the ZFLOW CFD code are briefly summarized. The solver uses a hybrid Finite Element (FE)/Finite Volume (FV) approach in which the finite volume metric quantities are formulated on the basis of the Lagrangian linear shape functions typically used in finite element methods [37]. The spatial approximation of the inviscid Navier-Stokes equations is constructed with a high resolution finite volume method suitable for general unstructured and hybrid grids. The high resolution upwind discretization is con-

structed on the basis of the Roe approximate Riemann solver [38], generalized to the case of fluids characterized by arbitrary equations of state according to the method of Vinokur and Montagné [39]. This class of discretization schemes is particularly well suited to the computation of high Mach number flows. The use of unstructured grids allows for the straightforward treatment of domains of arbitrarily complex geometry. Another important feature of ZFLOW is represented by the adopted implicit time integration scheme, which computes steady state solutions in a much more efficient way with respect to conventional explicit schemes. The gain in computational efficiency is crucial when complex EoS are needed for an accurate flow simulation. The ZFLOW solver has been successfully validated for ideal-gas simulations (see e.g., Refs. [16, 33]) and validation on a nonideal process is planned. The extension of ZFLOW to the viscous Reynolds-Averaged Navier-Stokes (RANS) equations will be documented soon.

3.2.2 The Thermodynamic Models

The CFD code ZFLOW is linked to a rich thermodynamic library for the calculation of properties of pure fluids and mixtures which has been extended to include the particular (secondary) thermodynamic functions required by the implicit upwind flow solver [32]. The software library [36, 40, 41] contains, amongst others, a cubic EoS and various state-of-the-art multiparameter EoSs, e.g., Martin-Hou [42], Benedict-Webb-Rubin, Span-Wagner [43, 44] and Starling [45] MPEoSs (TPSI, REFPROP [40]). The thermodynamic properties required by ZFLOW, including derivatives, are efficiently computed from their analytical expressions [16].

In this study, the thermodynamic behavior of the fluid is modeled with three types of EoSs that differ in complexity and accuracy: the polytropic ideal gas (PIG) model, the Peng-Robinson Stryjek-Vera modified (PRSV) cubic EoS and very accurate state-of-the-art multiparameter EoSs (MPEoS).

3.2.2.1 Polytropic Ideal Gas Law

The polytropic ideal gas (PIG) law model is given by the pressure equation supplemented by the ideal-gas isobaric specific heat:

$$P = \frac{RT}{v}, \quad C_P^0 = \frac{\gamma R}{\gamma - 1}, \tag{3.1}$$

where P is the pressure, T is the temperature and v is the specific volume. R is the specific gas constant which is defined as $R = \bar{R}/M$, where M is the molecular weight and $\bar{R} = 8.314$ J/(molK) is the universal gas constant. γ denotes the ratio

of the isobaric to the isochoric specific heat, $\gamma \equiv C_P^0/C_v^0$, where C_P^0 and C_v^0 are the ideal-gas isobaric and isochoric heat capacities, respectively. The ratio γ is constant under the polytropic assumption considered here and according to the energy equipartition theory bounded by $1 < \gamma \leq 5/3$.

3.2.2.2   Peng-Robinson-Stryjek-Vera EoS

Compared to the polytropic ideal gas EoS (3.1), a cubic EoS allows for more accurate predictions in the dense gas region and states close to the saturation line. Its accuracy is usually sufficient for the design and analysis of many technical applications. Moreover, its simple form requires limited input information, i.e., limited knowledge of the thermodynamic properties of the fluid, and can be easily extended to multi-components fluids by means of theoretically correct mixing rules [27, 46, 47, 48, 32]. However, it is still inherently inaccurate near the critical point (i.e., $P/P_c \gtrsim 0.9$) and on the liquid side at high reduced temperatures.

The Peng-Robinson-Stryjek-Vera [27] (PRSV) cubic EoS is of the form:

$$P = \frac{RT}{(v-b)} - \frac{a(T)}{v(v-b)+b(v-b)}, \tag{3.2}$$

where a and b are the coefficients of the contributions of, respectively, the attractive and short-range repulsive intermolecular forces. In the Stryjek-Vera modification [27] of the Peng-Robinson EoS, the temperature-dependent term $a(T)$ is dependent on a parameter denoted by k_1 [27] and the acentric factor ω. The new functional form has allowed the extension of the range of applicability of the EoS to the low reduced temperature region ($T/T_c \lesssim 0.7$) as well as to polar fluids. The main feature is that it allows for vapor-pressures estimates accurate within 2% of the experimental data. This reflects in an improved prediction performance of superheated vapor thermodynamic properties in the region adjacent to the saturation curve.

For the calculation of all caloric properties, the PRSV EoS (3.2) is supplemented by the ideal-gas contribution to the specific heat at constant pressure, which has been approximated here as a polynomial function of the temperature [49]:

$$C_P^0(T) = A + BT + CT^2 + DT^3. \tag{3.3}$$

3.2.2.3   Multiparameter EoS

The increased number of parameters in multiparameter equations of state (MPEoSs) allows for accurate computations of all relevant thermodynamic properties, with

the highest possible accuracy, which is required for the design and analysis of advanced technical applications as well as scientific purposes. After the initial development of MPEoSs for classes of fluids in the 1970s, the state of the art has become the MPEoSs formulated in terms of reduced Helmholtz energy, of which both the functional form and the parameters are optimized on experimental data, resulting in an EoS that is highly accurate. The functional form of these MPEoS can be substance-specific or it can be tailored to a specific class of substances, like the Starling EoS for light hydrocarbons [45]. For pure substances, Helmholtz-based MPEoSs can be classified into empirical reference EoSs and technical EoSs. The basic idea behind the concept of *reference EoS* is that a single equation should be able to describe all experimental thermodynamic property data available for a certain fluid within their experimental uncertainty. Reference EoSs therefore have a substance-specific functional form and are developed using thoroughly assessed experimental data for which only the most accurate and reliable data are chosen. In this way, the EoS itself can be used as a reference for all thermodynamic properties over the entire thermodynamic range, even in the close proximity of the critical point [30], like the Wagner-Pruß EoS for water [31], for which the uncertainty in the vapor phase is less than 0.1% and 0.2% for volumetric and caloric properties, respectively. For the calculation of all caloric properties, the MPEoSs used in this study are supplemented by the ideal-gas contribution to the specific heat at constant pressure that have been determined together with the MPEoSs [31, 10].

3.2.3   zFlow Validation: Simulation of the Ideal-Gas Flow around the VKI LS-89 blade

In this section the zFLOW solver linked to the accurate thermodynamic model is validated for the transonic fluid dynamic problem considered in this study, in which the expansion occurs at ideal-gas conditions. The validation of the the flow solver coupled with the thermodynamic models for simulations in the real-gas region is unfortunately hindered by a lack of experimental fluid dynamic data in this region. This is planned for the near future. Nonetheless, the validation of the solver linked to the accurate thermodynamic models for expansions at ideal-gas conditions, together with the validated high accuracy of all thermodynamic models even at strongly nonideal conditions (see Section 3.2.2.3), warrants the validity of the simulations of real-gas flows presented in this study.

The zFLOW code is validated by comparing the results of simulations to the measurements of two well-known and reliable turbomachinery test cases [50] for dry air at ideal-gas conditions. In both test cases, the geometry is the VKI LS-

89 blade, which is a standard high pressure turbine nozzle guide vane, mounted in a linear cascade. The first test case (MUR-43) is at subsonic flow conditions ($Ma_{is} = 0.84$), while the second test case (MUR-49) is at transonic flow conditions ($Ma_{is} = 1.02$). The isentropic Mach number Ma_{is} is the Mach number observed in case shock losses would be absent. The conditions are given in Table 4.3. Thermodynamic properties are calculated with a 19-parameter reference equation of state [51]. Even though such an equation of state is unnecessary given the ideal gas conditions of the simulations, the results verify the correct implementation of such complex thermodynamic models in the software.

All flow solutions have converged up to at least a reduction of five orders of magnitude measured in the L^2-norm of the conserved variables. The Mach number distribution along the blade surface obtained from the inviscid computation is compared to the experimental data of the test cases.

Table 3.1: *Test case conditions, from [50].*

		MUR43	MUR49
Total inlet pressure	P_{01}, bar	1.435	1.608
Pressure ratio	P_{01}/P_2, -	1.587	1.938
Total inlet temperature	T_{01}, °C	146.85	146.85
Compressibility factor at inlet	Z_1, -	1	1
Static outlet pressure	P_2, bar	1.333	2
Isentropic Mach number at outlet	$Ma_{2,is}$, -	0.84	1.02

The periodic grid is generated in a transformed domain, in which periodic boundaries are mapped into internal curves to simplify the task of obtaining periodic nodes [52]. In the transformed space the grid is generated by the front-advancing/Delaunay method [53] and then transformed back into the physical space of *XY*-coordinates by introducing a suitable cut. This translates into the saw-like edge of the periodic boundaries shown in Fig. 4.4. A sharp trailing edge is adopted to ensure correct trailing edge flow separation simulated with the inviscid solver.

In order to determine the error due to the discretization, a grid convergence study is performed by computing the solution on three increasingly finer grids using the accurate MPEoS. The fine grid and the coarse grid are generated by, respectively, halving and doubling the number of grid elements with respect to the initial grid. The coarse grid consists of 1302 nodes and 2032 elements, the
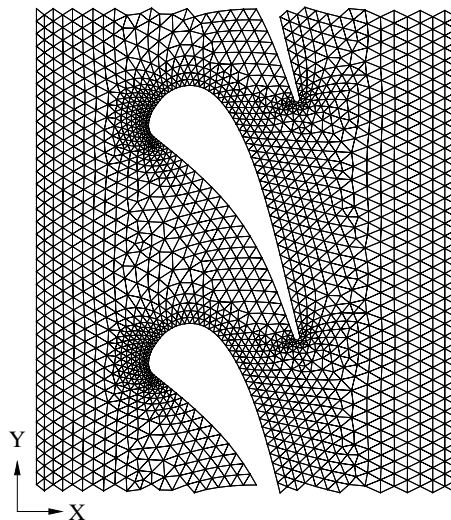
Figure 3.1: *Coarse grid (1302 nodes) of the VKI LS-89 blade. Periodicity allows the computations to be performed using only the top half of the grid shown here.*

(a)   (b)
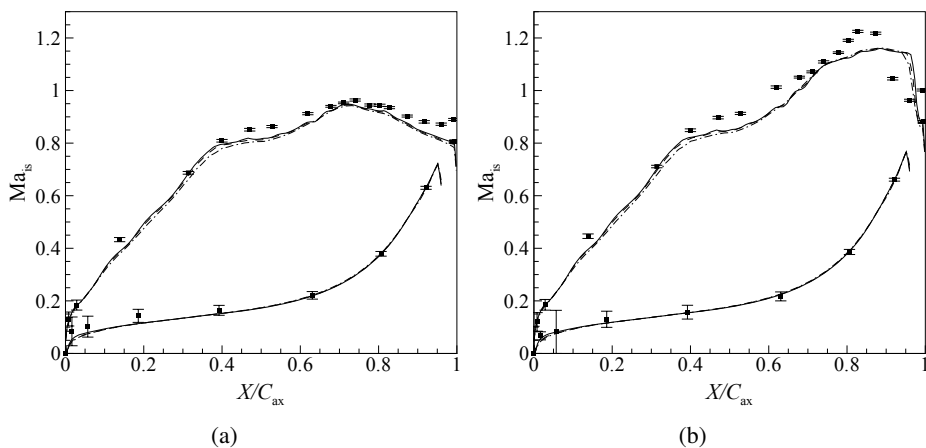
Figure 3.2: *Mach number distribution for the MUR43 test case (a) and the MUR49 test case (b). Shown are the experimental measurements (■) from [50] and the numerical solution on the coarse grid (– · – · –), the medium grid (– – –) and the fine grid (———).*

medium grid of 2383 nodes and 3958 elements and the fine grid of 4153 nodes

and 7184 elements. Fig. 4.4 shows the coarse grid and the blade geometry. The lines in Fig. 4.5(a) and 4.5(b) show the Mach number distributions for the MUR43 and MUR49 test cases, respectively, solved on the coarse, medium and fine grid. They are plotted as a function of the reduced coordinate X/C_{ax}, where X is the axial coordinate and C_{ax} is the axial blade chord. From this result, it appears that the computed solution on the fine grid is sufficiently grid-independent. The fine grid is therefore used for all subsequent simulations. Grid convergence was similarly checked for the subsequent simulations with steam, toluene and R245fa presented hereafter.

The ZFLOW code is validated for this transonic fluid dynamic problem by comparing the numerical solution to the experimental data of the test case, given in [50]. The static pressure measurement data have an uncertainty of 0.5%, leading to uncertainties in the isentropic Mach number as indicated by the error bars in Fig. 4.5. In general, the numerical results show a good agreement with the experimental results for both test cases. A discrepancy is however observed for the suction side, where numerical values fall outside of the experimental uncertainty range. In the MUR49 transonic test case (Fig. 4.5(b)), the location of the shock wave that terminates the supersonic region is predicted by ZFLOW to be at the end of the blade profile ($X/C_{ax} = 0.95$), whereas the measurements indicate that the shock wave is further upstream ($X/C_{ax} = 0.88$). This could be the result of the inability of the inviscid solver to simulate shock-boundary layer interaction. Still, the difference is small and the agreement is deemed satisfactory.

3.3 The Effect of the Thermodynamic Model on the Flow

The effect of the thermodynamic model on the flow field generated by an axial turboexpander is studied for three different fluids and two different process conditions. This is done using the geometry of the VKI LS-89 turbine stator and the pressure ratio of the MUR49 transonic expansion case used in the validation of Section 3.2.3. The pressure ratio is in the same range ($P_{01}/P_2 < 5$) as the majority of axial reaction turboexpanders [5]. For each fluid, the simulations employing the accurate predictions from the MPEoS are used as a reference with which the simulations employing the other EoSs are compared. The three selected fluids are water, toluene and R245fa (HFC245fa), because these molecules are representatives of a wide range of molecular complexities and also because they are used in practice as working fluids in Rankine power cycles and refrigeration cycles. The fluid-specific parameters in the three EoSs are given in Table 3.4.

The reference MPEoS used for steam is the IAPWS-95 formulation, which is

in the form of a fundamental equation explicit in the Helmholtz free energy with 51 terms [31]. In the vapor region that is of interest in this study, the uncertainty is less than 0.1% and 0.2% for volumetric and caloric properties, respectively. The short (12-term) nonpolar Helmholtz equation of state is adopted for toluene [10]. This MPEoS was recently developed for technical applications by optimization to a specific class of nonpolar or slightly polar fluids [43]. The coefficients of these short forms for the equations of state were fitted to substance-specific data [10]. Although this new technical equation suffers from a slight loss in accuracy compared to a MPEoS whose functional form is optimized for a specific fluid, their shorter forms allow for faster computations. For the determination of thermodynamic properties of R245fa, the polar version of the 12-term MPEoS as described in [10] is used. The MPEoSs for toluene and R245fa in the vapor region that is of interest in this study, have an estimated uncertainty of less than 1% and 2% for volumetric properties and caloric properties, respectively.

Critical data, acentric factor and values of the k_1 parameter in the PRSV EoS are taken from Ref. [27]. The relation for the ideal-gas contribution to the isobaric specific heat, C_P^0, used together with the PRSV EoS, is given in Eq. (4.1). The coefficients for steam and toluene, given in Table 3.4, are taken from Ref. [49]. For the refrigerant R245fa, they have been determined by fitting Eq. (4.1) to data obtained using the accurate MPEoS model. In the temperature range of interest, the average absolute deviations of the ideal-gas specific heat relation with respect to those used in the MPEoS models are 0.28%, 0.79% and 0.08% for steam, toluene and R245fa, respectively.

For the PIG model, the choice of the ideal-gas isobaric specific heat, C_P^0 in Eq. (3.1), determines the caloric behavior of the fluids and therefore affects their fluid dynamic behavior if the PIG model is used to compute thermodynamic properties [54, 55]. A correct value for C_P^0 must be chosen in order to ensure a fair comparison with the simulations employing more complex thermodynamic models. In this work, C_P^0 is evaluated at the critical temperature, i.e., $C_P^0 = C_P^0(T_c)$, since both the subcritical and the supercritical expansion occur close to the critical temperature, as is evident from Table 3.2. It is common practice in turbomachinery design to use an averaged ideal-gas isobaric specific heat, e.g., obtained by integration between the temperatures representative of the expansion, i.e., [55]:

$$\bar{C}_P^0 = \frac{1}{T_2 - T_{01}} \int_{T_{01}}^{T_2} C_P^0(T) dT. \qquad (3.4)$$

For the fluids and temperatures considered here, the resulting value of $\bar{C}_P^0$ is very close to $C_P^0(T_c)$ adopted in this study. For water for example, the values are

2051 J/kgK and 2054 J/kgK, respectively. Furthermore, a comparison showed that $C_P^0(T_c)$ leads to a slightly better agreement of the computational results obtained with the PIG model with those obtained with the accurate MPEoS. To ensure a comparison between the thermodynamic models that is as fair as possible, it was decided to evaluate C_P^0 at the critical temperature.

To investigate the influence of the EoSs on the flow parameters of real-gas expansions, two expansions in the dense-gas region are simulated, for which the inlet pressure and temperature are at higher reduced values in comparison with the validation case. The two expansions start from subcritical and supercritical inflow conditions, representing cases of moderate to high thermodynamic nonideality, respectively. Fig. 3.3 compares the subcritical process in the temperature-entropy diagram for the three considered fluids. It should be noted that the blade shape is designed for ideal-gas flows and it is therefore not expected to perform the same as for ideal-gas conditions.

3.3.1   Subcritical Inflow Conditions

Subcritical inlet flow conditions are first considered. The process conditions used for all three fluids are given in reduced terms in Table 3.2. For each fluid, the resulting dimensional process conditions are given in Table 3.3. The compressibility factor, defined as $Z \equiv (Pv)/(RT)$, is identically equal to unity for an ideal gas; it is therefore often used to quantify the nonideality of a thermodynamic state. In this case, the compressibility factor is approximately 0.9 for both the inlet and outlet states and this indicates that they are both mildly non-ideal.

Apart from assessing the magnitude of the difference in the flow parameters for the different EoSs, it is also shown how the former relate to the differences between the predictions of thermodynamic properties. The differences in the most relevant thermodynamic properties density and sound speed are determined and plotted in Fig. 3.4 as function of pressure (from outlet to inlet pressure) at the isentrope along which the subcritical expansion takes place. Here, the MPEoS is again used as a reference to estimate the deviation with respect to the PIG and PRSV models.

3.3.1.1   Steam

A computation on the fine grid using the accurate MPEoS is used to investigate the flow field of the expansion process at subcritical operation. The two-dimensional flow field is visualized in Fig. 3.5(a) and 3.5(b) by displaying respectively the variation of Mach number and pressure coefficient as defined in Eq. (4.1) with

Table 3.2: *Process conditions for the considered simulations in terms of reduced variables.*

		Subcritical	Supercritical
Reduced total inlet pressure	P_{01}/P_{c}	0.7	1.05
Reduced total inlet temperature	T_{01}/T_{c}	1.1	1.05
Pressure ratio	P_{01}/P_2	1.938	1.938

(a) Steam   (b) Toluene   (c) R245fa
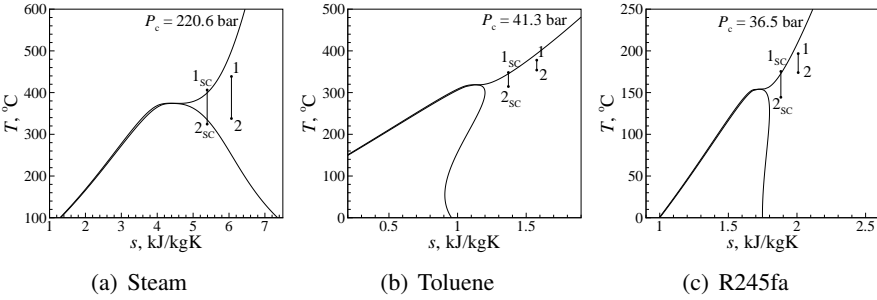
Figure 3.3: *Representation of the six expansion processes considered in this work in the temperature-specific entropy diagram. The inlet conditions are the same in terms of reduced temperature and pressure. For each fluid, one expansion starts from a supercritical state (denoted by 1_{SC} in the diagram) and the other from a subcritical state (1).*

streamlines throughout the blade passage. Fig. 3.5(c) shows the Mach number flow field based on the PIG model. From the inflow boundary on the left hand side of the domain, the fluid accelerates through the passage formed by the stator blade cascade to supersonic velocities (Fig 3.5(a)). At the blade's trailing edge, a shock wave can be observed which terminates the supersonic region. The numerical solution shows an unphysical over-expansion region at the trailing edge, since the actual turbulent trailing edge wake cannot be described by the Euler equations. The pressure coefficient, shown in Fig 3.5(b), decreases as the flow expands and increases across the shock wave.

The Mach number distribution along the blade surface is given in Fig. 3.6(a). The line that indicates early expansion (with a maximum in the Mach number) pertains to the suction side of the blade, the line with retarded expansion to the pressure side. Close to the trailing edge, the distribution is locally obscured by nonphysical overexpansion and dissipation at the trailing edge flow due to the

Table 3.3: *Parameters characterizing the expansion processes depicted in Fig. 3.3.*

	Subcritical			Supercritical		
	Steam	Toluene	R245fa	Steam	Toluene	R245fa
P_{01}, bar	154.5	28.9	25.5	231.7	43.3	38.2
T_{01}, °C	438.7	377.8	196.8	406.3	348.2	175.4
Z_1, -	0.81	0.79	0.81	0.58	0.57	0.60
P_2, bar	79.7	14.9	13.2	119.5	22.4	19.8
Z_2, -	0.83	0.88	0.88	0.59	0.88	0.89

(a) Sound speed

(b) Density
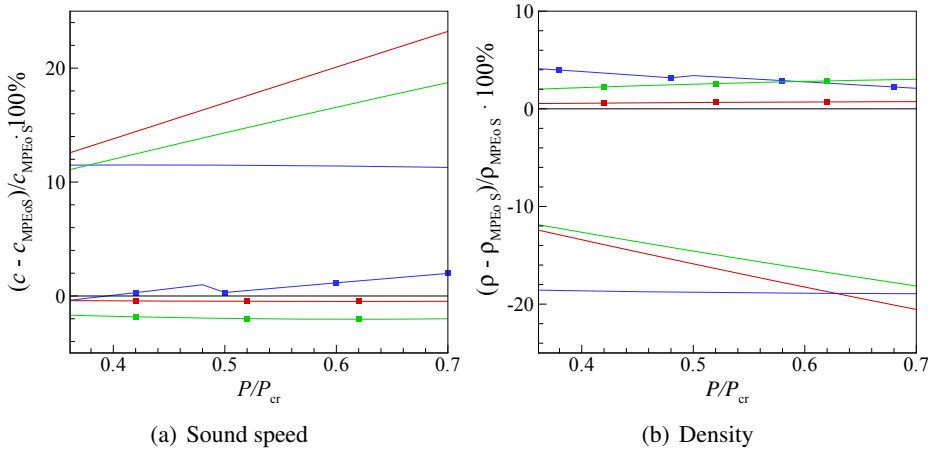
Figure 3.4: *Percentage difference of thermodynamic properties along the subcritical expansion isentrope computed based on the PRSV model (■) and the PIG model (no symbol) with respect to the values computed based on the MPEoS. Results are given for steam (——), toluene (——) and R245fa (——).*

assumption of inviscid flow and is therefore for the larger part not visualized in the figures. At the location $X/C_{ax} = 0.64$ and 0.70 the Mach number distribution of the suction side does not vary smoothly, indicating irregular expansion. The Mach number distribution appears surprisingly similar for all EoS models. Fig. 3.11(a) reveals that the difference in Mach number due to the use of the PIG model with respect to the reference model is approximately 2%, while it is approximately 3% if the PRSV model is employed (not taking into account the high error near the trailing edge, which is a result of nonphysical overexpansion).

Table 3.4: *Fluid properties and EoS parameters.*

Fluid		Steam	Toluene	R245fa
Chemical formula		H_2O	C_7H_8	$CF_3CH_2CHF_2$
Molecular weight	M, g/mol	18	92.1	134.1
Fundamental derivative	Γ^V_{min}, -	1.162	0.564	0.709
Critical pressure	P_c, bar	220.6	41.3	36.4
Critical temperature	T_c, °C	374	318.6	154.1
PIG parameter (Eq. (3.1))	γ	1.2912	1.0447	1.0608
PRSV parameters (Eq. (3.2))	k_1	-0.0664	0.0385	0.0060
	ω	0.3438	0.2632	0.3724
MPEoS parameters Ref.		[31]	[10]	[10]
Isobaric specific heat				
coefficients in Eq. (4.1)	A	32.2	-24.35	226.85
	$B \cdot 10$	1.92	512.5	28.16
	$C \cdot 10^3$	10.6	-276.5	335.45
	$D \cdot 10^6$	-3.6	49.11	-144.21
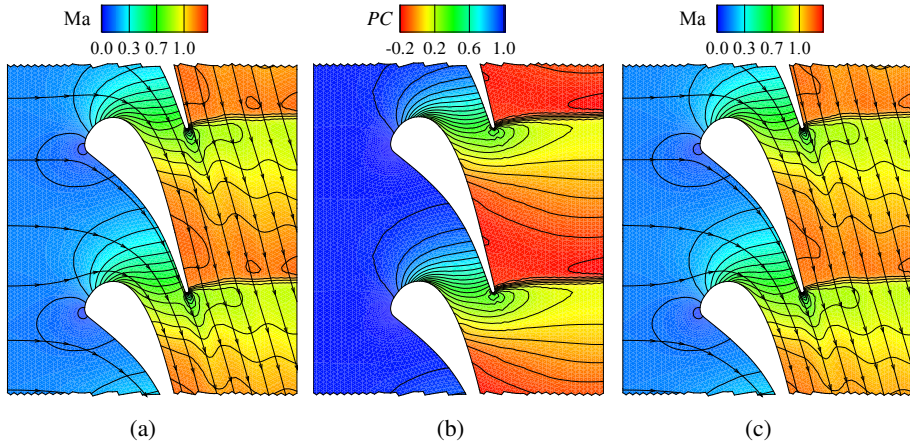
Figure 3.5: *Flow field distributions of steam: (a) Mach number and (b) pressure coefficient distributions and streamlines based on the MPEoS; (c) Mach number distribution and streamlines based on the PIG model.*

The distribution of the pressure coefficient defined as

$$PC = \frac{P - P_2}{P_{01} - P_2},\qquad(3.5)$$

where P_{01} is the total inlet pressure and P_2 the static outflow pressure, is shown in Fig.3.6(b). Its trend is opposite to that of the Mach number. Note that the same pressure values are prescribed at the inflow and outflow boundary for all EoSs. The PIG and PRSV models both compute the pressure along the blade profile with an accuracy of 1%, as shown in Fig 3.11(b). The differences in the predictions of density, sound speed and isochoric specific heat, are shown in Fig. 3.4 as a function of the pressure. Consequently, these differences are somewhat differently distributed in comparison with the distributions of the deviations along the blade surface.

The sound speed, denoted by c, is shown in Fig. 3.6(c). Simulations using the PIG model show a high sound speed of steam ($c = 651$ m/s), which decreases as the fluid expands. The PRSV and the MPEoS, on the other hand, predict a lower sound speed ($c = 584$ and 595 m/s, respectively) in the initial phase of the expansion, which is more realistic. The deviation in the sound speed predicted by the PIG model is approximately 11% and is constant along the blade surface as shown in Fig. 3.11(c). The PRSV EoS has a deviation in the sound speed below 3%. The same differences are obtained from a direct comparison of soundspeeds between the EoSs at the same conditions, shown in Fig. 3.4(a).

The Mach number distribution is surprisingly similar between the thermodynamic models. The relative difference in Mach number between the PIG model and the MPEoS (Fig. 3.11(a)) is at most 2%, which is very small compared to the relative difference in sound speed of approximately 11%. This results from the fact that the higher sound speed is compensated by a velocity magnitude (Fig. 3.6(d)) that is similarly higher (11%), as shown by the comparison in Fig. 3.11(d). The figure shows the percentage difference of velocity magnitude for the PIG model and PRSV with respect to the MPEoS.

Very large differences in densities between the EoS models can be observed in Fig. 3.6(e). At the leading edge, the difference based on the PIG model with respect to the MPEoS is as high as 19% (Fig. 3.11(e)). The large difference can be expected (see Fig. 3.4(b)), since pressure and temperature are the prescribed variables at inflow and outflow and density depends on the EoS model. The density error predicted by the PIG model is therefore equal to the deviation from ideal gas in terms of the compressibility factor (Fig. 3.6(f)). The maximum difference in density predicted by the PRSV EoS with respect to the MPEoS is 5% (not taking into account the high error at the trailing edge).

Table 3.5 lists the deviations in mass flow rate, total pressure loss coefficient and outflow angle as a result of using the PIG and PRSV models as compared to the MPEoS. The mass flow rate through the stator is given by $\dot{m} = \rho U A$, where ρ, U and A denote density, flow velocity and cross-sectional area, respectively. For the simulation employing the PIG model, the 19% underprediction of density combined with the 11% overprediction of velocity magnitude results in a net underprediction of the mass flow rate of 9.8%. A previous study [11] based on a cubic EoS in which the expansion of methane in a nozzle was simulated from reduced reservoir conditions $P_{01}/P_c = 5$ and $T_{01}/T_c = 1.4$ for pressure ratios between $1 < P_{01}/P_2 < 2.5$ showed a similar mass flow underprediction of the PIG model (14%) for the pressure ratio $P_{01}/P_2 = 1.9$ used in the present study.

If this turbine stator blade were designed by computing the thermodynamic properties using the PIG model, this large error in the predicted relation of mass flow with respect to pressure ratio would lead to a different pressure - mass flow characteristic, which would also affect the operation of the other components in the cycle, leading to suboptimal cycle performance. Note that the mass flow rate deviation obtained from the simulation using the PRSV model is 2.1%, which can often be considered acceptable for a technical application.

The same inflow temperature is prescribed for all EoSs (see Fig. 3.6(h)), but the relative difference in temperature (based on °C) becomes larger as the flow expands. As shown in Fig. 3.11(f), the deviation is small (1%) for the PIG model. For the PIG model, the constant value of the ideal-gas specific heat, C_P^0, is calculated using the MPEoS model. The fact that for the particular case of steam, a low-complexity fluid, the PIG model leads to low deviations in temperature along the expansion process, is explained in Section 3.3.2. For the simulations employing the PRSV model, the temperature deviates by at most 2.5%. The higher deviation observed for the PRSV model may be explained by the fact that, at reduced temperatures above approximately $T/T_c \gtrsim 0.9$ and close to the saturation curve (Fig. 3.12(a)), physically based cubic EoSs such as the PRSV EoS are known to perform less well for polar molecules (such as steam) as compared to nonpolar molecules [56, 27].

The shock wave located at the trailing edge (Fig. 3.5) leads to a loss of total pressure and thus reduces the overall efficiency of the expansion. The total pressure loss coefficient is defined as the mass-weighted average over the outflow boundary of $C_{PL} \equiv 1 - P_{02}/P_{01}$, where P_{01} is the total inlet pressure and P_{02} the local total outflow pressure. Its value relative to the one based on the MPEoS is 0.3% lower for the simulations employing the PIG model and 4% lower for the simulations employing the PRSV EoS, as reported in Table 3.5. The small devi-

ation for the PIG model is an exception as compared to the other fluids. This is explained from the fact that the total pressure loss is derived from caloric properties. As mentioned before, the PIG model is well suitable for predicting caloric properties of simple fluids such as steam, thus leading to the observed small deviation in total pressure loss for this particular fluid.

The deviation in the outflow angle β is also listed in Table 3.5. It is an important flow parameter in the context of turbomachinery design as it affects the design of the downstream rotor blade. For both the PIG and PRSV model the deviation in velocity magnitude from the values computed by the simulation employing the MPEoS (Fig. 3.11(d)) are approximately equal for the suction and pressure side of the blade. Consequently, the error in the outflow angle is small; less than two tenths of a degree for both EoSs.

3.3.1.2　Toluene

Toluene (C_7H_8), also known as methylbenzene, is a heavier molecule than steam and its molecule is more complex than both steam and R245fa. Owing to these properties, toluene is used in so-called Organic Rankine Cycle (ORC) turbogenerators [6, 7].

The two-dimensional flow fields for subcritical expansion obtained using the MPEoS are plotted in Fig. 3.7. Since the expansion is equal to the one for steam in terms of reduced inflow conditions and pressure ratio, the flow structure is similar. However, the Mach number distribution and the increased angle of the shock wave show that the flow attains higher Mach numbers as compared to steam. The pressure coefficient is similarly different.

Fig. 3.8 shows the surface distributions of the flow parameters for toluene. Even though toluene has different fluid characteristics, and consequently some flow parameters are different in absolute terms (velocity and density), their trend is is similar to steam. Differences can be seen in the compressibility factor in Fig. 3.8(f), which increases more steeply compared to steam, resulting in a thermodynamical outlet state that is closer to dilute gas conditions, and in the sound speed in Fig. 3.8(c), which in this case increases as the fluid expands. This behavior will be discussed in detail below.

The local fluctuation observed at $X/C_{ax} = 0.67$ of the suction side distribution calculated using the PIG model in the flow parameters Mach, pressure coefficient, velocity, density and temperature is the result of the onset of a weak trailing edge shock impinging on the suction side blade surface of the next stator blade. As can be observed by comparing Fig. 3.7(a) and Fig. 3.7(c), the weak shock wave simulated using the PIG model is locally stronger than the one obtained by employing

(a) Isentropic Mach number (b) Pressure coefficient (c) Sound speed

(d) Velocity (e) Density (f) Compressibility factor

(g) Fundamental gasdynamic derivative (h) Temperature
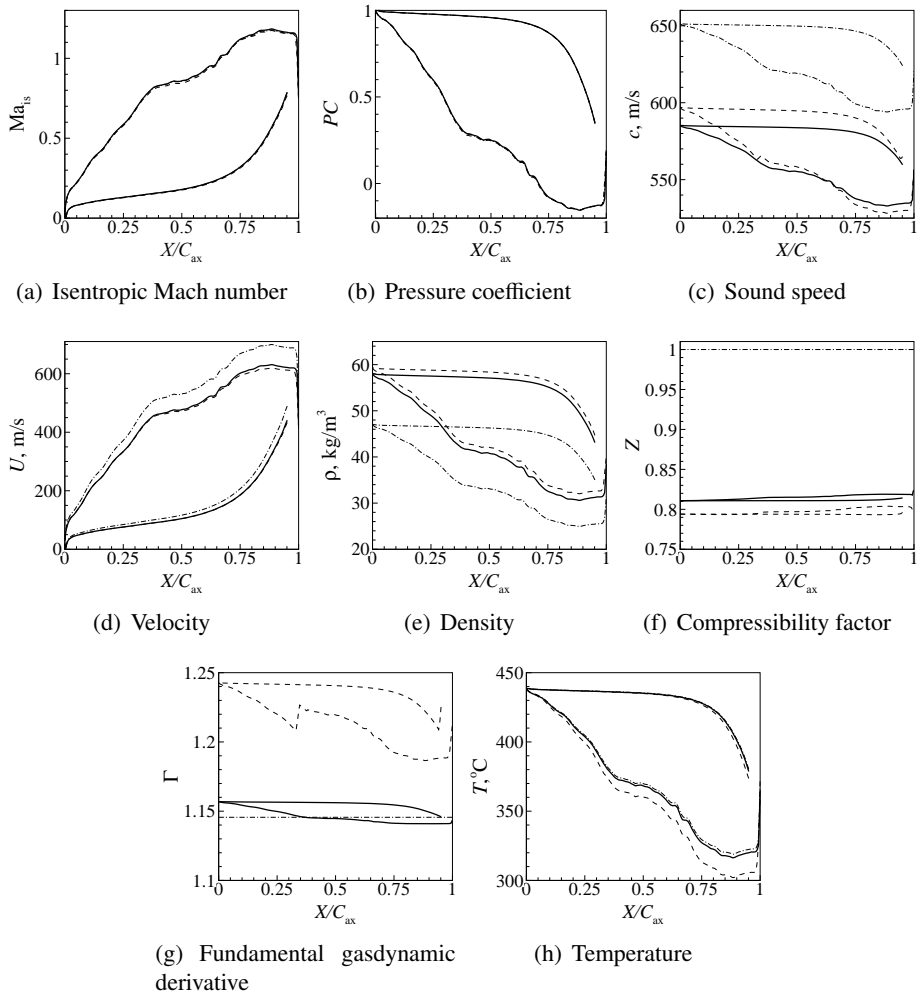
Figure 3.6: *Blade surface distributions of steam, computed based on the MPEoS (——),
PRSV (– – –) and PIG (– · – · –) model.*

the reference model, leading to local recompression. This means that, based on the
PIG model, the pressure gradient is locally adverse, thus possibly inducing bound-
ary layer separation in the real viscous flow. It is interesting to note that since this
nonmonotonicity is visible in the absolute velocity magnitude (Fig. 3.8(d)), but
not in the sound speed (Fig. 3.8(c)), this results in the most significant deviation
in the Mach number (Fig. 3.8(a) and 3.11(a)).

In the case of toluene, the deviations between the simulations performed with the PIG model with respect to the ones employing the MPEoS are appreciably larger than in the case of steam. The relative differences in the Mach number (Fig. 3.11(a)) and pressure (Fig. 3.11(b)) vary widely and reach values of 7% and 5%, respectively. Unlike the constant deviations observed for steam, for toluene the sound speed and velocity magnitude errors induced by the PIG model clearly decrease as the fluid expands towards the ideal gas region. At the inflow they are 23% and 18%, respectively (thus largely compensating each other to lead to the smaller aforementioned error in the Mach number), but both reduce to values of approximately 15% and 13%, respectively (maintaining the compensation). Also the error in density computed using the the PIG model is nonuniform along the blade surface and has a maximum value of 21%. The temperature at the outlet is overpredicted by at most 2%. Except for the temperature, all deviations of flow parameters computed using the PIG model with respect to the reference model decrease, since the flow expands to more ideal-gas conditions (see Table 3.3).

As the fluid expands, the more physically correct PRSV and MPEoS models predict an increase in sound speed (Fig. 3.8(c)), rising from $c \approx 202$ to a value of $c \approx 218$ m/s. The PIG model, on the contrary, incorrectly predicts a decreasing sound speed, which, under ideal gas theory, is always the case for an isentropic expansion. The correct increase in sound speed across an isentropic expansion as seen here can occur only for molecularly complex fluids within a certain thermodynamic region, which lies in the dense gas region [57]. The fundamental derivative of gasdynamics, denoted by Γ, is defined as:

$$\Gamma \equiv \frac{v^3}{2c^2}\left(\frac{\partial^2 P}{\partial v^2}\right)_s = 1 - \frac{v}{c}\left(\frac{\partial c}{\partial v}\right)_s \qquad (3.6)$$

Here, v is the specific volume and s is the specific entropy. The complexity of the fluid molecules causes the isentropic relation between sound speed and temperature to be inverted with respect to the ideal gas behavior for a finite range of pressures and temperatures in the single-phase region where $\Gamma < 1$. In this region, the sound speed increases across an isentropic expansion and decreases across an isentropic compression. The complexity of a fluid can be quantified by $\Gamma^V_{\min}$, the minimum value of the fundamental derivative along the saturation line, which is shown in Table 3.4. Note that Γ is the parameter that, if negative, indicates the possible occurrence of so-called nonclassical gasdynamic behavior [58, 59, 57]. Neither toluene, nor R245fa are molecularly complex enough to display a region of negative gamma for dense vapor states. Among the fluids compared in this study, toluene has the lowest value of $\Gamma^V_{\min}$ indicating that it is the most complex molecule.

Fig. 3.8(g) shows the distribution of the fundamental gasdynamic derivative for the subcritical expansion of toluene. The results for the MPEoS show that the entire expansion process occurs at $\Gamma < 1$, which is in accordance with the increase in sound speed observed in Fig. 3.8(c) for the PRSV and MPEoS models. Initially, its value is $\Gamma = 0.87$ (MPEoS and PRSV) and it increases to $\Gamma = 0.9\text{-}0.94$. The PIG model incorrectly predicts a value of $\Gamma = 1.022$, since for an ideal gas Eq. (3.6) reduces to a constant $\Gamma = (\gamma + 1)/2$.

The temperature (Fig. 3.8(h)) shows a comparatively small temperature drop, typical for the expansion of molecularly complex fluids.

Similarly to steam, also in the case of toluene does the use of the PIG model show large but compensating errors in sound speed and velocity, leading to a comparatively smaller deviation in Mach number.

The mass flow rate relative to the one based on the MPEoS is 6.2% lower for the PIG model and only 0.3% lower for the PRSV EoS. The total pressure loss coefficient, C_{PL} is 14% lower in case the PIG model is used and 11% higher in case the PRSV model is used. This is a result of the overprediction of the velocity magnitude (Fig. 3.8(d)), leading to a lower total pressure loss coefficient.

Unlike for steam, the error in the velocity magnitude (Fig. 3.11(d)) is not equal for the suction and the pressure sides induced by the PIG model. The difference causes an error in the outflow angle β of 0.8 degrees, which is significant for the design of turbomachinery blades. The error in the outflow angle induced by the use of the PRSV EoS is negligible (-0.02%).

3.3.1.3   R245fa

The hydrofluorocarbon R245fa is a non-flammable and non-toxic refrigerant that is used to synthesize polyurethane foam, because of its low thermal conductivity and zero ozone depleting potential. Compared to other refrigerants, it has a high critical temperature. Because of this, it has recently also been applied as a working fluid in ORCs for geothermal heat sources [4]. Its molecular weight is considerably higher than that of steam and toluene, as shown in Table 3.4, but its complexity, although lower, has the same order of magnitude of that of toluene.

The two-dimensional flow fields for the subcritical expansion obtained using the MPEoS are plotted in Fig. 3.9. The flow fields are nearly identical to those of toluene, even though R245fa is 45% heavier.

When comparing the real behavior of the fluids, i.e., based on the simulations using the MPEoS, it is noted that, due to its higher molecular weight, the expansion of R245fa shows even lower sound speeds (Fig 3.10(c)) than those of toluene; nonetheless, they are compensated by similarly lower velocities, result-

Figure 3.7: *Flow field distributions of toluene: (a) Mach number and (b) pressure coefficient distributions and streamlines based on the MPEoS; (c) Mach number distribution and streamlines based on the PIG model.*

ing in equal Mach number distributions (c.f., both fluids have a maximum Mach number of 1.28). The qualitative behavior of the flow parameters is similar to that of toluene. As expected, there is a considerable quantitative difference in density and temperature, which are respectively higher and lower due to the larger molecular weight of R245fa.

As expected, the distribution of the fundamental gasdynamic derivative Γ obtained using the MPEoS, depicted in Fig. 3.10(g), shows that the entire expansion process of this complex fluid occurs at $\Gamma < 1$, which is in accordance with the increase in sound speed observed in the simulations using the PRSV and MPEoS models (Fig. 3.10(c)). However, in the case of the expansion of R245fa, the value of Γ is higher than for toluene, resulting in a less pronounced increase in the speed of sound, as confirmed by Fig. 3.10(c). Values of the fundamental derivative of gasdynamics calculated with the PRSV model for R245fa are less accurate if compared to values for toluene calculated with the same equation of state. These differences in Γ are even more pronounced for steam (Fig. 3.6(g)). The origin of these differences is to be found in the different data on which the thermodynamic models are based, namely 1) the difference among the adopted critical temperature and pressure, 2) a small difference in the experimental data used to fit the vapor pressure 3) the different functional form. A full account of this topic is given in Ref. [60].

In the comparison of EoSs of Fig. 3.11, it is observed that for R245fa the de-

(a) Isentropic Mach number

(b) Pressure coefficient

(c) Sound speed

(d) Velocity

(e) Density

(f) Compressibility factor

(g) Fundamental gasdynamic derivative

(h) Temperature
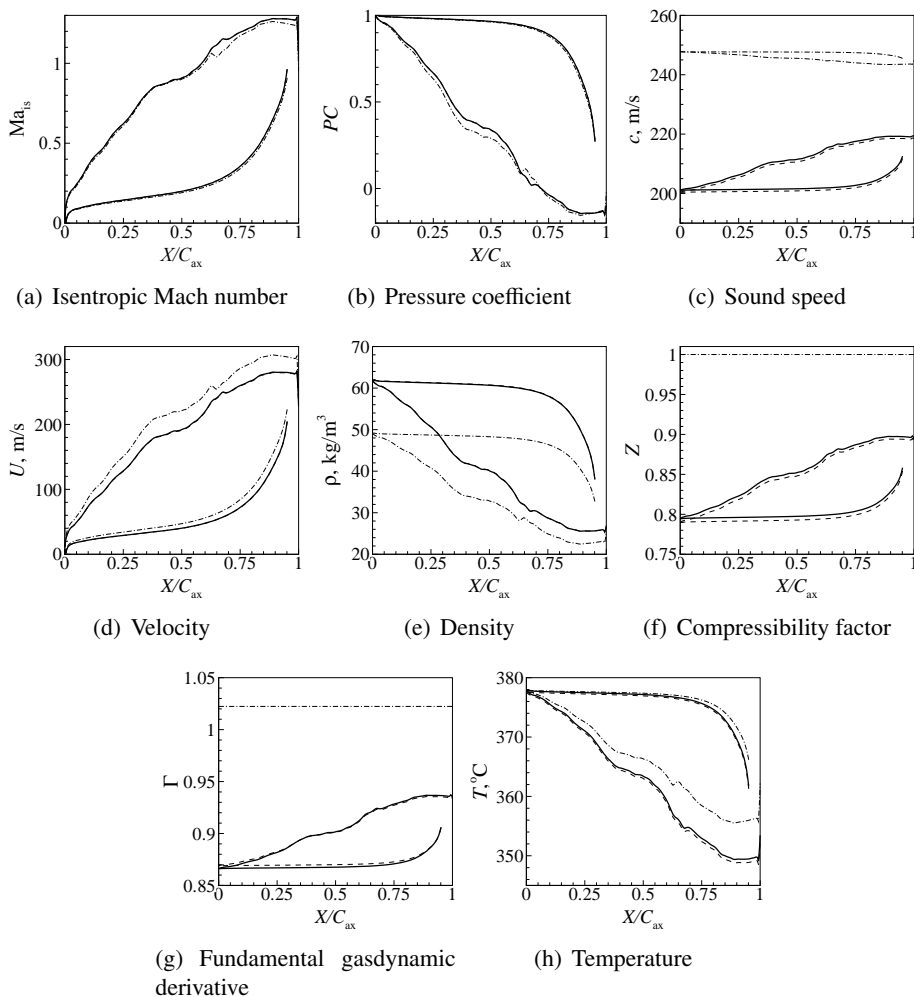
Figure 3.8: *Blade surface distributions of toluene, computed based on the MPEoS (———), PRSV (– – –) and PIG (– · – · –) model.*

viations resulting from the use of the PIG model in all flow parameters are similar to those of toluene; deviations in Mach, pressure and temperature are approximately 5% and errors in sound speed, velocity magnitude, density are approximately 20%. The only difference in comparison to toluene is that for all flow parameters except for temperature, the errors, although still large, have reduced slightly.

Compared to the PIG model, the use of the PRSV EoS leads to much smaller deviations in all flow parameters of the R245fa expansion; the maximum error is 1.5% in all parameters and only 0.2% in the temperature.

With respect to the errors in mass flow rate and outflow angle, similar values are obtained as for toluene. The deviations in the total pressure loss coefficient, however, have further increased to −26% (PIG) and −14% (PRSV).

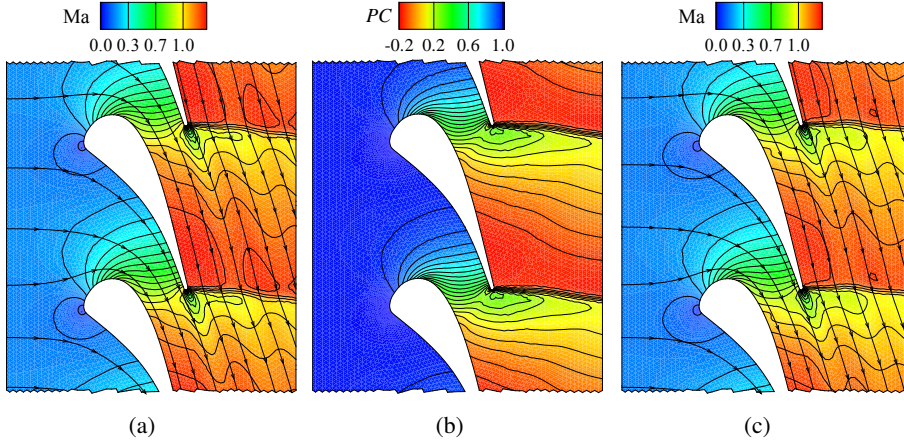(a)   (b)   (c)
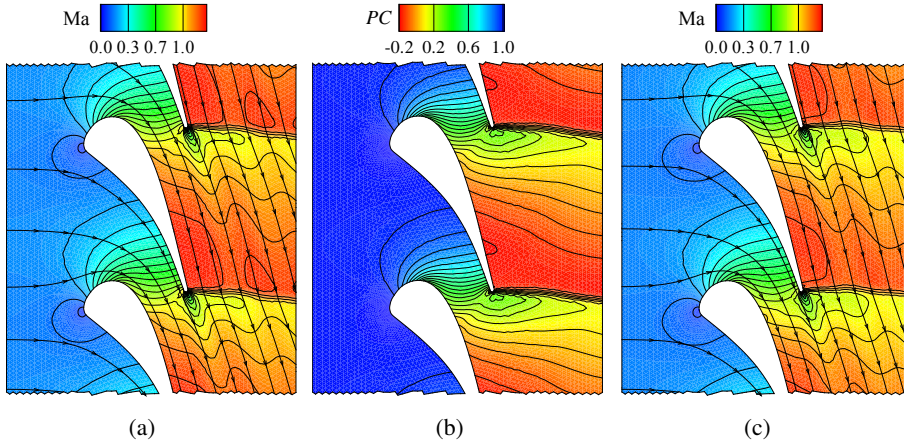
Figure 3.9: *Flow field distributions of R245fa: (a) Mach number and (b) pressure coefficient distributions and streamlines based on the MPEoS; (c) Mach number distribution and streamlines based on the PIG model.*

(a) Isentropic Mach number

(b) Pressure coefficient

(c) Sound speed

(d) Velocity

(e) Density

(f) Compressibility factor

(g) Fundamental gasdynamic derivative

(h) Temperature
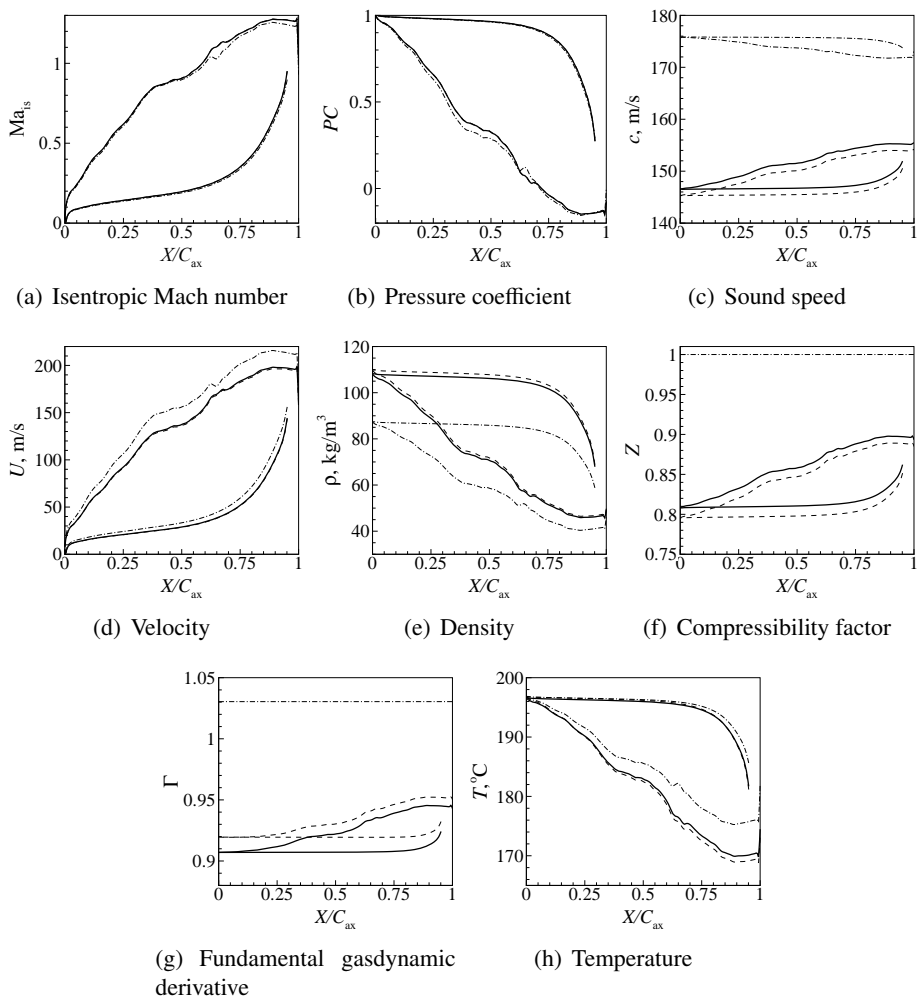
Figure 3.10: *Blade surface distributions of R245fa, computed based on the MPEoS (——), PRSV (– – –) and PIG (– · – · –) model.*

(a) Isentropic Mach number

(b) Pressure

(c) Sound speed

(d) Velocity

Figure 3.11: *Percentage difference of flow parameters along the blade surface, computed based on the PRSV model (■) and the PIG model (no symbol) with respect to the values computed based on the MPEoS. Results are given for steam (——), toluene (——) and R245fa (——). The blade suction and pressure sides are distinguished by the continuous and dashed lines, respectively.*

(e) Density   (f) Temperature

Figure 3.11: *Percentage difference of flow parameters along the blade surface, computed based on the PRSV model (■) and the PIG model (no symbol) with respect to the values computed based on the MPEoS. Results are given for steam (———), toluene (———) and R245fa (———). The blade suction and pressure sides are distinguished by the continuous and dashed lines, respectively.*

3.3.2   Corrected Polytropic Ideal Gas Model for Steam

As observed in the previous section, the deviations of the PIG model in density, speed of sound and velocity are constant in case of water, whereas for toluene and R245fa they vary along the blade surface. This peculiar behavior can be attributed to the fact that the PIG model is able to correctly approximate the qualitative behavior of isentropes of low complexity fluids, like steam. In the pressure range of interest of steam (Fig. 3.12(a)), the PIG model only leads to an absolute deviation in volumetric and volume-dependent properties, but is qualitatively correct. The constant absolute deviation for low complexity fluids in this thermodynamic region warrants the use of a corrected PIG model (ZPIG),

$$P = Z\frac{RT}{v},\tag{3.7}$$

where Z is a constant compressibility factor that assumes, e.g., the value at the inlet determined based on the generalized $P-v-T$-properties of gases (see, e.g., [61]). This approach is commonly used in turbomachinery practice for the thermody-

namic modeling of arbitrary fluids expanded at nonideal thermodynamic conditions. In case of steam it is shown to perfectly approximate the isentrope based on the MPEoS for a limited but large pressure range. The isentropes of complex fluids, like toluene (Fig. 3.12(b)) and R245fa (Fig. 3.12(c)), however, behave differently and they approximate isotherms [57], as shown in Fig. 3.12. For complex fluids, however, the PIG model no longer qualitatively represents the isentropes and therefore the ZPIG model can no longer be used, as evidenced by the fluid dynamic results.

(a) Steam	(b) Toluene	(c) R245fa
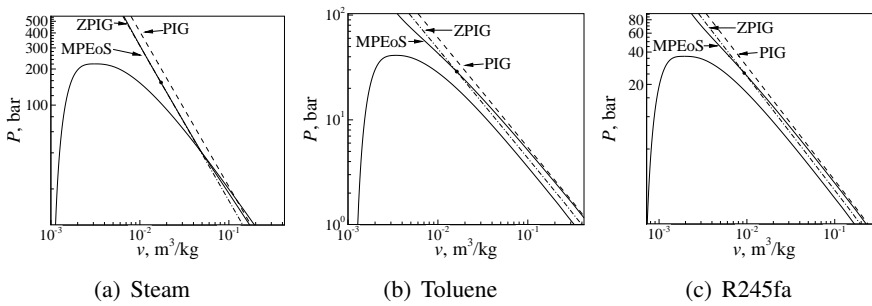
Figure 3.12: *Expansion isentropes as obtained using the MPEoS (———), PIG (– – –) and ZPIG (– · – · –) models in the pressure-specific volume diagrams (showing the saturation line) of steam, toluene and R245fa. In the ZPIG model, the compressibility factor Z is set to the value given in Table 3.3. The dotted intersection of MPEoS and ZPIG indicates the subcritical inlet state.*

3.3.3   Supercritical Inflow Conditions

In this section, the same study is conducted for an expansion from supercritical conditions, in order to investigate the influence of increased thermodynamic nonideality on the deviations of flow parameters entailed by the PIG and PRSV models. The pressure ratio is chosen equal to the subcritical expansion. The process conditions are given in reduced values in Table 3.2. The expansions from supercritical conditions for the three fluids, given in the $T - s$-diagrams in Fig. 3.3, show that the expansion takes place closer to the critical points of the fluids. As a result, the compressibility factor at the inlet, given in Table 3.3, is lowered to $Z \approx 0.6$ for all fluids, indicating strong thermodynamic nonideality. As the fluid expands to lower pressures, the compressibility factor also increases. At the outlet it is $Z \approx 0.9$, which is approximately equal to the one in the mildly nonideal subcritical expansion.

Since the expansion occurs closer the critical point, it also approaches the vapor saturation line of the fluids. This poses no problem in case of toluene and R245fa, which are retrograde fluids, but in the case of steam, condensation occurs, as shown in the $T - s$-diagram in Fig. 3.3(a). Since the zFLOW solver is not yet able to compute two-phase flows, the results for steam cannot be presented in this case.

For conciseness, only the distributions of the errors in the flow parameters for the PIG and PRSV models with respect to the MPEoS model are presented and they are given in Fig. 3.13. A comparison of the distributions of toluene and R245fa shows that the error distributions ensuing from the PIG model are qualitatively similar to the subcritical error distributions presented in the previous section (see Fig. 3.11). On the other hand, the inflow state of this expansion is now closer to the critical temperature (Table 3.2) at which the ideal-gas ratio of specific heats γ is determined, which may locally mitigate the deviation.

As expected from the lower compressibility factor, all errors associated with the PIG model are quantitatively significantly higher for the supercritical expansion as visible in Fig. 3.13. The error in the Mach number ensuing from the PIG model has approximately doubled to $8-10\%$ for toluene and $7-10\%$ for R245fa. The pressure error has doubled to maxima of 9% for toluene and 7% for R245fa. The supercritical expansion takes place closer to the critical point, where the thermodynamic speed of sound has its minimum value. As a result, the error in the sound speed ensuing from the PIG model has more than doubled to maxima of 52% and 63% for R245fa and toluene, respectively. This increase is again balanced by similarly higher (both quantitatively and qualitatively) maximum velocity errors of 50% for toluene and 42% for R245fa, except for the location where the weak trailing edge shock wave impinges. As can be expected from the compressibility factor in Table 3.3, the maximum errors in density caused by the use of the PIG model have increased to 43 and 40% for toluene and R245fa, respectively. For the supercritical expansion, the PIG model overpredicts temperatures by as much as 7% and 13% for toluene and R245fa, respectively.

Even for the supercritical strongly nonideal expansion, using the PRSV leads to errors of at maximum 3% in all investigated flow parameters, except for the total pressure loss.
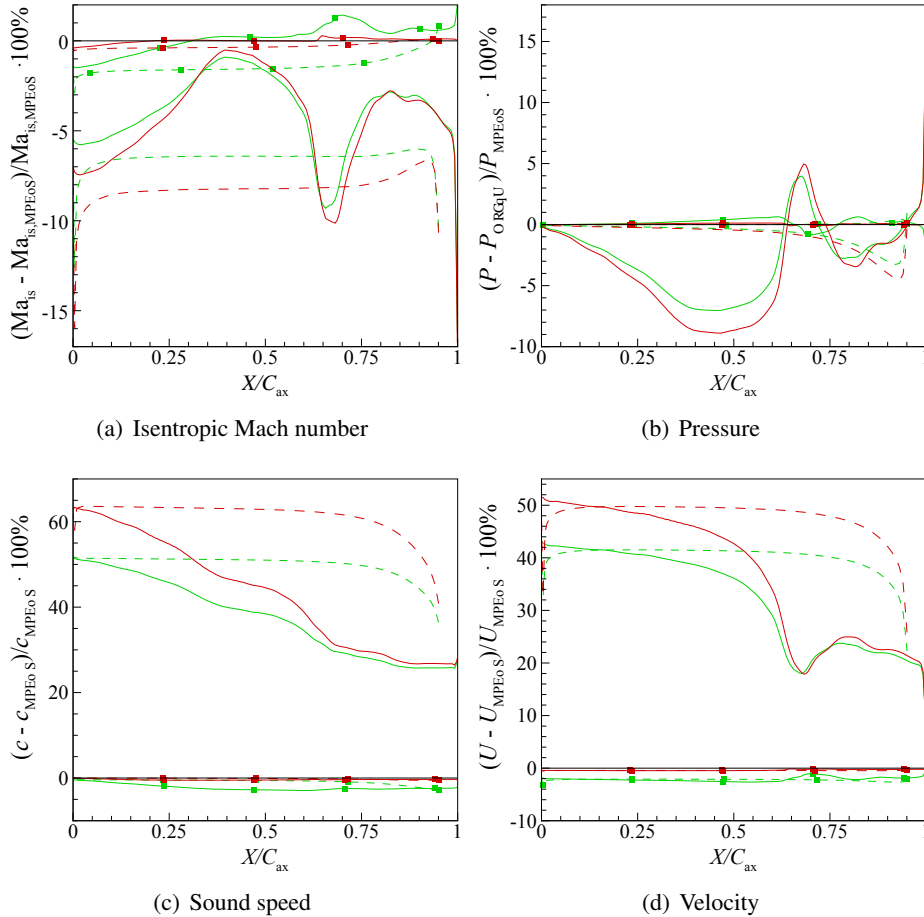
(a) Isentropic Mach number

(b) Pressure

(c) Sound speed

(d) Velocity

Figure 3.13: *Supercritical expansion: percentage difference of flow parameters along the blade surface, computed based on the PRSV model (■) and the PIG model (no symbol) with respect to the values computed based on the MPEoS. Results are given for toluene (——) and R245fa (——). The blade suction and pressure sides are distinguished by the continuous and dashed lines, respectively.*

At the trailing edge ($X/C_{ax} = 1$) the deviation from ideal gas behavior is low and approximately equal to the one for the subcritical expansion as indicated by the outlet compressibility factor Z_2 in Table 3.3. The throat is located at $X/C_{ax} \approx 0.66$ on the blade suction side, where the thermodynamic nonideality is still high, thus leading to larger errors. The error in the mass flow rate induced by the PIG model is a result of the combined errors in density and velocity at the
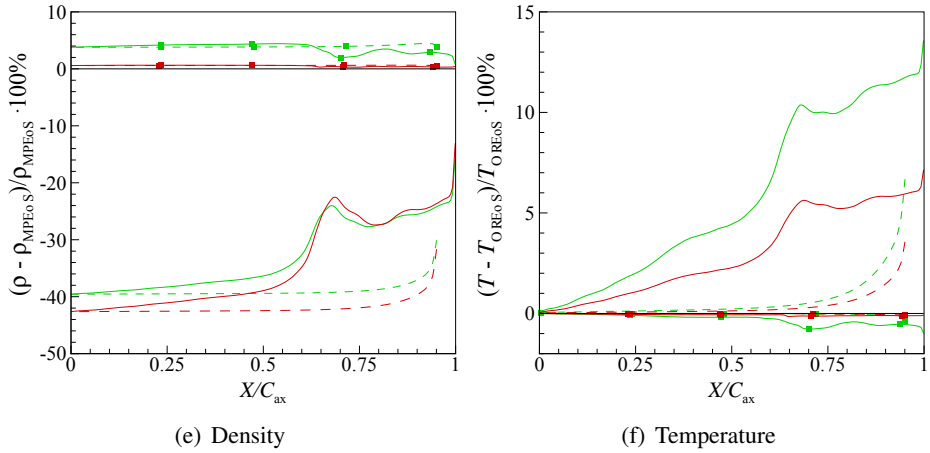
(e) Density

(f) Temperature

Figure 3.13: *Supercritical expansion: percentage difference of flow parameters along the blade surface, computed based on the PRSV model (■) and the PIG model (no symbol) with respect to the values computed based on the MPEoS. Results are given for toluene (———) and R245fa (———). The blade suction and pressure sides are distinguished by the continuous and dashed lines, respectively.*

throat location. As can be seen from Table 3.5, it has decreased to approximately −14% for both toluene and R245fa. Compared to this, the errors ensuing from the PRSV model are much smaller and have remained small; 0.2% and 1.7% for toluene and R245fa, respectively.

The errors in C_{PL}, induced by the PIG model are −30% and −27% for toluene and R245fa, respectively. The errors have increased with respect to the subcritical expansion case as a result of the increased overprediction of the velocity magnitude as evident from Fig. 3.13(d). For the PRSV model, the errors in C_{PL} are much lower, viz., 0.4% for toluene and 2.5% for R245fa.

As a result of the increased nonideality of the supercritical expansion, an even larger overprediction of the velocity at the suction side is observed in the simulations using the PIG model. The overprediction at the pressure side has increased less. Consequently, the PIG model predicts increased turning of the flow for the supercritical expansion. The outflow angle error caused by the use of the PIG model is 2°C for toluene and 1.7°C for R245fa. Again, in case the PRSV model is used, this error is low; negligible for toluene and −0.2°C for R245fa.

Table 3.5: *Percentage difference of the mass flow rate ($\Delta \dot{m}$), total pressure loss coefficient (ΔC_{PL}) and outflow angle ($\Delta \beta$) for the PIG and PRSV EoS models with respect to the values computed based on the MPEoS. The total pressure loss coefficient is defined as the mass-weighted average over the outflow boundary of $C_{PL} \equiv 1 - P_{02}/P_{01}$, where P_{01} is the total inlet pressure and P_{02} the local total outflow pressure.*

	$\Delta \dot{m}$, %		ΔC_{PL}, %		$\Delta \beta$, °	
	PIG	PRSV	PIG	PRSV	PIG	PRSV
Subcritical						
Steam	-9.8	2.1	-0.32	-4	0.06	0.12
Toluene	-6.2	-0.25	-14	11	0.78	-0.02
R245fa	-6.4	0.63	-26	-14	0.71	-0.04
Supercritical						
Toluene	-14	0.15	-30	0.38	2	0
R245fa	-14	1.7	-27	2.5	1.7	-0.22

3.4   Computational Cost

In many engineering applications, the computational cost of a CFD simulation is, like accuracy, an important aspect. This is particularly true for automated design optimization procedures, which commonly evaluate a large number of different designs and usually require a CFD computation for each design. A valuable comparison of the thermodynamic models should therefore include a comparison of the computational cost. Table 3.6 shows the CPU time required for the convergence of the subcritical expansion case for steam discussed in Section 3.3.1.1. Computations using the PRSV and MPEoS model take approximately 9 and 11 times (respectively) as long as compared to the PIG model.

The large computational resources required for the PRSV and MPEoS models can be largely attributed to the saturation state calculations. For each thermodynamic property evaluation using the PRSV or MPEoS model, the fluid phase is first determined from a saturation state calculation. Depending on whether the state is in the single-phase or in the vaporliquid mixture region, the desired property is evaluated in a different way. The saturation state calculation is often an iterative procedure, making it very costly as compared to the subsequent evaluation of the properties. If it is known a priori that the simulated process occurs in the vapor region, as it is in this case, then saturation checks are not needed and can be left out. In this way, the cost of the computations (Table 3.6) is reduced

by a factor 4 to 5. With this reduction, the computations without saturation state calculations require only 2 (PRSV) and 3 (MPEoS) times as much time as the computations that employ the PIG model. Care must however be taken especially for processes that take place close to the saturation line, for which it is not know beforehand whether or not saturation occurs locally, e.g., due to overexpansion.

Table 3.6: *CPU time required for the convergence of the subcritical expansion case for steam (see Section 3.3.1.1) on the fine grid (4153 grid nodes) computed using an Intel Pentium 4 2.8 GHz processor. In all cases convergence (a reduction of the residuals by five orders of magnitude) was obtained after 436 iterations.*

Thermodynamic model	saturation (VLE) calculations	CPU time, s	time/time$_{PIG}$	time/time$_{noVLE}$
PIG	no	141	-	-
PRSV	no	263	2x	-
PRSV	yes	1332	9x	5x
MPEoS	no	416	3x	-
MPEoS	yes	1549	11x	4x

3.5   Conclusions

The state-of-the-art inviscid zFLOW CFD solver coupled with a fluid property library containing several thermodynamic models, including highly accurate ones, has been used to simulate the fluid dynamics of turboexpander processes in thermodynamic conditions affected by strong real-gas effects.

This chapter presented a quantitative comparison of the effect of using thermodynamic models of various degree of complexity with regard to the application to fluid dynamic simulations of turboexpanders operated in this thermodynamic region. The considered thermodynamic models are, in order of increasing complexity, the polytropic ideal gas (PIG) law, the Peng-Robinson-Stryjek-Vera (PRSV) cubic EoS and multiparameter EoS (MPEoS). The investigated processes are moderately nonideal (compressibility factor of $0.8 < Z < 0.9$) subcritical expansions and highly nonideal (compressibility factor of $0.6 < Z < 0.9$) supercritical expansions. The chosen fluids were steam, toluene and R245fa. The same pressure ratio was adopted for all cases and the two inlet conditions are specified in reduced terms (the reference values being the critical temperature and pres-

sure of the considered fluids). A standard transonic turbine stator blade geometry was used as example of a turboexpander. Distributions of fluid dynamic parameters along the blade surface and performance parameters based on the two EoSs have been compared to those obtained using highly accurate multiparameter EoSs (MPEoSs) of the respective fluids.

Prior to the comparative simulations, the ZFLOW solver linked to the accurate thermodynamic model was successfully validated for the transonic fluid dynamic problem under consideration. For the validation, however, the expansion occurs at ideal-gas conditions. Experimental data of fluid expansions at nonideal (e.g. supercritical) conditions is unfortunately not yet available, hindering the validation of the flow solver linked to the accurate thermodynamic model for these conditions. This is planned for the near future. Nonetheless, the validation of the solver and thermodynamic model at ideal-gas conditions and the guaranteed high accuracy of the thermodynamic model even at strongly nonideal conditions warrant the validity of the simulations of real-gas flows presented in this study. For the presented simulations it was furthermore demonstrated that grid convergence is obtained.

The comparison of the fluid dynamics between the three thermodynamic models shows that, as expected, using the simplest model, the PIG model, for a moderately nonideal expansion (compressibility factor of $0.8 < Z < 0.9$) leads to large deviations. The deviations are nonuniformly distributed, except for steam. For the most complex fluid, toluene, the large errors (maximum of the blade distribution) are encountered in the density (-20%), sound speed (25%) and velocity (18%). However, other fluid dynamic parameters such as the Mach number (7%), pressure (5%) and temperature (4%) also deviate considerably as a result of using the PIG model. The aforementioned deviations cause similar errors in the integral stator performance parameters. In spite of the fact that the density and velocity errors are opposite in sign, using the PIG model still causes a high error in the mass flow rate, which is consistent for the three fluids and highest for steam (-10%). In case of toluene and R245fa, the total pressure loss due to the trailing edge shock wave is largely underpredicted (-25%) and the error in the outflow angle is 0.8 degrees.

Not surprisingly, employing the PIG model for a highly nonideal (compressibility factor of $0.6 < Z < 0.9$) supercritical expansion leads to even higher errors in comparison with the subcritical expansion. The maximum errors encountered in the density (-43%), sound speed (73%), velocity (50%), Mach number (-10%), pressure (-9%) and temperature (12%) have all increased. The stronger deviations are therefore also observed in the predictions of overall performance param-

eters; the mass flow is underpredicted by 14%, the total pressure loss by 30% and the outflow angle is off by 2%.

For the subcritical expansion, adopting the physically more correct cubic PRSV model instead leads to comparatively small errors of < 1.5% (toluene and R245fa) and < 4% (steam) in all flow parameters along the blade wall. Similarly, the mass flow rate of steam based on the PRSV EoS is off by at most 2.1% and the error in the outflow angle is negligibly small. The error in the total pressure loss coefficient, however, is as high and in some cases higher than the one observed for the PIG model. The PRSV model is reasonably accurate even for the the highly nonideal supercritical expansion. The errors in the sound speed, velocity and density are at most 4%, in the Mach number at most 2%, and only 1% for the temperature. Correspondingly, the integral performance parameter values are only slightly higher.

For the expansion of steam, which has a low molecular complexity, the deviations in the flow parameter are the smallest and uniformly distributed. In case of low complexity fluids like water, the deviations in density, speed of sound and velocity ensuing from the use of the PIG model are constant along the isentropic expansion, because the PIG model is able to correctly approximate the qualitative behavior of isentropes of low complexity fluids in a limited region. The absolute deviation can in this case be reduced by employing the PIG model corrected by a constant compressibility factor. The high nonuniform deviation in the sound speed observed for R245fa and toluene is caused by the inability of the PIG model to describe the increasing sound speed upon isentropic expansion of complex fluids in the dense gas region. However, for all three fluids, the sound speed and velocity are both overpredicted to more or less the same degree, leading to a smaller error in the Mach number.

For the more complex fluids R245fa and toluene, the deviations are larger and vary strongly along the isentropic expansion. It is found that using the PIG model leads to the largest deviations in case of toluene, which is the more complex fluid. Deviations in almost all flow variables are largest for this fluid, the exception being the temperature.

It is important to note that the mentioned error values associated with the PIG model are in fact lower bounds for the considered expansion conditions, because the accuracy of the PIG model is strongly dependent on the choice of the ratio of the specific heats. For the expansions studied in this work, the specific heat evaluated at the critical temperature is used as it leads to minimal thermodynamic deviations in the results using the PIG model with respect to the accurate MPEoS, ensuring a fair comparison.

The mentioned error levels are significant and can have drastic consequences on the performance of any turboexpander. The mentioned overpredictions of the velocity magnitude and outflow angle, for instance, strongly affect the design of the downstream rotor blade. The results of this study can in this respect be useful as guidelines for designers of (turbo)expanders operating in the nonideal-gas region, as it provides an indication of the magnitude and variation of the flow variable errors as result of using a low-complexity thermodynamic model for real-gas CFD simulations, e.g., in case a MPEoS for a certain fluid is not available or due to computational-time requirements. It is envisioned that in the future CFD methods will be thoroughly validated and will have become much more accurate and reliable allowing them to be used as a design tool coupled with automatic optimization. In that case, even small errors as a result of inaccurate thermodynamic modeling might play a role. Although the mentioned deviations are obtained using a practical geometry, the conclusions apply to inviscid expansions in nozzles in general.

In many engineering applications, the computational cost of a CFD simulation is, like accuracy, an important aspect. Computations using the PRSV and MPEoS model take approximately 9 and 11 times (respectively) as long as compared to the PIG model. The large computational resources required for the PRSV and MPEoS models can be largely attributed to saturation-check calculations. Computations without saturation state calculations require only 2 (PRSV) and 3 (MPEoS) as much time as the computations that employ the PIG model.

Nomenclature

A	=	coefficient in ideal gas isobaric specific heat equation
a	=	coefficient of attractive forces
b	=	coefficient of repulsive forces
C	=	specific heat, blade chord, coefficient
c	=	speed of sound
k	=	parameter in Peng Robinson equation of state
Ma	=	Mach number
M	=	molecular weight
$\dot{m}$	=	mass flow rate

P	=	pressure, power
PC	=	pressure coefficient
R	=	specific gas constant
$\bar{R}$	=	universal gas constant
s	=	entropy
T	=	temperature
U	=	velocity
v	=	specific volume
X	=	stator axial coordinate
Y	=	stator circumferential coordinate
Z	=	compressibility factor

Greek symbols

β	=	stator outflow angle
Δ	=	difference
Γ	=	fundamental derivative of gasdynamics
γ	=	ratio of specific heat capacities
ρ	=	density
ω	=	acentric factor

Subscripts

0	=	total (or stagnation)
1	=	stator inlet
2	=	stator exit
ax	=	axial
c	=	critical point
is	=	isentropic
MPEoS	=	based on the multiparameter equation of state
min	=	minimum
P	=	isobaric, pressure
PL	=	total pressure loss
x	=	stator axial coordinate

Superscripts

0	=	ideal-gas contribution
V	=	saturated vapor

Acronyms

CFD	=	Computational Fluid Dynamics
MPEoS	=	multiparameter equation of state
ORC	=	Organic Rankine Cycle
PIG	=	polytropic ideal gas law
PRSV	=	Peng-Robinson Stryjek-Vera modified cubic equation of state
ZPIG	=	polytropic ideal gas law, corrected by
		a constant compressibility factor, $P = Z\rho RT$

References

[1] H.M. Curran. Use of Organic Working Fluids in Rankine Engines. *Journal of Energy*, 5(4):218–223, 1981.

[2] G. Angelino, M. Gaia, and E. Macchi. A review of Italian activity in the field of organic Rankine cycles. In *VDI Berichte - Proceedings of the International VDI Seminar*, volume 539, pages 465–482, Düsseldorf, 10–12 September 1984. VDI Verlag.

[3] I. Obernberger, P. Thonhofer, and E. Reisenhofer. Description and evaluation of the new 1000 kW ORC process integrated in the biomass CHP plant in Lienz, Austria. *Euroheat and Power*, 10:1–17, 2002.

[4] J. J. Brasz and B. P. Biederman. Low temperature waste heat power recovery using refrigeration equipment. In *21st International Congress of Refrigeration 2003, Washington, DC, ICR0587*, 2003.

[5] H.P. Bloch and C. Soares. *Turboexpanders and Process Applications*. Gulf Professional Publishing, 2001.

[6] J. Hoffren, T. Talonpoika, J. Larjola, and T. Siikonen. Numerical simulation of real-gas flow in a supersonic turbine nozzle ring. *J. Eng. Gas Turb. Power*, 124(2):395–403, April 2002.

[7] J.P. van Buijtenen, J. Larjola, T. Turunen-Saaresti, J. Honkatukia, H. Esa, J. Backman, and A. Reunanen. Design and validation of a new high expansion ratio radial turbine for ORC applications. In *Proceedings of the 5th European Conference on Turbomachinery*, pages 1–14, 2003.

[8] R.D. Goodwin. Toluene thermophysical properties from 178 to 800 K at pressures to 1000 bar. *J. Phys. Chem. Ref. Data*, 18(4):1565–1636, 1989.

[9] J. Harinck, T. Turunen-Saaresti, and P. Colonna. Predictions of performance and flow fields of a high-expansion-ratio radial ORC turbine. Technical report ET-2262, Delft University of Technology, Process & Energy department, Leeghwaterstraat 44, 2628 CA Delft, The Netherlands, July 2007. (Confidential report).

[10] E.W. Lemmon and R. Span. Short fundamental equations of state for 20 industrial fluids. *J. Chem. Eng. Data*, 51(3):785–850, 2006.

[11] W. Bober and W. L. Chow. Nonideal Isentropic Gas Flow Through Converging-Diverging Nozzles. *J. Fluids Eng.*, 112:455–460, 1990.

[12] J. B. Anders, W. K. Anderson, and A. V. Murthy. Transonic Similarity Theory Applied to a Supercritical Airfoil in Heavy Gases. *J. Aircr.*, 36(6):957–964, November-December 1999.

[13] D. Drikakis and S. Tsangaris. Real gas effects for compressible nozzle flows. *J. Fluids Eng.*, 115:115–120, 1993.

[14] B. Wagner and W. Schmidt. Theoretical Investigation of Real Gas Effects in Cryogenic Wind Tunnels. *AIAA J.*, 16(6):580–586, 1978.

[15] W. K. Anderson. Numerical Study of the Aerodynamic Effects of Using Sulfur Hexafluoride as a Test Gas in Wind Tunnels. Technical Paper 3086, NASA, NASA Langley Research Center, Hampton, VA, May 1991.

[16] P. Colonna and S. Rebay. Numerical simulation of dense gas flows on unstructured grids with an implicit high resolution upwind Euler solver. *Int. J. Num. Meth. Fluids*, 46:735–765, 2004.

[17] P. Cinnella and P. Congedo. A numerical solver for dense gas flows. In *34th AIAA Fluid Dynamics Conference and Exhibit*, number AIAA 2004-2137, pages 1–12. AIAA, June-July 2004.

[18] P. Cinnella and P.M. Congedo. Inviscid and viscous aerodynamics of dense gases. *Journal of Fluid Mechanics*, 580:179–217, 2007.

[19] C. Cravero and A Satta. A CFD model for real gas flows. In *Proceedings of ASME Turbo Expo*, number 2000-GT-518, pages 1–10, New York, NY, May 2000. ASME.

[20] P. Boncinelli, F. Rubechini, A. Arnone, M. Cecconi, and C. Cortese. Real gas effects in turbomachinery flows - A Computational Fluid Dynamics model for fast computations. *J. Turbomach.*, 126:268–276, April 2004.

[21] M. Cirri, P. Adami, and F. Martelli. Development of a CFD Real Gas Flow Solver for Hybrid Grid. *Int. J. Numer. Methods Fluids*, 47(8-9):931–938, March 2005.

[22] J. Patek. Functional forms to describe thermodynamic properties of gases for fast calculations. *ASME Journal of Engineering for Gas Turbine and Power*, 118:210–213, 1996.

[23] T. Turunen-Saaresti, J. Tang, and J Larjola. A practical real gas model in CFD. In P. Wesseling, E. Onate, and J. Périau, editors, *European Conference on Computational Fluid Dynamics (ECCOMAS CFD 2006)*, Egmond aan Zee, The Netherlands, September 2006.

[24] J.D. van der Waals. *On the continuity of the gas and liquid state*. PhD thesis, University of Leiden, 1873.

[25] A. C. Aldo and B. M. Argrow. Dense Gas Flows in Minimum Length Nozzles. *J. Fluids Eng.*, 117:270–276, 1994.

[26] D. Y. Peng and D. B. Robinson. A new two-constant equation of state. *Ind. Eng. Chem. Fundam.*, 15:59–64, 1976.

[27] R. Stryjek and J. H. Vera. PRSV: An improved Peng-Robinson equation of state for pure compounds and mixtures. *Can. J. Chem. Eng.*, 64:323–333, 1986.

[28] H.D. Kim, J.H. Lee, K.A. Park, T. Setoguchi, and S. Matsuo. A study of the critical nozzle for flow rate measurement of high-pressure hydrogen gas. *Journal of Thermal Science*, 16(1):28–32, March 2007.

[29] R. Span. *Multiparameter Equations of State - An Accurate Source of Thermodynamic Property Data*. Springer-Verlag, Berlin, 2000.

[30] R. Span, W. Wagner, E. W. Lemmon, and R. T. Jacbosen. Multiparameter equations of state - recent trends and future challenges. *Fluid Phase Equilib.*, 183–184:1–20, 2001.

[31] W. Wagner and A. Pruss. The IAPWS Formulation 1995 for the Thermodynamic Properties of Ordinary Water Substance for General and Scientific Use. *J. Phys. Chem. Ref. Data*, 31(2):387–535, 2002.

[32] P. Colonna and P. Silva. Dense gas thermodynamic properties of single and multicomponent fluids for fluid dynamics simulations. *ASME J. Fluids Eng.*, 125:414–427, 2003.

[33] P. Colonna, A. Guardone, J. Harinck, and S. Rebay. Numerical investigation of dense gas effects in turbine cascades. In *15th U.S. National Congress on Theoretical and Applied Mechanics Conference, Boulder, CO*, 2006.

[34] P. Colonna, S. Rebay, J. Harinck, and A. Guardone. Real-gas effects in ORC turbine flow simulations: influence of thermodynamic models on flow fields and performance parameters. In *ECCOMAS CFD 2006 Conference, Egmond aan Zee, NL*, 2006.

[35] P. Colonna, J. Harinck, S. Rebay, and A. Guardone. Real-gas effects in organic rankine cycle turbine nozzles. *AIAA Journal of Propulsion and Power*, 24(2):282–294, 2008.

[36] P. Colonna and T. Van der Stelt. Fluidprop: A program for the estimation of thermophysical properties of fluids. Energy Technology section, Delft University of Technology, The Netherlands (www.fluidprop.com)., 2005.

[37] V. Selmin. The node-centered finite volume approach: bridge between finite differences and finite elements. *Computer Methods in Applied Mechanics and Engineering*, 102(1):107–138, 1993.

[38] P. L. Roe. Approximate Riemann solvers, parameter vectors, and difference schemes. *Journal of Computational Physics*, 43(2):357–372, 1981.

[39] M. Vinokur and J. L. Montagné. Generalized Flux-Vector Splitting and Roe Average for an Equilibrium Real Gas. *Journal of Computational Physics*, 89(2):276–300, 1990.

[40] E. W. Lemmon, M. O. McLinden, and M. L. Huber. REFPROP - REFerence fluid PROPerties. software, ©NIST 2002.

[41] W. C. Reynolds. *Thermodynamic properties in S.I.* Department of Mechanical Engineering - Stanford University, Stanford, CA, 1979.

[42] J. J. Martin and Y. C. Hou. Development of an equation of state for gases. *AIChE J.*, 1(2):142–151, June 1955.

[43] R. Span and W. Wagner. Equations of state for technical applications. II. Results for nonpolar fluids. *Int. J. Thermophys.*, 24(1):41–109, January 2003.

[44] R. Span and W. Wagner. Equations of state for technical applications. I. Simultaneously optimized functional forms for nonpolar and polar fluids. *Int. J. Thermophys.*, 24(1):1–39, January 2003.

[45] K. E. Starling. *Equation of state and computer prediction - Fluid Thermodynamic PropertiesforLightPetroleum Substances*. Gulf Publishing Co., Huston, TX, 1973.

[46] D. S. H. Wong and S. I. Sandler.   A theoretically correct mixing rule for cubic equations of state. *AIChE J.*, 38:671–680, 1992.

[47] D. S. H. Wong, S. I. Sandler, and H. Orbey.   Equation of state mixing rule for nonideal mixtures using available activity coefficient model parameters and that allows extrapolation over large ranges of temperature and pressure. *Ind. Eng. Chem. Res.*, 31:2033–2039, 1992.

[48] G. Angelino and P. Colonna.   Multicomponent working fluids for Organic Rankine Cycles (ORCs). *Energy*, 23(6):449–463, 1998.

[49] B. E. Poling, J. M. Prausnitz, and J. P. O'Connell. *The Properties of Gases and Liquids*.   Chemical Engineering Series. McGraw-Hill, New York, 5th edition, 2001.

[50] T. Arts, M. Lambert de Rouvroit, and A. W. Rutherford.   Aero-thermal investigation of a highly loaded transonic linear turbine guide vane cascade. Technical Note 174, Von Karman Institute for Fluid Dynamics, September 1990.

[51] S.G. Penoncello E.W. Lemmon, R.T. Jacobsen and D.G. Friend.   Thermodynamic properties of air and mixtures of nitrogen, argon, and oxygen from 60 to 2000 K at pressures to 2000 MPa. *J. Phys. Chem. Ref. Data*, 29(3):331–385, 2000.

[52] A Guardone and S Rebay.   Unstructured periodic grid generation.   In *Proceedings of the ECCOMAS CFD 2006 Conference*, Egmond aan Zee, The Netherlands, 2006.

[53] S. Rebay.   Efficient Unstructured Mesh Generation by Means of Delaunay Triangulation and Bowyer–Watson Algorithm. *Journal of Computational Physics*, 106(1):125–138, 1993.

[54] J. D. Northall.   The influence of variable gas properties on turbomachinery computational fluid dynamics. *Journal of Turbomachinery*, 128:632, 2006.

[55] F. Rubechini, M. Marconcini, A. Arnone, M. Maritano, and S. Cecchi.   The impact of gas modeling in the numerical analysis of a multistage gasturbine. In *ASME Turbo Expo 2006: Power for Land, Sea & Air, Barcelona, Spain, 8-11 May, ASME paper GT 2006-90129*, 2006.

[56] M. M. Abbott.   Cubic Equations of State. *AIChE J.*, 19:596–601, 1973.

[57] P. Colonna and A. Guardone. Molecular interpretation of nonclassical gas-dynamics of dense vapors under the van der waals model. *Phys. Fluids*, 18(5):056101–1–14, 2006.

[58] J. F. Monaco, M. S. Cramer, and L. T. Watson. Supersonic flows of dense gases in cascade configurations. *J. Fluid Mech.*, 330:31–59, 1997.

[59] B. P. Brown and B. M. Argrow. Application of Bethe-Zel'dovich-Thompson fluids in organic Rankine cycle engines. *J. Propul. Power*, 16(6):1118–1123, November-December 2000.

[60] P. Colonna, N.R. Nannan, A. Guardone, and T. P. Stelt van der. On the computation of the fundamental derivative of gas dynamics Gamma, using equations of state. *Fluid Phase Equilibria*, 2009. (accepted for publication).

[61] R.H. Aungier. *Turbine Aerodynamics: Axial-flow and radial-inflow turbine design and analysis*. ASME Press, New York, 2006.

Part II

Applications

The second part of this thesis is concerned with applications of supercritical and dense gas flows. It presents two studies that detail how dense-gas effects are manifested in turbomachinery flows of next-generation energy convertors and points out implications for their fluid dynamic performance and design. This work is supplemented with two chapters that document preliminary results of additional work. The first addition is directed towards the flow simulation of supercritical free-jets and the second documents the development and application of the optimization system for unconventional dense-gas fluid dynamic designs.

Chapter 4 investigates dense-gas effects occurring in stator nozzles of subcritical and supercritical Organic Rankine Cycles (ORCs). In particular supercritical ORCs offer a potential efficiency increase that has not yet been exploited in current practice. Two-dimensional Euler simulations of an existing axial ORC stator nozzle are carried out using a CFD code, which is linked to an accurate thermodynamic model for the working fluid (siloxane MDM). The implications of dense-gas and supercritical expansions for the geometrical design of supercritical stator nozzles are discussed, as well as the peculiar characteristics such as low sound speed and velocity, high density and mass flow rate.

Chapter 5 presents a numerical study of the flow field through the stator of an existing radial ORC turbine operating with toluene at a very high expansion ratio. The analysis takes into consideration the influence on the simulated flow field of three numerical flow solvers, two fluid thermodynamic models and two well-known turbulence models.

Chapter 6 introduces the flow structure of supersonic free-jets, followed by the validation of the inviscid zFLOW code for the supersonic free-jet fluid dynamic case. This work serves as the first step towards the simulation and validation of zFLOW for highly underexpanded free jets generated by the expansion of supercritical fluids for the purpose of particle production processes.

Chapter 7 documents the development and preliminary results of the application of the optimization system unconventional dense-gas fluid dynamic designs such as BZT nozzles, ORC stator nozzles and turbomachinery components of next-generation energy converters in general. The expansion and compression processes of these cycles involve unconventional fluid dynamics due to dense-gas effects and possibly nonclassical gasdynamic phenomena in case of BZT fluids. This demands unconventional nozzle shapes, the optimal design of which would

benefit considerably from automated optimization systems based on advanced algorithms, such as the one developed and documented in this chapter.

4

Real-Gas Effects in Organic Rankine Cycle Turbine Nozzles

Abstract   *Organic Rankine Cycle (ORC) turbogenerators are a viable option as stationary energy converters for external heat sources, in the low power range (from few kW up to few MW). The fluid dynamic design of ORC turbines can benefit from CFD tools which are capable of properly taking into account real-gas effects occurring in the turbine, which typically expands in the nonideal-gas thermodynamic region. In addition, the potential efficiency increase offered by supercritical ORCs, which entails even stronger real-gas effects, has not yet been exploited in current practice. In this study real-gas effects occurring in subcritical and supercritical ORC nozzles have been investigated. Two-dimensional Euler simulations of an existing axial ORC stator nozzle are carried out using a CFD code, which is linked to an accurate thermodynamic model for the working fluid (siloxane MDM). The cases analyzed include the expansions starting from actual subcritical conditions, i.e., the design-point and part-load operation, and three expansions starting from supercritical conditions. Results of the simulations of the existing nozzle for current operating conditions can be used to refine its design. Moreover the simulations of the nozzle expansions starting from supercritical conditions show that a nozzle geometry with a much higher exit-to-throat area ratio is required in order to obtain an efficient expansion. Other peculiar characteristics of supercritical expansions such as low sound speed and velocity, high density and mass flow rate, are discussed.*

4.1   Introduction

Organic Rankine Cycle (ORC) turbogenerators are a viable option as stationary energy converters for external heat sources, in the low power range (from few kW up to few MW). The working principle of an ORC turbogenerator is the same as for a conventional steam power plants, except for the working fluid, which is formed by organic molecules. The choice of the fluid allows for the optimal design of the turbine, depending on the temperature of the heat source and the power range [1, 2, 3]. Steam turbines in the low power range cannot reach the same level of efficiency of ORC turbines with the same level of technology. The optimal design of a steam turbine for such a low power range requires many stages, small blade dimensions and very high rotational speeds, which in turn may lead to severe efficiency problems if the flow becomes locally supersonic and shocks may occur in the flow field. On the contrary, a turbine operated with an organic fluid can reach very high isentropic efficiency with just one or two stages rotating at much lower speed. In some cases the turbine can be directly coupled to the electrical generator (3000 rpm). Other advantages with respect to steam cycle turbines

include [4, 5, 6]:

- fully dry expansion: superheating can be avoided and there is no efficiency loss associated with condensation in the last stage of the turbine.

- Moderate maximum pressure: requirements on materials are far less stringent.

- Possibly higher pressure in the condenser: depending on the fluid, the condenser can be super-atmospheric therefore avoiding the need for a dearator.

- In some cases the working fluid can also be used as a lubricant for the turbine shaft bearings.

- Overall very high reliability; the plants are usually fully automated and can sustain unattended operation.

The main thermodynamic restriction affecting ORC technology is the limit on the maximum cycle temperature, which is bound by the thermal stability of the fluid in combination with the containing material. However, in this power range techno-economic constraints would limit the maximum temperature of steam cycles to a level comparable to the thermal stability of ORC working fluids in stainless steel, i.e., between 300 and 400 °C.

ORC turbogenerators with an installed power adding up to $\sim 1,000$ MW$_e$ are employed to convert low grade geothermal heat into electricity and so called low-temperature ORC technology can be considered mature [7, 8, 9]. Recent projections indicate that the potential for the application of such a technology is globally $\sim 60,000$ MW$_e$ [10]. The working fluids for these applications are usually hydrocarbons of the alkanes class and refrigerants like R134a or R245fa. Heat source temperatures range from less than 100°C up to 150°C (pressurized geothermal water).

More recently, ORC turbogenerators are rapidly spreading as energy converters for biomass fuels, most often in combined-heat-and-power (CHP) applications [11, 12]. Transportation costs for biomass dictate a small design power output, if the aim is the conversion of its calorific content into electricity. Presently, ORC technology is possibly the best option in the small power range. The working fluids currently adopted for high-temperature ORC plants are the light members of the siloxanes class and toluene. The maximum cycle temperature ranges from approximately 260°C up to more than 300°C.

It can be noted that the mentioned applications of ORC technology can all be classified as sustainable, and this technology is also very promising for the

conversion into electricity of other fully sustainable energy source, like solar radiation [13] and waste heat recovery from industrial processes, other engines and, in the future, high temperature fuel cells [14, 15]. ORCs coupled with solar concentrators were considered in the past as a viable option to power the international space station [16, 17, 18, 19, 20, 21], and also, coupled with a nuclear isotope heat source [22, 23], for deep-space missions.

The process flow diagram of an ORC is depicted in Fig. 4.1. The corresponding thermodynamic cycle is represented in the T-s plane in Fig. 4.2(a): in this exemplary case of a high-temperature ORC, the working fluid is Octamethyltrisiloxane (MDM, $Si_4O_3C_8H_{24}$), which also corresponds to the fluid chosen for the analyses presented in this study.

The motivation for this study stems from two considerations. Firstly, the fluid-dynamic design of ORC turbines has possibly reached a far lower level of sophistication, if compared to gas or steam turbines. One of the reasons is the lack of CFD tools capable of properly taking into account real-gas effects in the computation of thermodynamic properties, a necessary feature for the accurate design of ORC blade passages. Secondly, a considerable improvement in efficiency could be reached by resorting to supercritical cycle configurations [5, 17, 4, 14]. This option is still widely unexplored and all existing applications employ either the saturated or the slightly superheated cycle configuration. Reaching supercritical operating conditions in an ORC presents far lower technological challenges, if compared to steam power plants because pressures would be one order of magnitude smaller and temperatures would still be considered mild. Among the research needs which must be addressed, the fluid dynamic design of unconventional supercritical turbines demands for CFD tools capable of simulating flows occurring in a highly nonideal thermodynamic region. This work represents a first step in this direction.

The numerical simulation of compressible flows occurring in a thermodynamic region characterized by strong deviations from the so called ideal-gas behavior is a research field which is possibly still in its infancy, see, e.g., Ref. [24]. A quite comprehensive review can be found, e.g., in Ref. [25], where the CFD software tool adopted in this study is also described and validated. To the knowledge of the authors the only other reference that, like this work, presents fluid-dynamic simulations of an ORC turbine stator concerns a centrifugal ORC turbine employing toluene as the working fluid [26].

This work takes as exemplary starting point the geometry of an existing ORC nozzle designed for a 300 kW_e CHP axial turbogenerator employing siloxane MDM as working fluid and the combustion of biomass as primary energy source.

A brief overview regarding the thermodynamic efficiency of supercritical ORC cycles is presented in the following section. Here also some technical aspects are shortly addressed. The recently developed thermodynamic model of the working fluid is summarized in Section 4.3. Section 4.4 contains a quasi-one-dimensional analysis of supersonic expansions through converging-diverging nozzles, which can be used as the basis for setting appropriate boundary conditions for the design of multidimensional turbine blades. The core of this work is formed by the fluid flow simulations and their analysis shown in Section 4.5. Several cases are examined: the base case is the simulation of the flow occurring for design operating parameters. The usefulness of the software tool is demonstrated further by the analysis of the flow for part-load operation. Finally the flow through the same geometry is simulated for three operating conditions featuring the inflow at supercritical conditions. The analysis of the results can be used as a starting point for the design of such unconventional turbines. The concluding section summarizes the main issues and outlines future lines of investigation.

4.2   Supercritical Cycle Configurations

To quantify the possible efficiency increase of supercritical ORCs, a brief thermodynamic analysis of the influence of the maximum cycle pressure on the cycle performance is presented. The operating parameters for the base case, given in Table 4.1, are typical of an existing biomass fueled plant, cogenerating warm water for process purposes. The cycle process is represented in Fig. 4.2(a). It is a superheated cycle in which the amount of superheating has been increased ($T_{max} = 305$ °C) with respect to the current design ($T_{max} = 270.5$ °C), so that the maximum temperature can be kept fixed. This allows for a parametric study of the influence of the maximum pressure solely. Such a maximum temperature is still within the thermal stability limit of the fluid [17, 3] and it could be reached if, for instance, the current practice of adopting an intermediate thermal oil loop were abandoned in favor of higher efficiency.

The calculations are carried out with Cycle Tempo [27], an extensively tested software package for the design and analysis of energy conversion systems. The same thermodynamic library [28] that is linked to the CFD code employed in this study is also linked to this steady-state system simulation software. The thermodynamic model for the working fluid MDM contained in the library is described in Section 4.3. Typical design values were used as input data for the isentropic efficiencies of the turbine and the pump, and for the pinch-points of the heat exchangers. The operating conditions of the cycle and the assumed component effi-

ciencies are listed in Table 4.1. The given condensation temperature is typical of cogeneration applications. The maximum temperature is limited by the thermal stability of the fluid, taking into account a certain safety margin. Subsequently, the maximum cycle pressure is increased, keeping constant all conditions mentioned in Table 4.1. In Fig. 4.2(a) both the superheated and a supercritical (SC) thermo-dynamic cycle (with a turbine inlet total pressure of $P_A = 18$ bar) are depicted in a T-s diagram.

Table 4.1: *Possible ORC design-point operating conditions for cogeneration of electricity and warm water. The working fluid is siloxane MDM.*

Working fluid		MDM
Power output	P_e, kW	300
Turbine inlet total pressure	P_A, bar	8
Turbine inlet total temperature	T_A, °C	305
Pressure ratio	P_A/P_B	36
Condensation pressure	P_D, bar	0.22
Condensation temperature	T_D, °C	103
Regenerator pressure loss	ΔP_{regen}, bar	0.1
Flue gas inlet temperature	T_G, °C	350
Flue gas mass flow rate	$\dot{m}_G$, kg/s	12.5
Primary heat exchanger pinch-point	$\Delta T_{pinch,PHE}$, °C	15
Regenerator pinch-point	$\Delta T_{pinch,regen}$, °C	10
Cooling water temperature inlet	T_I, °C	60
Cooling water temperature outlet	T_K, °C	90
Turbine isentropic efficiency	$\eta_{is,t}$	0.87
Pump isentropic efficiency	$\eta_{is,p}$	0.65
Electric generator efficiency	η_{gen}	0.98

The first-law total cycle efficiency, defined as the ratio of the net delivered mechanical power and the heat added to the cycle in the primary heat exchanger together with the electrical power output, are plotted as a function of the maximum cycle pressure, i.e., the turbine inlet total pressure, in Fig. 4.2(b). Fig. 4.2(b) shows that the cycle efficiency increases with pressure and has a maximum for slightly supercritical conditions. The power output increases steadily with the maximum cycle pressure, the only limiting factor being avoiding condensation throughout the expansion.
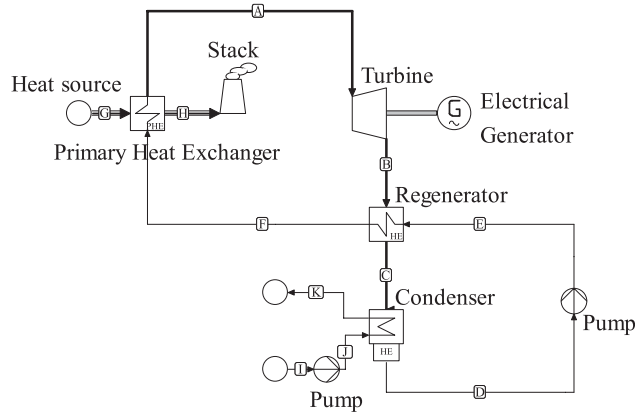
Figure 4.1: *Process flow diagram of an Organic Rankine Cycle Turbogenerator.*

(a)

(b)
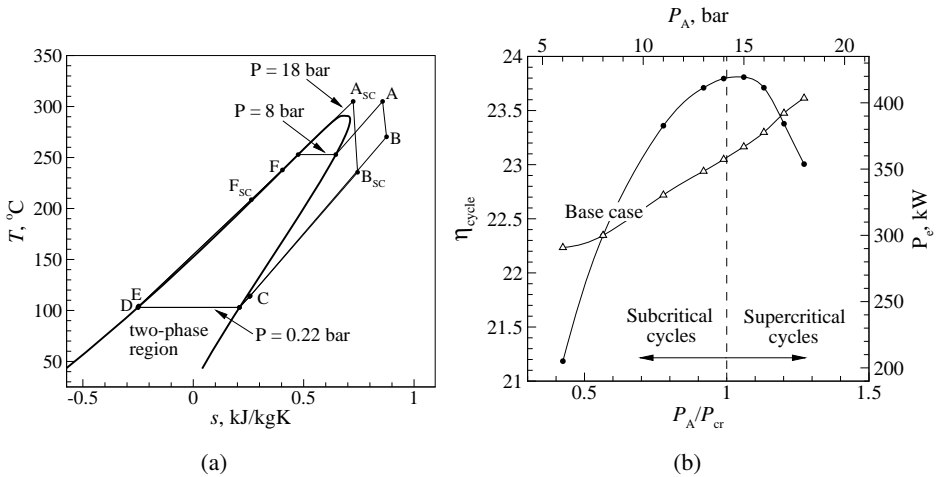
Figure 4.2: *a) Superheated and supercritical (SC) ORC in the temperature-entropy diagram of siloxane MDM. b) Cycle efficiency ($\bullet$) and electric power output ($\triangle$) as function of turbine inlet pressure. All other design parameters except the maximum cycle pressure and power output are kept fixed and their values are listed in Table 4.1.*

As a consequence of the improved heat source utilization, a larger primary heat exchanger is required in case of a supercritical ORC. The regenerated heat decreases only marginally, so that the required regenerator size remains approxi-

mately the same. Turbine expansion ratio increases and, as apparent from Fig. 4.2(a), the temperature drop over the turbine also becomes larger, indicating a correspondingly larger enthalpy drop, which may necessitate a multi-stage turbine and thus higher investment cost. The increase in pressure means a much higher pump power consumption, therefore pump efficiency and investment cost become more important cost-determining factors. Apart from the design of turbines expanding from supercritical inlet conditions, other areas of research demand include supercritical heat exchangers and possibly new control strategies.

4.3   The Thermodynamic Model

The working medium of the ORC in this study, the siloxane MDM (Octamethyltrisiloxane), has a high molecular weight of $M = 236.53$ g/mol. Its critical pressure and temperature are $P_{cr} = 14.2$ bar and $T_{cr} = 290.9°C$, respectively [29]. A part of the processes in the cycle simulations and flow simulations presented in this study occur at close-to-critical or supercritical conditions and are therefore thermodynamically highly nonideal. For this reason, all thermodynamic property evaluations are based on a state-of-the-art multi-parameter functional form for equations of state (MPEoS) developed by Span and Wagner [30]. This MPEoS allows for accurate computations of all relevant thermodynamic properties over the entire thermodynamic range (even close to the critical point) with the accuracy required for design and analysis of advanced technical applications. The Span-Wagner (SW) EoS has superior accuracy and numerical stability compared with older MPEoSs [30].

Recently, work has been done on the development of 12-parameter SW-type EoSs for selected siloxanes [31, 32]. Parameters for a SW-type EoS were also recently optimized for siloxane MDM, the working medium of the ORC in this study [33]. Details about the functional forms and features of the equation of state applied to siloxanes can be found in [31]. A comparison of the predictions of this MPEoS with experimental data, given in Table 4.2, shows very good agreement. Further details are provided in a manuscript that is submitted for publication.

For the calculation of all caloric properties, the SW EoS is supplemented by the ideal gas contribution to the specific heat at constant pressure, which has been approximated here as a polynomial function of the temperature:

$$C_P^0(T) = A + BT + CT^2 + DT^3. \tag{4.1}$$

The polynomial coefficients for selected siloxanes have been first reported in a work describing the thermodynamic optimization of ORCs [40] and these

Table 4.2: *Performance of the Span-Wagner EoS regarding the prediction of experimental thermodynamic data of MDM. The performance is assessed by means of the average percentage deviation (DEV) of experimental data with respect to computed values; adapted from [33].*

Property	Source	P-range, bar	T-range, K	DEV, %
Saturated liquid density, ρ^L	[34]	–	426–564	0.56
	[35]	–	273–333	0.12
Saturated vapor density, ρ^V	[34]	–	460–564	0.84
Vapor-pressure, P^{sat}	[36]	–	346–436	0.46
	[34]	–	322–564	0.66
	[37]	–	344–418	9.67
P-ρ-T data in superheated vapor region	[38]	0.36–3.77	448-573	0.60
P-ρ-T data in subcooled liquid region	[39]	1.01325	300–412	0.00

parameters were recently refined by means of experimental measurements and ab-initio molecular simulations [32].

4.4 Quasi-One-Dimensional Isentropic Flow Analysis for Subcritical and Supercritical Inlet Pressures

In this section, the effect of an increase in the inlet total pressure on the isentropic expansion process in the ORC turbine is investigated by considering quasi-one-dimensional isentropic flow in a converging-diverging nozzle. As is well-known, the isentropic transformation based on the ideal gas law states that the Mach number is dependent only on the ratio of static exit-to-total inlet pressure and on the ratio of specific heats. However, in the case of an ORC expansion, typically occurring in the dense gas region, the ideal gas law is not valid. This is even more so for expansions that occur at close-to-critical and supercritical pressures. For this reason, the analysis is based on the accurate SW EoS (Eq. 1) that was discussed in the previous section.

The isentropic gas flow through a nozzle of variable cross sectional area $A = A(x)$ can be computed by means of the mass and energy conservation equations,

which, for an arbitrary section x of the duct, can be written as

$$(\rho u A)_x = \text{const} \qquad \left(h + \frac{1}{2}u^2\right)_x = h_{0x} = \text{const.}$$

These equations are here used to show that the exit-to-throat area ratio $A_r = A_2/A_t$ is a function of the pressure ratio $P_r = P_{01}/P_2$, the inlet total pressure P_{01}, and the entropy s. Notice that, as is well known, in the ideal gas case A_r is instead function of P_r only, and is given by

$$A_r = P_r^{\frac{1}{\gamma}}\left[\frac{2}{\gamma-1}\left(\frac{\gamma+1}{2}\right)^{\frac{\gamma+1}{\gamma-1}}\left(1 - P_r^{\frac{1-\gamma}{\gamma}}\right)\right]^{-\frac{1}{2}},$$

where $\gamma = C_P/C_v$ is the ratio of heat capacities at constant pressure and volume.

For convenience, in the following all the thermodynamic quantities are regarded as functions of pressure and entropy, i.e.,

$$\rho = \rho(P, s), \qquad c^2(P, s) = \left(\frac{\partial P}{\partial \rho}\right)_s, \qquad h = h(P, s),$$

where the entropy s is considered as a constant prescribed parameter.

By virtue of the mass conservation equation, the area ratio A_r can be written as a ratio of momentum at the throat and at the exit of the nozzle, i.e., as

$$A_r = \frac{A_2}{A_t} = \frac{\rho_t c_t}{\rho_2 u_2}. \tag{4.2}$$

In order to compute ρ_t and c_t, the pressure P_t at the throat is needed. By solving the energy equation written at the throat

$$h(P_{01}, s) = h(P_{0t}, s) = h(P_t, s) + \frac{1}{2}c^2(P_t, s)$$

for the unkown pressure P_t, we can compute $P_t = P_t(P_{01}, s)$. The momentum at the throat $(\rho c)_t$ is then given by

$$\rho(P_t, s)c(P_t, s), \qquad P_t = P_t(P_{01}, s) \tag{4.3}$$

and is therefore a function of P_{01} and s only. The exit momentum is finally given by

$$(\rho u)_2 = \rho\left(\frac{P_{01}}{P_r}, s\right)\sqrt{2\left[h(P_{01}, s) - h\left(\frac{P_{01}}{P_r}, s\right)\right]}, \tag{4.4}$$

and is therefore a function of P_r, P_{01} and s. Because of Eq. (4.2), (4.3), (4.4), the area ratio A_r is also a function of P_r, P_{01} and s, say

$$A_r = f(P_r, P_{01}, s).$$

The above equation can be iteratively used to obtain the inverse relation

$$P_r = g(A_r, P_{01}, s). \tag{4.5}$$

All thermodynamic properties are evaluated for entropy $s_{SC1} = s(P, T) = s(18$ bar, 304.6 °C), using the accurate EoS for MDM [33]. This entropy value is representative for both subcritical and supercritical turbine inlet conditions. The value of the entropy is chosen high enough to avoid condensation during expansion, and representative of typical ORC turbine expansions. The entropy is kept fixed by increasing the inlet total temperature for the higher inlet total pressures. Evaluating Eq. (4.5) for exit-to-throat area ratios $A_r = [1, 2, ..., 10]$, for a range of inlet total pressures $4 \le P_{01} \le 34$ bar and $s = s_{SC1}$, produces the pressure ratio required for a correctly expanded nozzle as function of inlet total pressure in the real-gas thermodynamic region of MDM along the specified isentrope. The relation plotted in Fig. 3(a) shows that in the nonideal thermodynamic region, as inlet total pressure is increased, for a particular nozzle (with fixed exit-to-throat area ratio), the pressure ratio must be decreased in order to obtain a correct expansion.

As noticed before, the isentropic transformation based on the ideal gas law states that the design P_r for a given value of A_r is independent of P_{01}, whereas in the nonideal case P_r decreases as P_{01} is increased. This means that for the same inlet total pressure, the ideal gas case exit pressure $P_{2,id}$ is lower than the real exit pressure $P_{2,re}$. If a nozzle operating in nonideal conditions is designed according to the ideal gas model, that is, if the back pressure is set to $P_{2,id}$, then additional expansion has to occur at the exit of the nozzle to further expand the gas from the actual exit pressure $P_{2,re}$ to the lower $P_{2,id}$. In this case the flow would be underexpanded, and a free-jet would be formed downstream the nozzle, accompanied by strong shock waves which would significantly deteriorate the turbine performance, as shown by the numerical results presented in the next section.

4.5 Real-Gas Effects in an ORC Stator Blade Passage

The zFLOW program [25] is employed to demonstrate the effect of inlet total pressure on the two-dimensional flow field of a real-gas expansion process that typically occurs in ORC nozzles. To this purpose, an existing nozzle geometry has
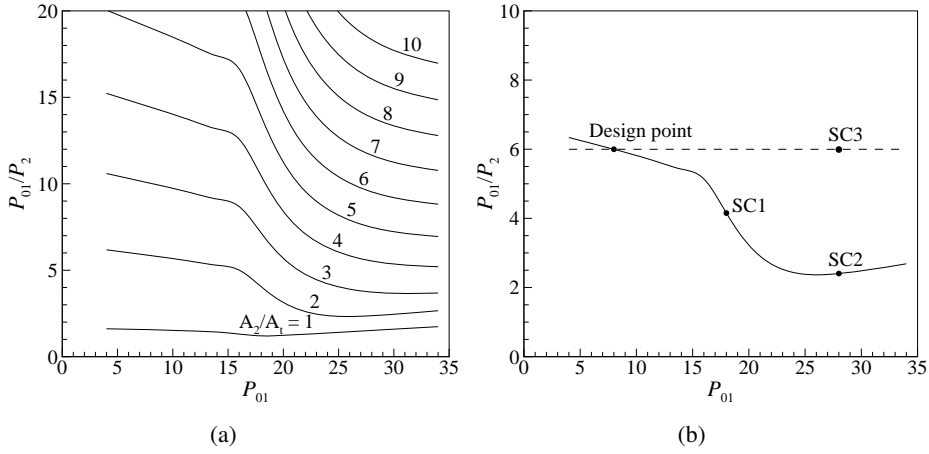
Figure 4.3: *a) Relation between inlet total pressure and pressure ratio for correctly expanded nozzles in the real-gas thermodynamic region of MDM along isentrope $s = s(P,T) = s(8\ bar, 270.5\ °C)$. Lines denote nozzles that have different exit-to-throat area ratio A_2/A_t. b) Same relation for a correctly expanded nozzle with an exit-to-throat area ratio of $A_2/A_t = 2.04$, which is equal to the stator passage of this study (see Fig. 4.6(a)).*

been adopted, even if it has been designed for subcritical inlet conditions for which real-gas effects are mild [41]. The objective is therefore to show that a blade shape specifically designed for supercritical conditions would considerably improve the performance of the stator.

4.5.1 The Euler Solver

Numerical solutions of the two-dimensional Euler equations are computed with the ZFLOW program [25], linked to the mentioned fluid property library containing several thermodynamic models and a large set of fluid data, including those for the MDM working fluid [28]. All derivatives of thermodynamic properties required by ZFLOW are computed analytically [42]. The main features characterizing the CFD code ZFLOW are briefly summarized. The solver is a hybrid between the Finite Element (FE) and Finite Volume (FV) methods in which the finite volume metric quantities are formulated on the basis of the lagrangian polynomial shape functions typically used in finite element methods [43]. The spatial approximation of the Euler equations is constructed with a high resolution finite volume method suitable for general unstructured and hybrid grids. The high resolution up-

wind discretization is constructed on the basis of the Roe approximate Riemann solver [44], generalized to the case of fluids characterized by arbitrary equations of state according to the method of Vinokur and Montagné [45]. This class of discretization schemes is particularly well suited to the computation of high Mach number flows such as those occurring in an ORC turbine. The use of unstructured grids allows for the straightforward treatment of domains of arbitrarily complex geometry. Another important feature of ZFLOW is represented by the adopted implicit time integration scheme, which computes steady state solutions in a much more efficient way with respect to conventional explicit schemes [25]. The gain in computational efficiency is crucial when complex EoS are needed for an accurate flow simulation. The ZFLOW solver has already been successfully validated for ideal-gas simulations [25, 46]. To the knowledge of the authors no experimental data of organic flows in the so-called real-gas thermodynamic region are available. An experimental setup aimed at gasdynamic measurements of these type of flows is therefore planned. The extension of ZFLOW to the viscous Reynolds-Averaged Navier-Stokes (RANS) equations will be published soon.

4.5.2   Validation: Recovery of Ideal-Gas Results Around the VKI LS-89 Blade

Validation of the ZFLOW solver for dense-gas flows in turbine cascades is currently not possible due to the mentioned lack of experimental data. For the moment, the best alternative is to validate the ZFLOW code linked to the mentioned fluid property library containing the MPEoSs for a turbomachinery test case that describes several expansions occurring in the thermodynamic region where the ideal gas law would apply.

The results of simulations are thus compared to the measurements of two well-known and reliable turbomachinery test cases [47] for dry air at ideal-gas conditions. In both test cases, the geometry is the VKI LS-89 blade, which is a standard high pressure turbine nozzle guide vane, mounted in a linear cascade. The first test case (MUR-43) is at subsonic flow conditions ($Ma_{is} < 0.84$), the second test case (MUR-49) at transonic flow conditions ($Ma_{is} < 1.02$). The conditions are given in Table 4.3.

For the prediction of the thermodynamic properties of air a 19-parameter EoS is used [48].

The periodic grid is generated in a transformed domain, in which periodic boundaries are mapped into internal curves to simplify the task of obtaining periodic nodes [49]. In the transformed space the grid is generated by the front-advancing/Delaunay method [50] and then transformed back into the physical

Table 4.3: *Test case conditions, from [47].*

		MUR43	MUR49
Total inlet pressure	P_{01}, bar	1.435	1.608
Expansion ratio	P_{01}/P_2, -	1.587	1.938
Total inlet temperature	T_{01}, °C	146.85	146.85
Compressibility factor at inlet	Z_1, -	1	1
Static outlet pressure	P_2, bar	1.333	2
Isentropic Mach number at outlet	$Ma_{2,is}$, -	0.84	1.02

space of *XY*-coordinates by introducing a suitable cut. This translates into the saw-like edge of the periodic boundaries shown in Fig. 4.4.
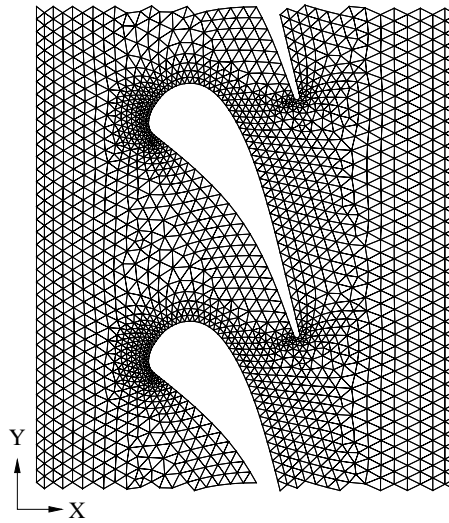
Figure 4.4: *Cascade of two stacked coarse grids.*

All flow solutions have converged up to at least a reduction of five orders of magnitude measured in the L^2-norm of the conserved variables. The numerical solution of the Mach number distribution along the blade surface is compared to the experimental data of the test cases.

To determine the discretization error level, a grid convergence study is per-
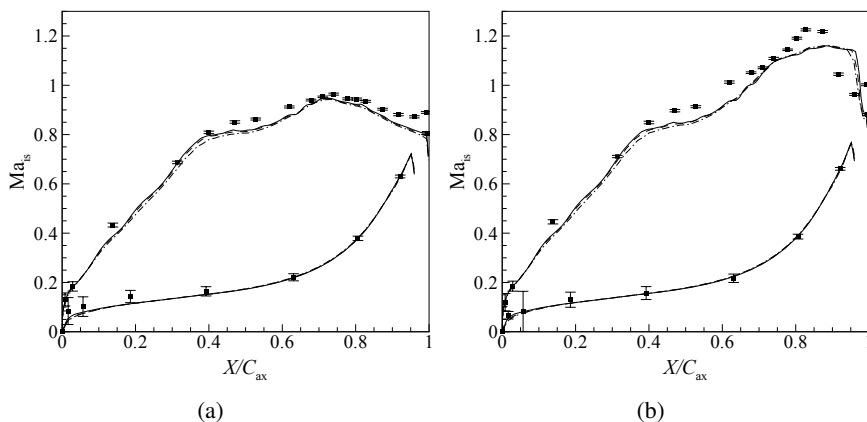
Figure 4.5: *Mach number distribution for the MUR43 test case (a) and the MUR49 test case (b). Shown are the experimental measurements (■) from [47] and the numerical solution on the coarse grid (– · – · –), the medium grid (– – –) and the fine grid (———).*

formed by computing the solution on three increasingly finer grids using the accurate MPEoS. The fine grid and the coarse grid are generated by, respectively, halving and doubling the number of grid elements with respect to the initial medium grid. The coarse grid consists of 1302 nodes and 2032 elements, the medium grid of 2383 nodes and 3958 elements and the fine grid of 4153 nodes and 7184 elements. Fig. 4.4 shows the coarse grid and the blade geometry. The lines in Fig. 4.5(a) and 4.5(b) show the Mach number distributions for the MUR43 and MUR49 test cases, respectively, solved on the coarse, medium and fine grid. They are plotted as a function of the coordinate reduced with the axial blade chord, X/C_{ax}. From the results, it appears that the solution computed using the fine grid is grid independent.

The zFLOW code is validated for this transonic fluid dynamic problem by comparing the numerical solution to the experimental data of the test case, given in Ref. [47]. The static pressure measurement data have an uncertainty of 0.5%, leading to uncertainties in the isentropic Mach number as indicated by the error bars in Fig. 4.5. The comparison pertaining to the subsonic test case MUR43, shown in Fig. 4.5(a), shows good agreement between numerical and experimental results. For the transonic test case MUR49, shown in Fig. 4.5(b), the agreement is good. The location of the shock wave that terminates the supersonic region is predicted by zFLOW at the end of the blade profile ($X/C_{ax} = 0.95$), whereas the

measurements indicate that the shock wave is further upstream ($X/C_{ax} = 0.88$). Still, the difference is small and the agreement is good enough.

4.5.3   ORC stator blade passage

The flow field through the two-dimensional axial stator nozzle of an existing ORC turbine operated with the siloxane MDM as working fluid is chosen as a practical example. Three cases are considered: the design point of the existing turbine stator, part-load operation and operation at supercritical pressures. The turbine operating conditions of each case, which are also the prescribed boundary conditions in the simulations (except for the compressibility factor), are given in Table 4.4. The expansions are given in the temperature-entropy diagram in Fig. 4.6(b). The inlet conditions of all flow simulations presented in this study lie on the same isentrope as indicated in the quasi-one-dimensional isentropic flow analysis of Section 4.4. The entropy is kept fixed by increasing the inlet total temperature for higher inlet total pressures.

The passage, as shown in Fig. 4.6(a), has been designed without the use of an accurate two-dimensional real-gas CFD simulation tool, as this was not available at the time of the design. Instead, its design is based on the contour of a 1-D nozzle. It is essentially the bottom part of a converging-diverging nozzle that has been curved in order to obtain the desired stator outflow angle. It should be noted that in the figures, the aspect ratio is distorted, because the turbine design is confidential property of the manufacturer. The throat area A_t and exit area A_2 in a turbine passage are defined as shown in Fig. 4.6(a). For the current passage, the exit-to-throat area ratio was determined to be $A_2/A_t = 2.04$, where the passage is assumed to be rectangular so that the area ratio equals the length ratio.

Table 4.4: *Turbine stator operating conditions for the the geometry of Fig. 4.6(a).*

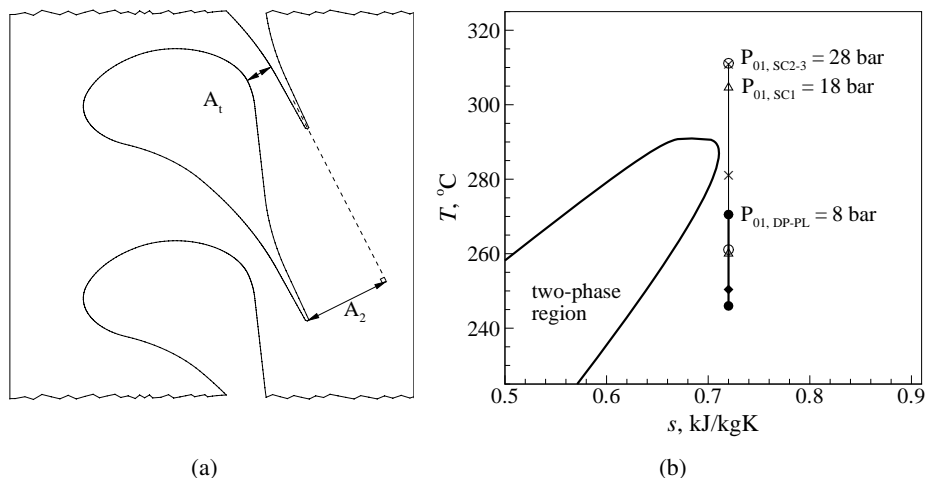|	Design point	Part load	SC1	SC2	SC3
P_{01}/P_2, -	6	4	4.15	2.40	6
P_{01}, bar	8	8	18	28	28
T_{01}, °C	270.5	270.5	304.6	311.1	311.1
Z_{01}, -	0.72	0.72	0.26	0.32	0.32
P_2, bar	1.33	2	4.33	11.65	4.67
Z_2, -	0.96	0.93	0.86	0.55	0.85

(a)   (b)

Figure 4.6: *a) Definition of throat area A_t and exit area A_2 in the turbine blade passage. This passage has an exit-to-throat area ratio of $A_2/A_t = 2.04$. The figure aspect ratio is deformed, since the blade design is confidential property of the manufacturer. b) Simulated expansions in the temperature-entropy diagram of MDM: Design point (● and thick line), Part load (◆), SC1 (△), SC2 (×), SC3 (○).*

The accurate multi-parameter EoS by Span and Wagner discussed in Section 4.3 is used as thermodynamic model. In practice, the polytropic ideal gas (PIG) law is often adopted for the design of turbines. In ORC nozzles, however, the fluid flow is in nonideal thermodynamic conditions, so that the PIG model is not fully justified. Under supercritical conditions, the associated errors are even larger. To demonstrate the relevance of this error in the calculation of the fluid-dynamic parameters, the fluid-dynamic simulations are also computed based on the PIG model. The PIG model is given by $P = RT/v$. The specific gas constant is defined as $R = \mathcal{R}/M$, where the universal gas constant is $\mathcal{R} = 8.314$ J/(molK). The other necessary information for the calculation of all caloric properties is the ideal gas specific heat at constant pressure which is $C_P^0 = \gamma R/(\gamma - 1)$. For the PIG model, a constant ratio of specific heats of $\gamma = 1.01733$ is adopted, which is calculated from the isobaric and isochoric ideal gas specific heats evaluated at the critical temperature, as this characteristic temperature is, in this case, close to the turbine inlet temperature (cf. Table 4.4). Evaluating the specific heat ratio at an intermediate temperature between the inlet and the outlet temperature does not alter the results, as the change in gamma is almost non-appreciable (from 1.01733

to 1.01795 at most).

The periodic computational grid is generated using the same procedure as described in Subsection 4.5.2. A grid convergence study was conducted to ensure that the solution was grid independent [41].

The "best practice" solution procedure involves starting from a uniformly distributed initial flow field. Starting from a flow field solution of a similar problem, if available, is preferred as it reduces the number of iterations. This strategy is even mandatory for the simulation of problems with high expansion ratios, which do not converge if started from a uniformly distributed initial flow field. An optimal convergence rate is obtained using the implicit backward Euler time-integration scheme, starting with a standard outflow boundary condition and a low CFL number for the initial 10 iterations in order to avoid computational blowup. Subsequently, the more realistic nonreflecting version of the outflow boundary condition is adopted [51] and, in order to allow for very large pseudo-time steps, the CFL number is automatically increased as the solution converges [25]. All flow solutions are converged up to at least six orders of magnitude measured in the L_2-norm of all the conserved variables.

It should be noted that the Euler solver used in this work permits to investigate the main inviscid features of the flow field through the stator passage, which are the focus of this investigation. Viscous phenomena such as boundary layers and a turbulent wake, which are present in the real flow field, can not be taken into account yet.

4.5.4 Design-Point Simulation

The stator blade passage has been designed both in terms of expansion ratio and two-dimensional shape for the design-point operating conditions as reported in Table 4.4.

The compressibility factor, defined as $Z = Pv/RT$, is identically equal to unity for an ideal gas; it is therefore often used to quantify the nonideality of the thermodynamic state. As indicated by the values of the compressibility factor at the inlet and the outlet of the nozzle given in Table 4.4, only a limited portion of the expansion through this turbine stator passage occurs in the nonideal gas thermodynamic region. This might be due to the fact that a lack of real-gas CFD simulation tools such as ZFLOW has limited the design of ORC turbines operating at thermodynamic conditions that deviate further from ideality, even if they might be more thermodynamically favorable.

Fig. 4.7(a) shows the computed flow field based on the accurate SW EoS visualized by equidistant iso-Mach lines and streamlines. From the inflow boundary

on the left hand side of the domain, the fluid accelerates through the passage formed by the stator blade cascade to supersonic velocities. At the blade trailing edge, a small region of slight over-expansion can be observed in the iso-Mach line plot. Further downstream, the flow appears to be slightly over-expanded, as it is bent slightly into itself resulting in a very weak oblique shock. Nonetheless, some weak shocks are unavoidable in this curved geometry and the blade passage appears to be reasonably well-designed for the specified (design-point) pressure ratio.

(a) Design-point   (b) Part-load

Ma

0.0 0.3 0.6 0.9 1.1 1.4 1.7 2.0
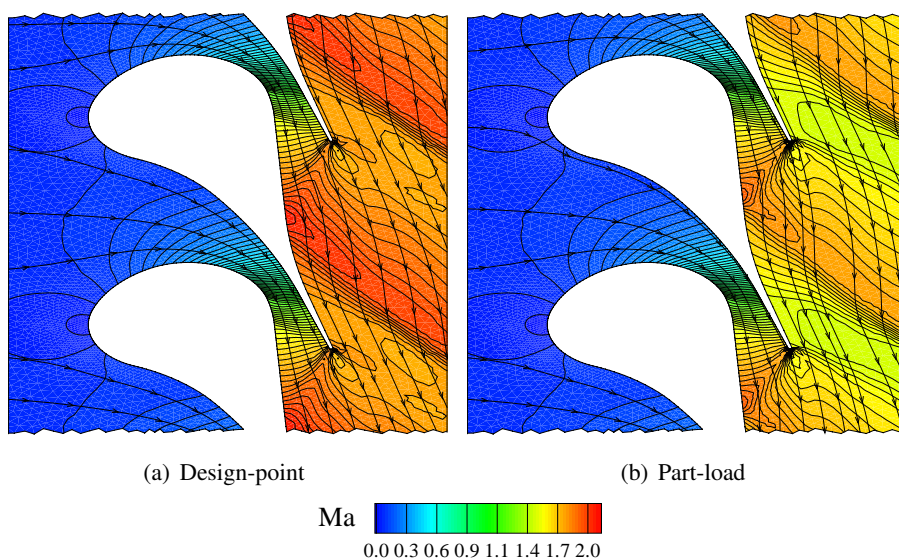
Figure 4.7: *Flow fields (iso-Mach and streamlines) at design-point and part-load operation. Operating conditions are given in Table 4.4.*

Fig. 4.9 shows the blade surface distributions of isentropic Mach number, pressure coefficient, speed of sound, velocity, density and compressibility factor. To clearly visualize parameter changes also for the rear part of this high-turning blade, the distributions are plotted as function of the reduced coordinate S/C, starting from the leading edge defined by $X/C_{\mathrm{ax}} = 0$. To show the effect of the thermodynamic nonideality on the blade surface distributions, the distributions computed based on the ideal gas law are shown in the same figure. It is noted that for design-point and part-load conditions this nonideality is relatively mild (see Table 4.4).

The isentropic Mach number distribution is given in Fig. 4.8(a). The line that

(a) Isentropic Mach number

(b) Pressure coefficient

(c) Sound speed

(d) Velocity

Figure 4.8: *Blade surface distributions at design point (thick lines) and part load (thin lines) based on the accurate SW EoS (solid lines) and on the PIG EoS (dashed lines). Operating conditions are given in Table 4.4.*

indicates early expansion (with a maximum in the Mach number) pertains to the suction side of the blade, the line with retarded expansion ending at $S/C = 0.92$ to the pressure side. The isentropic Mach number distribution of the suction side does not vary smoothly at the location $S/C = 0.52$-0.6 , indicating irregular expansion. More importantly, there exists a high peak at $S/C = 0.92$ on the suction side, corresponding to the point of impingement of the weak oblique shock emanating from the trailing edge of the top blade of the passage. This shock wave recompresses the flow downstream, which is detrimental to the desired continuous

(a) Density   (b) Compressibility factor

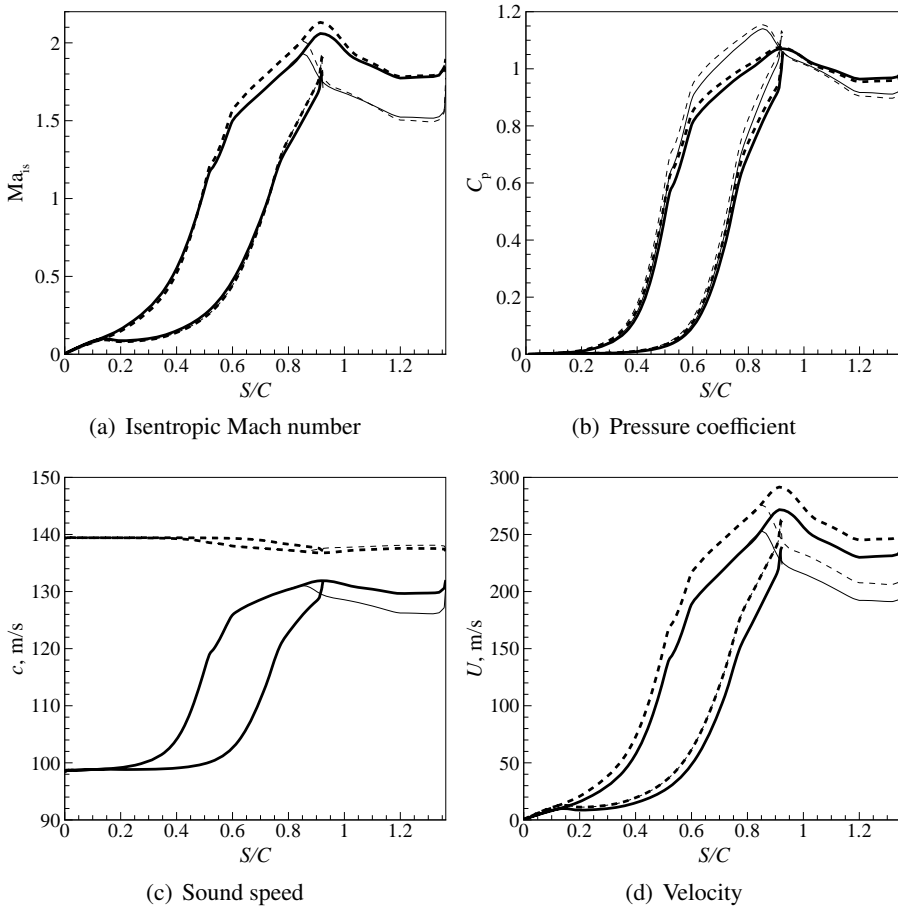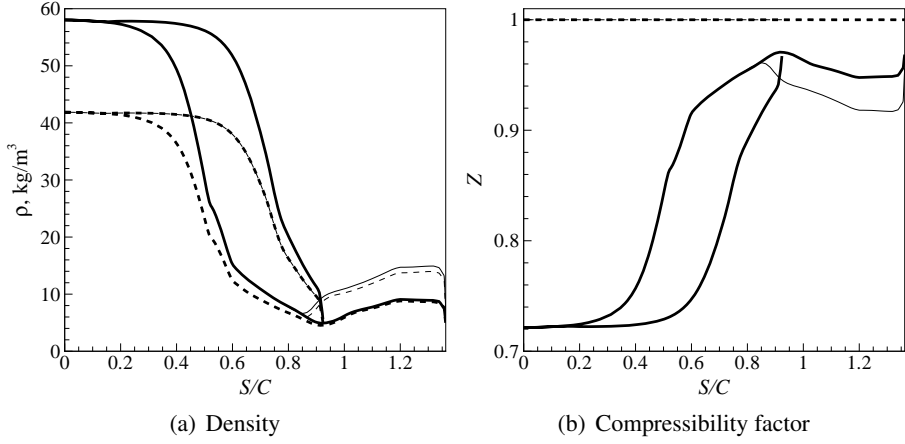Figure 4.9: *(continued) Blade surface distributions at design point (thick line) and part load (thin line) based on the accurate SW EoS (continuous line) and on the PIG EoS (dashed line). Operating conditions are given in Table 4.4.*

and smooth expansion along the entire blade surface. In the real viscous case and depending on the Reynolds number, the adverse pressure gradient may introduce the risk of boundary layer separation and associated increase in losses. In this study, this loss mechanism cannot be taken into account. Nonetheless, it is evident that there is room for improvement in the design of this blade. The isentropic Mach number distribution based on the ideal gas law appears quite similar to the isentropic Mach number distribution based on the accurate SW EoS. Nonetheless, the isentropic Mach number according to PIG is 10% lower at the leading edge ($S/C = 0$), where the nonideality is higher as indicated by the compressibility factor in Fig. 4.9(b). The initial high nonideality has, however, little effect on the absolute value of the isentropic Mach number since the latter is initially very low. Further downstream, at $S/C \approx 0.7$ on the suction side as well as at $S/C \approx 0.9$ on the pressure side, the isentropic Mach number based on the PIG EoS is 5% higher.

The distribution of the pressure coefficient defined as

$$C_P \equiv \frac{P_{01} - P}{P_{01} - P_2}, \tag{4.6}$$

is shown in Fig.4.8(b). Its trend is similar to the one of the isentropic Mach number.

The sound speed is shown in Fig. 4.8(c). Since the inlet state is relatively close to the critical point, the speed of sound is initially low ($c = 93$ m/s), but increases

considerably as the fluid expands, ultimately reaching a value of $c \approx 128$ m/s. Such an increase in sound speed across an isentropic expansion can occur only for molecularly complex fluids within a certain thermodynamic region [52]. The PIG model incorrectly predicts a 48% higher initial sound speed ($c \approx 137$ m/s) which decreases only slightly during expansion, which, under ideal-gas theory, is always the case for an isentropic expansion.

The trend of the velocity magnitude, shown in Fig. 4.8(d), is also similar to that of the isentropic Mach number. Similarly to what is observed for the isentropic Mach number, the PIG model incorrectly predicts higher values for the velocity, the maximum error being 35%. This explains the relatively limited error in isentropic Mach number of only 10%.

Density at the blade leading edge is high, but decreases as the fluid expands into the dilute ideal gas region. Since pressure and temperature are the prescribed variables at inflow and outflow, the density depends on the EoS model. The density resulting from the computation based on PIG is initially 30% lower, but this difference monotonically decreases to 3% along the rear part of the blade, as the fluid expands toward lower pressure (ideal gas) states.

Although based on the PIG model the velocities are higher, the densities are much lower, thus partially compensating each other but resulting in a net 6% lower mass flow rate if compared to the SW EoS (see Table 4.5(a)).

The distribution of the compressibility factor shown in Fig. 4.9(b) expresses the deviation from the ideal gas law. This nozzle has been designed for inlet conditions corresponding to a slightly superheated vapor at a reduced pressure $P_{01}/P_{cr} \approx 0.56$, with a large pressure ratio so that the process evolves very rapidly toward lower pressure states (near ideal gas). Indeed the distribution of the compressibility factor confirms that only in the initial phase of the expansion through the blade nozzle (i.e., only along the first half of the blade surface) in both the design-point and part-load case, the flow is thermodynamically nonideal. Significant real-gas effects are therefore present only in this initial region. The predicted performance of the nozzle blade in design conditions is therefore not heavily affected by the chosen thermodynamic model even if some differences have indeed been proven.

4.5.5   Part-Load Simulation

Because ORCs can operate at part-load conditions, the associated performance is important. To get an idea of the changes in the flow field and possible deterioration of the performance, part-load simulations are carried out. It is assumed that for part-load operation, the total pressure at the inlet is controlled to remain at $P_{01} = 8$

Table 4.5: *Performance parameter differences between EoSs and between stator operating points. The pressure loss coefficient is defined as the mass-weighted average over the outflow boundary of $C_{PL} \equiv 1 - P_{02}/P_{01}$, where P_{01} is the total inlet pressure and P_{02} the local total outflow pressure.*

(a) Percentage difference of the mass flow rate ($\Delta \dot{m}$) and pressure loss coefficient (ΔC_{PL}) based on the PIG model with respect to the accurate values based on the SW EoS, for the indicated operating condition.

(b) Percentage difference of the mass flow rate ($\Delta \dot{m}$) and pressure loss coefficient (ΔC_{PL}) with respect to design-point values, for the part-load and supercritical cases analyzed in this work.

	$\Delta \dot{m}, \%$	$\Delta C_{PL}, \%$		$\Delta \dot{m}, \%$	$\Delta C_{PL}, \%$
Design point	−6	−3	Design point	0	0
Part load	−6	6	Part load	0	41
SC1	−24	−13	SC1	171	61
SC2	−50	1100	SC2	533	−63
SC3	−50	−79	SC3	533	354

bar. This can be accomplished by e.g., partial-arc admission. In this particular part-load condition, the pressure ratio, P_2/P_{01}, is reduced from 6 to 4, so that the backpressure is higher (see Table 4.4).

The computation using the accurate SW EoS is again used to investigate the flow field of the expansion process. Fig. 4.7(b) shows the computed flow field visualized by equidistant iso-Mach lines and streamlines. As shown in the figure, at part-load operation the flow becomes over-expanded halfway along the blade suction surface and the weak oblique shock becomes stronger. Indeed, the pressure loss is 41% higher in comparison to design-point operation.

The surface distributions at part load are plotted in Fig. 4.9. Here, thin lines pertain to part-load distributions. It can be observed that in all blade distributions the initial part ($S/C < 0.75$) is the same for design point and part load, because the stator nozzle is choked (this is confirmed by the mass flow rate being equal to that of design point, as shown in Table 4.5(b)). An exception is the pressure coefficient (Fig. 4.8(b)), since its definition, given by Eq. (4.1), depends on the outlet pressure P_2. The difference with respect to design-point operation is that since the pressure ratio is reduced, firstly, the isentropic Mach number after expansion is lower (Fig. 4.8(a)) and, secondly, the outflow pressure is higher so that the final part of the expansion occurs in the nonideal thermodynamic region for a

larger portion (see Fig. 4.9(b)). This leads to a larger deviation of sound speed, velocity magnitude and density if the PIG model is compared to the SW model. In part-load conditions, the PIG EoS predicts 6% stronger shock waves if compared to the accurate SW EoS, as indicated by the pressure loss coefficient given in Table 4.5(a). The pressure loss coefficient is defined as the mass-weighted average over the outflow boundary of $C_{\mathrm{PL}} \equiv 1 - P_{02}/P_{01}$.

4.5.6   Supercritical Simulations

Flow simulations at supercritical inlet pressures are performed to demonstrate the effect of supercritical inlet total pressures on the two-dimensional flow field of the expansion process and the required reduction pressure ratio in order to obtain correctly expanded flow.

Three supercritical operating conditions are considered, indicated by SC1, SC2 and SC3 in Table 4.4. SC1 and SC2 represent two possible operating conditions at moderate and high inlet total pressure that are above the critical pressure: $P_{01}/P_{\mathrm{cr}} = 1.27$ and 1.98, respectively. To obtain correctly expanded flow, the pressure ratios of SC1 and SC2 are decreased according to the real-gas quasi-one-dimensional flow analysis of Section 4.4 as shown in Fig. 4.3(b), so that $P_{01}/P_2 = 4.15$ and 2.40, respectively. The SC3 case has an inlet total pressure equal to the SC2 case ($P_{01}/P_{\mathrm{cr}} = 1.98$), but the pressure ratio is deliberately not set according to the results of the real-gas quasi-one-dimensional flow analysis, but according to the PIG model which means a pressure ratio equal to design point ($P_{01}/P_2 = 6$), as indicated in Fig. 4.3(b). The resulting expansion cases are also given in the temperature-entropy diagram in Fig. 4.6(b).

Fig. 4.10 shows the computed flow fields of the supercritical cases visualized by equidistant iso-Mach lines and streamlines. The SC1 and SC2 cases show a correctly expanded flow field, without the formation of shocks. This confirms the correctness of the relation between inlet total pressure and pressure ratio. In fact, flow field of the SC2 case (Fig. 4.10(b)) appears to have a more uniform Mach distribution, indicating that the very weak oblique shock that is present even in the design-point flow field is absent in the SC2 case. This is confirmed by the pressure loss coefficient (Table 4.5(b)), which is 63% lower in comparison to its value at design point. This again puts in evidence that it may be possible to further improve the design of the stator for design-point conditions. Another important result is that the use of a blade geometry designed for sub-critical operating conditions would lead to rather unsatisfactory Mach numbers and pressure coefficient distributions along the blade (Fig. 4.12), if employed for nozzles expanding from supercritical inlet conditions. These Mach number and pressure distributions may

suggest the deterioration of the turbine performance.

The SC3 case shows highly underexpanded flow as it exits the stator passage, as was expected from the results of the real-gas quasi-one-dimensional flow analysis in Section 4.4. Even after having undergone the expansion process in the stator passage, the pressure at the exit is still considerably higher than the back pressure, so that the flow expands further in a free-jet that is formed downstream of the stage, as indicated in Fig. 4.10(c) by the distinct slip line originating from the trailing edge. The means for further expansion is provided for by an expansion fan that originates from the trailing edge and extends inwardly. Further downstream, at the other side of the blade trailing edge, the flow is subjected to a strong shock wave. Consequently, the pressure loss coefficient is 354% higher in comparison to the design-point value (see Table 4.5(b)). This undesirable flow field would be the result if an ORC turbine stage that is intended to operate at supercritical pressures were designed based on computations that employ the ideal gas law.

The SC3 case is also computed based on the PIG model and compared to the design-point computation based on the PIG model. As expected, the two flow fields, shown in Fig. 4.11, are identical. This shows, as is well-known, that under the PIG model the flow field of the expansion process is not dependent on inlet total pressure, but only on static outlet-to-total inlet pressure ratio. A comparison between the PIG and SW EoS for the design-point case has already been given in Section 4.5.4.

The blade distributions of the relevant parameters show more clearly the real-gas effects occurring at supercritical pressures. They are plotted for the three supercritical cases SC1, SC2 and SC3. The distributions for the design point are included to serve as a basis for comparison.

The Mach number is necessarily equal to unity at the throat for all cases, therefore the isentropic Mach number distribution along the blade surface, shown in Fig. 4.12(a), shows a similar trend for all cases. For higher pressures (increasing from design point to SC1 and further to SC2), the subsonic isentropic Mach number upstream of the throat is lower. The isentropic Mach number indicates that, in the moderately supercritical case SC1, expansion is absent for some length just downstream of the throat but then continues similarly to the design-point case. For the highly supercritical cases SC2 and SC3, the expansion occurs very rapidly at the throat. For the SC3 case, the free-jet provides further expansion from $S/C = 0.85$ onward. The pressure coefficients in Fig. 4.12(b) show similar trends for all cases, except for SC3 where the free-jet expansion is clearly visible.

The speed of sound has a minimum at the thermodynamic critical point. For

(a) SC1   (b) SC2

(c) SC3

Ma

0.0 0.3 0.6 0.9 1.1 1.4 1.7 2.0
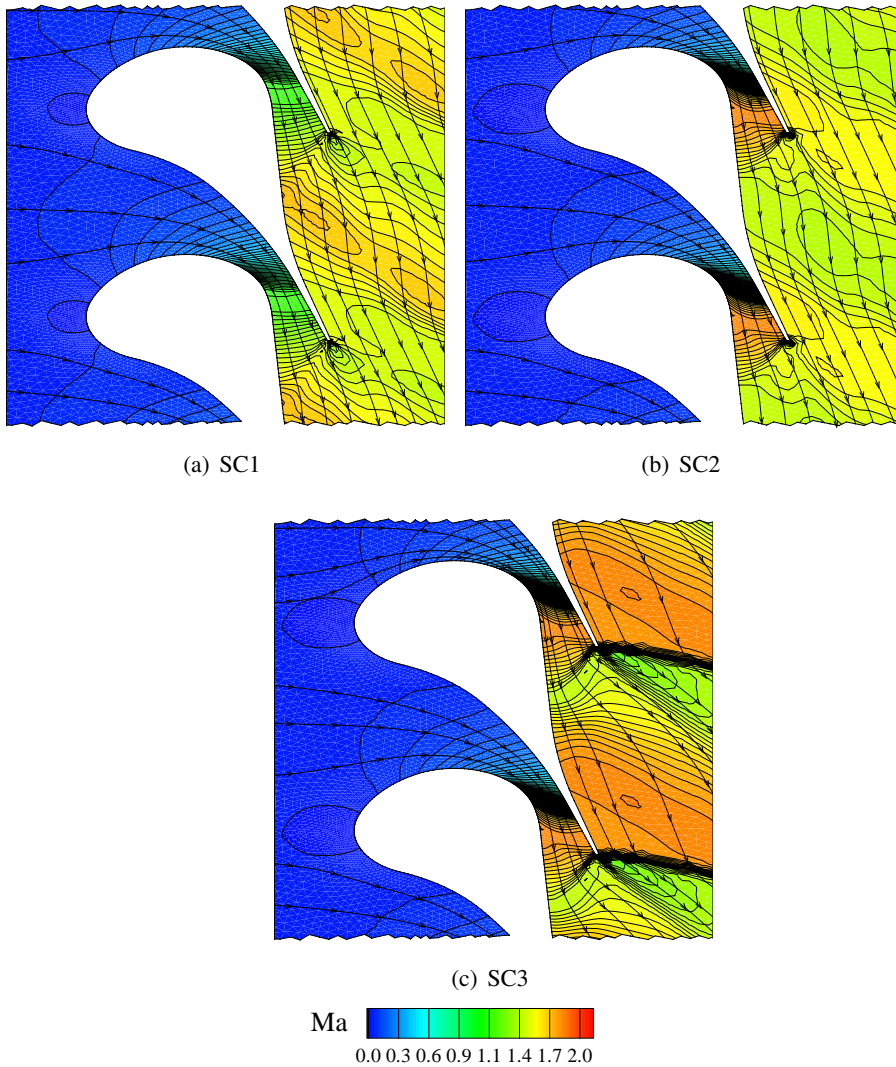
Figure 4.10: *Flow fields (iso-Mach and streamlines) at supercritical operation. Operating conditions are given in Table 4.4.*

supercritical expansions, the speed of sound decreases and has a minimum ($c =$ 49.2 m/s) where the critical pressure is crossed. This can be observed in Fig. 4.12(c). It also shows large variations in speed of sound during expansion in the three supercritical cases. The SC1 case, being closest to the critical point, has the lowest

(a) Design point computed using PIG   (b) SC3 computed using PIG

Ma

0.0 0.3 0.6 0.9 1.1 1.4 1.7 2.0
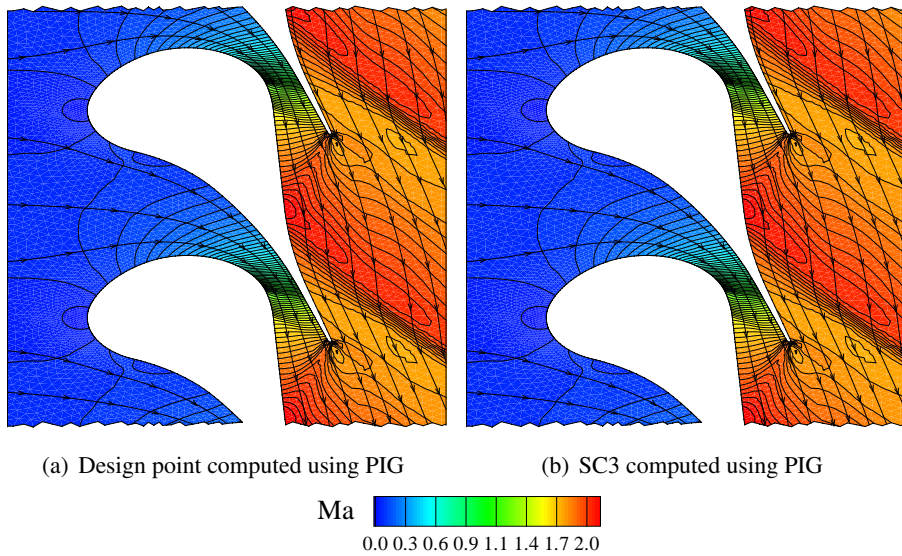
Figure 4.11: *Flow fields (iso-Mach and streamlines) computed using the PIG model. Operating conditions are given in Table 4.4.*

inlet speed of sound; the SC2 and SC3 cases, being highly supercritical, have a very high speed of sound at the inlet. Their speed of sound shows a strong decrease, followed by a strong increase, which is even larger than the increase in the velocity magnitude (Fig. 4.12(d)), leading to a decreasing isentropic Mach number (Fig. 4.12(a) for $0.6 < S/C < 0.8$) during expansion (cf. Fig. 4.12(b)). This phenomenon is discussed in more detail in Ref. [53].

The velocity magnitude, shown in Fig. 4.12(d), is considerably lower for all supercritical cases if compared to the design-point case. This is because the pressure ratio is lower for the SC1 and SC2 case, which corresponds to a lower enthalpy drop and therefore lower velocities. In the SC3 case (which has a pressure ratio equal to design point), the reduction in enthalpy drop with respect to the design point is still present, though not as large. In this case, the reduction in enthalpy drop is due to real-gas thermodynamic behavior at these nonideal conditions; the enthalpy drop becomes smaller as inlet pressure is increased at constant pressure ratio.

Along a given isentrope, density increases as pressure is increased, resulting in the high compressibility for supercritical states. Indeed, it can be observed in Fig. 4.13(a) that the densities of the moderately supercritical case SC1 are much

(a) Isentropic Mach number

(b) Pressure coefficient

(c) Sound speed

(d) Velocity
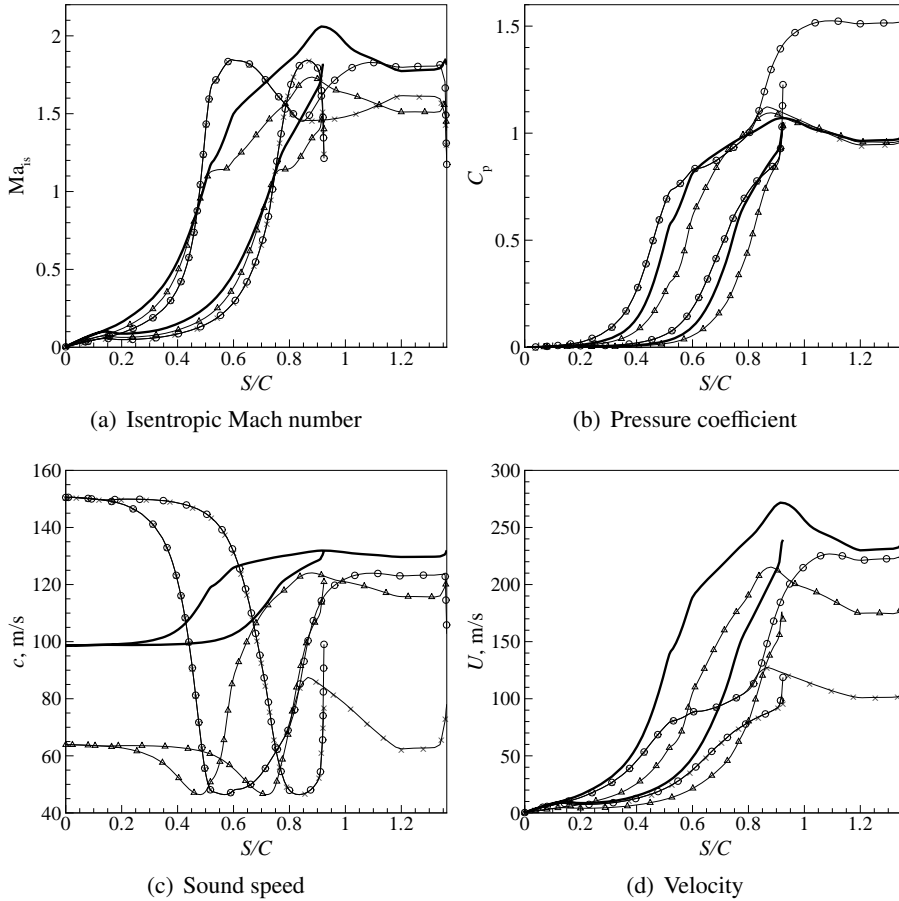
Figure 4.12: *Blade surface distributions of design-point and SC cases. Design point (thick line), SC1 (△), SC2 (×), SC3 (○).*

higher in comparison to the design point. This is even more so for the highly supercritical cases SC2 and SC3. Volumetric expansion ratios of 7.8, 12.9, 4.1 are observed for the cases design point, SC1 and SC2, respectively.

Even though the velocity is only slightly lower, the density is much higher for the supercritical cases (higher compressibility), resulting in a mass flow rate that is much higher in comparison to design point; a factor 1.7 and 5.3 higher for SC1 and SC2/SC3, respectively (see Table 4.5(b)).

The compressibility factor, shown in Fig. 4.13(b), shows that the supercritical cases deviate from the PIG law in terms of $P - v - T$-behavior far more than for
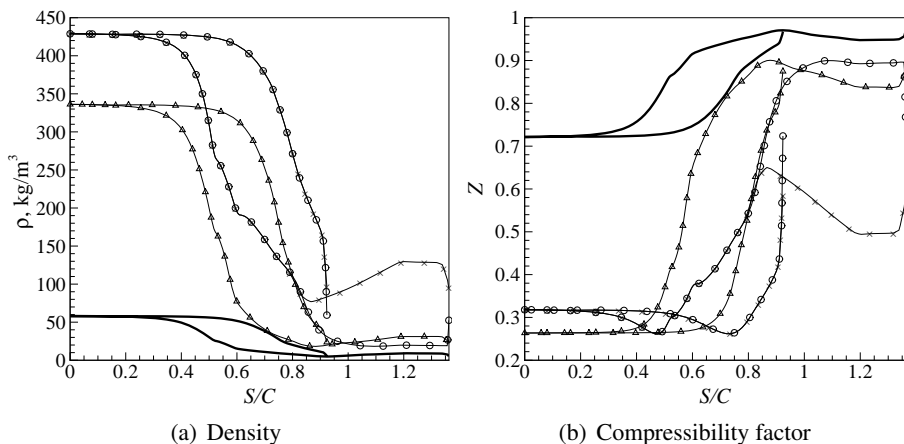
(a) Density   (b) Compressibility factor

Figure 4.13: *(continued) Blade surface distributions of design-point and SC cases. Design point (thick line), SC1 (△), SC2 (×), SC3 (○).*

the design-point case. The initial deviation is as high as 74% and 68% for SC1 and SC2, respectively. After the critical pressure has been crossed, the nonideality is reduced to less than 20% (SC1) and 50% (SC2).

4.6   Conclusions

This chapter presented an investigation on real-gas effects in ORC nozzle flows for inlet conditions at sub- and supercritical pressures. It is known that supercritical ORCs are thermodynamically more efficient, however they are not yet adopted in practice. One of the reasons is that suitable tools for the fluid-dynamic design of the turbine geometry operating at supercritical conditions have not been available until recently.

The first part of the investigation is based on a quasi-one-dimensional isentropic nozzle analysis (the first step in the design of any nozzle) employing an accurate thermodynamic model. It showed that the pressure ratio needs to be significantly reduced to obtain efficient expansion if the same stator nozzle is to be used or, reversely, a nozzle geometry with a much higher exit-to-throat area ratio is required in order to obtain an efficient expansion at supercritical pressures.

In the second part, real-gas two-dimensional inviscid fluid-dynamic simulations of an actual ORC stator blade cascade with siloxane MDM as working fluid have been carried out for five different operating conditions. The flow simulations

were performed with the CFD code zFLOW, which is linked to a library containing accurate thermodynamic models. The validation of zFLOW on the well-known test case of the VKI LS-89 transonic turbine blade showed good agreement with experimental data. The subsequently analyzed cases of the ORC stator blade cascade include a simulation of the flow in design and part-load conditions and three simulations of expansions starting at supercritical inlet pressures.

The results, illustrated by two-dimensional flow fields, distributions of relevant flow variables along the blade surface and two integral performance parameters, show the aforementioned real-gas effect in more detail. Moreover, the results show additional real-gas effects in the supercritical expansions such as the low speed of sound and low velocity as compared to design-point conditions. Furthermore, the supercritical expansions are characterized by very high densities and mass flow rates.

The results obtained for the supercritical cases show that the significant nonideal flow effects lead to rather unsatisfactory Mach numbers and pressure coefficient distributions along the blade which may substantially deteriorate the turbine performance. This demonstrates that standard design methods are not well suited to obtain a proper design in strongly nonideal thermodynamic regions, and that in such flow conditions CFD simulations employing accurate thermodynamic models could lead to a significantly improved design.

Future work will focus on the extension of the analysis by means of Navier-Stokes simulations (to take into account viscous losses and shock-induced boundary-layer separation) and blade shape optimization to demonstrate improved performance.

Nomenclature

A	=	cross-sectional area
c	=	speed of sound
C	=	specific heat, blade chord, coefficient
h	=	static enthalpy
M	=	molecular weight
Ma	=	Mach number
n	=	parameter in Span-Wagner equation of state
P	=	pressure, power
R	=	specific gas constant
$\mathcal{R}$	=	universal gas constant
s	=	entropy

S	=	curvilinear distance along the blade profile
T	=	temperature
u	=	velocity
v	=	specific volume
X	=	nozzle axial coordinate
Z	=	compressibility factor

Greek symbols

δ	=	reduced density
Δ	=	difference
$\dot{m}$	=	mass flow rate
η	=	efficiency
γ	=	ratio of specific heat capacities
ψ	=	reduced Helmholtz energy
ρ	=	density
τ	=	inverse of reduced temperature

Subscripts

0	=	total (or stagnation)
1	=	nozzle inlet
2	=	nozzle exit
A	=	turbine inlet total
ax	=	axial
B	=	turbine outlet
cr	=	critical point
D	=	condensor outlet
e	=	electric
gen	=	electric generator
G	=	flue gas inlet
i	=	ideal gas
I	=	cooling water inlet
is	=	isentropic
K	=	cooling water outlet
max	=	cycle maximum
p	=	pump
P	=	isobaric, pressure

PL	=	pressure loss
pinch	=	pinch-point
PHE	=	primary heat exchanger
r	=	exit-to-throat ratio
re	=	real gas
regen	=	regenerator
t	=	nozzle throat, turbine
v	=	isochoric
x	=	nozzle axial coordinate

Superscripts

0	=	ideal-gas contribution
L	=	saturated liquid
r	=	real-gas contribution
sat	=	saturation
V	=	saturated vapor

Acronyms

CFD	=	Computational Fluid Dynamics
ORC	=	Organic Rankine Cycle

References

[1] H.M. Curran. Use of Organic Working Fluids in Rankine Engines. *Journal of Energy*, 5(4):218–223, 1981.

[2] G. Angelino, M. Gaia, and E. Macchi. A review of Italian activity in the field of organic Rankine cycles. In *VDI Berichte - Proceedings of the International VDI Seminar*, volume 539, pages 465–482, Düsseldorf, 10–12 September 1984. VDI Verlag.

[3] P. Colonna. *Fluidi di Lavoro Multi Componenti Per Cicli Termodinamici di Potenza (Multicomponent Working Fluids for Power Cycles)*. PhD thesis, Politecnico di Milano, October 1996.

[4] T. C. Hung. Waste heat recovery of organic Rankine cycle using dry fluids. *Energ. Convers. Manage.*, 42(5):539–553, 2001.

[5] J. E. Boretz. Supercritical organic Rankine engines (SCORE). In *21st Intersociety Energy Conversion Engineering Conference (IECEC)*, volume 3, pages 2050–2054, Washington, DC, August 1986. ACS.

[6] T. Yamamoto, T. Furuhata, N. Arai, and K. Mori. Design and testing of the organic Rankine cycle. *Energy*, 26(3):239–251, 2001.

[7] L. Y. Bronicki. Electrical power from moderated temperature geothermal sources with modular mini-power plants. *Geothermics*, 17(1):83–92, 1988.

[8] C. Kutscher. The status and future of geothermal electric power. In *American Solar Energy Society (ASES) Conference*, number NREL/CP-550-28204, pages 1–6. National Renewable Energy Laboratory (NREL), June 2000.

[9] L.Y. Bronicki. Organic rankine cycles in geothermal power plants - 25 years of Ormat experience. In *GRC 2007 Annual Meeting, Reno NV*, 2007.

[10] R.Bertani. What is Geothermal Potential? *International Geothermal Association News*, 53:1–3, 2003.

[11] I. Obernberger, P. Thonhofer, and E. Reisenhofer. Description and evaluation of the new 1000 kW ORC process integrated in the biomass CHP plant in Lienz, Austria. *Euroheat and Power*, 10:1–17, 2002.

[12] T. Savola, C. J. Fogelholm, and I. Keppo. Small-scale biomass CHP plant and district heating. VTT research notes 2301, Helsinki University of Technology, Helsinki, Finland, 2005.

[13] V. Hassani and H. W. Price. Modular trough power plants. In *Solar Forum 2001: Solar Energy: The Power to Choose*, pages 1–7, Washington, DC, April 21–25 2001. ASME.

[14] G. Angelino and P. Colonna. Organic Rankine cycles for energy recovery from molten carbonate fuel cells. In *35th Intersociety Energy Conversion Engineering Conference (IECEC)*, number 2000-3052, pages 1–11. AIAA, July 2000.

[15] G. Angelino and P. Colonna. Air cooled siloxane bottoming cycle for molten carbonate fuel cells. In *Fuel Cell Seminar*, pages 667–670, October 2000.

[16] D. W. Chaudoir, R. E. Niggeman, and T. J. Bland. A solar dynamic ORC power system for space station application. In *20th Intersociety Energy Conversion Engineering Conference (IECEC)*, number 859085, pages 1.58–1.65. SAE, August 1985.

[17] G. Angelino and C. Invernizzi. Cyclic methylsiloxanes as working fluids for space power cycles. *J. Sol. Energ. - Trans. ASME*, 115(3):130–137, 1993.

[18] G. Heidenreich, T. Bland, and R. Niggemann. Receiver for solar dynamic organic rankine cycle (orc) powered space station. In *Proceedings of the 20th IECEC, Miami Beach*, 859220, pages 1.228–1.245, 1985.

[19] R. L. Cole, J. C. Demirgian, and J. W. Allen. Predicting toluene degradation in organic Rankine cycle engines. In *22nd Intersociety Energy Conversion Engineering Conference (IECEC)*, volume 3, pages 1402–1407, New York, NY, August 1987. AIAA.

[20] V.N. Havens, D.R. Ragaller, and D. Namkoong. Solar dynamic organic rankine cycle heat rejection system simulation. In *Proceedings of the 22th IECEC, Philadelphia*, 879284, pages 222–226, 1987.

[21] R.V. Boyle, M.G. Coombs, and C.T. Kudija. Solar dynamic power option for the space station. In *Proceedings of the 23th IECEC, Denver*, 889163, pages 319–328, 1988.

[22] J. Blumenberg and H.O. Ruppe. Comparison of nuclear and solar power plants with turboelectric generations for application in space. *Acta Astronautica*, 12(5):293–307, 1985.

[23] K.L. Meier, W.L. Kirchner, and G.J. Willcut. Compact reactor/ORC power source. In *Presented at the Intersociety Energy conversion Engineering Confrence, San Diego, CA, 25 Aug.*, 1986.

[24] B. P. Brown and B. M. Argrow. Application of Bethe-Zel'dovich-Thompson fluids in organic Rankine cycle engines. *J. Propul. Power*, 16(6):1118–1123, November-December 2000.

[25] P. Colonna and S. Rebay. Numerical simulation of dense gas flows on unstructured grids with an implicit high resolution upwind Euler solver. *Int. J. Numer. Meth. Fl.*, 46(7):735–765, 2004.

[26] J. Hoffren, T. Talonpoika, J. Larjola, and T. Siikonen. Numerical simulation of real-gas flow in a supersonic turbine nozzle ring. *J. Eng. Gas Turb. Power*, 124(2):395–403, April 2002.

[27] T. P. van der Stelt, Woudstra N., and P. Colonna. Cycle-Tempo: a program for thermodynamic modeling and optimization of energy conversion systems, 1985-2004.

[28] P. Colonna and T. Van der Stelt. Fluidprop: A program for the estimation of thermophysical properties of fluids. Energy Technology section, Delft University of Technology, The Netherlands (www.fluidprop.com)., 2005.

[29] R.L. Rowley, W.V. Wilding, J.L. Oscarson, Y. Yang, N.A. Zundel, T.P. Daubert, and R.P. Danner. *DIPPR data compilation of pure chemical properties*. Taylor & Francis Publishing Company, New York, NY, 2004.

[30] R. Span and W. Wagner. Equations of state for technical applications. I. Simultaneously optimized functional forms for nonpolar and polar fluids. *Int. J. Thermophys.*, 24(1):1–39, January 2003.

[31] P. Colonna, N. R. Nannan, A. Guardone, and E. W. Lemmon. Multiparameter equations of state for selected siloxanes. *Fluid Phase Equilib.*, 244:193–211, 2006.

[32] N. R. Nannan, P. Colonna, C. M. Tracy, R. L. Rowley, and J. J. Hurly. Ideal-gas heat capacities of dimethylsiloxanes from speed-of-sound measurementsandab initio calculations. *Fluid Phase Equilib.*, 257:102–113, 2007.

[33] P. Colonna, N. R. Nannan, and A. Guardone. Multiparameter equations of state for siloxanes: $[(CH_3)_3\text{-Si-O}_{1/2}]_2\text{-[O-Si-}(CH_3)_2]_{i=1...3}$, and [O-Si-$(CH_3)_2]_6$. *Fluid Phase Equilib.*, 263(2):115–130, 2008.

[34] D. D. Lindley and H. C. Hershey. The orthobaric region of octamethyl-trisiloxane. *Fluid Phase Equilib.*, 55:109–124, 1990.

[35] C. B. Hurd. Studies of siloxanes. I. The specific volume and viscosity in relationtotemperatureand costitution. *J. Am. Chem. Soc.*, 68:364–370, 1946.

[36] O. L. Flaningam. Vapor pressures of poly(dimethylsiloxane) oligomers. *J. Chem. Eng. Data*, 31(3):266–272, 1986.

[37] I. I. Skorokhodov, V. E. Ditsent, N. A. Terentéva, and M. N. Zolotareva. Pressure of the saturated vapor of polydiorganosiloxane. 1. Polydimetyl-siloxane. *Deposited Doc. VINITI N2725-71 dep.*, page 11, 1971.

[38] D.H. Marcos, D.D. Lindley, K.S. Wilson, W.B. Kay, and H.C. Hershey. A (P, v, T) study of tetramethylsilane, hexamethyldisiloxane, octamethyl-trisiloxane,andtoluenefrom 423 K to 573 K in the vapor phase. *J. Chem. Thermodyn.*, 15:1003–1014, 1983.

[39] I. A. McLure, A. J. Pretty, and P. A. Sadler. Specific volumes, thermal pressure coefficients, and derived quantitiesoffive dimethylsiloxane oligomers from 25 to 140 ° C. *J. Chem. Eng. Data*, 22(4):372–376, 1977.

[40] G. Angelino and P. Colonna. Multicomponent working fluids for Organic Rankine Cycles (ORCs). *Energy*, 23(6):449–463, 1998.

[41] P. Colonna, J. Harinck, S. Rebay, and A. Guardone. Real-gas effects in organic rankine cycle turbine nozzles. *AIAA Journal of Propulsion and Power*, 24(2):282–294, 2008.

[42] P. Colonna and P. Silva. Dense gas thermodynamic properties of single and multi-component fluids for fluid dynamics simulations. *J. Fluid Eng.-T. ASME*, 125(3):414–427, 2003.

[43] V. Selmin. The node-centered finite volume approach: bridge between finite differences and finite elements. *Computer Methods in Applied Mechanics and Engineering*, 102(1):107–138, 1993.

[44] P. L. Roe. Approximate Riemann solvers, parameter vectors, and difference schemes. *Journal of Computational Physics*, 43(2):357–372, 1981.

[45] M. Vinokur and J. L. Montagné. Generalized Flux-Vector Splitting and Roe Average for an Equilibrium Real Gas. *Journal of Computational Physics*, 89(2):276–300, 1990.

[46] P. Colonna, A. Guardone, J. Harinck, and S. Rebay. Numerical investigation of dense gas effects in turbine cascades. In *15th U. S. National Congress on Theoretical and Applied Mechanics (USNCTAM)*, June 2006.

[47] T. Arts, M. Lambert de Rouvroit, and A. W. Rutherford. Aero-thermal investigation of a highly loaded transonic linear turbine guide vane cascade. Technical Note 174, Von Karman Institute for Fluid Dynamics, September 1990.

[48] S.G. Penoncello E.W. Lemmon, R.T. Jacobsen and D.G. Friend. Thermodynamic properties of air and mixtures of nitrogen, argon, and oxygen from 60 to 2000 K at pressures to 2000 MPa. *J. Phys. Chem. Ref. Data*, 29(3):331–385, 2000.

[49] A Guardone and S Rebay. Unstructured periodic grid generation. In *Proceedings of the ECCOMAS CFD 2006 Conference*, Egmond aan Zee, The Netherlands, 2006.

[50] S. Rebay. Efficient Unstructured Mesh Generation by Means of Delaunay Triangulation and Bowyer–Watson Algorithm. *Journal of Computational Physics*, 106(1):125–138, 1993.

[51] M.B. Giles. Non-reflecting boundary conditions for Euler equation calculations. *AIAA Journal*, 28(12):2050–2058, 1990.

[52] P. Colonna and A. Guardone. Molecular interpretation of nonclassical gas dynamics of dense vapors under the van der Waals model. *Phys. Fluids*, 18:056101–1–14, 2006.

[53] G.H. Schnerr and P. Leidner. Diabatic Supersonic Flows of Dense Gases. *Physics of Fluids A*, 3(10):2445–2458, 1991.

5

Computational Study of a High-Expansion Ratio Radial Organic Rankine Cycle Turbine Stator

Abstract *There is a growing interest in Organic Rankine Cycle (ORC) turbogenerators as stationary energy converters for external heat sources. ORC turbogenerators can efficiently utilize external heat sources at low to medium temperature in the small to medium power range. ORC turbines typically operate at very high pressure ratio and expand the organic working fluid in the dense-gas thermodynamic region, thus requiring CFD solvers coupled with accurate thermodynamic models for their performance assessment and design. This chapter presents a comparative numerical study on the simulated flow field generated by a stator nozzle of an existing high-expansion ratio radial ORC turbine with toluene as working fluid. The analysis covers the influence on the simulated flow fields of the real-gas flow solvers* FLUENT, FINFLO *and* ZFLOW, *of two turbulence models and of two accurate thermodynamic models of the fluid. The results show that* FLUENT *is by far the most dissipative flow solver, resulting in large differences in all flow quantities and appreciably lower predictions of the isentropic nozzle efficiency. If the combination of the* $k - \omega$ *turbulence model and* FINFLO *solver is adopted, a shock-induced separation bubble appears in the calculated results. The bubble affects in particular the variation of flow velocity and angle along the stator outlet. The accurate thermodynamic models by Lemmon-Span and Goodwin lead to small differences in the flow field, especially if compared to the large deviations that would be present if the flow were simulated based on the ideal gas law. However, the older and less accurate thermodynamic model by Goodwin does differ significantly from the more accurate Lemmon-Span thermodynamic model in its prediction of the specific enthalpy difference, which leads to a considerably different value for the specific work and stator isentropic efficiency. The above differences point to a need for experimental validation of flow solvers in real-gas conditions, if CFD tools are to be applied for performance improvements of high expansion-ratio turbines operating partly in the real-gas regime.*

5.1   Introduction

It is expected that the use of small-scale turbogenerators will become more widespread in the future, due to the possible scenario of distributed power generation and energy recovery in both developed and developing countries. Small-scale turbogenerators commonly employ radial turbines with a high expansion ratio. Examples of such energy converters are the Organic Rankine Cycle (ORC) power plant [1] and expanders used to recover energy from high pressure streams, typically in chemical and petrochemical processes [2, 3] or refrigeration and cryogenic systems.

In ORC turbogenerators, the working fluid is an organic substance, which allows for the efficient application of the Rankine cycle principle also to the energy conversion of low-temperature heat sources (starting from approximately 90°C) and for low-power output (from few kW$_e$ up to few MW$_e$). Current applications of ORC turbogenerators are the electricity generation from low-grade geothermal heat reservoirs, from biomass fuel, and the energy recovery from turbogas or reciprocating engines and from industrial waste heat. The installed power of geothermal ORC plants now totals approximately 1000 MW$_e$ [4] and can be considered a mature technology [5]. ORC systems designed for comparatively high-temperature heat sources have demonstrated to be a viable technology for small-scale biomass-fired combined-heat-and-power energy conversion [6, 7, 8, 9]. The use in the near future of ORC power systems coupled with solar concentrators [10], high-temperature fuel cells [11] and for domestic cogeneration is also very attractive.

The selection of the working fluid is key to the achievement of high isentropic efficiency of the turboexpander, which is usually single-stage and often features a low peripheral speed and optimal dimensions. Other advantages include i) simple cycle configuration even for large sink/source temperature ratio, because of the non-extractive desuperheating regeneration, ii) dry expansion of the fluid through the turbine is easily achievable and often even without superheating of the vapor at the inlet, iii) the minimum and maximum pressure of the thermodynamic cycle can be selected independently of the sink/source temperatures (to a certain degree) iv) the supercritical cycle configuration can be obtained with low maximum cycle pressure and also if the heat source is at low temperature [12, 13]. In addition, it can be shown that, the heat of vaporization of organic fluids being much lower than that of water, a better match between the heating trajectory of the working fluid and the cooling trajectory of the heat source can be achieved. As a result, the heat source can be cooled to a significantly lower temperature [14]. Classes of substances that are currently employed as working fluids in ORC power plants are the linear or cyclic hydrocarbons, the refrigerants and the siloxanes. The optimization of a mixture as a working fluid has also been proposed [15].

Expansions in ORC turbines are characterized by two distinguishing features. Owing to the use of heavy and molecularly complex substances as working fluids, the expansion features a small specific enthalpy drop, which allows for the adoption of only one or two stages, without running into the problem of high rotational speed and associated penalties on efficiency [12]. As a consequence though, the expansion pressure ratio per stage is typically very high (5-50), especially for radial turbines (50-150), so that the flow through the stator nozzle is highly su-

personic [16]. The second important difference with respect to steam and gas turbines is the fact that the initial part of the expansion process takes place comparatively close to the critical point of the working fluid, in the so-called dense-gas or real-gas thermodynamic region, where the ideal gas law does not apply. Complex thermodynamic models of organic fluids are therefore required for the correct and accurate (computational) fluid dynamic design and performance evaluation of high-expansion ratio ORC turbines.

The need for fluid dynamic simulations of expansions in the dense-gas region has lead to the interfacing of existing finite-volume CFD solvers with programs for the estimation of thermodynamic properties of fluids, featuring various degrees of accuracy (see, e.g., Refs. [17, 18, 19, 20, 21, 22, 23, 24, 13, 25]). Examples of such CFD programs are the FINFLO solver which has been extended to allow for real-gas simulations [19] in order to aid the aerodynamic design of the stator of an ORC turbine [26], and ZFLOW [24, 27, 25], which was specifically developed with the aim of creating a highly accurate real-gas flow simulation program, capable of treating complex geometries. The commercial CFD code FLUENT can also be interfaced with real-gas thermodynamic models [28]. FINFLO, ZFLOW and FLUENT have been validated for turbomachinery expansions in the ideal-gas thermodynamic region by comparison with experimental data [29, 30, 31, 19, 24, 13]. However, due to the lack of measurements of flows occurring in the dense-gas region, none of the codes have been validated on dense-gas flows. Without proper validation, these programs cannot be used as a predictive tool for the design of ORC turbines.

The aim of the work documented in this chapter is two-fold. On the one hand the study has the objective of demonstrating the possibility of effectively simulating, using state-of-the-art models, real-gas flows through blade passages of ORC turbine stators characterized by large pressure ratios; on the other hand, the investigation focuses also on the assessment of different flow solvers, turbulence models and accurate thermodynamic models on the results. The results of the simulations are discussed quite extensively and the outcome of this study is summarized in the concluding remarks, which also reports plans for future research.

5.2 The Test Case: The Stator of the Tri-O-Gen Radial Turbine

The test case for this study is the expanding flow of dense toluene ($C_6H_5CH_3$) vapor in the stator nozzle of a radial ORC turbine. This is the main component of the 150 kW$_e$ combined heat and power ORC turbogenerator manufactured by Tri-O-Gen B.V. The turbine and main pump of this ORC system are mounted on the

same shaft, together with the high-speed electrical generator, shown in Fig. 5.1(a). This arrangement allows for a compact and hermetic unit to be effectively integrated with the other components. Selected design specifications of the turbine are listed in Table 5.1. The aerodynamic design of the Tri-O-Gen turbine [19, 26] was performed with the help of the FINFLO flow solver interfaced to the thermodynamic property data of toluene, calculated with the model developed by Goodwin [32]. This study presents simulations of the Tri-O-Gen stator performed with a more accurate thermodynamic model developed by Lemmon and Span [33], as well as with the three mentioned CFD solvers (FINFLO, ZFLOW and FLUENT), and several turbulence models.

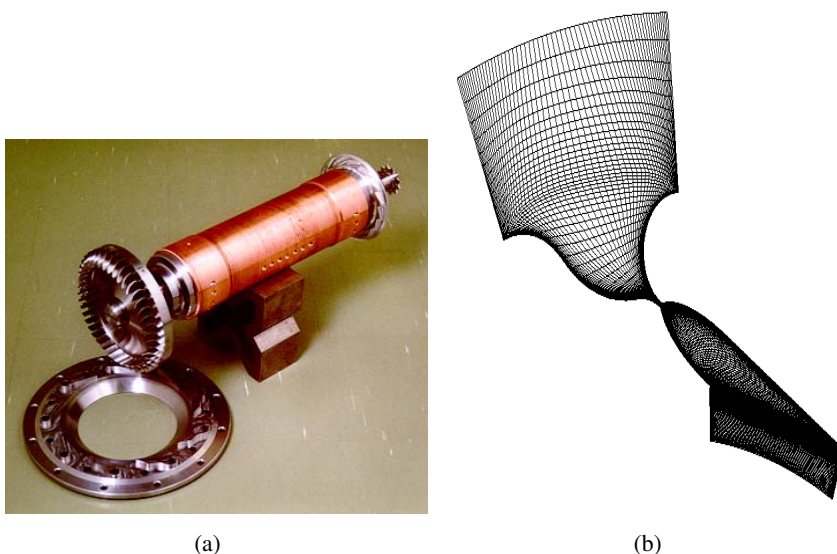
| (a)   (b) |

Figure 5.1: *a) The stator and rotor of the Tri-O-gen ORC turbine. The main pump, the rotor of the electrical generator, and the rotor of the turbine are mounted on the same shaft. b) Coarse 2D computational grid (11,264 cells) of the stator nozzle for the viscous simulations. The figure aspect ratio is deformed, since the blade design is confidential property of the manufacturer.*

5.2.1 Convergence Criteria and Grid Dependency Study

The flow through the stator nozzle ring is mainly two-dimensional in the radial plane and the influence of the endwall boundary layers on the flow field is assumed

Table 5.1: *ORC turbine specifications and boundary conditions for the CFD simulations.*

Total inlet pressure	p_{01}, bar	31.9
Total inlet temperature	T_{01}, °C	314.5
Stator static backpressure	p_2, bar	0.55
Turbine overall pressure ratio	p_{01}/p_4, -	120.5
Mass flow rate	$\dot{m}$, kg/s	1.24
Working fluid		Toluene

to be small. A coarse and a fine 2D structured computational grid, Fig. 5.1(b), have been generated and consist of 11,264 and 26,112 quadrilateral cells, respectively.

Since the turbulence models implemented in FINFLO are of the low-Reynolds type, the grids were generated such that the non-dimensional wall distance y^+ is of order 1 or smaller at the first cell adjacent to the wall [28]. This quantity is shown in Fig. 5.2. The y^+ values are rather high near the throat and this is correct since the boundary layer is very thin at that location. However, the y^+ values are close to 1 in the zone where the boundary layer is thicker and affected by oblique shock waves. Results are only slightly different with the finer grid. It can therefore be concluded that the computational results are grid-independent with both FINFLO and FLUENT.
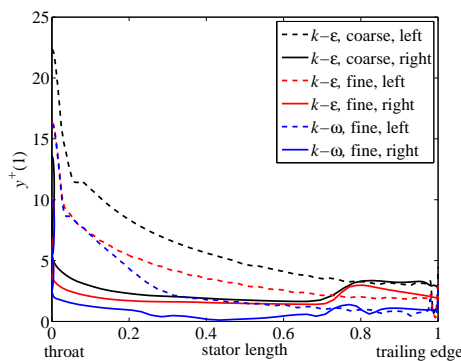

Figure 5.2: *Value of y^+ at the first cell along the left wall (dashed lines) and the right wall (continuous lines) of the nozzle passage. The data refer to the $k-\epsilon$ (black and red) and the $k-\omega$ (blue) turbulence models, and to the coarse and fine grids.*

For the FINFLO simulations, the largest differences between the solutions obtained using the two grids are observed for the density and the pressure at the throat (about 0.4 %). The differences observed in the grid-convergence study performed with FLUENT are largest at the outlet of the stator: the pressure and the density calculated with the fine and the coarse grid differ by about 3 % and this corresponds to 2.6 kPa and 0.05 kg/m^3, respectively. It can therefore be concluded that the computational results are grid-independent with both FINFLO and FLUENT.

The convergence of the simulations was ensured by monitoring the residuals and the maximum change in the pseudo-time of the mass flow entering and leaving the computational domain. The iterations were continued until the scaled residuals decreased to 10^{-3} for all the conservation equations except for the energy equation, for which the limiting value was set to 10^{-6}. For these values of the residuals, the density does not change anymore and the difference in mass flow rate is smaller than 0.8%.

One of the flow solvers that is evaluated in this work, ZFLOW, is currently being extended to allow for viscous computations. However, at the time of writing, it was only possible to perform inviscid computations. Therefore, in order to compare the results of simulations performed with ZFLOW to the ones performed with the other CFD programs, an inviscid grid has been generated. The grid consists of 32,486 triangular cells. A grid-independent solution of the flow-field was verified also in this case.

5.2.2   Influence of real gas behavior

Flows of dense gases are different from their ideal-gas counterparts, first of all because of the different volumetric relation, leading to quantitative deviations. In addition, for fluids that are complex enough, the dependence of the variation of the speed of sound on density along isentropes in the dense-gas region is inverted, leading also to significant qualitative differences in the fluid dynamics [25]. The current test case has inlet conditions at reduced pressure and temperature (reduced with their respective critical point values) of 0.77 and 0.99, respectively, corresponding to a compressibility factor of 0.61. Given the common practice, it is important to remark that fluid dynamic simulations of this stator nozzle based on the polytropic ideal gas model would lead to strong average deviations from true fluid flow behavior [25, 13]. On average these deviations are at least approximately 10% for Mach number and pressure distributions, 50% for the flow velocity and sound speed (where the sound speed would incorrectly decrease instead of increase), 40% for the density, 15% for the mass flow rate, 30% for the total pressure loss and 2° for the flow exit angles.

5.3   Models

5.3.1   Flow Solvers

Both FINFLO [18, 19] and FLUENT [28] solve the Navier-Stokes equations employing a finite-volume technique for spatial discretization and Roe's flux-difference splitting [34]. FINFLO can make use of Chien's $k - \epsilon$ [35] and Menter's $k - \omega$ turbulence models [36]. Both turbulence models are of the low-Reynolds number type, which implies that no wall functions are used and the flow is solved down to the walls. In FLUENT, the $k - \epsilon$ turbulence model is the one suggested by Launder and Spalding [37], with standard wall functions. The $k - \omega$ turbulence model used in combination with FLUENT is based on the model by Wilcox [38]. At that time, the possibility of instead using Menter's $k - \omega$ turbulence model with FLUENT, which would allow for a more fair comparison with FINFLO, was not known to the authors.

ZFLOW [24, 27, 13, 39, 40, 25, 41] solves the inviscid Navier-Stokes (Euler) equations and is linked to the FLUIDPROP library for the calculation of thermophysical properties of fluids and mixtures according to a number of models [42]. The solver adopts a hybrid Finite Element (FE)/Finite Volume (FV) approach in which the finite volume metric quantities are formulated on the basis of the Lagrangian linear shape functions typically used in finite element methods [43]. The spatial approximation of the inviscid Navier-Stokes equations is constructed with a high-resolution finite volume method suitable for general unstructured and hybrid grids. The high-resolution upwind discretization is constructed on the basis of the Roe approximate Riemann solver [34], generalized to the case of fluids characterized by arbitrary equations of state according to the method of Vinokur and Montagné [44]. This class of discretization schemes is particularly well suited to the computation of high Mach number flows. The ZFLOW solver has been successfully validated for cases of complex inviscid flows occurring in the ideal gas thermodynamic region (see e.g., Refs. [24, 13]) and validation on a dense-gas process is planned [45]. ZFLOW is currently being extended to solve the viscous Reynolds-Averaged Navier-Stokes (RANS) equations [39, 41].

All the solvers employ an implicit integration algorithm. This is important, because the computation of steady-state solutions using an implicit integration scheme is much more efficient if compared to conventional explicit schemes, if the calculation of thermodynamic states account for a considerable amount of computational time [24].

5.3.2 Thermophysical Models for Toluene and their Comparison

The thermodynamic model developed by Goodwin for toluene [32] is based on a non-analytic multiparameter volumetric equation of state, which was obtained by fitting experimental data available up to 1988. For the simulations documented herein, the Goodwin thermodynamic model is complemented by the transport property model reported in the VDI journal [46].

More recently Lemmon and Span developed a technical equation of state for 20 industrial fluids, among which toluene [33]. The 12-parameter thermodynamic model is formulated in terms of the Helmholtz function [47, 48, 49]. This equation of state is based on a much larger and more recent set of experimental data, which are carefully evaluated. The Helmholtz formulation guarantees high computational efficiency. For the simulations reported in this work, the Lemmon-Span thermodynamic model is complemented by a transport property model based on the Extended Corresponding States (ECS) theory, which takes propane as the reference fluid [50]. Propane is a well-measured fluid, therefore it is reasonable to assume that the prediction of transport properties for this fluid are accurate for engineering applications. Therefore the prediction of transport properties for toluene, using propane as a reference fluid, may be assumed to be of the same quality. This cannot be said from a quantitative viewpoint, however, since in the region of interest, no experimental data are available for toluene. The ECS model for toluene was used because it is the most recent transport property model and is implemented in REFPROP library developed and maintained by the National Institute of Standards and Technology [51].

Table 5.2 shows a comparison of the reported accuracy for relevant thermodynamic properties for the Lemmon-Span and the Goodwin models. It should be noted that the reported accuracy is benchmarked on different data; therefore a direct comparison is misleading. Nonetheless, the reported accuracy of the Lemmon-Span model is in general higher than for the Goodwin model, even though the Lemon-Span model is based (and benchmarked) on a much larger data set, which includes highly accurate measurements that have been conducted between 1989 and 2004.

To provide a first comparison of the two models in the thermodynamic region of interest, values of specific enthalpy, specific entropy and density calculated with these two thermodynamic models and their differences are presented in Fig. 5.3(a). To account for the different reference thermodynamic states of the two models, the specific enthalpy and specific entropy are normalized with respect to their respective values at 1.01325 bar and 400 K. The pressures and temperature range covers the expansion of the fluid through the ORC turbine at design conditions.

Table 5.2: *Reported accuracy of the Lemmon-Span (LS) and the Goodwin (GDW) thermodynamic models in the thermodynamic region of interest.*

Property	LS [33]	GDW [32]
Isobaric specific heat	< 2% (overall) 0.5% ($T \leq 290°C$)	< 3%
Density	0.05%	0.11%
Speed of sound	1%	0.66%

The figure shows that the difference between the thermodynamic properties is larger at higher pressure. This is expected since this thermodynamic region is closer to the critical point, where real gas effects are more pronounced and where accurate experimental data are mandatory in order to obtain good estimations with equations of state. The Lemmon-Span model is therefore expected to perform especially better in this thermodynamic region, as it is fitted on data that were not available when the model by Goodwin was developed. At the inlet of the nozzle the difference in enthalpy is 4.0 %, in entropy 6.5 % and in density 4.3 %. At the outlet the corresponding differences are 0.04 %, 0.02 % and 0.12 %, respectively.

In order to compare the two transport property models, values of dynamic viscosity and thermal conductivity are presented in Fig. 5.3(b). The transport property values are clearly much larger for the VDI model and the largest differences are observed at lower temperatures. The order of magnitude, however, is the same, which results in negligible effects in the fluid dynamics, if compared to the influence of deviations in thermodynamic properties. The relative displacement thickness of a turbulent boundary layer is approximated by $\delta/x = 0.02\text{Re}_x^{-1/7}$, where $\text{Re}_x = \frac{\rho c x}{\mu}$ is the Reynolds number and ρ, c, x and μ denote density, flow velocity, distance from the leading edge and dynamic viscosity, respectively. This shows that the largest differences in transport properties given in Fig. 5.3(b) therefore lead to a relative displacement thickness that is at maximum only 5% thinner. Similarly, the Prandtl number, given by $\text{Pr} = \frac{C_p \mu}{\lambda}$, where C_p and λ are the isobaric specific heat and the thermal conductivity, respectively, is at maximum 50% different. However, in case of forced convection, the heat transfer is more dependent on the order of magnitude of the Prandtl number, which does not change in this case. The negligible effect of the transport property deviations was also verified by comparing simulations with the FINFLO solver using both transport property models.
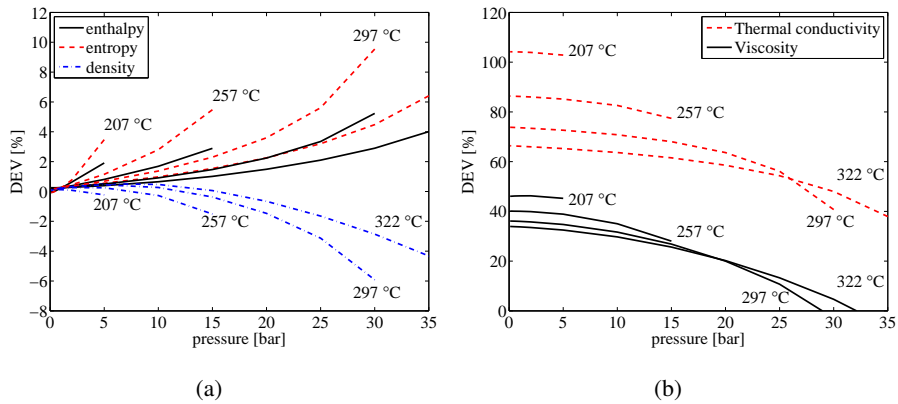
Figure 5.3: *Comparison between thermodynamic and transport property models for toluene in the thermodynamic region of interest. a) Percentage deviations of enthalpy, entropy and density along several isotherms as calculated with the Goodwin [32] model with respect to values calculated with the Lemmon-Span [33] equation of state. b) Percentage differences of viscosity and thermal conductivity along several isotherms calculated with the VDI [46] model with respect to values calculated with the ECS [50] model.*

Interface between Thermophysical Models and Flow Solvers

ZFLOW and FLUENT are directly linked to the libraries, FLUIDPROP and REFPROP respectively, providing estimates of the necessary thermophysical properties. Thermodynamic variables and their partial derivatives required by the implicit time integration scheme [52], are evaluated analytically, together with transport properties. FINFLO, on the other hand, employs polynomial fits for the computationally efficient evaluation of thermophysical properties [20]. Prior to the simulations, two sets of polynomial fits are generated from fluid property data tables obtained by running stand-alone the appropriate program. In one case the table is based on the Goodwin thermodynamic model, while the data for the transport properties are calculated according to the model reported in the VDI journal [46]. In the other, the table is obtained from the Lemmon-Span model, where the transport properties are calculated from the ECS model described in the previous section. Polynomial fits are generated for density, internal energy, dynamic viscosity and thermal conductivity. The specified variables are the pressure and the temperature. The fitting curve is obtained with fourth-order polynomial functions and multivariable regression was utilized to solve for the unknown coefficients.
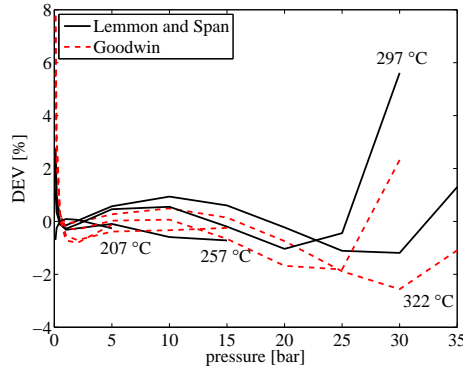
Figure 5.4: *Percentage deviation of density estimations given by polynomial fits [20] with respect to the original data, calculated with the two equations of state [32, 33].*

Polynomial fits, like look-up tables, are flexible, relatively simple to implement and allow for property evaluation at limited extra cost with respect, for instance, to the ideal gas model. A disadvantage is their inherently lower accuracy due to the introduction of fitting or interpolation errors. In Fig. 5.4 the accuracy of the polynomial fits is presented. The maximum deviation with respect to density in the pressure and temperature range of interest is about 3%. Such maximum deviation occurs at the inlet of the nozzle, namely at the highest temperature and pressure.

5.4   Influence of Fluid Thermodynamic Models on Energy Balances

Based on pressure and temperature measurements taken at the turbine inlet of an ORC plant under testing, the calculation using the Goodwin thermodynamic model predicts a specific enthalpy drop due to the expansion through the turbine that is 6.3% higher than the one predicted by means of the Lemmon-Span model. A detailed energy-balance study [53] that relates the enthalpy drop to the measured electrical power output and power absorbed by the main pump showed that the predictions based on the Goodwin equation of state would lead to an improbably high estimation of the isentropic efficiency of the turbine (87%), given the very large expansion ratio. The use of the Lemmon-Span thermodynamic model leads to a more realistic isentropic turbine efficiency of 82%. This is expected

since closer to the critical point, accurate experimental data are mandatory in order to obtain good estimations with equations of state. The Lemmon-Span model is therefore expected to perform especially better in this thermodynamic region, as it is fitted on data that were not available when the model by Goodwin was developed. The use of the Lemmon-Span thermodynamic model shows that, for the ORC power plant operating at design conditions, 6% less shaft power can actually be obtained with respect to the power output estimated by the design calculations, which relied on the Goodwin thermodynamic model.

5.5   Simulation Results

Computed flow field solutions obtained using the different models and flow solvers are systematically compared. In all simulations the pressure and temperature at the stator inlet and pressure ratio are specified. In the figures visualizing the comparison, the aspect ratio is altered, because the blade design is confidential property of the manufacturer. Moreover, only relative differences in fluid properties, as well as scaled overall turbine performance parameters are tabulated and plotted. An overview of results is presented in Table 5.3, which compares the typical differences in relevant flow and performance parameters observed for the various models. For conciseness, only key differences are described in more detail.

5.5.1   Effect of Flow Solvers

Fig. 5.5 shows the Mach number contours of the flow through the turbine stator as calculated using FLUENT and FINFLO, both based on the $k - \epsilon$ turbulence model and the Lemmon-Span thermodynamic model and the Extended Corresponding States-based transport property model. As can be noted, the structure of the flow field is similar. An oblique shock emerges from the trailing edge of the stator nozzle, because the flow entering the mixing region (i.e. the region after the trailing edge) can not maintain its direction due to the flow coming from the adjacent stator. The flow is turned into itself, which, at supersonic velocities, leads to the emergence of an oblique shock wave. The oblique shock wave is reflected from the opposite stator-vane wall towards the outlet of the computational domain and the turbine-rotor inlet. The flow structure is typical of radial high-expansion ratio turbines.

The Mach number at the stator outlet as calculated by FINFLO is higher and the shock wave calculated with FLUENT is less inclined (i.e., directed more towards the normal of the flow direction). This indicates that the oblique shock predicted
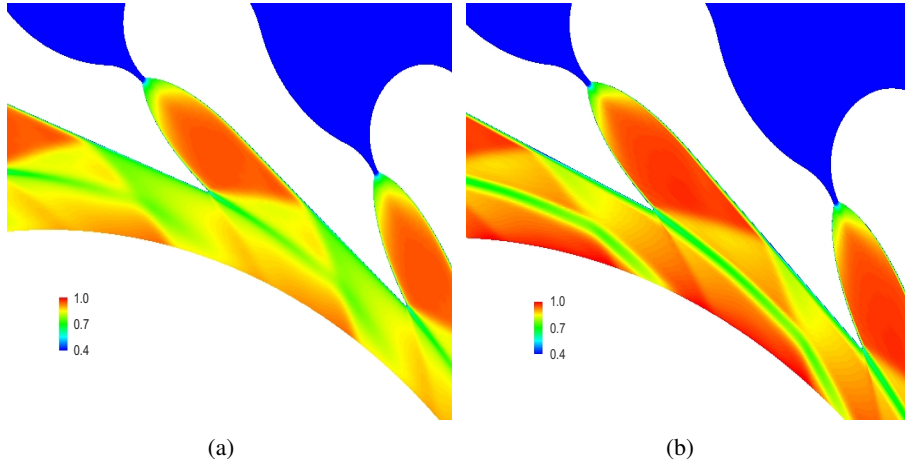
(a)   (b)

Figure 5.5: *Comparison of scaled Mach number fields of the flow through the turbine stator nozzle as calculated by (a) the* FLUENT *and (b) the* FINFLO *viscous flow solvers, respectively. Both flow solvers employ the $k - \epsilon$ turbulence model and the Lemmon-Span thermodynamic model for toluene. The Mach number fields are scaled by one outlet value for reasons of confidentiality requested by the manufacturer.*

by FLUENT is stronger, namely more dissipative, than the one predicted by FIN-FLO. This results into a dramatically lower nozzle isentropic efficiency (6%-point lower for $k - \omega$ and 8%-point lower for $k - \epsilon$) than the one obtained using FINFLO, regardless of the thermodynamic model. The same difference can be observed in the comparison of the inviscid flow fields simulated using ZFLOW and FLUENT (inviscid solver), see Fig. 5.6. Here, the shock wave as predicted by FLUENT is approximately 6% stronger than the one predicted by ZFLOW in terms of the dimensionless shock strength $(p_B - p_A)/(\rho_A a_A^2)$, where A and B denote pre- and post-shock states, respectively. FLUENT also predicts a distinct dissipative wake, which, for inviscid simulations, is purely numerical. These two effects lead to a total pressure loss coefficient $(1 - p_{02}/p_{01})$ that is 32% higher in the case of simulations performed with FLUENT. It is likely that the cause for the consistently more dissipative behavior of FLUENT compared to FINFLO and ZFLOW can be found in the different numerical schemes employed by the solvers. This could be the result of design criteria adopted for a commercial software package, where a somewhat more dissipative characteristic could be favored for the sake of robustness and of a better convergence behavior, at the cost of accuracy.

(a)   (b)
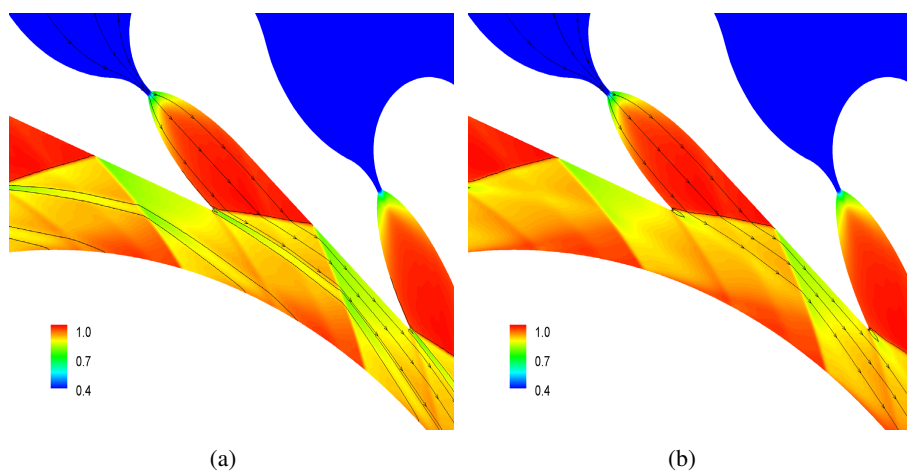
Figure 5.6: *Comparison of scaled Mach number fields of the flow through the turbine stator nozzle as calculated by (a) the inviscid* FLUENT *and (b) the inviscid* ZFLOW *solvers, respectively. Both flow solvers employ the Lemmon-Span thermodynamic model for toluene. The Mach number fields are scaled by one outlet value for reasons of confidentiality requested by the manufacturer. Streamlines and equidistant isolines of total pressure are also indicated.*

Table 5.3: *Typical percentage differences of area-averaged values obtained for the comparison of the models under investigation. The percentage differences are calculated considering* FINFLO *with respect to* FLUENT *(for the $k-\omega$ turbulence model),* ZFLOW *with respect to* FLUENT*, $k-\epsilon$ with respect to $k-\omega$ turbulence model (for Finflo). The accurate thermodynamic models are the Goodwin model with respect to the more recent Lemmon-Span model. The differences in isentropic efficiency and outflow angles are given in percentage-points and degrees, respectively.*

| | | Flow solvers | | Turbulence models (Finflo) | Accurate thermodynamic models | Ideal-gas model (from [25]) |
		FINFLO w.r.t. FLUENT (viscous, $k-\omega$)	ZFLOW w.r.t. FLUENT (inviscid)			
Inlet density	ρ_{01}	0	0	0	-2.1	-40
Outlet pressure	p_2	-16	-6.1	-0.2	1	5
Outlet density	ρ_2	-15	-5.7	-0.4	1	-30
Outlet Mach number	Ma_2	5.3	1.7	-0.5	0	-8
Outlet velocity	c_2	5.3	1.5	-0.5	0	20
Outlet flow angle	α_2, °	-1.5	0.6	-0.4	0	2
Mass flow rate	$\dot{m}$	1.8	-0.1	0.1	-0.8	-14
Isentropic nozzle efficiency	η, %-points	6	n.a.	0	0	n.a.
Specific work	$\dot{W}/\dot{m}$	n.a.	n.a.	n.a.	6	n.a.

5.5.2   Effect of Fluid Thermodynamic Models

The effect on the flow simulation of using different thermodynamic models, namely the equations of state of Lemmon-Span and of Goodwin, is obtained by comparing results obtained with the FINFLO solver. Relevant results are shown in Table 5.3. The differences in the calculated flow parameters appear noticeably small and these are not affected by the choice of the turbulence model. Notice, however, that the Goodwin thermodynamic model does differ significantly from the more accurate Lemmon-Span thermodynamic model in its prediction of the density at the inlet, which is relatively close to the thermodynamic critical point, and the specific enthalpy difference across the complete turbine expansion. The latter leads to a considerably different value for the specific work and stator isentropic efficiency, as described in Section 5.4.

5.5.3   Effect of Turbulence Models

The comparison of the $k - \epsilon$ and $k - \omega$ turbulence models is conducted using the viscous flow solvers adopted in this study. As expected, the overall flow structure does not strongly depend on the chosen turbulence model. However, in the simulation performed with FINFLO and the $k - \omega$ turbulence model shown in Fig. 5.7, a significant difference is observed close to the wall, at the location where the shock wave from the trailing edge is reflected. Here, the $k - \omega$ turbulence model predicts a separation bubble which does not occur if the flow is simulated by means of FLUENT. A separation bubble is highly unsteady and might exist in the actual flow field for this backpressure. At the boundary layer, where the flow field becomes subsonic, the pressure gradient over the shock wave causes the fluid to flow from the high pressure zone to the low pressure zone. The highest pressure is right after the shock wave and therefore the fluid moves upstream in the boundary layer, determining the separation bubble, as shown in Fig. 5.8

The separation bubble affects the direction of both the oblique shock as well as the trailing edge wake (Fig. 5.7). Although it does not have a significant effect on the average values at the stator outlet (see Table 5.3), it does significantly affect the circumferential distribution of flow quantities at the stator outlet/rotor inlet, as shown in Fig. 5.9(b) and Fig. 5.10(b). The maximum periodic change in the flow angle at rotor inlet increases from 8° to 11° and the maximum variation in velocity decreases from 17% to 13%.

1.0
0.7
0.4

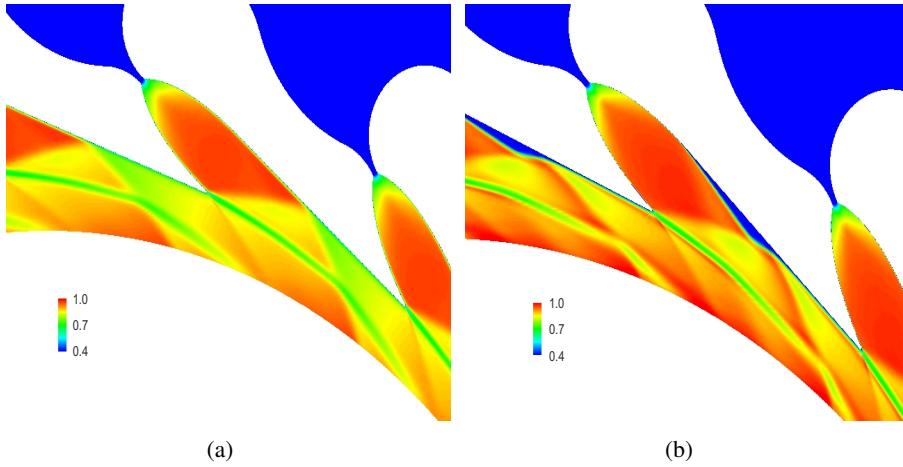(a)   (b)

Figure 5.7: *Comparison of scaled Mach number fields of the flow through the turbine stator nozzle as calculated by (a)* FLUENT *and (b)* FINFLO, *both employing the* $k - \omega$ *turbulence model. The latter combination predicts a shock-induced separation bubble.*
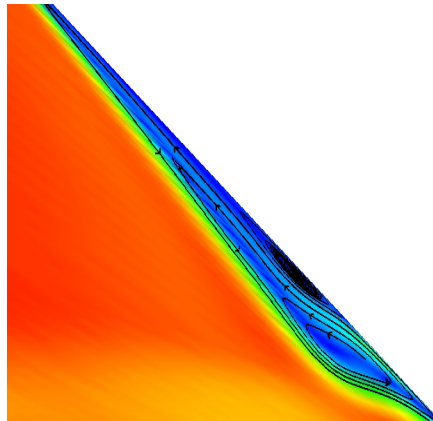

Figure 5.8: *Close-up of the separation bubble located near the right stator wall as predicted by the* FINFLO *flow solver using the* $k - \omega$ *turbulence model.*
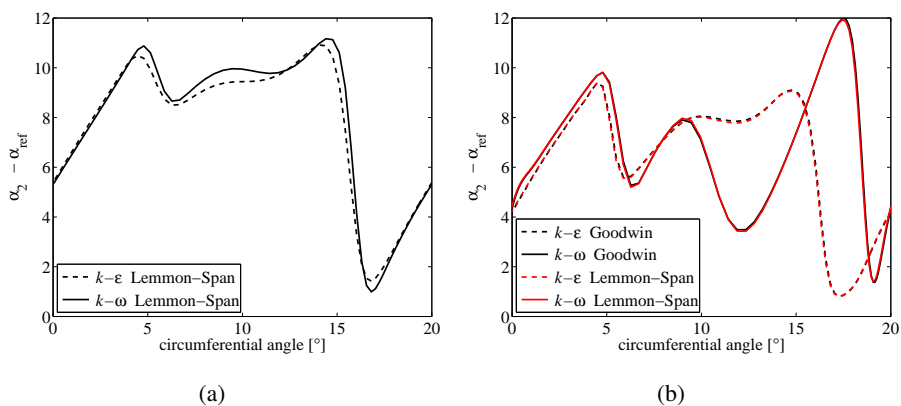
Figure 5.9: *Comparison of the outflow angle with respect to a reference value calculated with (a)* FLUENT *and (b)* FINFLO *using different turbulence models. Both are plotted as a function of the circumferential rotor angle, where the range corresponds to exactly one periodic stator nozzle outlet. The outflow angle is calculated from the radial direction (the lower the value, the more radial is the flow).*
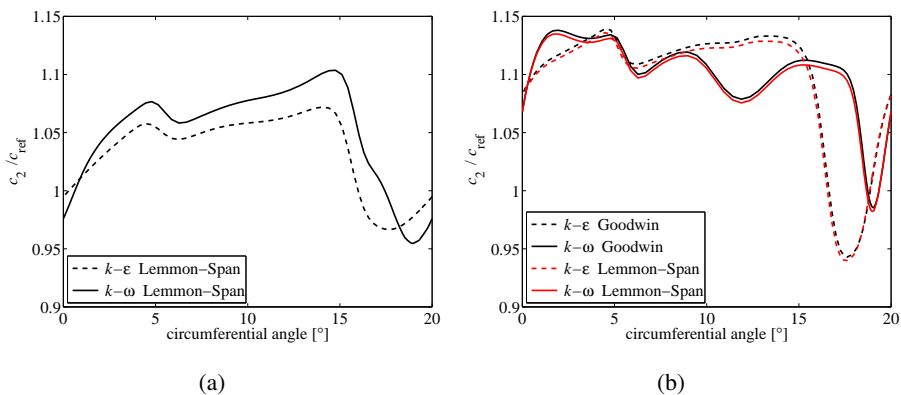

Figure 5.10: *Comparison of the outflow velocity normalized with a reference value as computed by (a)* FLUENT *and (b)* FINFLO *using different turbulence models. The range of the plotted circumferential rotor angle corresponds to exactly one periodic stator nozzle outlet.*

5.6   Conclusions

The work documented in this chapter demonstrates the ability of simulating high-expansion real-gas flows which typically occur in ORC turbine stators, using CFD solvers linked to accurate models for the estimation of the thermophysical properties of the working fluid. The influence of different numerical solvers, fluid thermodynamic models and turbulence models on the simulated flow field has been analyzed.

    With respect to the FINFLO and ZFLOW solvers, the commercial FLUENT solver predicts much stronger shock waves and a more dissipative wake, resulting in a dramatically (6 to 8%-point, depending on the turbulence model) lower isentropic stator efficiency. This could be the result of design criteria adopted for a commercial software package, where a somewhat more dissipative characteristic could be favored for the sake of robustness and of a better convergence behavior, at the cost of accuracy. The two accurate thermodynamic models, namely the equations of state of Lemmon-Span and of Goodwin, lead to small differences in the flow field, especially if compared to the large deviations that would be present if the flow were simulated based on the polytropic ideal gas model. However, the Goodwin thermodynamic model does differ significantly from the more accurate Lemmon-Span thermodynamic model in its prediction of the specific enthalpy difference across the expansion, which leads to a considerably different (6%) value for the specific work and stator isentropic efficiency, and in its prediction of the density at the turbine inlet (2%). Both can be attributed to the fact that the inlet conditions are relatively close to the critical point of the working fluid, where the the thermodynamic properties predicted by the Goodwin thermodynamic model deviate from those based on the more accurate Lemmon Span model. The two tranport property models that are used in combination with the thermodynamic models lead to differences for the predictions of the dynamic viscosity and thermal conductivity that are large compared to the deviations in thermodynamic properties. However, the practical meaning of these differences, i.e., their effect on the flow, e.g., on boundary layer thickness and forced convection heat transfer, is small. The negligible effect of the transport property deviations on the adiabatic simulations was also verified by comparing simulations with the FINFLO solver using both transport property models. The $k - \epsilon$ and $k - \omega$ turbulence models have minor influence on the results, except for the $k - \omega$ turbulence model in combination with the FINFLO solver. For this case, a separation bubble is present at the location where the shock wave reflects on the stator wall. The separation bubble affects the shock wave and wake, in turn affecting in particular the variation of flow velocity and angle along the stator outlet. Averaged quantities at the stator outlet are not

affected significantly.

The above differences point to a need for experimental validation of the flow solvers by comparison to measurements on flows in dense-gas conditions, if CFD tools are to be applied for performance improvements and design of high expansion-ratio turbines operating partly in the real-gas regime. A gain of a few percentage points in the isentropic efficiency of the turbine would lead to a relevant increase in overall conversion efficiency. Such an increase can be obtained at the cost of research and development activities, but has no impact on the capital investment for the power plant.

The extension of the study using three-dimensional viscous-turbulent simulations performed with zFLOW is planned in the near future. Activities are underway for coupling this flow solver to shape-optimization algorithms. Current plans include also the validation of the CFD code using experimental data obtained with a high-temperature Ludwieg-tube for the generation of transonic flows of dense organic vapors, which is in the commissioning phase at the Delft University of Technology.

Nomenclature

a	=	sound speed
c	=	flow velocity
C	=	specific heat
k	=	turbulent kinetic energy
$\dot{m}$	=	mass flow rate
Ma	=	Mach number
p	=	pressure
Pr	=	Prandtl number
Re	=	Reynolds number
T	=	temperature
y	=	wall distance

Greek symbols

α	=	outflow angle
δ	=	displacement thickness
ϵ	=	dissipation rate of turbulent kinetic energy
λ	=	thermal conductivity
μ	=	dynamic viscosity
ρ	=	density
ω	=	specific dissipation rate of turbulent kinetic energy

Subscripts

01	=	stator inlet total conditions
02	=	stator outlet total conditions
04	=	turbine outlet total conditions
2	=	stator outlet conditions
4	=	turbine outlet conditions
A	=	pre-shock state
B	=	post-shock state
p	=	isobaric
th	=	stator throat conditions
x	=	distance from the leading edge

Superscripts

+	=	nondimensional

Acronyms

CFD	=	Computational Fluid Dynamics
DEV	=	Deviation
ECS	=	Extended Corresponding State
ORC	=	Organic Rankine Cycle

References

[1] A. W. Adams. *Encyclopedia of Energy Technology and the Environment*, chapter Organic Rankine engines, pages 2157–2161. John Wiley & Sons Ltd., 1995.

[2] H.P. Bloch and C. Soares. *Turboexpanders and Process Applications*. Gulf Professional Publishing, 2001.

[3] N.G. Kirillov. Analysis of modern natural gas liquefaction technologies. *Chem. Petrol. Eng.*, 40(7-8):401–406, 2004.

[4] L.Y. Bronicki. Organic rankine cycles in geothermal power plants - 25 years of Ormat experience. In *GRC 2007 Annual Meeting, Reno NV*, 2007.

[5] L. Y. Bronicki. Electrical power from moderated temperature geothermal sources with modular mini-power plants. *Geothermics*, 17(1):83–92, 1988.

[6] R. Bini and E. Manciana. Organic Rankine cycle turbogenerators for combined heat and power production from biomass. In *Proceedings of the 3rd Munich Discussion Meeting "Energy Conversion from Biomass Fuels: Current Trends and Future Systems"*, number 96A00412, pages 1–8, 22–23 October 1996.

[7] I. Obernberger, P. Thonhofer, and E. Reisenhofer. Description and evaluation of the new 1000 kW ORC process integrated in the biomass CHP plant in Lienz, Austria. *Euroheat and Power*, 10:1–17, 2002.

[8] R. Bini, A. Duvia, A. Schwarz, M. Gaia, P. Bertuzzi, and W. Righini. Operational results of the first biomass CHP plant in Italy based on Organic Rankine Cycle turbogenerator and overview of a number of plants in operation in Europe since 1998. In *Proceedings of 2nd World Biomass Conference*, pages 1–6, Rzym, Poland, 2004.

[9] U. Drescher and D. Brüggemann. Fluid selection for the organic Rankine cycle (ORC) in biomass power and heat plants. *Appl. Therm. Eng.*, 27:223–228, 2007.

[10] H. Yamaguchi, X. R. Zhang, K. Fujima, M. Enomoto, and N. Sawada. Solar energy powered Rankine cycle using supercritical CO_2. *Appl. Therm. Eng.*, 26(17-18):2345–2354, 2006.

[11] G. Angelino and P. Colonna. Organic Rankine cycles for energy recovery from molten carbonate fuel cells. In *35th Intersociety Energy Conversion Engineering Conference (IECEC)*, number 2000-3052, pages 1–11. AIAA, July 2000.

[12] G. Angelino, M. Gaia, and E. Macchi. A review of Italian activity in the field of organic Rankine cycles. In *VDI Berichte - Proceedings of the International VDI Seminar*, volume 539, pages 465–482, Düsseldorf, 10–12 September 1984. VDI Verlag.

[13] P. Colonna, J. Harinck, S. Rebay, and A. Guardone. Real-gas effects in organic Rankine cycle turbine nozzles. *J. Propul. Power*, 24(2):282–294, March–April 2008.

[14] J. Larjola. Electricity from industrial waste heat using high-speed organic Rankine cycle (ORC). *Int. J. Prod. Econ.*, 41(1-3):227–235, October 1995.

[15] G. Angelino and P. Colonna. Multicomponent working fluids for organic Rankine cycles (ORCs). *Energy*, 23(6):449–463, 1998.

[16] A. Verneau. Supersonic turbines for organic fluid Rankine cycles from 3 to 1300 kW. In *Small High Pressure Ratio Turbines*, VKI Lecture Series 1987-07. Von Karman Institute, June 15–18 1987.

[17] P. Colonna, S. Rebay, and P. Silva. Computer simulations of dense gas flows using complex equations of state for pure fluids and mixtures and state-of-the-art numerical schemes. Scientific report, Università di Brescia, Via Branze, 38, 25123 Brescia, Italy, March 2002.

[18] J. Hoffren. Adaptation of FINFLO for real gases. Technical Report 102, Helsinki University of Technology, Laboratory of Applied Thermodynamics, 1997.

[19] J. Hoffren, T. Talonpoika, J. Larjola, and T. Siikonen. Numerical simulation of real-gas flow in a supersonic turbine nozzle ring. *J. Eng. Gas Turb. Power*, 124(2):395–403, April 2002.

[20] T. Turunen-Saaresti, J. Tang, and J Larjola. A practical real gas model in CFD. In P. Wesseling, E. Onate, and J. Périau, editors, *European Conference on Computational Fluid Dynamics (ECCOMAS CFD 2006)*, Egmond aan Zee, The Netherlands, September 2006.

[21] P. Boncinelli, F. Rubechini, A. Arnone, M. Cecconi, and C. Cortese. Real gas effects in turbomachinery flows - A Computational Fluid Dynamics model for fast computations. *J. Turbomach.*, 126:268–276, April 2004.

[22] P. Cinnella and P. Congedo. A numerical solver for dense gas flows. In *34th AIAA Fluid Dynamics Conference and Exhibit*, number AIAA 2004-2137, pages 1–12. AIAA, June-July 2004.

[23] P. Cinnella and P.M. Congedo. Inviscid and viscous aerodynamics of dense gases. *Journal of Fluid Mechanics*, 580:179–217, 2007.

[24] P. Colonna and S. Rebay. Numerical simulation of dense gas flows on unstructured grids with an implicit high resolution upwind Euler solver. *Int. J. Numer. Meth. Fl.*, 46(7):735–765, 2004.

[25] J. Harinck, P. Colonna, A. Guardone, and S. Rebay. Influence of thermodynamic models in 2D flow simulations of turboexpanders. *J. Turbomach.*, 132(1), 011001, 2010.

[26] J.P. van Buijtenen, J. Larjola, T. Turunen-Saaresti, J. Honkatukia, H. Esa, J. Backman, and A. Reunanen. Design and validation of a new high expansion ratio radial turbine for ORC applications. In *Proceedings of the 5*[th] *European Conference on Turbomachinery*, pages 1–14, 2003.

[27] P. Colonna, S. Rebay, J. Harinck, and A. Guardone. Real-gas effects in ORC turbine flow simulations: Influence of thermodynamic models on flow fields and performance parameters. In P. Wesseling, E. Onate, and J. Périau, editors, *European Conference on Computational Fluid Dynamics (ECCOMAS CFD 2006)*, pages 1–18, September 2006.

[28] FLUENT Inc., Lebanon, NH. *FLUENT 6.3 Documentation*, 2006.

[29] H. Pan. Two-dimensional Navier-Stokes computations of subsonic and supersonic flows through turbine cascades. Technical Report B-40, Series B, Helsinki University of Technology, Finland, 1993.

[30] P. Rautaheimo, E. Salminen, and T. Siikonen. Numerical simulation of the flow in the NASA low-speed centrifugal compressor. Technical Report 119, Helsinki University of Technology, Finland, 1995.

[31] H. Pitkänen and T. Siikonen. Simulation of viscous flow in a centrifugal compressor. Technical Report B-46, Series B, Helsinki University of Technology, Finland, 1995.

[32] R.D. Goodwin. Toluene thermophysical properties from 178 to 800 K at pressures to 1000 bar. *J. Phys. Chem. Ref. Data*, 18(4):1565–1636, 1989.

[33] E.W. Lemmon and R. Span. Short fundamental equations of state for 20 industrial fluids. *J. Chem. Eng. Data*, 51(3):785–850, 2006.

[34] P. L. Roe. Approximate Riemann solvers, parameter vectors, and difference schemes. *J. Comput. Phys.*, 43:357–372, 1981.

[35] K.Y. Chien. Predictions of channel and boundary-layer flows with a low-Reynolds number turbulence model. *AIAA Journal*, 20(1):33–38, 1982.

[36] F. R. Menter. Zonal two equation $k - \omega$ turbulence models for aerodynamic flows. In *24th AIAA Fluid Dynamics Conference*, number 93-2906, 1993.

[37] B.E. Launder and D.B. Spalding. *Lectures in Mathematical Models of Turbulence*. Academic Press, London, 1978.

[38] D. C. Wilcox. *Turbulence modelling in CFD*. DCW Industries Inc., La Canada, CA, 1998.

[39] S. Rebay, D. Pasquale, J. Harinck, and P. Colonna. A Reynolds-averaged Navier Stokes solver coupled to accurate thermodynamic and transport property models. In B. A. Schrefler and U. Perego, editors, *8th World Congress on Computational Mechanics and 5th European Congress on Computational Methods in Applied Sciences and Engineering (WCCM8 ECCOMAS 2008)*. IACM, CIMNE, June 30 – July 5, 2008.

[40] P. Colonna, A. Ghidoni, J. Harinck, S. Rebay, and F. Sussarello. 3D simulation of a radial ORC turbine stator nozzle using accurate thermodynamic models. In B. A. Schrefler and U. Perego, editors, *8th World Congress on Computational Mechanics and 5th European Congress on Computational Methods in Applied Sciences and Engineering (WCCM8 ECCOMAS 2008)*. IACM, CIMNE, June 30 – July 5, 2008.

[41] S. Rebay, P. Colonna, D. Pasquale, and A. Ghidoni. Simulation of the turbulent dense gas flow through the nozzle of an organic Rankine cycle turbine. In F. Heitmeir, F. Martelli, and M. Manna, editors, *Proceedings of the 8th European Turbomachinery Conference*, pages 1137–1148, March 2009.

[42] P. Colonna and T. Van der Stelt. Fluidprop: A program for the estimation of thermophysical properties of fluids. Energy Technology section, Delft University of Technology, The Netherlands (www.fluidprop.com)., 2005.

[43] V. Selmin. The node-centred finite volume approach: bridge between finite differences and finite elements. *Comp. Meths. Appl. Mech. Eng.*, 102:107–138, 1993.

[44] M. Vinokur and J. L. Montagné. Generalized flux-vector splitting and Roe average for an equilibrium real gas. *J. Comput. Phys.*, 89:276, 1990.

[45] P. Colonna, A. Guardone, N. R. Nannan, and C. Zamfirescu. Design of the dense gas flexible asymmetric shock tube. *J. Fluid Eng.-T. ASME*, 130(3):034501–1–6, March 2008.

[46] VDI. *VDI-Wärmeatlas: Berechnungsblätter für den Wärmeubergang (Gebundene Ausgabe)*. Springer, Berlin, 2002. ISBN: 354041200X.

[47] R. Span. *Multiparameter Equations of State - An Accurate Source of Thermodynamic Property Data*. Springer-Verlag, Berlin, 2000.

[48] R. Span and W. Wagner. Equations of state for technical applications. I. Simultaneously optimized functional forms for nonpolar and polar fluids. *Int. J. Thermophys.*, 24(1):1–39, January 2003.

[49] R. Span and W. Wagner. Equations of state for technical applications. II. Results for nonpolar fluids. *Int. J. Thermophys.*, 24(1):41–109, January 2003.

[50] M. L. Huber, A. Laesecke, and R. A. Perkins. Model for the viscosity and thermal conductivity of refrigerants, including a new correlation for the viscosity of R134a. *Ind. Eng. Chem. Res.*, 42:3163–3178, 2003.

[51] E. W. Lemmon, M. O. McLinden, and M. L. Huber. *NIST Reference Fluid Thermodynamic and Transport Properties–REFPROP, version 7.0*. Physical and Chemical Properties Division, National Institute of Standards and Technology, Boulder, CO, August 2002.

[52] P. Colonna and P. Silva. Dense gas thermodynamic properties of single and multi-component fluids for fluid dynamics simulations. *J. Fluid Eng.-T. ASME*, 125(3):414–427, 2003.

[53] J. Harinck, T. Turunen-Saaresti, and P. Colonna. Performance and CFD analyses of a high-expansion ratio radial ORC turbine. Scientific Report ET-2262, Delft University of Technology, Process and Energy Department, Energy Technology Section, Leeghwaterstraat 44, 2628 CA Delft, The Netherlands, October 2007.

6

Supersonic Free-jet Expansion from an Axisymmetric Nozzle

6.1   Introduction

A free jet is a jet of fluid that exhaust, from a nozzle or an orifice, into a large unconfined volume of another fluid. Supersonic free jets are widely used in engineering applications such as propulsive jets and rocket engines [1], sootblowers in boilers [2] and burners in the steelmaking industry. They have also been studied by physicists with the aim of extracting molecular beams from free jets to examine the structure and chemical physics of small clusters [3]. An example of a supersonic free jet is shown in Fig. 6.1.
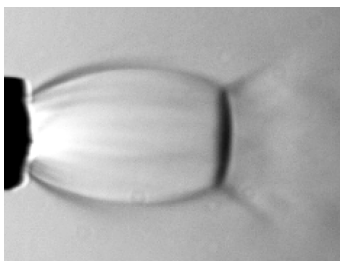

Figure 6.1: *Schlieren image of a supersonic free jet formed by the expansion of nitrogen from a reservoir pressure at 34 bar through an orifice to ambient conditions at atmospheric pressure, from Ref. [4].*

Considerable interest currently exists in the supersonic free-jet expansion of supercritical fluids (SCF), because of the role this rapid expansion plays in the production of nanoscale particles for powders, aerosols or for growing films. In fact, this research project has been partly funded to provide simulation aids to study SCF processes, starting with the Rapid Expansion of Supercritical Solutions (RESS).

In the RESS process, very small particles are produced through the nucleation of compounds dissolved in a supercritical solvent, such as carbon dioxide. The expansion of the supercritical solution through an orifice or capillary tube to subcritical conditions typically leads to pressure ratios of 100-200, resulting in a supersonic free jet being formed. The supercritical reservoir conditions lead to the occurrence of dense-gas effects across the expansion. The expansion rapidly decreases the solubility of the compound so that particles of nano/micro size precipitate and separate from the solution. The RESS process has been studied for nearly 25 years and several reviews are available that describe the properties and uses of the process [5, 6, 7] as well as studies that focus on the (quasi-one-dimensional)

modeling of the fluid dynamics of the process [8, 9, 10, 11, 12].

This chapter first describes the flow structure of supersonic free jets, followed by the validation of the inviscid ZFLOW code for the supersonic free-jet fluid dynamic case. Supersonic free jets pose a difficult and possibly paradigmatic problem: the physics is complex and the simulation numerically hard. It should moreover be noted that at the small scale of the RESS process, controlled free-jet experiments become difficult due to low measurement resolutions. The work presented here serves as the first step towards the simulation and validation of ZFLOW for supersonic free jets generated by the expansion of supercritical fluids.

6.2   Supersonic Free Jets

In a steady supersonic free-jet flow, a nozzle is connected to a plenum chamber or reservoir in which a fluid is at rest at pressure P_{01}. The nozzle discharge reservoir or ambient is at a lower discharge or back pressure P_2. The fluid thus expands (partially) inside the nozzle and forms a supersonic jet outside of the nozzle, in the discharge reservoir. If the pressure at nozzle exit is equal to the back pressure, the nozzle is called "correctly expanded". Conversely, depending on the nozzle shape and back pressure, the flow at the nozzle exit may still be underexpanded, meaning that further expansion is necessary to reach the back pressure. This expansion then takes place inside the free jet and affects its structure considerably. These types of nozzle flow are part of the classical nozzle fluid dynamic problem as covered by fluid dynamic text books [13].

The characteristic structure of a free jet is depicted in Fig. 6.2. It shows a region of hypersonic expansion confined by barrel-shaped shock waves, which is terminated by a strong shock with circular surface normal to the axis of symmetry, called a Mach disk. For a detailed description of the flow features, the reader is referred to Ref. [14].

Much work has been done experimentally [16, 17, 15, 18, 19, 20, 21], analytically [22, 23] and numerically [24, 25, 26, 27, 28, 29, 30, 31] on the structure of axisymmetric supersonic free jets. However, most of the studies on jets have been restricted to correctly-expanded jets from supersonic nozzles or mildly underexpanded jets from sonic nozzles. Little experimental information is available on highly underexpanded jets with pressure ratios above 50 and even less on highly underexpanded jets from supercritical stagnation conditions that also feature dense-gas effects.

One experimental study investigated the influence of various parameters, including some (subcritical) thermodynamic conditions, on the structure of a highly
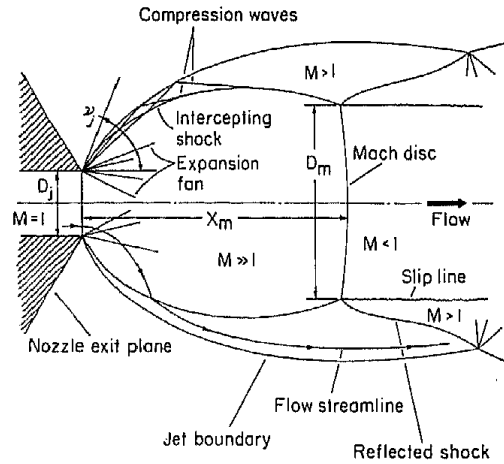
Figure 6.2: *Flow field structure of a highly underexpanded free jet, from Ref. [15].*

underexpanded free jet [15]. The authors found that the Mach disk location is insensitive to the ratio of specific heats, condensation, nozzle lip geometry and absolute inlet pressure value. The diameter of the Mach disk, jet boundary, intercepting shock were found to decrease at high subcritical stagnation density and high specific heat ratio and increase with condensation.

Few experimental data are available on free jets formed by the expansion of fluids from supercritical reservoir conditions. As part of the research into hydrocarbon-fueled supersonic combustion ramjet (scramjet) engines for aerospace applications, experimental and numerical studies have been carried out on the supersonic free jet formed by the injection of supercritical methane/ethylene mixtures into a subcritical nitrogen environment [32, 33]. These studies report that the Mach disk location of the supercritical ethylene jet matches that of an ideal-gas jet. The size of the Mach disk and the expansion angle, however, increase as the injection temperature approaches the critical value, which is a dense-gas effect.

Another study investigated, both experimentally and numerically, the structure of supersonic free-jet expansions of supercritical carbon dioxide impacting on a flat plate [12]. Although reasonable agreement was found between the experimental and numerical results for the pressure, the temperature difference was large and the measurements suffered from poor spacial accuracy due to the small scale of the experiment; the nozzle diameter was 0.05 mm, whereas the diameter

of the wall aperture used to measure total pressure and that of the thermocouple were 0.1 and 0.25 mm, respectively. The study concluded that the quasi-one-dimensional approximation often used by RESS investigators is quite reasonable as a first approximation.

6.3   Inviscid Validation for the Ideal-Gas Underexpanded Supersonic Free-Jet Case

In an effort to validate the zFLOW code for simulations of free-jet expansions, even though only in the case in which the fluid behaves as an ideal gas, results of simulations have been compared to the measurements documented in Ref. [21]. In these experiments, nitrogen was expanded at thermodynamic conditions in the ideal-gas region. The measurement data include pitot pressure values along the axis of symmetry and Schlieren photographs. Although at ideal-gas conditions the free-jet expansion is independent from the absolute reservoir state and only depends on the pressure ratio and ratio of the specific heats, the experimental conditions are given here for completeness. The range of stagnation pressures is $P_{01} = 5, 6, \ldots, 10$ bar, the stagnation temperature is $T_{01} = 20°C$ and the back pressure is $P_2 = 1$ bar. Experimental data pertaining to nozzle geometry 1.5C in the study is used for the validation.

The zFLOW code [34], as described in Section 4.5.1, is used to simulate the inviscid two-dimensional axisymmetric flow field generated by the expansion. Although the gas is ideal, zFLOW uses a complex equation of state, therefore the correct implementation of the code is validated. The computations were performed on an unstructured grid made of 5702 nodes and 9950 triangular elements. The axisymmetric numerical domain with converging-diverging nozzle is shown in Fig. 6.3. Constant pressure boundary outflow conditions equal to the back pressure P_2 are enforced at the side (top and bottom) and far right boundaries. Constant subsonic inflow conditions in terms of pressure and temperature are imposed at the far left boundary to ensure that the flow total conditions at the nozzle inlet are equal to the reservoir stagnation values, namely P_{01} and $T_{01} = 20°C$. Perfect slip and axial symmetry are applied for the nozzle wall and flow centerline, respectively. The thermodynamic properties of nitrogen are calculated with the Helmholtz-based multiparameter equation of state of Kunz and Wagner [35]. The polytropic ideal gas law for nitrogen with ratio of specific heats $\gamma = 1.4$ was used for the first iterations for computational efficiency.

The steady underexpanded free-jet fluid dynamic problem is difficult to solve numerically, especially for high pressure ratios. This is caused by the complex

flow field structure that features various subsonic and supersonic regions (see Fig. 6.2), corresponding to a mixed elliptic-hyperbolic system of equations, with strong discontinuities in the flow variables. The numerical solution to this problem therefore takes a very large number of iterations (more than 5000) to reach convergence. If started with the complex equation of state from a uniform initial flow field, the computation is likely to blow up. It is empirically found that a robust and efficient convergence strategy is to get a first approximate solution adopting the ideal gas law and a first-order accurate spatial discretization scheme. This itself is already difficult but often successfully obtained by starting from a lower pressure ratio, which is gradually increased to the desired value. This step typically requires around 1000 iterations. Subsequently, the complex equation of state and second-order accurate scheme are employed step by step and the computation is continued until the equation residuals meet the convergence criteria (a reduction by three orders of magnitude), which requires an additional 4000 iterations. One solution, if computed using an Intel Pentium 4 2.8 GHz processor, typically requires more than four hours.
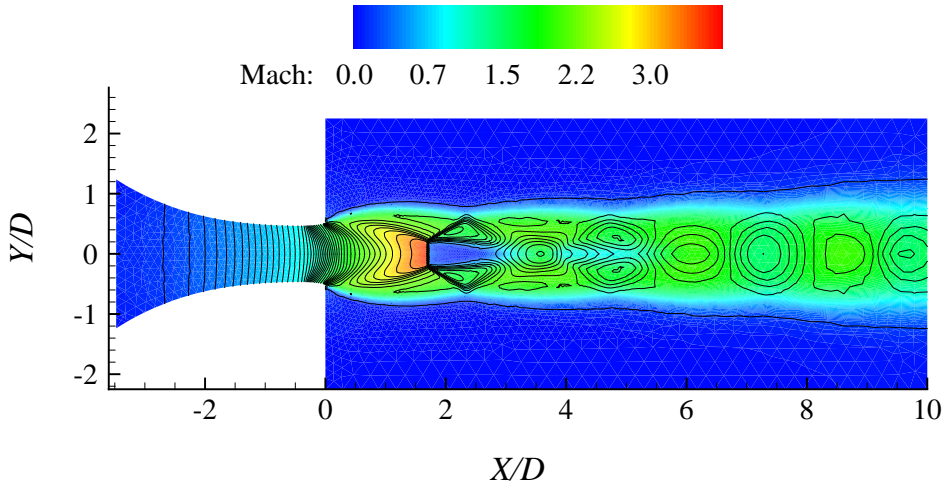

Figure 6.3: *Computed Mach number distribution and iso-density lines of a free-jet expansion of nitrogen at pressure ratio $P_2/P_{01} = 8$. The flow enters the nozzle inlet from a plenum chamber on the far left, passes the nozzle outlet and forms a free jet to accommodate further expansion to atmospheric pressure.*

Fig. 6.3 shows the Mach number distribution computed with ZFLOW. All the relevant features are well captured by the numerical scheme. The experimen-

tal Schlieren image that visualizes the spatial variation in density is compared to its numerical counterpart in Fig. 6.4 for the pressure ratio $P_2/P_{01} = 8$, which shows a good agreement. The location of the Mach disk is dependent on, amongst
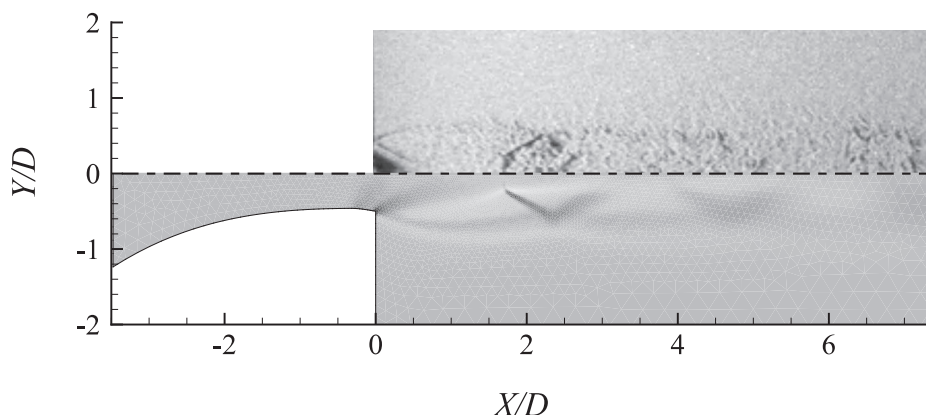

Figure 6.4: *Comparison of the experimental Schlieren photograph (top half, from Ref. [21]) and numerical solution (bottom half) of an ideal-gas nitrogen underexpanded free-jet for the pressure ratio $P_2/P_{01} = 8$. The Mach disk at this pressure ratio is located at $X_m/D = 1.7$.*

other parameters, the pressure ratio. The latter was varied in the experiment and the Mach disk location, nondimensionalized with the nozzle diameter, is plotted against the pressure ratio in Fig. 6.5. The figure shows locations obtained from the experimental Schlieren images, the numerical results and an empirical formula proposed by Driftmyer [18]:

$$\frac{X_m}{D} = \sqrt{\frac{\gamma}{2}\frac{P_e}{P_2}\text{Ma}_{e,\text{design}}^2},$$
(6.1)

where the subscript e denotes nozzle exit conditions. Again, experimental and numerical results show good agreement.

The total pressure values along the axis of symmetry of the free jet are compared in Fig. 6.6 for the pressure ratio $P_2/P_{01} = 8$. A very good agreement between experimental and numerical results is found up to the Mach disk location. As pointed out in Ref. [21], downstream of the Mach disk, viscosity plays a major role in the transfer of momentum across the slip line (see Fig. 6.2) that separates the subsonic region downstream of the Mach disk and the outer supersonic flow.
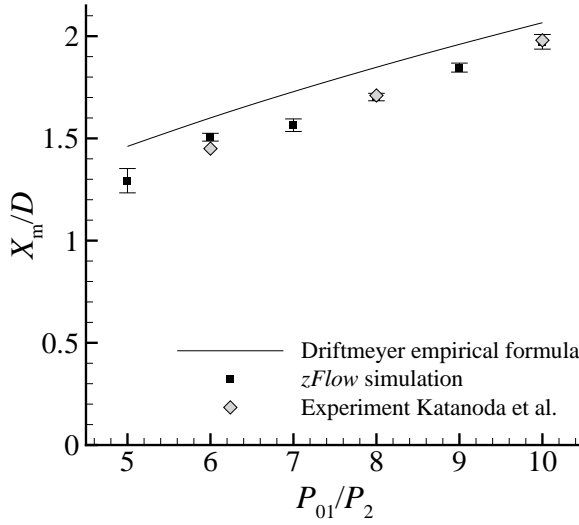
Figure 6.5: *Nondimensional Mach disk location for different values of the pressure ratio. Experimental data are taken from from Ref. [21]. Error bars in the numerical results represent the uncertainty related to the determination of the shock position, the shock being spread across three computational elements.*

This viscous effect cannot be captured by the inviscid simulation, which explains the difference in total pressure downstream in Fig. 6.6.

Figure 6.6:   *Total pressure distribution along the free-jet centerline at pressure ratio $P_2/P_{01} = 8$. Experimental data are taken from from Ref. [21].*

6.4   Conclusions

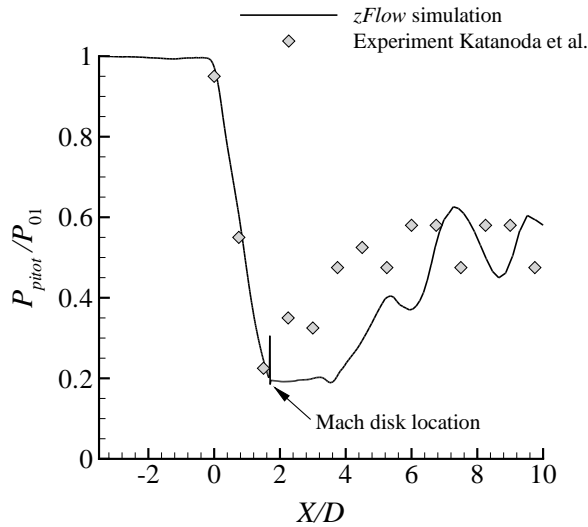The above results show that the ZFLOW inviscid code is well able to represent the underexpanded free-jet fluid dynamic problem, except for the parts that are dominated by viscous effects. This shortcoming will be overcome through the extension of the code to the solution of the Reynolds-Averaged Navier-Stokes equations and the addition of a turbulence model in the axisymmetric plane, which is planned for the near future. This will allow for accurate computation of the dense-gas supersonic free-jet problem and therefore for more insight into the fluid dynamics of the complete RESS process.

The aforementioned code can be used as a predictive method, which is a prerequisite for the improvement and optimization of the RESS process. Provided that it is sufficiently efficient and robust, it could even be used in combination with the optimization method that have been developed as part of this work (see Chapter 7). This advanced system would allow the entire RESS process be optimized, e.g., determining the optimal stagnation conditions and nozzle geometry, to obtain, for instance, a prescribed supersaturation profile or, with the implementation of a particle nucleation model, a desired particle size distribution.

Nomenclature

D	=	nozzle diameter
Ma	=	Mach number
P	=	pressure
X	=	X-coordinate along axis of symmetry
Y	=	Y-coordinate in radial direction

Greek symbols

γ	=	ratio of specific heats

Subscripts

01	=	stagnation state of reservoir
2	=	outlet state
m	=	Mach disk
e	=	nozzle exit
design	=	design conditions

Acronyms

RESS	=	Rapid Expansion of Supercritical Solutions
SCF	=	Supercritical Fluids

References

[1] G.P. Sutton and O. Biblarz. *Rocket Propulsion Elements*. Wiley, John & Sons, Inc., 7th edition, 2001.

[2] M. Eslamiana, A. Pophalia, M. Bussmanna, and H.N. Tan. Breakup of brittle deposits by supersonic air jet: The effects of varying jet and deposit characteristics. *International Journal of Impact Engineering*, 36(2):199–209, 2009.

[3] J. Mukherjee, L.M. Gantayet, and S.A. Ahmad. Free jet expansion of atomic beam: simulation studies of some parameters. *J. Phys. D: Appl. Phys.*, 33:1386–1392, 2000.

[4] C.A. Davy. Surface flow measurement of supersonic impinging microjets. M.Sc. Thesis, Florida State University, FAMU - FSU College of Engineering, 2003.

[5] R. Matson, D. andPeterson and R. Smith. Production of powders and films by the rapid expansion of supercritical solutions. *Journal of Materials Science*, 22:1919–1928., 1987.

[6] Y. Arai. *Supercritical Fluids: Molecular Interactions, Physical Properties, and New Applications*. Springer, 2001.

[7] Y. Sun. *Supercritical fluid technology in materials science and engineering: syntheses, properties, and applications*. CRC Press, 2002.

[8] X. Kwauk and P. Debenedetti. Mathematical modeling of aerosol formation by rapid expansion of supercritical solutions in a converging nozzle. *J. Aerosol Science*, 24:445–469, 1993.

[9] E. Reverchon and P. Pallado. Hydrodynamic modeling of the ress process. *Journal of Supercritical Fluids*, 9(4):216–221, 1996.

[10] M. Weber and M. Thies. *Supercritical fluid technology in materials science and engineering*, chapter Understanding the RESS Proces, pages 387–437. CRC Press, 2002.

[11] B. Helfgen, M. Türk, and K. Schaber. Hydrodynamic and aerosol modelling of the rapid expansion of supercritical solutions (ress-process). *The Journal of Supercritical Fluids*, 26(3):225–242, 2003.

[12] I. Khalil and D.R. Miller. The Structure of Supercritical Fluid Free-Jet. *AIChE J.*, 50(11):2697–2704, 2004.

[13] J. D. Anderson. *Fundamentals of Aerodynamics*. McGrawHill, 2003.

[14] M. Abbet. Mach disk in underexpanded exhaust plumes. *AIAA Journal*, 9(3):512–514, 1971.

[15] S Christ, P.M. Sherman, and D.R. Glass. Study of the highly underexpanded sonic jet. *AIAA Journal*, 10(10):1384–1386, 1966.

[16] E.S. Love, C.E. Grigsby, L.P. Lee, and M.J. Woodling. Experimental and theoretical studies of axisymmetric free jets. Technical Report TR R-6 (19980228067), NASA, 1959.

[17] H. Ashkenas and F.S. Sherman. *Experimental methods in rarified gas dynamics.* Academic Press, New York, 1966.

[18] R.T. Driftmyer. A correlation of freejet data. *AIAA Journal*, 10(8):1093–1095, 1972.

[19] I.S Chang and W.L. Chow. Mach disk from underexpanded axisymmetric nozzle flow. *AIAA Journal*, 12(8):1079–1082, 1974.

[20] J. Panda and R.G. Seasholtz. Measurement of shock structure and shock-votex interaction in underexpanded jets using rayleigh scattering. *Physics of Fluids*, 11(12):3761–3777, 1999.

[21] H. Katanoda, Y. Miyazato, M. Masuda, and K. Matsuo. Pitot pressures of correctly-expanded and underexpanded free jets from axisymmetricsupersonicnozzles. *Shock Waves*, 10:95–101, 2000.

[22] C.K.W. Tam. On the noise of a nearly ideally expanded supersonic jet. *Journal of Fluid Mechanics*, 51:69–96, 1972.

[23] Y.K. Bülent and M.Ö Volkan. Scaling parameters for underexpanded supersonic jets. *Physics of Fluids*, 14(12):4206–4215, 2002.

[24] S.M. Dash and R.D. Thorpe. Shock-capturing method for one- and two-phase supersonic exhaust flow. *AIAA Journal*, 19:842–851, 1981.

[25] P. Woodward and P. Colella. The numerical simulation of two-dimensional fluid flow with strong shocks. *Journal of Computational Physics*, 54:115–173, 1984.

[26] T. Saito, H. Nakatsuji, and K. Teshima. Numerical simulation and visualization of freejet flow-fields. *Trans. Japan Soc. Aero Space Sci.*, 34:161–165, 1986.

[27] K. Teshima and M. Sommerfeld. Visualization and numerical simulation of supersonic microjets. *Experiments in Fluids*, 5(3):197–200, 1987.

[28] A.T. Thies and C.K.W. Tam. Computation of turbulent axisymmetric and nonaxisymmetric jet flows using the k-ϵ model. *AIAA Journal*, 34:309–316, 1996.

[29] M. Jugroot, P.T. Clinton, B.A. Groth1, V.B. Thomson, and B.A. Collings. Numerical investigation of interface region flows in mass spectrometers: neutral gas transport. *J. Phys. D: Appl. Phys.*, 37:1289–1300, 2004.

[30] T.S. Cheng and K.S. Lee. Numerical simulations of underexpanded supersonic jet and free shear layer using weno schemes,. *International Journal of Heat and Fluid Flow*, 26(5):755–770, 2005.

[31] A. Guardone and L. Vigevano. Finite element/volume solution to axisymmetric conservation laws. *Journal of Computational Physics*, 224(2):489–518, 2007.

[32] C.K. Lin, S.K. Cox-Stouffer, and T.A. Jackson. Structures and phase transition processes of supercritical methane/ethylene mixtures injected into a subcritical environment. *Combustion Science and Technology*, 178:129–160, 2006.

[33] A.M. Star, J.R. Edwards, and T.A. Jackson. Numerical simulation of injection of supercritical ethylene into nitrogen. *AIAA Journal of Propulsion and Power*, 22(4):809–819, 2006.

[34] P. Colonna and S. Rebay. Numerical simulation of dense gas flows on unstructured grids with an implicit high resolution upwind Euler solver. *Int. J. Num. Meth. Fluids*, 46:735–765, 2004.

[35] O. Kunz, B. Klimeck, W. Wagner, and M. Jaeschke. The GERG-2004 wide-range reference equation of state for natural gases and other mixtures gerg tm15 2007. *Fortschr.-Ber. VDI, VDI-Verlag*, 557, 2007.

7

Fluid Dynamic Design Optimization

7.1   Introduction

The total conversion efficiency of energy conversion systems is dependent on the efficiency of its components. In particular the efficiency of the turbomachinery components is crucial and can be attained mainly by improvements in fluid dynamic performance. The design process of fluid dynamic geometries has commonly been based on a combination of experience and trial-and-error, since in almost all cases the performance of a geometry can only be determined after experimentation or simulation.

For conventional turbomachinery, the design process includes the choice of machine type, determination of velocity triangles, performance prediction based on semi-empirical loss models and fluid dynamic simulation of the stator and rotor blades. Depending on the results, modifications are made to the design in an attempt to improve it, and one or more design phases are repeated, making it an iterative design process. In addition, various performance goals and requirements have to be considered and possibly weighed, such as high efficiency, reliability and manufacturability and low cost and weight. As a result, turbomachinery design processes are highly complex. For modern steam and gas turbines nowadays, the final design phase is therefore often semi-automated, relying partly on mathematical algorithms to find geometry modifications that improve its performance. The relatively high development and capital investment costs of these components and their crucial importance for the overall system performance justify the development of sophisticated optimization systems even for small performance gains, especially in competitive markets such as theirs. In recent years, powerful optimization systems have been developed for turbomachinery applications that use even more advanced optimization algorithms in combination with predictive methods [1, 2, 3].

In case of turbomachinery design for next-generation energy conversion technologies that involve unconventional fluid dynamics, such as close-to-critical real-gas effects and possibly nonclassical gasdynamic phenomena of Bethe-Zel'dovich-Thompson (BZT) fluids, there is a lack of designer experience and lack of existing designs that can serve as a reference for the design process. Automated optimization is therefore a particularly powerful tool for the design of turbomachinery components for next-generation energy conversion technologies. Examples include supercritical and superheated Organic Rankine Cycle (ORC) turbines; future small-scale ORCs for domestic use, as they require highly complex fluids and will possibly operate at supercritical pressures; the compressor and turbine components that operate at super- and transcritical conditions in the transcritical condensation cycle, the supercritical Brayton cycle and the transcritical vapor

compression cycle; supercritical fluid processes for the production of nanoscale particles and many more applications, as described in Chapter 1. The present chapter documents the development and preliminary results of the application of the optimization system for unconventional real-gas fluid dynamic designs.

7.2   Methods

Optimization methods are essentially computer algorithms that direct the search for more optimal designs, where each design is represented by a set of geometry (or design) variables, e.g., a set of blade profile coordinates, and one or more performance variables, e.g., the efficiency. Since the performance is a function of the geometry, a performance variable represents an objective function, to be optimized by changing the design variables.

7.2.1   Optimization Strategy

Optimization strategies can be subdivided into local and global methods. Local methods start from one user-specified design and perform perturbations on the design variables in a direction that is based on certain information about performance improvement, most often the gradient of the design performance with respect to the design modifications. Global methods apply a set of several designs simultaneously that are mutually compared, combined and altered to obtain a set of designs whose performance is maximized.

Due to the highly nonlinear physics that govern this optimization problem, a highly multimodal fitness function with numerous local optima can be expected [3]. In this case local methods, relying on gradient information, entail a high risk of convergence to local optima without finding the globally optimal design. Moreover, it can be difficult or impossible to provide a local method with a feasible initial design. To avoid this risk, global methods are preferred for the first optimization phase. One of the disadvantage of global methods is that they require performance evaluations for a very large number of designs, which, if the performance evaluation is based on a CFD computation, can be very expensive in terms of time and computational resources. In that case, it is possible to use an additional component that provides quick predictions of the design performance, which partially substitute the CFD computations.

The global optimization strategy described in the following is based on a Genetic Algorithm (GA) as global optimization method, zFLOW as CFD solver and an Artificial Neural Network (ANN) as inexpensive predictive method. Similar

global optimization systems have been developed for conventional (See Refs. [4, 3, 2, 5]) and unconventional (see Refs. [6, 7]) fluid dynamic optimizations. The originality of the work presented here is the acceleration achieved by means of an optimal use of the ANN and the application to the optimization of internal nozzle flows of BZT fluids and, in the near future, flows in ORC turbine nozzles.

7.2.2   Genetic Algorithm

A Genetic Algorithm (GA) is a numerical technique that simulates Darwin's evolutionary theory in order to find the optimum design [8, 1]. According to this theory, an individual (a design) with favorable genetic characteristics (values of the design variables that represent a design) will more likely to survive and produce more performant offsprings. By selecting them as parent, the next generation will have better individuals than the previous one. The operational principle of a standard GA is shown in Fig. 7.1. Pairs of individuals (parents) that have a relatively good performance, i.e., favorable objective function values, are selected from an initially random population of $n_{\text{population}}$ designs, each represented by a real or binary-coded string. Genetic material of this string is subsequently exchanged between them (crossover) and altered within one child (mutation). This process is repeated over a number of generations. The best individual of the last generation is the solution of the GA optimization process. Typically, a GA requires thousands of performance evaluations to converge to an optimal design.

Since GAs use a population of designs, these global optimization methods are able to find the vicinity of the global optimum even if the objective function features local optima [3]. Moreover, in case of optimizations with multiple objective functions, such as the application presented in this chapter, global optimization methods such as the GA are in fact necessary. Due to the population-based approach, however, GAs require a large number of objective function evaluations, which is a drawback particularly if the evaluations require computationally intensive fluid dynamic simulations.

The GA used in this optimization system is the Multiobjective Genetic Algorithm (MOGA-II) developed by Poloni [9, 10], which is implemented in the *modeFrontier* optimization environment [11]. In addition to the classical operators selection, crossover and mutation, this GA also employs directional crossover and elitism, i.e, the best individual of a generation is always copied to new generation and hence preserved.
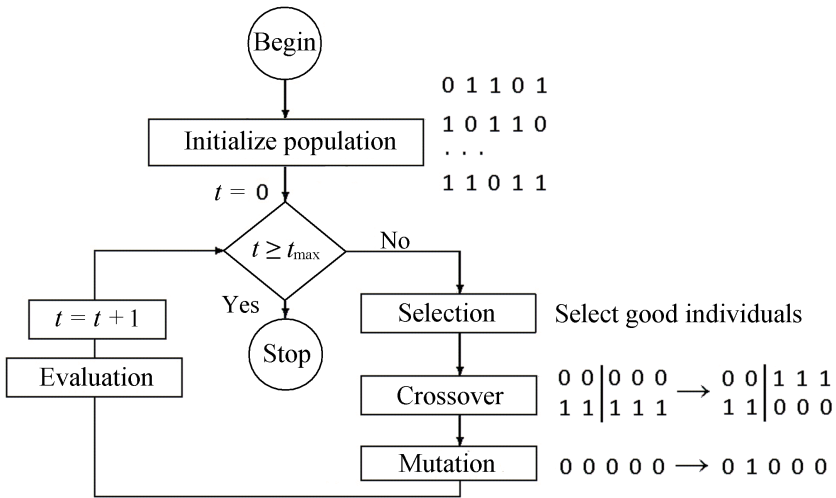
Figure 7.1: *Flowchart of the working principle of a GA, in which t denotes the number of generations.*

7.2.3 Artificial Neural Network

The computational cost of hundreds or thousands of CFD computations that are required by the GA can be prohibitively time-consuming in case of three-dimensional and/or turbulent Reynolds-Averaged Navier Stokes computations, since these solutions typically take several hours to compute. To alleviate this burden and shorten required computational time, inexpensive approximate methods such as response surfaces, Radial Basis functions, Kriging models or Artificial Neural Networks (ANN) can be used. These approximation algorithms partially substitute the CFD computations in the optimization process [12] and serve as inexpensive predictive methods. Artificial Neural Networks are mathematical models that try to simulate the structure and functional aspects of biological neural networks. They offer the greatest degree of flexibility with respect to function representation and generalization capabilities, i.e., the ability to predict the performance of new designs that are very different from already known designs [12]. The former is a required quality for the aim of this study, since the model should be able to approximate possibly highly nonlinear objective functions that can arise from the nonlinearity of the physics combined with possibly complex functions representing, for instance, cost and manufacturability objectives.

An Artificial Neural Network (ANN) is a nonlinear statistical data modeling
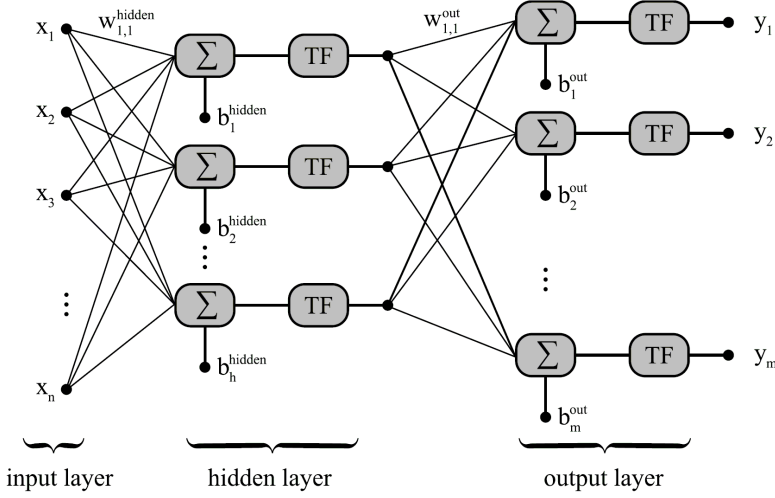
Figure 7.2: *Layout of an ANN with one hidden layer [5].*

tool that can be considered as a simulation of a very small part of the human brain [13, 14]. Fig. 7.2 gives a schematic view of the architecture of a neural network. It consists of a connective network of elementary processing units called nodes or neurons. These neurons are arranged in one input layer, one or more intermediate 'hidden' layers (see Fig. 7.2) and one output layers and joined with connections of different intensity, controlled by weights (denoted by w in Fig. 7.2). The output signal of each node is a transfer function (TF) of a weighted (w) summation of its input signals plus a bias (b):

$$in_j = \sum_{i=1}^{n} w_{i,j}^{hidden} \cdot x_i + b_j^{hidden}. \tag{7.1}$$

The bias acts as an activation threshold to the transfer function. A variety of transfer functions exist, but the sigmoid function is used in most cases:

$$out_j = TF(in_j) = \frac{1}{1 + e^{-in_j}}. \tag{7.2}$$

The resulting complex functional form allows the ANN to model highly nonlinear relationships between inputs and outputs, limited only by the number of hidden nodes chosen by the user. For the ANN to be used in predictive mode, it

first needs to be fitted or 'trained' on a set of given input and output vector samples, in this case a set of designs and their performance values. Training the ANN is done by finding, utilizing a gradient-based method, the connection weights w and biasses b that minimize the least-squares error of the output vectors for the set of training samples.

The ANN adopted in this study is a classical feed-forward Neural Network with one hidden layer, which is trained using an efficient Levenberg-Marquardt back-propagation training algorithm [15]. This ANN is implemented in the *modeFrontier* optimization environment [11].

7.2.4   Optimal settings for ANN and GA

A general methodology to determine the optimum number of hidden neurons does not exist. However, a theoretical upper limit is usually imposed by the number of available training samples [5]. It is believed that the degrees of freedom of the ANN should not exceed the number of training samples, comparable to having at least as many equations as unknowns. The degrees of freedom of the ANN, controlled by the number of hidden nodes, is equal to the number of available training samples if

$$n_{\text{h}}^{\text{crit}} = \frac{n_{\text{train}} \cdot n_{\text{out}} - n_{\text{out}}}{n_{\text{in}} + n_{\text{out}} + 1}, \tag{7.3}$$

where $n_{\text{h}}^{\text{crit}}$ is the critical number of hidden nodes and n_{train}, n_{in} and n_{out} denote the number of training samples and number of input and output nodes, respectively.

The optimal settings for the ANN (number of hidden nodes $n_{\text{h}}^{\text{crit}}$) and GA (population size $n_{\text{population}}$) were determined for $N = 5$, 10 and 20 design variables by performing numerical experiments on test functions. The Rosenbrock and Rastrigin test functions (see Ref. [16]) were selected as they feature the same characteristics that the fitness or objective function of the real optimization problem may have; they are ill-conditioned and have numerous local optima, respectively [3, 17].

It was found that an ANN with a number of hidden nodes of about twice the critical number of hidden nodes shows a considerably improved approximation behavior as compared to the critical number of nodes in terms of regression residual, mean relative error and the Euclidean distance of the ANN global optimum to the test function global optimum in the search space spanned by the design variables. Contrary to expectation, this means that an underdetermined system, i.e., a model that has a number of degrees of freedom that is higher than the number of training samples, performs better, as was also found by some other authors [18].

Note that such a model is prone to overfitting, featuring large spurious oscillations in its function.

For more information on the optimal settings for the GA, the reader is referred to Ref. [3].

7.3   Application

7.3.1   Optimization Acceleration using ANN shown on Test Function

This section aims to show that, by partially substituting the function evaluation with an ANN as inexpensive predictive method, can indeed reduce the number of function evaluations and thereby the duration of an optimization. A test function is used instead of a full fluid dynamic optimization for the sake of repeatability and better performance evaluation, since the optimum of the test function is known a-priori. The results are compared to an optimization that employs only a GA. The test function is a modified version of the DeJong test function with a global minimum at $x_i = 0.3$, for $i = 1, \ldots, N$ [16]. Ten design variables are used ($N = 10$), since this corresponds with the number of design variables required for defining 2D fluid dynamic designs with accuracy and flexibility later on.

First, the initial ANN is trained on a database consisting of 64 samples distributed in the 10-dimensional search space using a Design of Experiments (DOE) technique called Fractional Factorial together with a center sample [12]. This technique attempts to provide the ANN with the most crucial information using as few samples as possible, reducing redundancy and second and third order effects. Fractional Factorial initialization was also used for the distribution of 65 training samples in the aforementioned tests with the ANN.

A GA optimization run is performed using inexpensive function values provided by the trained ANN. The solution is a design that is (or is close to) the global minimum of the ANN. However, since the ANN gives predictions based information contained in a very limited number of training samples, the function value and location (the design variable values) for the solution that is optimal according to the ANN are likely to be different if evaluated with the true test function, as shown in Fig. 7.3. Therefore, this design is validated by evaluating its function value using the test function. The design and its true function value are then added to the training database, a new ANN is trained on the augmented training database and the cycle is repeated by running a new GA optimization on the newly trained ANN. During this iterative process, the ANN gradually learns from its mistakes and, on average, its predictions become more accurate with the increasing number
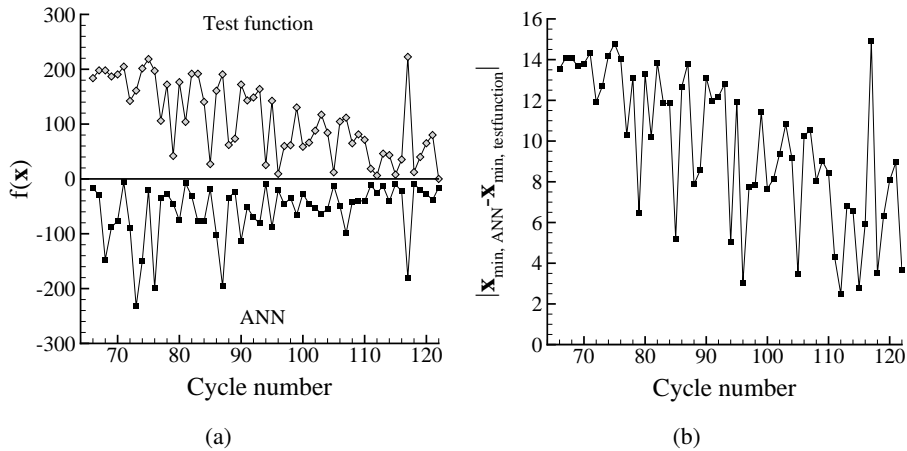
Figure 7.3: *a) Function value of test function and ANN during optimization process; b)*
Euclidean distance of the global minimum of the ANN to the global minimum of the test
function.

of validations, as shown in Fig. 7.4. The process is stopped if no more improve-
ments can be a achieved or if the optimization has evaluated a design that shows
satisfactory improvement. The exemplary optimization with GA and ANN pre-
sented in Fig. 7.4 shows a faster average decrease towards more optimal values
if compared to an optimization that employs only a GA. It is able to find a good
design ($f(\mathbf{x}) = 6.3$) requiring 112 function evaluations, whereas the GA requires
164 function evaluations to find an equally good design. This is a considerable
and important improvement if one considers that each function evaluation may
take in the order of hours in case of fluid dynamic optimizations.

As mentioned before, this overdetermined ANN model is prone to overfitting,
featuring large spurious oscillations in its function, leading to the oscillations in
the convergence behavior observed in Figs 7.3 and 7.4. Overfitting can be avoided
by means of 'early stopping' [19]. In that case the training of the ANN is stopped
if the error with respect to a second set of samples increases, so as to improve the
generalization behavior of the ANN. Unfortunately, this is not possible with the
ANN version implemented in the *modeFrontier* optimization environment. On the
other hand, it must be noted that scientific studies into this aspect do not provide a
univocal proof that early stopping indeed improves generalization behavior [19].
The spurious oscillations caused by overfitting may also be beneficial, as they pre-
vent premature convergence and promote exploration of the search space, which
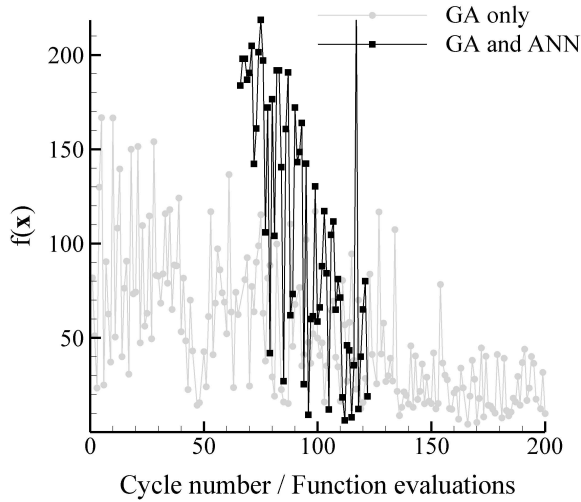
Figure 7.4: *Comparison of test function optimization using only the GA (grey) and using the GA with inexpensive predictor ANN (black). The ANN results are offset, since the training of the first ANN requires 65 function evaluations.*

especially important for highly nonlinear optimization problems. After having found a good design that is close to optimal, the near-perfect optimal design may possibly be found by employing early stopping during the subsequent ANN trainings and/or by switching from the GA to a local gradient-based method for the final minute improvements.

7.3.2   Optimization of a BZT Nozzle

As an example of an optimization involving unconventional nonclassical gasdynamics, this section presents the shape optimization of the divergent part of a nozzle meant for expanding Bethe-Zel'dovich-Thompson (BZT) fluid to a specified Mach number. A simple 2D axisymmetric nozzle is considered and the flow is assumed to be inviscid. Such a CFD computation on average takes only seven minutes, thus eliminating the need for the ANN in the optimization process.

As detailed in Section 2.2, due to the complexity of the fluid molecule and in a small region in a limited thermodynamic region close to saturation, BZT fluids can exhibit nonclassical gasdynamic phenomena, such as rarefaction shock waves. BZT fluids can feature a local decrease in the Mach number upon expansion,

which instead increases monotonically for an isentropic ideal-gas expansion [20, 21, 22, 23]. As shown in Ref. [17], geometries across which BZT flows expand are particularly difficult to optimize for the GA, because the near-optimal flow field is characterized by extremely weak shocks, making the optimization problem ill-conditioned.

For the case described here, the BZT fluid D_6 is selected [24]. Using a zero-dimensional isentropic expansion approach, the thermodynamic conditions at the inlet were determined that maximize the nonmonotonicity of the distributions of the Mach number and cross-sectional area along the expansion pressure. This simple approach cannot relate the pressure nor the cross-sectional area distribution to the nozzle axis coordinate. This would require a solution of either the Euler or Navier-Stokes equations and hence will be part of the result of the optimization.

7.3.2.1 Objective Functions

Two objective functions are to be optimized simultaneously: 1) the aerodynamic performance in terms of shock-free isentropic expanding flow and uniform Mach number equal to Ma = 1.5 along the outlet boundary and 2) the nozzle length, where a short nozzle is preferred, e.g., for reducing weight or cost. These objectives are formulated as two objective functions that should be minimized, that is

$$f_1(\mathbf{x}) = \sqrt{(1.5 - \mathrm{Ma}_X(i))^2 + (\mathrm{Ma}_Y(i))^2} + 10(1 - |P_{02}|) \qquad (7.4)$$

and

$$f_2(\mathbf{x}) = L, \qquad (7.5)$$

in which $\mathrm{Ma}_X(i)$ and $\mathrm{Ma}_Y(i)$ are the X and Y-components of the Mach number at the i-th grid node along the outlet boundary, P_{02} is the total pressure at the nozzle outlet and L is the nozzle length.

7.3.2.2 Nozzle Shape Parameterization

The divergent part of the nozzle geometry is parameterized in order to limit the number of unknowns to be optimized. The parameterization needs to be efficient, i.e., it must require only few design variables, flexible, i.e., able to represent many different shapes, smooth, meaning free of spurious oscillations, and intuitive.

The optimization presented here employs a polynomial spline to define the nozzle shape, but work is underway to improve the shape parameterization using B-splines. The coordinates of the three control points of the spline (x_1, y_1, x_2, y_2, x_3, y_3) are the six design variables, combined in design variable vector $\mathbf{x}$, of the

optimization problem. These control points are bounded to certain ranges, which are indicated in Fig. 7.5. Furthermore, constraints are imposed on combinations of the coordinate values, e.g., to eliminate the possibility of control point two, (x_2, y_2), moving upstream with respect to control point one, (x_1, y_1), see Fig. 7.5.

7.3.2.3 Flow Field Computation using ZFLOW solver

The ZFLOW code [25], as described in Section 4.5.1, is used to compute the flow field solution required to evaluate the aerodynamic performance. Similar structured quadrilateral grids with the same number of cells are generated for all computations to guarantee a comparable accuracy for all the evaluations. As fluid thermodynamic model, the multiparameter equation of state for D_6 is employed [24]. A subsonic inlet boundary condition with reservoir conditions $P_{01} = 18.26$ bar and $T_{01} = 385.55°C$ is imposed, which corresponds to a fundamental derivative of gasdynamics, as introduced in Chapter 2, of $\Gamma_{01} = 4.27$. As supersonic outlet boundary condition a Mach number of Ma $= 2$ is imposed, which is slightly higher than the desired nozzle outlet Mach number Ma $= 1.5$, which should avoid the possible occurrence of recompression shocks.

7.3.2.4 Results

The multi-objective optimization is carried out in parallel on 10 cores of a computational cluster, where each CFD computation is handled by a single core. This exploits the population-based optimization method of the GA. After approximately 3000 function evaluations, a Pareto front is formed that represents the trade-off between aerodynamic performance and nozzle length. One of the Pareto-optimal designs is selected and depicted in Fig. 7.5. This nozzle has both zero total pressure losses, a uniform Mach number outlet of 1.5 and a minimally short length.

The unconventional nonclassical gasdynamic phenomenon that can be observed in this nozzle flow is the nonmonotone Mach number profile along the nozzle axis; in a limited region the Mach number reduces while the flow expands. For slightly different inlet stagnation conditions, the nozzle would have two throats and/or the Mach number would even show a subsonic region embedded in the supersonic region of the divergent part of the nozzle [26, 20, 21]. To obtain the shape of such a correctly expanded nozzle would therefore not be possible with other design methods such as the Method of Characteristics that is commonly used for nozzle design [27]. This is because this method can only be used to design nozzle sections that embed supersonic flow, since it relies on the
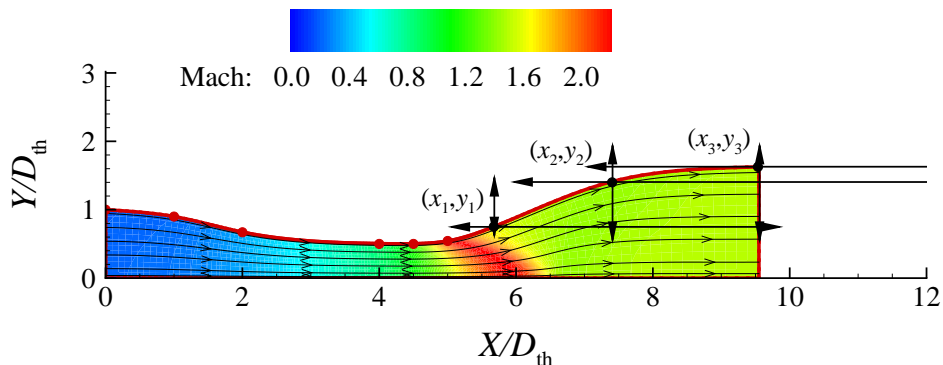
Figure 7.5: *Optimal nozzle shape and flow field for expanding BZT fluid D_6 to Ma = 1.5 from the reservoir conditions $P_{01} = 18.26$ bar and $T_{01} = 385.6°C$. The control points of the polynomial (the optimized design variables) are indicated by the black dots, which are bounded to respective ranges (the search space) represented by the arrows.*

hyperbolic nature of the partial differential equations that govern the flow.

7.4 Conclusions

The optimization of real-gas and nonclassical fluid dynamic designs greatly benefits from a computer-automated global optimization approach. One such optimization method is presented in this chapter. The high number of fluid dynamic evaluations required by a global optimization can be mitigated by an ANN as inexpensive predictive method, which is shown to accelerate the optimization process. The optimization system that has been developed offers a considerable potential for applied research aimed at improving the energy conversion efficiencies of technologies that involve real-gas fluid dynamics. In fact, few alternative methods exist. Secondly, it offers possibilities for extending the theoretical research into BZT flows to optimal expansions in two and three dimensions, paving the way for the exploitation of nonclassical gasdynamic phenomena.

As a result, the work presented here has sparked the interest of several ORC manufacturers (Tri-O-Gen B.V., Turboden s.r.l./Pratt&Whitney Power Systems) and gas turbine technology developers (MTT B.V.) and has subsequently lead to the first follow-up project aimed at improving the performance of an ORC turbine using the methods developed here. It will also be used to support the design of an organic-fluid wind tunnel that will be constructed at the Politecnico di Milano.

Nomenclature

b	=	bias
D	=	nozzle diameter
i	=	grid node number along the outlet boundary
L	=	nozzle length
Ma	=	Mach number
n	=	number (of nodes)
P	=	pressure
TF	=	Transfer Function
w	=	weight
x	=	design variable vector
X	=	X-coordinate along axis of symmetry
Y	=	Y-coordinate in radial direction

Subscripts

01	=	stagnation state of reservoir
02	=	total conditions at outlet
h	=	hidden
in	=	input
out	=	output
population	=	population
th	=	throat
training	=	training samples
X	=	X-component
Y	=	Y-component

Superscript

crit	=	critical

Acronyms

BZT	=	Bethe-Zel'dovich-Thompson
CFD	=	Computational Fluid Dynamics
DOE	=	Design of Experiments
ORC	=	Organic Rankine Cycle

References

[1] J. Periaux and H. Deconinck, editors. *Introduction to Optimization Methods and Tools for Multidisciplinary Design in Aeronautics and Turbomachinery*, VKI Lecture Series LS 2008-07. von Karman Institute for Fluid Dynamics, June 2008.

[2] R.A. Van den Braembussche. *Optimization and Computational Fluid Dynamics*, volume Part II, chapter Numerical Optimization for Advanced Turbomachinery Design, pages 147–189. Springer Berlin Heidelberg, 2008.

[3] J. Harinck, J.P. Van Buijtenen, R.A. Van den Braembussche, and Z. Alshalihi. Optimisation of a 3D radial turbine by means of an improved genetic algorithm. In *Proceedings of the 6th European Conference on Turbomachinery, Fluid Dynamics and Thermodynamics*, pages 1033 – 1042, Lille, France, March 2005.

[4] S. Pierret. *Designing Turbomachinery Blades by Means of the Function Approximation Concept Based on Artificial Neural Network, Genetic Algorithm and the Navier-Stokes Equations*. PhD thesis, von Karman Institute for Fluid Dynamics., 1999.

[5] T. Verstraete. *Multidisciplinary turbomachinery component optimization considering performance, stress, and internal heat transfer*. PhD thesis, von Karman Institute for Fluid Dynamics, 2008.

[6] P.M. Congedo, C. Corre, and P. Cinnella. Airfoil shape optimization for transonic flows of bethe-zel'dovich -thompson fluids. *AIAA journal*, 45(6):1303–1316, 2007.

[7] P. Cinnella and P.M. Congedo. Optimal airfoil shapes for viscous transonic flows of bethezeldovichthompson fluids. *Computers & Fluids*, 37(3):250–264, 2008.

[8] David E. Goldberg. *Genetic Algorithms in Search, Optimization and Machine Learning*. Addison-Wesley Longman Publishing Co., Inc., Boston, MA, 1989.

[9] C. Poloni and V. Pediroda. *Genetic Algorithms and Evolution Strategies in Engineering and Computer Science*, chapter GA coupled with computationally expensive simulations: tools to improve efficiency., page 267288. John Wiley and Sons, England, 1997.

[10] S. Poles. Moga-ii an improved multi-objective genetic algorithm. Technical report, ESTECO, 2003.

[11] *modeFRONTIER 4.0, ESTECO srl, modeFRONTIER User Manual*.

[12] T.W. Simpson, J.D. Peplinski, P.N. Koch, and J.K. Allen. Metamodels for computer-based engineering design: Survey and recommendations. *Engineering with Computers*, 17:129150, 2001.

[13] S. Haykin. *Neural Networks ,*. Number ISBN 0 13 273350 1. Prentice Hall, 2nd edition edition, 1999.

[14] M. Smith. *Neural Networks for Statistical Modeling*. Number ISBN 1-850-32842-0. International Thomson Computer Press, Boston, 1996.

[15] M.T. Hagan and M.B. Menhaj. Training feedforward networks with the Marquardt algorithm. *IEEE Transactions on Neural Networks*, 5(6), 1994.

[16] H. Pohlheim. GEATbx: Genetic and evolutionary algorithm toolbox. URL: http://www.geatbx.com/docu/fcnindex-01.html, 2009.

[17] P. Cinnella and P.M. Congedo. GA-hardness of dense gas optimization problems. In *Proceedings of the 15th IASTED International Conference on Applied Simulation and Modeling, ASM 2006, Rhodes, Greece, 26-28 June 2006.*, 2006.

[18] S. Lawrence, C.L. Giles, and A. Chung Tsoi. Lessons in neural network training: Overfitting may be harder than expected. In *Proceedings of the Fourteenth National Conference on Artificial Intelligence (AAAI-97)*, page 540545, Menlo Park, California, 1997. AAAI Press.

[19] W.A. Sarle. Stopped training and other remedies for overfitting. In *Proceedings of the 27th Symposium on the Interface of Computing Science and Statistics*, pages 352–360, 1995.

[20] M.S. Cramer and N.R. Fry. Nozzle flows of dense gases. *Phys. Fluids A*, 5(5):1246–1259, 1993.

[21] G.H. Schnerr and P. Leidner. Diabatic Supersonic Flows of Dense Gases. *Physics of Fluids A*, 3(10):2445–2458, 1991.

[22] A. Kluwick. Internal flows of dense gases. *Acta Mechanica*, 169:123–143, 2004.

[23] P. Colonna, J. Harinck, S. Rebay, and A. Guardone. Real-gas effects in organic rankine cycle turbine nozzles. *AIAA Journal of Propulsion and Power*, 24(2):282–294, 2008.

[24] P. Colonna, N. R. Nannan, and A. Guardone. Multiparameter equations of state for siloxanes: $[(CH_3)_3\text{-Si-O}_{1/2}]_2\text{-[O-Si-}(CH_3)_2]_{i=1...3}$, and $[O\text{-Si-}(CH_3)_2]_6$. *Fluid Phase Equilib.*, 263(2):115–130, 2008.

[25] P. Colonna and S. Rebay. Numerical simulation of dense gas flows on unstructured grids with an implicit high resolution upwind Euler solver. *Int. J. Num. Meth. Fluids*, 46:735–765, 2004.

[26] M. S. Cramer and L. M. Best. Steady, isentropic flows of dense gases. *Phys. Fluids A*, 3(1):219–226, 1991.

[27] A. C. Aldo and B. M. Argrow. Dense Gas Flows in Minimum Length Nozzles. *J. Fluids Eng.*, 117:270–276, 1994.

8

Conclusions and Perspectives

8.1   Conclusions

This thesis presents theoretical and numerical research conducted into various aspects of the fluid dynamics of supercritical, transcritical, and dense-gas expansions. These expansions are of primary importance in the development of the next generation of thermodynamic energy conversion systems. The motivation for this work stems from the importance of gaining a better understanding of super- and transcritical flows in order to be able to take advantage of the potential efficiency gains offered by employing super- and transcritical thermodynamic cycles in the energy systems of the future. To this purpose, this thesis addresses research questions of how the different thermodynamic behavior of supercritical and dense gases and different working fluid characteristics change the fluid dynamic behavior upon expansion.

The work is divided in self-contained chapters, each addressing a specific subtopic, with its own concluding remarks. The general conclusions and their practical implications are treated in the following.

8.1.1   Part I: Fundamental Aspects

The first part is focussed on the theoretical and fundamental physics of supercritical and dense-gas flows of fluids and its dependence on fluid characteristics.

Conclusions
In isentropic expansions, the Mach number does not depend on the molecular weight of the fluid, but only on molecular complexity and pressure ratio. Remarkably enough, the Mach number can either increase or decrease with molecular complexity, depending on the considered pressure ratio. The post-expansion speed of sound and flow velocity, however, are dependent on both molecular complexity and weight, as well as on the inlet total temperature. The exit flow velocity was found to be a monotonically increasing function of molecular complexity regardless of the expansion ratio, whereas the speed of sound increases monotonically with molecular complexity for high pressure ratios. It should be noted that the sound speed and flow velocity depend much more strongly on molecular weight than on molecular complexity, which in realistic expansions often obscures the influence of the latter. For dense-gas and supercritical expansions, the deviation from gas ideality affects the change in monotonicity in the exit speed of sound and exit Mach number at a given expansion ratio.

Secondly, the effect of using thermodynamic models of various degree of complexity if applied to inviscid flow field simulations of dense-gas and transcritical

(turbo)expanders was investigated. The considered thermodynamic models were, in order of increasing complexity, the polytropic ideal gas law (PIG), the Peng-Robinson-Stryjek-Vera (PRSV) equation of state, which represents the class of cubic equations of state and, thirdly, highly accurate multiparameter equations of state (MPEoS), which were adopted as benchmark reference.

Using the PIG model for moderately nonideal subcritical expansions leads to large deviations with magnitudes of at least $18 - 25\%$ in density, sound speed, velocity and total pressure loss and at least $4 - 10\%$ in Mach number, pressure, temperature and mass flow rate. Lower sound speed values are compensated by similarly lower expansion velocities, leading to a Mach number distribution that is surprisingly similar between the thermodynamic models. The PIG model applied to highly nonideal supercritical expansions leads to a doubling of the deviations' magnitudes. The advantage of the PIG model is that its computational cost is roughly one eleventh (or one third if saturation-checks in the MPEoS are omitted) of the cost of the MPEoS.

For moderately nonideal subcritical expansions, adopting the physically more correct cubic PRSV model leads to comparatively smaller deviations, namely $< 4\%$ in all flow parameters, except for the total pressure loss error, which is comparable to that of the PIG model. The PRSV model is reasonably accurate even for highly nonideal supercritical expansion, for which the errors are at most 4%. The computational cost of the PRSV model is roughly nine times higher than the cost of the PIG model (or twice as high if saturation-checks in the PRSV are omitted).

Contrary to low complexity fluids like water, for complex fluids like toluene and R245fa the deviations in density, speed of sound and velocity ensuing from the use of the PIG model vary strongly along the isentropic expansions. The cause is the PIG model's inability to correctly approximate the qualitative behavior of isentropes of molecularly complex fluids. This invalidates the approach commonly used in practice of correcting the PIG model with a properly chosen constant compressibility factor.

Implications and utilization

The above conclusions can have the following practical implications and utilization. The determination of the influence of the molecular complexity can help to explain the dependence of fluid dynamic expansions on fluid characteristics in various applications. For instance, it can support the determination of the correct similitude criteria in high-Reynolds number transonic wind tunnels employing heavy gases as the working fluid. The outcome is also applicable in the design of

turbines for Organic Rankine Cycle (ORC) turbogenerators. These power plants are suitable for the conversion of an external heat source into electricity in the low-power range (few kW up to few MW), by virtue of an organic working fluid, whose molecule is both complex and heavy. The results of this study show that the low rotational speed typical of ORC turbines is made possible by the high molecular weight of the organic working fluid, not by its complexity.

   The conclusions regarding the influence of thermodynamic models can, amongst others, be useful as guidelines for designers of (turbo)expanders operating in the nonideal-gas region, as it provides an indication of the magnitude and variation of the flow variable errors caused by the adoption of a low-complexity thermodynamic model for real-gas CFD simulations, e.g., in case a MPEoS for a certain fluid is not available or due to computational-time requirements. It is envisioned that in the future CFD methods will be thoroughly validated and will have become much more accurate and reliable allowing them to be used as a design tool coupled with automatic fluid dynamic optimization. In that case, even small errors resulting from the inaccurate computation of thermodynamic properties might play a role.

8.1.2   Part II: Applications

The second part presents two studies of the aforementioned flows in existing applications of thermodynamic energy conversion cycles. It also documents preliminary results of the simulation of supersonic free-jets and the development of an optimization system that is required for the design of unconventional real-gas fluid dynamic designs. The following conclusions can be drawn from this part.

Conclusions
Real-gas effects occurring in stator nozzles of subcritical and supercritical ORCs have been investigated. Two-dimensional Euler simulations of an existing axial ORC stator nozzle were carried out using a CFD code, which is linked to an accurate thermodynamic model for the working fluid (siloxane MDM). The results show that, in order to obtain efficient super- and transcritical expansions in supercritical ORCs, the pressure ratio needs to be significantly reduced to obtain efficient expansion if the same stator nozzle is to be used or, reversely, a nozzle geometry with a much higher exit-to-throat area ratio is required. Furthermore, super- and transcritical expansions are characterized by a low sound speed and velocity and a very high density and mass flow rate as compared to subcritical expansions.

   Various flow solver submodels were compared for the case of the simulated

flow field of an existing radial ORC stator nozzle with very high expansion ratio. In addition to real-gas effects, the flow fields of such ORCs are characterized by a distinct shock wave structure. The models under investigation included the real-gas flow solvers FLUENT, FINFLO and ZFLOW, two turbulence models and two accurate thermodynamic models of the working fluid toluene. The results showed that the commercial flow solver FLUENT is by far the most dissipative flow solver, resulting in large differences in all flow quantities and appreciably lower predictions of the isentropic nozzle efficiency. If the combination of the $k - \omega$ turbulence model and FINFLO solver is adopted, a shock-induced separation bubble appears in the calculated results, which affects in particular the variation of flow velocity and angle along the stator outlet. The accurate thermodynamic models by Lemmon-Span and Goodwin lead to small differences in the flow field, especially if compared to the large deviations that would be present if the flow were simulated based on the ideal gas law. However, the older and less accurate thermodynamic model by Goodwin does differ significantly from the more accurate Lemmon-Span thermodynamic model in its prediction of the specific enthalpy difference, which leads to a considerably different value for the specific work and stator isentropic efficiency. The above differences point to a need for experimental validation of flow solvers in real-gas conditions, if CFD tools are to be applied for performance improvements of high expansion-ratio turbines operating (partly) in the dense-gas regime.

In the above study, two different transport property models are used in combination with the thermodynamic models. The differences in their predictions of the dynamic viscosity and thermal conductivity are large compared to the deviations in thermodynamic properties. However, the practical meaning of these differences, i.e., their effect on the flow, e.g., on boundary layer thickness and forced convection heat transfer, is small. The negligible effect of the transport property deviations on the adiabatic simulations was also verified by comparing simulations with the FINFLO solver using both transport property models.

The inviscid ZFLOW code was validated for the underexpanded free-jet fluid dynamic case. The flow solver is well able to represent supersonic free-jets, except for the parts that are dominated by viscous effects. This work serves as the first step towards the simulation and validation of ZFLOW for highly underexpanded free jets generated by the expansion of supercritical fluids for the purpose of particle production processes.

A global optimization system for unconventional real-gas fluid dynamic designs was developed. The system comprises a Genetic Algorithm, an Artificial Neural Network (ANN) and the ZFLOW flow solver. Considerable acceleration of

the global optimization strategy, which typically requires a very high number of fluid dynamic evaluations, was achieved by means of an optimal use of the ANN. Preliminary results have been obtained by applying it to the optimization of a nozzle expanding a Bethe-Zel'dovich-Thompson (BZT) fluid.

Implications and utilization

The above conclusions can have the following practical implications and utilization. Supercritical ORCs offer a potential efficiency increase with respect to currently operated subcritical ORCs, but have not yet been exploited in current practice. One of the reasons is that, due to the scarcity of experimental evidence and lack of knowledge about the fluid dynamics and heat transfer properties of supercritical and transcritical flows, it is very difficult to accurately design optimal stator nozzle shapes and optimal heat exchangers for operation at supercritical conditions. The results of this study reveal the required changes in stator nozzle design for super- and transcritical operation.

The preliminary results of the global optimization system that has been developed illustrate the potential of this system for the design of unconventional supercritical and dense-gas fluid dynamic shapes needed for next-generation energy conversion technologies. It offers possibilities for applied research aimed at improving the energy conversion efficiencies of technologies that involve real-gas fluid dynamics. The preliminary results have already attracted the attention of several ORC manufacturers (Tri-O-Gen B.V., Turboden s.r.l.) and gas turbine manufacturers (MTT B.V.) and has subsequently lead to the first follow-up project aimed at improving the performance of an ORC turbine design using the methods developed here. It will possibly also be used to support the design of an organic-fluid wind-tunnel that will be built at the Politecnico di Milano. Secondly, it offers possibilities for extending the theoretical research into BZT flows to optimal expansions in two and three dimensions, paving the way for the exploitation of nonclassical gasdynamic phenomena.

8.2 Perspectives

The research conducted during this work has led to a better understanding of the fluid dynamics of expansions of super-, trans- and close-to-critical dense-gas fluids. It has extended the possibilities for exploiting these flows in next-generation energy conversion systems. To further the development of these energy conversion systems, the research of fluid dynamics of super- and close-to-critical dense-gas fluids will need to proceed in the following directions.

There is a need for experimental fluid dynamic data of super- and close-to-critical flows. The current lack of measurement data has hampered the validation of real-gas flow solvers. There is no reason to believe that flow solvers that are validated for ideal-gas conditions and subsequently linked to accurate thermodynamic models that are based on first principles and validated for a wide range of thermodynamic conditions cannot be trusted for inviscid flow simulations at thermodynamically nonideal conditions. However, their future validation should provide the necessary basis for using real-gas solvers to support fundamental research into this type of flows. Reliable experimental data is also necessary to explain the small discrepancies observed between flow simulations based on different flow solvers and thermodynamic and turbulence models, for further (sub)model development and for submodel selection based on suitability for certain applications. Current research plans at the Delft University of Technology therefore include also the validation of the zFLOW code using experimental data obtained with the Flexible Asymmetric Shock Tube (FAST), a high-temperature Ludwieg-tube for the generation of transonic flows of dense organic vapors (see Fig. 8.1(a)), which is in the commissioning phase at the Delft University of Technology [1, 2, 3, 4]. Future experiments could, e.g., be performed on the supersonic flow in a turbine stator nozzle cascade operating in the supercritial range, as shown in Fig. 8.1(b). Pressure measurements could be obtained using small-scale Pitot tubes. With optical access to the stator ring or cascade, techniques such as Schlieren photography or Particle Image Velocimetry (PIV) could provide valuable experimental results regarding flow velocities and direction.

(a)
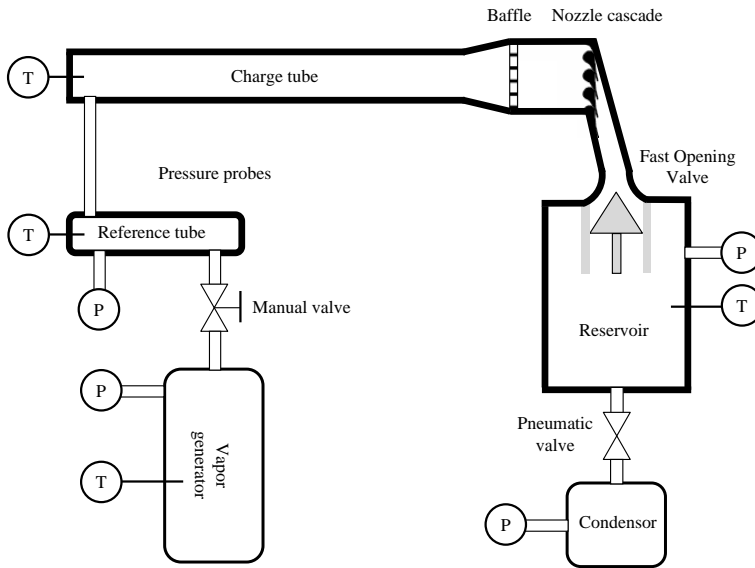
(b)

Figure 8.1: *a) The Flexible Asymmetric Shock Tube (FAST) being commissioned at TU Delft, with Dr. Ryan Nannan behind the controls. b) Current research plans include the extension of the capabilities of this high-temperature Ludwieg-tube to allow for experiments of super- and transcritical expansions in a supersonic stator nozzle cascade with optical measurement techniques. Reliable experiments would provide valuable measurement data for the validation of real-gas flow solvers.*

Viscous turbulent flows at super- and close-to-critical conditions merit further investigation for several reasons. Accounting for viscosity and turbulence in fluid dynamic analysis of ORC turbines would allow for the assessment of viscous losses such as mixing in the turbulent wake with respect to inviscid shock losses and study the influence of viscous phenomena such as shock wave-boundary layer interaction and separation bubbles on the flow field and design. Validated viscous real gas solvers could also be used as a tool to support fundamental research, as for example the interaction of expansion shocks with boundary layers in BZT fluids, which is a relevant phenomenon in shock tube experiments with BZT fluids. Furthermore, these tools could be used to study the anomalous heat transfer of flows at super- and close-to-critical conditions, which, like supercritical expansions, is a research topic that requires further investigation to enable the development of next-generation energy conversion technology such as supercritical ORCs. Real-gas flow solvers such as zFLOW should therefore be extended to the Reynolds-Averaged Navier-Stokes equations in coordinate systems relevant for the mentioned applications and be implemented with an efficient and robust turbulence model. These activities are currently underway.

The global optimization system that has been developed can be applied to various research studies involving super- and close-to-critical flows and in development projects for next-generation energy converters. The global optimization approach based on a Genetic Algorithm is robust in its ability to consistently approach the global optimum design. Finding the exact global optimum design can take a prohibitively large number of flow solutions. The final marginal performance improvements could be gained by extended the global method with a local optimization method such as, e.g., a gradient-based method, which could, for instance, obtain gradient information in an efficient way from the solution of the adjoint equations. With respect to future optimizations of three-dimensional viscous-turbulent flows, it is crucial that the employed flow solver is sufficiently efficient and robust. The efficiency could possibly be improved through the implementation of multigrid acceleration, possibly in combination with the high-order Discontinuous Galerkin method, in the zFLOW solver.

Finally, it should be noted that these research and development activities concerning next-generation energy conversion systems require investments, but they are one-time upfront and have a permanent high yield. For instance, a gain of a few percentage points in the isentropic efficiency of a turbine would lead to a relevant increase in overall system conversion efficiency. Such an increase would require a single investment, but, since it does not entail more costly manufacturing, has no significant impact on the capital investment of energy conversion

systems manufactured in series.

Nomenclature

k	=	turbulent kinetic energy
P	=	pressure
T	=	temperature

Greek symbols

ω	=	specific dissipation rate of turbulent kinetic energy

Acronyms

CFD	=	Computational Fluid Dynamics
FAST	=	Flexible Asymmetric Shock Tube
MPEoS	=	multiparameter equation of state
ORC	=	Organic Rankine Cycle
PIG	=	polytropic ideal gas law
PIV	=	Particle Image Velocimetry
PRSV	=	Peng-Robinson (Stryjek-Vera modified) cubic equation of state

References

[1] C. Zamfirescu and P. Colonna and A. Guardone and R. Nannan. Experimental Options to Investigate BZT Effects in Dense Gases. Scientific Report, Delft University of Technology, Process and Energy Department, Energy Technology Section, Mekelweg 2, 2628 CD Delft, The Netherlands, August 2005.

[2] C. Zamfirescu and P. Colonna. Preliminary Design of the Flexible Asymmetric Shock Tube (FAST) for Dense Gas Experiments. Scientific Report, Delft University of Technology, Process and Energy Department, Energy Technology Section, Mekelweg 2, 2628 CD Delft, The Netherlands, December 2005.

[3] N.R. Nannan and C. Zamfirescu and P. Colonna. Detailed Design of the Flexible Asymmetric Shock Tube (FAST) Facility at the P&E Department of the Delft University of Technology. Technical Report, Delft University of Technology, Process and Energy Department, Energy Technology Section, Mekelweg 2, 2628 CD Delft, The Netherlands, October 2007.

[4] P. Colonna and A. Guardone and N.R. Nannan and C. Zamfirescu. Design of the Dense Gas Flexible Asymmetric Shock Tube. *J. Fluid Eng.-T. ASME*, 130(3):034501-1–6, 2008

Acknowledgement

During these four-plus years I have learned a great deal and have come to know many people, many of whom I consider good friends. This work is also the result of their valuable support during this research period.

First of all, I would like to sincerely thank my supervisor, Piero Colonna. I consider myself lucky to have had you as my doctoral supervisor; without your attention, enthusiasm and guidance my work would most likely not have been this productive. I also greatly appreciate your openness and our discussions about science, people and societies. I admire your vision and belief in the future course that the research and development of energy technologies should follow, and your positive attitude and perseverance under sometimes difficult circumstances.

I am grateful to my promotor, Geert-Jan Witkamp, for his openness, supporting discussions and faith. You allowed us the freedom to determine and pursue the research directions documented in this thesis.

I want to express my gratitude to Alberto Guardone for the assistance that he provided in numerous ways, most notably his considerable help in improving and shaping the paper documented in Chapter 2. This paper, in its present form, would not have been possible without your help.

I am grateful to Stefano Rebay, Antonio Ghidoni and David Pasquale for their support, hospitality and discussions on the numerical and fluid dynamic aspects of our projects. I very much enjoyed the periods in 2005 and 2009 that I spent in Italy, working at the Università degli Studi di Brescia. For me, it has been a unique opportunity to really get to know a country, culture, meet new people and learn the language from within. I would like to thank Piero Colonna and Stefano Rebay for offering me the possiblity to do this.

Many thanks go out to Teemu Turunen-Saaresti for the pleasant cooperation, which resulted in the paper documented in Chapter 5, and for teaching us about the research and actual development of Organic Rankine Cycle technology taking place at the Lappeenranta University of Technology. Thanks also for your humor and for bringing some much-needed Northern European (Finnish) culture into the group, which nicely complemented the presence of the Southern European one.

I would like to express my gratitude to the examination committee. I appreciate their interest in my work and their time devoted to reading and evaluating this dissertation.

I acknowledge the Delft Centre for Sustainable Industrial Processes (DCSIP), represented by Andrzej Stankiewicz, for its financial support that has enabled this research project.

Thanks to all of my colleagues and friends at the Process and Energy department at TU Delft, current and former, and friends I know through them, for their company and for sharing their work and life experiences. There are too many of you to mention explicitly and I value all of your friendships equally, so please allow me to cut short and say: thank you all! We have spent many enjoyable moments together; I hope to be able to continue this in the future.

I would like to especially thank my parents, family and all my close friends, for their continuous support during this work and for supporting my future plans. I am looking forward to catching up on some quality time together now that this monumental work is finally finished. Enough said, let's party!!

John Harinck
Delft, October 31, 2009

Curriculum Vitae

John Harinck was born on December 4, 1978 in Breda, the Netherlands. After graduating from secondary school in 1997, he began his studies in mechanical engineering at Delft University of Technology. As chairman of the student association of the Energy Technology section in 2002, he organized several extracurricular activities for students and staff including an international study tour. He carried out his graduation assignment at the Von Karman Institute for Fluid Dynamics in Rhode-Saint-Genèse, Belgium. In 2004 he obtained his MSc degree with honors. In the following year, he started his doctoral research in the field of advanced energy systems. During this period he worked as a guest researcher at the Universitá degli Studi di Brescia in Italy for eight months, coached several MSc students and co-organized two minisymposia on his research topic at international conferences. The results of his doctoral research have been published in various high-ranking international journals and presented at several conferences.

Publications
Journal articles:

J. Harinck, A. Guardone and P. Colonna, The Influence of Molecular Complexity on Expanding Flows of Ideal and Dense Gases, *Physics of Fluids*, **21**(8), 2009.

J. Harinck, A. Guardone and P. Colonna, Influence of Thermodynamic models in 2D Flow Simulations of Turboexpanders, *ASME Journal of Turbomachinery*, **132**(1), 011001, 2010.

P. Colonna, J. Harinck, S. Rebay, A. Guardone, Real-Gas Effects in Organic Rankine Cycle Turbine Nozzles, *AIAA Journal of Propulsion and Power*, **24**(2), 282-294, 2008.

J. Harinck, T. Turunen-Saaresti, P. Colonna, S. Rebay, J.P. van Buijtenen, Computational Study of a High-Expansion Ratio Radial ORC Turbine Stator, *ASME Journal of Engineering for Gas Turbines and Power*, 2009. (in print)

Conference papers:

S. Rebay, D. Pasquale, J. Harinck, and P. Colonna, A Reynolds-averaged Navier Stokes solver coupled to accurate thermodynamic and transport property models. In: *8th World Congress on Computational Mechanics and 5th European Congress on Computational Methods in Applied Sciences and Engineering (WCCM8 EC-COMAS 2008)*, B. A. Schrefler and U. Perego (editors), IACM, CIMNE, June 30 - July 5, 2008.

P. Colonna, A. Ghidoni, J. Harinck, S. Rebay, and F. Sussarello, 3D simulation of a radial ORC turbine stator nozzle using accurate thermodynamic models. In: *8th World Congress on Computational Mechanics and 5th European Congress on Computational Methods in Applied Sciences and Engineering (WCCM8 ECCO-MAS 2008)*, B. A. Schrefler and U. Perego (editors), IACM, CIMNE, June 30 - July 5, 2008.

P. Colonna, A. Guardone, J. Harinck, and S. Rebay, Numerical Investigation of Dense Gas Effects in Turbine Cascades, In: *Proceedings of the 15th U.S. National Congress on Theoretical and Applied Mechanics*, Boulder (CO), US, June, 2006.

P. Colonna, S. Rebay, J. Harinck and A. Guardone, Real-Gas Effects in ORC Turbine Flow Simulations: Influence of Thermodynamic Models on Flow Fields and Performance Parameters. In: *Proceedings of the European Conference on Computational Fluid Dynamics 2006*, Egmond aan Zee, The Netherlands, September, 2006.

J. Harinck, J.P. Van Buijtenen, R.A. Van den Braembussche, Z. Alshalihi. Optimisation of a 3D Radial Turbine by means of an Improved Genetic Algorithm. In: *Proceedings of the 6th European Conference on Turbomachinery, Fluid Dynamics and Thermodynamics*, pp. 1033 - 1042, Lille, France, March, 2005.

Technical reports:

J. Harinck, T. Turunen-Saaresti, and P. Colonna, Performance and CFD analyses of a high-expansion ratio radial ORC turbine, Delft University of Technology, Process and Energy Department, Energy Technology Section, Leeghwaterstraat 44, 2628 CA Delft, The Netherlands, Scientific Report ET-2262, October 2007, (CONFIDENTIAL).

H. Spliethoff, J. Harinck, C. Ceballos Castillo, et.al. Renewable energy on the California energy market, Delft University of Technology, Technical report, 82 pag., Delft, 2001.